

# Pedestal Characteristics and MHD Stability of H-Mode Plasmas in TCV

THÈSE N° 4917 (2011)

PRÉSENTÉE LE 14 JANVIER 2011  
À LA FACULTÉ SCIENCES DE BASE  
CRPP - PHYSIQUE DU TOKAMAK TCV  
PROGRAMME DOCTORAL EN PHYSIQUE

ÉCOLE POLYTECHNIQUE FÉDÉRALE DE LAUSANNE

POUR L'OBTENTION DU GRADE DE DOCTEUR ÈS SCIENCES

PAR

Andreas PITZSCHKE

acceptée sur proposition du jury:

Prof. N. Grandjean, président du jury  
Dr R. Behn, directeur de thèse  
Dr S. Medvedev, rapporteur  
Dr O. Sauter, rapporteur  
Prof. H. Zohm, rapporteur



ÉCOLE POLYTECHNIQUE  
FÉDÉRALE DE LAUSANNE

Suisse  
2011

“I refuse to prove that I exist, ” says God, “for proof denies faith, and  
without faith I am nothing”.

“But,” says Man, “the Babel fish is a dead giveaway, isn’t it? It could not  
have evolved by chance. It proves that you exist, and so therefore, by  
your own arguments, you don’t. QED.”

“Oh dear, ” says God, “I hadn’t thought of that, ” and promptly  
disappears in a puff of logic.

Hitchhiker’s Guide to the Galaxy, Douglas Adams

# Abstract

The tokamak à configuration variable (TCV) is unique in its ability to create a variety of plasma shapes and to heat the electron population in high density regimes using microwave power at the third harmonic of the electron cyclotron frequency. In the frame of this thesis, the impact of plasma shaping and heating on the properties of the edge transport barrier (ETB) in the high confinement mode (H-mode) was studied. This mode of operation is foreseen as one of the reference scenarios for ITER, the International Tokamak Experimental Reactor, which is being built to demonstrate the feasibility of thermonuclear fusion using magnetic confinement.

A feature of H-mode regime operation are edge localized modes (ELMs), instabilities driven by the steep pressure gradients that form in the plasma edge region due to a transport barrier. During an ELM event, energy and particles are expelled from the plasma in a short burst. This will cause serious problems with respect to the heat load on plasma facing components in a tokamak of the size of ITER. Understanding of the phenomena associated with ELMs is thus required and dedicated investigations of their theory and experimental observations are carried out in many laboratories worldwide. This thesis presents several experimental and numerical investigations of tokamak behavior for configurations where the plasma edge plays an important role.

From the experimental viewpoint, studies of transport barriers are challenging, as plasma parameters change strongly within a narrow spatial region. As part of the work presented here, the TCV Thomson scattering system was upgraded to meet the requirements for diagnosing electron temperature and density with high spatial resolution in the region of internal and external transport barriers. Simultaneously, the data analysis was significantly improved to cope with statistical uncertainties and alleviate eventual systematic errors.

For measurements of the time evolution of density and temperature profile during the

---

ELM cycle, the low repetition rate of the lasers used for Thomson scattering is a limiting. Although the system on TCV comprises 3 laser units that may be triggered in sequence with time separations down to 1 ms, time evolution over longer periods can only be reconstructed from repetitive events. In this context, an adjustment of the laser trigger to improve the synchronization with the ELM event is an advantage. A method was developed and implemented to generate a synchronizing trigger sequence, by a real-time monitoring of the D-alpha emission, which provides a marker for the ELM event.

Recently, a “snowflake” (SF) divertor configuration, proposed as a possible solution to reduce the plasma-wall interaction by changing the divertor’s poloidal magnetic field topology, was generated, for the first time, in TCV. A numerical code (KINX), based on a magnetohydrodynamic model (ideal MHD), was used to investigate the stability limits of this configuration under H-mode conditions and compare them with a similar standard single-null equilibrium. In a series of experiments, improved energy confinement was found and explained by improved stability of the edge region in the SF configuration.

The influence of the pedestal structure in ELMy H-mode plasmas on the energy confinement and on ELM energy losses was investigated. The different ELM regimes found in TCV were analyzed, in particular the transition between type-III to type-I ELMs. The operational boundary of each ELM regime was characterized and verified by ideal MHD stability simulations for the ETB region. Recent studies on the scaling of the pedestal width with normalized poloidal pressure were confirmed. Using the capabilities of TCV, the influence of plasma shaping on pedestal parameters and MHD stability limits was investigated.

In the past, models were developed to describe the onset of type-I ELMs, which are associated with modes in the ETB region arising from a coupling of pressure- and current-driven instabilities (coupled kink-ballooning modes). Experimental studies were performed to trace the temporal evolution of pedestal parameters characterizing the ETB during an ELM cycle. The results of these experiments were analyzed using information from MHD stability calculations. It is concluded that these models are capable of predicting limits as necessary conditions for ELM activity, but are not sufficient to fully explain ELM triggering.

KEYWORDS: plasma physics, nuclear fusion, tokamak, TCV, Thomson scattering, high confinement mode, edge localized modes, ideal magnetohydrodynamic model

# Kurzfassung

Der Tokamak “à configuration variable” (TCV) besitzt die einzigartige Fähigkeit, eine Vielzahl von Plasmaformen zu realisieren und die Elektronenpopulation in Hochdichteplasmen mit Hilfe von elektromagnetischen Wellen zu heizen. Im Rahmen dieser Arbeit wurde der Einfluss von verschiedenen Plasmaformen und Heizleistungen auf die Eigenschaften der Randtransportbarriere (ETB) im “high confinement mode” (H-mode) untersucht. Die Plasmaentladung in H-mode ist eins der Referenzscenarios für ITER, “International Tokamak Experimental Reaktor”, welcher sich in der Bauphase befindet und die Realisierbarkeit von thermonuklearer Fusion basierend auf dem Konzept des magnetischen Einschlusses demonstrieren soll.

Der H-mode ist gekennzeichnet durch eine Transportbarriere in der äußeren Region des Plasmas. In der Region der Transportbarriere, Wärme- und Teilchentransport sind stark verringert, sodaß steile Druckgradienten entstehen können, welche zyklisch auftretende Plasmaintabilitäten, “edge localized modes” (ELMs), hervorrufen. Während dem Auftreten eines ELMs werden Plasmaenergie und -teilchen in Form eines kurzen Pulses aus dem Plasma ausgeworfen, der eine Gefahr für die inneren Reaktorkomponenten darstellt. Das Verständnis dieses Phänomens ist äußerst wichtig für zukünftige Fusionsreaktoren. Die Physik dieses Phänomen wird weltweit von Forschungseinrichtungen experimentell und theoretisch untersucht. Diese Arbeit präsentiert diesbezüglich ein Vielzahl von experimentellen Untersuchungen und deren Interpretation durch numerische Simulationen.

Die experimentelle Untersuchung von Transportbarrieren ist sehr anspruchsvoll, da sich die charakteristischen Plasmagrößen innerhalb der Transportbarriere stark verändern können. Ein großer Teil der experimentellen Untersuchungen wurden mit Hilfe des TCV Thomsonstreusystems durchgeführt. Das System wurde zur Messung von hochauflösenden Profilen von Elektronentemperatur und -dichte angepasst und erweitert. Zu-

---

dem wurde das Datenanalyseverfahren stark verbessert um statistische und systematische Fehler zu minimieren.

Die Messung der zeitlichen Entwicklung der Temperatur- und Dichteprofile während eines ELM-Zyklus war auf Grund der niedrigen Messfrequenz der Diagnostik limitiert. Obwohl das Meßsystem aus 3 unabhängigen Lasereinheiten besteht, welche mit einem Zeitversatz von minimal 1 ms gefeuert werden können, musste die gesamte Profilentwicklung mit Hilfe von mehreren wiederholbaren Experimenten rekonstruiert werden. In diesem Kontext ist die Synchronisierung der Lasersteuerung mit dem Auftreten eines ELMs ein Vorteil. Zu diesem Zweck wurde ein Kontrollmechanismus entworfen und implementiert, welcher Lasertriggers basierend auf der Messung der  $D_\alpha$ -Lichtemission in Echtzeit generiert.

Die “snowflake” (SF) Divertorkonfiguration wurde kürzlich zur Verringerung der Wechselwirkungen zwischen Plasma und Reaktorwand vorgeschlagen. Diese Konfiguration wurde durch Optimierungen der magnetischen Feldtopologie zum ersten Mal in TCV realisiert. Der numerische Code KINX, basierend auf dem magneto-hydrodynamischen (ideale MHD) Plasmamodell, wurde zur Untersuchung der H-mode Plasmastabilitätsgrenzen in dieser Konfiguration verwendet und dessen Resultate mit der herkömmlichen Plasmakonfiguration (“single-null”) verglichen. In einer Reihe von Experimenten in dieser Konfiguration wurde ein erhöhter Energieeinschluss gemessen, welcher durch die Verbesserung der Plasmastabilitätsgrenzen erklärt werden konnte.

Der Einfluss der H-mode Transportbarriere auf die Energieeinschlusszeit und die durch ELMs hervorgerufenen Energieverluste wurde untersucht für drei verschiedene ELM-Regime. Die Stabilitätsgrenzen von H-mode Plasmen in TCV wurden charakterisiert und durch ideale MHD-Rechnungen verifiziert. Untersuchungen der Skalierung der Barrierenbreite als Funktion des normierten poloidalen Drucks wurden bestätigt. Zudem wurde der Einfluss von verschiedenen Plasmaformen auf die Barrieren- und Plasmaeigenschaften untersucht und mit Hilfe der idealen MHD interpretiert.

In der Vergangenheit wurden Modelle entwickelt, die das Auftreten von Typ-I ELMs beschreiben, welche in Fusionsplasmen erwartet werden und durch hohe ELM-Energien gekennzeichnet sind. Diese Klasse von ELMs wird mit dem Auftreten von druck- und stromgetriebenen Instabilitäten (“coupled kink-ballooning mode”) in Verbindung gebracht. Experimentelle Untersuchungen zur zeitlichen Entwicklung der Barriere wurden durchgeführt und deren Ergebnisse in Zusammenhang mit der idealen MHD-Theorie gebracht.

---

Es konnte gezeigt werden, dass die quantitativen Vorhersagen dieser Modelle gut mit den Messungen übereinstimmen, allerdings nicht den ELM-Trigger beschreiben können.

SCHLÜSSELWÖRTER: Plasmaphysik, nukleare Fusion, Tokamak, TCV, Thomsonstreuung, “high confinement mode”, “edge localized modes”, ideales magneto-hydrodynamisches Plasmamodell

# Sommario

Il tokamak a configurazione variabile (TCV) presenta la caratteristica peculiare di permettere la creazione di una grande varietà di configurazioni del plasma (plasma shaping) ed inoltre di riscaldare la popolazione elettronica in regimi ad alta densità, per mezzo di microonde alla terza armonica della frequenza elettronica di ciclotrone. Nell'ambito di questa tesi è stata studiata l'influenza della configurazione del plasma e del suo riscaldamento sulle proprietà delle barriere presenti nella zona periferica del plasma stesso (edge transport barrier, ETB), nel modo di confinamento denominato H-mode. Si prevede che questo modo di funzionamento sia una delle configurazioni di riferimento per ITER (International Tokamak Experimental Reactor). Esso verrà realizzato allo scopo di dimostrare la fattibilità della fusione termonucleare utilizzando il confinamento magnetico.

Una caratteristica fondamentale del funzionamento in H-mode è il verificarsi degli ELMs (edge localized modes), instabilità causate dalla presenza di elevati gradienti di pressione che si formano nella zona periferica del plasma (edge) a causa di una barriera di trasporto. Durante un ELM le particelle e l'energia sono espulse dal plasma in una scarica molto rapida. Questo evento potrebbe provocare seri problemi di carico termico su di alcuni componenti a contatto con il plasma in un tokamak delle dimensioni di ITER. La piena comprensione dei fenomeni associati agli ELMs è dunque di fondamentale importanza e studi teorici ed osservazioni sperimentali sono intrapresi in molti laboratori in tutto il mondo. Questa tesi presenta numerose osservazioni sperimentali e simulazioni numeriche del comportamento del tokamak in configurazioni in cui la zona dell'edge gioca un ruolo importante.

Dal punto di vista sperimentale gli studi sulle barriere di trasporto sono di difficile realizzazione, siccome i parametri di plasma variano ampiamente in una regione spaziale di dimensioni ridotte. Parte del lavoro qui presentato consiste nel miglioramento del sistema di scattering Thomson di TCV, al fine di soddisfare i requisiti per la raccolta



---

dei dati relativi alla temperatura elettronica e alla densità, con alta risoluzione spaziale, nella regione in cui sono localizzate le barriere di trasporto esterne ed interne. Contemporaneamente l'analisi dei dati raccolti è stata significativamente migliorata per quanto concerne l'incertezza statistica e la correzione di eventuali errori sistematici.

La bassa frequenza di ripetizione dei laser utilizzati per lo scattering Thomson rappresenta un limite alla misurazione dell'evoluzione temporale della densità e della temperatura durante un ciclo ELM. Sebbene il sistema disponibile su TCV sia composto da 3 laser che possono essere azionati in sequenza con un intervallo temporale minimo di 1ms, tuttavia l'evoluzione temporale su intervalli più lunghi può essere ricostruita solo tramite eventi ripetuti. La regolazione dell'istante di azionamento del laser (trigger), al fine di migliorare la sincronizzazione con un evento ELM, è stata quindi di grande aiuto in questo ambito. Un nuovo metodo per la generazione di una sequenza di azionamento dei laser, basato sul monitoraggio in tempo reale dell'emissione D-alpha (che caratterizza l'evento ELM), è stato studiato ed implementato.

Recentemente è stata realizzata per la prima volta in TCV una nuova configurazione di divertore denominata "snowflake" (SF). Proposta come possibile soluzione per ridurre le interazioni plasma-parete, prevede la modifica della topologia del campo magnetico poloidale del divertore. Il codice numerico KINX, basato sul modello magneto-idrodinamico ideale (MHD), è stato utilizzato per investigare i limiti di stabilità di questo regime in condizioni H-mode e per paragonarle ad un simile equilibrio standard "single-null". In una serie di esperimenti si è effettivamente verificato un miglioramento del confinamento energetico, giustificato da una crescente stabilità nella zona dell'edge nella configurazione SF.

È stata inoltre investigata l'influenza della struttura del pedestal negli ELMy H-mode sul confinamento e sulla perdita dell'energia durante il verificarsi di un ELM. Sono stati analizzati i diversi regimi ELM riscontrati in TCV, in particolare la transizione da tipo-III a tipo-I. Il limite di funzionamento di ciascun tipo di regime ELM è stato descritto e verificato tramite simulazioni MHD per la regione ETB. Recenti studi nell'ambito della variazione (scaling) della larghezza del pedestal con la pressione poloidale normalizzata sono stati confermati. Sfruttando le possibilità operative di TCV, sono stati studiati l'influenza della forma del plasma sui parametri del pedestal e sui limiti della stabilità MHD.

In passato sono stati sviluppati alcuni modelli per descrivere l'insorgere degli ELMs tipo-I. Essi sono associati alla presenza di un accoppiamento fra le instabilità dovute alla

---

pressione e quelle dovute alla corrente (modi accoppiati kink-ballooning). Alcuni studi sperimentali sono stati realizzati per tracciare l'evoluzione temporale dei parametri del pedestal che caratterizzano la regione EBT durante un ciclo ELM. I risultati di questi esperimenti sono stati analizzati utilizzando le informazioni ottenute dagli studi di stabilità MHD. Si conclude che questi modelli sono in grado di predire le condizioni necessarie al svilupparsi di una instabilità di tipo ELM, ma non sono sufficienti per una spiegazione esaustiva delle cause scatenanti un ELM.

PAROLE CHIAVE: fisica del plasma, fusione nucleare, tokamak, TCV, scattering Thomson, high confinement mode, edge localized modes, modello magnetoidrodinamico ideale.

# Contents

<b>1. Introduction</b>	<b>1</b>
1.1. Nuclear fusion . . . . .	1
1.1.1. Magnetic confinement . . . . .	2
1.1.2. Tokamak principle . . . . .	2
1.1.3. Plasma heating . . . . .	4
1.1.4. Power plant concept and improved plasma scenarios . . . . .	5
1.2. Tokamak à configuration variable . . . . .	6
1.2.1. The Tokamak . . . . .	6
1.2.2. Electron cyclotron heating . . . . .	7
1.2.3. Selected diagnostics . . . . .	8
1.3. Motivation for the thesis . . . . .	12
1.4. Outline of the thesis . . . . .	13
<b>2. Selected chapters of Tokamak physics</b>	<b>15</b>
2.1. Ideal MHD . . . . .	15
2.1.1. Assumptions and validity . . . . .	15
2.1.2. Tokamak equilibrium . . . . .	17
2.2. High confinement mode . . . . .	19
2.2.1. Phenomenology of edge localized modes . . . . .	20
2.2.2. Confinement and transport in H-mode . . . . .	22
2.2.3. Scaling of pedestal height and width . . . . .	23
2.3. Ideal MHD stability analysis . . . . .	26
2.3.1. Normal mode formulation and eigenvalue problem . . . . .	26
2.3.2. Extended energy principle . . . . .	27
2.3.3. Basic types of instabilities and numerical approach . . . . .	29

2.3.4. General organization of the calculations . . . . .	31
<b>3. Thomson scattering diagnostic</b>	<b>35</b>
3.1. Theory of Thomson scattering . . . . .	35
3.1.1. Non-relativistic dipole approximation . . . . .	36
3.1.2. Relativistic effects and spectral density function . . . . .	38
3.2. The Thomson scattering system on TCV . . . . .	39
3.2.1. Laser system and beam path . . . . .	39
3.2.2. Collection optics and fiber bundles . . . . .	41
3.2.3. Polychromators and detectors . . . . .	41
3.3. Optimization for the measurement of transport barriers . . . . .	44
3.3.1. Optimization of the viewing optics for the high resolution measurement of transport barriers . . . . .	44
3.3.2. Optimization of the polychromators for high temperature measurements . . . . .	52
3.4. Improvements in the data processing . . . . .	55
3.4.1. Ratio evaluation method . . . . .	55
3.4.2. Robust non-linear least-square fitting approach . . . . .	57
3.5. Calibration of the Thomson scattering system . . . . .	62
3.5.1. Laboratory calibrations . . . . .	62
3.5.2. In-situ calibrations . . . . .	63
3.5.3. Cross-diagnostic calibration . . . . .	63
3.6. Measurement and interpretation of the pedestal profiles . . . . .	65
3.6.1. Measurement of the electron contribution by Thomson scattering and its interpretation . . . . .	65
3.6.2. Measurement of the ion temperature by CXRS . . . . .	67
3.6.3. Dependence of ion temperature as function of electron temperature in the pedestal region . . . . .	69
3.7. Synchronized laser triggering on ELMs . . . . .	70
3.7.1. PC-based multi-channel controller . . . . .	71
3.7.2. Modes of operation and laser triggering . . . . .	72
3.7.3. Triggering on ELMs . . . . .	73
3.7.4. ELM pacing . . . . .	79
3.8. Conclusion . . . . .	81

<b>4. The snowflake divertor</b>	<b>83</b>
4.1. Snowflake divertor magnetic configuration . . . . .	83
4.1.1. Properties of the snowflake divertor . . . . .	84
4.1.2. L-mode experiments on TCV . . . . .	84
4.2. Ideal MHD stability properties of snowflake diverted H-mode . . . . .	86
4.2.1. Construction of the equilibria . . . . .	87
4.2.2. Impact of bootstrap current on edge magnetic shear . . . . .	89
4.2.3. Ideal MHD stability analysis of the edge pedestal region . . . . .	91
4.3. Dependence of pedestal stability on plasma parameters . . . . .	95
4.3.1. Procedures to modify equilibrium . . . . .	96
4.3.2. Radial position of the maximum pressure gradient . . . . .	96
4.3.3. Upper triangularity and upper squareness . . . . .	100
4.3.4. Elongation . . . . .	102
4.4. Snowflake experiments . . . . .	104
4.4.1. H-mode experiments on TCV . . . . .	105
4.4.2. Edge pedestal properties . . . . .	107
4.4.3. MHD stability of the edge pedestal . . . . .	109
4.5. Conclusion . . . . .	111
<b>5. H-mode scenarios in TCV</b>	<b>112</b>
5.1. H-mode regimes with type-III, large and type-I ELMs . . . . .	112
5.1.1. Influence of the input power on the ELM characteristics . . . . .	114
5.1.2. Operational boundary in pedestal region in ELMy H-mode plasmas	118
5.1.3. Properties of the electron pedestal parameters . . . . .	120
5.1.4. Scaling of the pedestal width . . . . .	126
5.2. Influence of the pedestal on energy confinement and transport . . . . .	131
5.2.1. Energy confinement . . . . .	131
5.2.2. Relation between central and pedestal electron temperature and density . . . . .	135
5.2.3. Electron thermal transport in the pedestal . . . . .	136
5.2.4. Density peaking . . . . .	137
5.3. Impact of plasma shaping on pedestal parameters . . . . .	139
5.3.1. ELM behavior . . . . .	143
5.3.2. Pedestal properties . . . . .	144

5.3.3. Variation of MHD stability with shaping . . . . .	148
5.4. Conclusion . . . . .	153
<b>6. Temporal evolution of the H-mode pedestal during an ELM cycle</b>	<b>155</b>
6.1. Diagnostic methods and discharge operation parameters . . . . .	156
6.1.1. Coherent data averaging and binning technique . . . . .	156
6.1.2. Discharge characteristics . . . . .	158
6.2. Temporal evolution of pedestal properties . . . . .	158
6.2.1. Type-I ELMs . . . . .	159
6.2.2. Large ELMs . . . . .	165
6.2.3. Type-III ELMs . . . . .	170
6.2.4. Displacement of the edge pedestal during the ELM cycle . . . . .	174
6.3. Identification of the pedestal pressure gradient limit by ideal MHD . . . . .	178
6.3.1. Type-I ELMs . . . . .	179
6.3.2. Large ELMs . . . . .	180
6.3.3. Type-III ELMs . . . . .	181
6.4. Conclusion . . . . .	182
<b>7. Summary and conclusion</b>	<b>184</b>
<b>A. Code settings</b>	<b>187</b>
A.1. CHEASE settings . . . . .	187
A.2. CAXE settings . . . . .	188
A.3. KINX settings . . . . .	190
<b>B. KINX convergence studies</b>	<b>192</b>
B.1. Vertical stability . . . . .	192
B.2. Higher toroidal mode numbers . . . . .	192
<b>C. Ideal MHD stability diagrams for snowflake diverted H-mode</b>	<b>196</b>
C.1. Snowflake and snowflake-like configurations . . . . .	197
C.2. Snowflake and snowflake-like configurations for different radial positions . . . . .	198
C.3. Snowflake configuration with different upper triangularity . . . . .	199
C.4. Snowflake configuration with different upper squareness . . . . .	200
C.5. Snowflake configuration with different elongation . . . . .	201

<b>D. H-mode electron pedestal profiles during an ELM cycle</b>	<b>202</b>
D.1. Type-I ELMs . . . . .	203
D.2. Large ELMs . . . . .	206
D.2.1. Type-III ELMs . . . . .	209

**References**

**Curriculum vitae**

# List of Tables

1.1. TCV machine parameters . . . . .	6
3.1. Limits of spatial resolution of the TS system . . . . .	45
3.2. Interference filter characteristics for the polychromators of the TS-MAIN system . . . . .	51
3.3. Interference filter characteristics for the polychromators of the TS-EDGE system . . . . .	52
3.4. Properties of M-estimators . . . . .	59
3.5. Plasma parameters of the pedestal profile measurement examples . . . . .	68
4.1. Growth rate $\gamma$ of the $n = 0$ ideal MHD-mode for $r_w = 10$ (no-wall limit) and the central Alfvén wave frequency $\omega_A$ . . . . .	86
4.2. Shape and plasma parameters from the SF-like SN and SF equilibria . . . . .	89
4.3. Some parameter of the MHD-stability analysis with varying radial position of the maximum pressure gradient . . . . .	97
4.4. Inflection point in the safety factor profile for different radial positions of the edge barrier . . . . .	99
4.5. Pedestal profile quantities of the SN and SF+ configuration . . . . .	108
4.6. Safety factor and shape parameters for SN and SF+ configuration . . . . .	110
5.1. H-mode plasma parameters . . . . .	113
5.2. Temperature pedestal width and gradient as a function of pedestal temperature and density . . . . .	123
5.3. Density pedestal width and gradient as a function of pedestal temperature and density . . . . .	125



6.1. H-mode discharge characteristics . . . . . 159

# List of Figures

1.1. Schematic of the coil configuration of a tokamak . . . . .	3
1.2. TCV plasma heating system . . . . .	7
1.3. Line of sights of the CXRS diagnostic . . . . .	10
1.4. Line of sights of the DMPX diagnostic . . . . .	11
2.1. Schematic representation of the barrier position and width . . . . .	33
3.1. Laser beam path of the TS-system on TCV . . . . .	40
3.2. Setup of the TS viewing chords . . . . .	42
3.3. 4-channel filter polychromator . . . . .	43
3.4. Convolution of test profile . . . . .	46
3.5. Comparison of DMPX and TS profile . . . . .	47
3.6. Optimization of the TCV-TS viewing chords for various plasma scenarios	49
3.7. Technical design of the TS observational optics fiber bundles . . . . .	50
3.8. Gradient measurements in eITB discharges . . . . .	51
3.9. Spectral response function and $S/N$ approximation for the 4-channel poly- chromator . . . . .	53
3.10. Spectral response function and $S/N$ approximation for the 3-channel poly- chromator . . . . .	54
3.11. Comparison of results from REM and LSQM . . . . .	60
3.12. Work-flow sketch of the LSQM algorithm . . . . .	61
3.13. Interferometer measurement inversion by SVD . . . . .	64
3.14. TCV vessel cross section and viewing chords of TS-EDGE . . . . .	66
3.15. Examples of H-mode pedestal profile measurements by TS-EDGE . . . . .	67
3.16. Pedestal ion temperature measurement by CXRS . . . . .	69

3.17. Ion temperature versus electron temperature at the pedestal . . . . .	70
3.18. Timing scheme for external triggering . . . . .	74
3.19. Sketch of the rt laser control algorithm . . . . .	75
3.20. Results from rt laser control in ELMy H-mode . . . . .	76
3.21. Shift of the laser timebase in realtime towards an ELM . . . . .	76
3.22. Plasma parameters during ELM cycle . . . . .	78
3.23. Magnetic triggering of ELMs . . . . .	80
3.24. Locking of the ELM frequency to the imposed vertical plasma oscillation	81
4.1. Magnetic equilibrium reconstruction of snowflake diverted discharge in L-mode . . . . .	85
4.2. Vertical stability of snowflake diverted discharge in L-mode . . . . .	86
4.3. Current density and pressure profile for synthetic snowflake-diverted H-mode equilibria . . . . .	87
4.4. Plasma boundary of the SF-like SN and SF equilibria . . . . .	88
4.5. Safety factor and magnetic shear from the SF-like SN and SF equilibria with and without bootstrap current . . . . .	90
4.6. Comparison of the edge pedestal stability of the SF-like SN and SF equilibria	92
4.7. Mode structure of SF-like SN and SF configurations for $n = 1$ . . . . .	94
4.8. Ideal MHD-stability limits of the pedestal as function of the radial position of the maximum pressure gradient . . . . .	98
4.9. Sensitivity of the MHD-stability limits of the pedestal upon upper triangularity . . . . .	101
4.10. Sensitivity of the MHD-stability limits of the pedestal upon upper squareness	102
4.11. Sensitivity of the MHD-stability limits of the pedestal upon elongation .	103
4.12. Single-null and snowflake plus configuration in H-mode . . . . .	105
4.13. Plasma parameters of single-null and snowflake plus configuration in H-mode	106
4.14. ELM frequency versus plasma elongation and ECH deposition location .	107
4.15. Electron pedestal profiles and safety factor and magnetic shear profiles for SN and SF+ configuration . . . . .	108
4.16. Ideal MHD-stability of the edge pedestal for SN and SF+ . . . . .	110
5.1. H-mode plasma shapes . . . . .	114
5.2. ELM energy loss versus ELM frequency . . . . .	115
5.3. Examples of normalized $D_\alpha$ emissions . . . . .	116

---

5.4. ELM frequency versus reciprocal collisionality . . . . .	117
5.5. Fractional power loss per ELM . . . . .	117
5.6. Operational boundary in pedestal region . . . . .	119
5.7. Electron temperature pedestal properties . . . . .	122
5.8. Electron density pedestal properties . . . . .	124
5.9. $\beta_{\theta,ped}$ as a function of $\beta_{\theta,ped,X}$ . . . . .	127
5.10. Pressure pedestal width as a function of $\beta_{\theta}$ . . . . .	128
5.11. Normalized pedestal width as a function of toroidal and poloidal gyro radius, pedestal electron density, collisionality and empirical scaling law .	130
5.12. ELM energy loss versus pedestal stored energy . . . . .	132
5.13. ELM energy loss versus pedestal stored energy and poloidal beta . . . . .	133
5.14. Energy confinement enhancement factor as a function of the normalized power $P_{tot}/P_{thr}$ . . . . .	134
5.15. Electron temperature and density profile stiffness . . . . .	136
5.16. Electron thermal transport in the pedestal region . . . . .	137
5.17. Density peaking in H-mode . . . . .	138
5.18. Plasma shapes and parameters for different upper triangularity and square- ness . . . . .	141
5.19. Plasma shapes and parameters for different plasma elongations . . . . .	142
5.20. Dependence of ELM characteristics upon plasma shaping . . . . .	144
5.21. Electron pedestal temperature, density and pressure as a function of plasma shape . . . . .	145
5.22. Electron pedestal temperature, density and pressure width as a function of plasma shape . . . . .	146
5.23. Normalized electron pedestal temperature, density and pressure gradient as a function of plasma shape . . . . .	147
5.24. MHD stability diagram for high upper squareness . . . . .	149
5.25. MHD stability diagram for negative upper triangularity . . . . .	150
5.26. MHD stability diagram for high elongation . . . . .	152
5.27. MHD stability diagram for small elongation . . . . .	152
6.1. Histograms of number of profiles used for fitting of temporal evolution of H-mode pedestal during an ELM cycle . . . . .	157

6.2.	Coherently averaged signals from the gas valve (normalized), central and edge line-integrated density and central and edge soft X-ray emission (normalized) for a type-I ELM cycle . . . . .	160
6.3.	Temporal evolution of the electron temperature pedestal in type-I ELMy H-mode . . . . .	162
6.4.	Temporal evolution of the electron density pedestal in type-I ELMy H-mode	163
6.5.	Temporal evolution of the electron pressure pedestal in type-I ELMy H-mode	164
6.6.	Coherently averaged signals from the gas valve (normalized), central and edge line-integrated density and central and edge soft X-ray emission (normalized) for a large ELM cycle . . . . .	166
6.7.	Temporal evolution of the electron temperature pedestal in ELMy H-mode discharges with large ELMs . . . . .	167
6.8.	Temporal evolution of the electron density pedestal in ELMy H-mode discharges with large ELMs . . . . .	168
6.9.	Temporal evolution of the electron pressure pedestal in ELMy H-mode discharges with large ELMs . . . . .	169
6.10.	Coherently averaged signals from the gas valve, central and edge line-integrated density and central and edge soft X-ray emission for a type-III ELM cycle . . . . .	170
6.11.	Temporal evolution of the electron temperature pedestal in type-III ELMy H-mode . . . . .	171
6.12.	Temporal evolution of the electron density pedestal in type-III ELMy H-mode . . . . .	172
6.13.	Temporal evolution of the electron pressure pedestal in type-III ELMy H-mode . . . . .	173
6.14.	Edge pedestal displacement during the ELM cycle . . . . .	175
6.15.	Temporal evolution of electron pedestal during the type-I ELM cycle . . . . .	176
6.16.	Ideal MHD stability map for H-mode plasma with type-I ELMs . . . . .	180
6.17.	Ideal MHD stability map for H-mode plasma with large ELMs . . . . .	181
6.18.	Ideal MHD stability map for H-mode plasma with type-III ELMs . . . . .	182
B.1.	Convergence of KINX for $n = 0$ and different grid sizes . . . . .	193
B.2.	KINX eigenvalues as function of grid size . . . . .	194
B.3.	KINX eigenvalues as function convergence stabilization parameter . . . . .	195

C.1. Ideal MHD-stability of the edge pedestal for synthetic snowflake-diverted H-mode equilibria . . . . .	197
C.2. Ideal MHD-stability of the SF edge pedestal for different radial positions of the edge pedestal . . . . .	198
C.3. Ideal MHD-stability of the SF edge pedestal for different upper triangularities	199
C.4. Ideal MHD-stability of the SF edge pedestal for different upper squareness	200
C.5. Ideal MHD-stability of the SF edge pedestal for different elongation . . .	201
D.1. Electron temperature edge profiles from H-mode plasmas with type-I ELMs	203
D.2. Electron density edge profiles from H-mode plasmas with type-I ELMs . .	204
D.3. Electron pressure edge profiles from H-mode plasmas with type-I ELMs . .	205
D.4. Electron temperature edge profiles from H-mode plasmas with large ELMs	206
D.5. Electron density edge profiles from H-mode plasmas with large ELMs . .	207
D.6. Electron pressure edge profiles from H-mode plasmas with large ELMs . .	208
D.7. Electron temperature edge profiles from H-mode plasmas with type-III ELMs	209
D.8. Electron density edge profiles from H-mode plasmas with type-III ELMs	210
D.9. Electron pressure edge profiles from H-mode plasmas with type-III ELMs	211

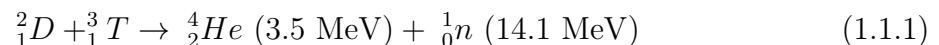
# 1. Introduction

The enormous destructive power of the  $^{235}\text{U}$ -fueled atomic bomb dropped on Hiroshima on August 6, 1945, which killed 75,000 people, and the  $^{239}\text{Pu}$ -fueled bomb dropped on Nagasaki three days later touched off a violent debate after World War II about the building of the next superweapon a fusion, or “hydrogen”, bomb. Alumni of the Manhattan project, who had developed the atomic bomb, were divided on the issue. Ernest Lawrence and Edward Teller fought for the construction of the fusion device. J. Robert Oppenheimer and Enrico Fermi argued against it. The decision was made to develop the weapon, and the first artificial fusion reaction occurred when the hydrogen bomb was tested in November 1952.

The history of fusion research is therefore the opposite of fission research. With fission, the reactor came first, and then the bomb was built. With fusion, the bomb was built long before any progress was made toward the construction of a controlled fusion reactor. Almost 60 years after the first hydrogen bomb was exploded, the feasibility of controlled fusion reactions is still open to debate.

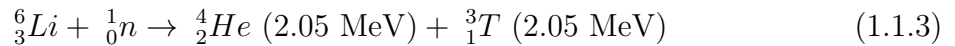
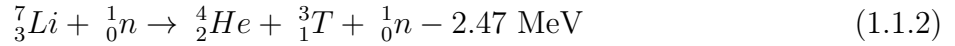
## 1.1. Nuclear fusion

The reaction that is most likely to fuel the first fusion reactor is the thermonuclear D-T, or deuterium-tritium, reaction. This reaction fuses two isotopes of hydrogen D and T to form helium and a neutron:



Its ignition temperature lays above  $10^8$  K to overcome the repulsion force of the positively charged nuclei.

Deuterium is naturally abundant in hydrogen being one part in 6700. The oceans would provide enough deuterium for approximately  $10^{11}$  times today's annual global electricity consumption [1]. Unlike deuterium, tritium is quasi non-existent in nature due to its half life time of 12.3 years. However, it can be bred from Lithium by neutron induced fission reaction:



Natural resources of Lithium in the sea water are estimated to meet the global energy consumption for  $10^6 - 10^7$  years [1]. Thus, nuclear fusion promises a practically inexhaustible source of energy.

### 1.1.1. Magnetic confinement

At the temperature required for fusion, any substance will exist as a completely ionized gas, the so called plasma. Globally, the electrostatic charge of the ions is neutralized by an equal number of electrons. Locally, the charged particles are subjected to the Lorentz force which bends the particle trajectory to a helical one around the magnetic field lines. The radial extent, or gyro-radius, of this trajectory for a particle of mass  $m$  and charge  $q$  is given by

$$\rho = \frac{mv_{\perp}}{qB}, \quad (1.1.4)$$

where  $v_{\perp}$  is the velocity of the particle perpendicular to the magnetic field  $B$ . In the case of a homogeneous velocity distribution,  $v_{\perp}$  can be expressed by the plasma temperature  $T$  as  $v_{\perp} = (2kT/m)^{1/2}$  with the Boltzmann constant  $k$ . This effect is used as method to protect the wall of a reactor from the high temperatures of the fusion plasma by introducing a gap between the outer plasma surface and the reactor wall.

The presence of the magnetic field highly restricts the perpendicular direction of motion, whereas the parallel is unaffected. Collisions among particles, however, introduce a diffusive perpendicular cross field transport of particles and also give rise to a resistivity in the parallel direction.

### 1.1.2. Tokamak principle

A straight magnetic field configuration suffers from plasma losses at both ends. This can be avoided by either compressing the plasma column at its extremities by an additional



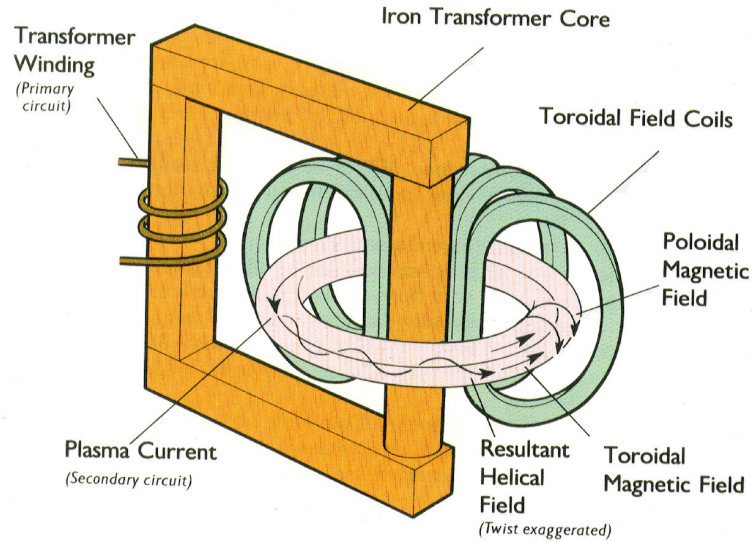


**Figure 1.1.:** Schematic of the coil configuration of a tokamak.

magnetic field - magnetic bottle - or by reconnecting one extremity of the magnetic field lines with the other in form of a torus. Only latter configuration confines sufficiently well particles with high velocities parallel to the magnetic field lines and is used for the so called tokamak design, the Russian acronym for “toroidal chamber with magnetic coils” (see figure 1.1).

The reconnection of the magnetic field lines in form of a torus leads to bending of them and hence creates an inhomogeneity in their distribution - a compression of the field lines on its inner side and a decompression on the outer side. This curvature and gradient of the field leads to drift motions of ions and electrons in opposite vertical direction resulting in a separation of charge and consequently an electric field. The electric field is perpendicular to the magnetic field and causes an outward  $\mathbf{E} \times \mathbf{B}$ -drift of the entire plasma. The outward drift is compensated by a toroidal current  $I_{tor}$  producing a poloidal magnetic field  $B_{pol}$  which, together with a toroidal magnetic field  $B_{tor}$ , leads to a twisted magnetic field topology. An additional vertical magnetic field  $B_v$  is required to attain the balance in the radial forces. The plasma pressure gradient  $\nabla p$  gives rise to an outward directed force that is canceled out by the Lorentz force resulting from  $B_v$ .

In a tokamak, the transformer principle is used to create the plasma current and to heat the plasma. The central celenoid acts as the primary coil and the plasma ring as the secondary coil with a single winding. It has the advantage of retaining the toroidal symmetry, but allows only pulsed operation which is undesirable for a future fusion power plant based on the tokamak principle. Thus, a major effort is being undertaken

to develop alternative ways of driving the plasma current, such as beam-wave driven or pressure gradient driven currents.

The magnetic structure in a tokamak consist of an infinite set of nested toroidal magnetic surfaces, the so called flux surfaces. These surfaces represent regions of constant pressure, current density and magnetic field. The twist of the field lines in each surface is characterized by the safety factor  $q$ , whereas

$$q = \frac{\Delta\varphi}{2\pi} = \frac{rB_\phi}{RB_\theta}, \quad (1.1.5)$$

with plasma minor and major radii  $r$  and  $R$  and the toroidal and poloidal magnetic fields  $B_\phi$  and  $B_\theta$ . Here  $\Delta\varphi$  denotes the change in toroidal angle  $\varphi$  associated with a change of  $2\pi$  in poloidal angle when following the field lines on a magnetic surface. The profile of  $q$  is mainly determined by  $B_{pol}$ , or the current density  $\mathbf{j}$ , and plays a crucial role in the magneto-hydrodynamic (MHD) stability (see chapter 2). On rational values of  $q$ , ideal MHD instabilities can develop leading to destabilization of parts or the whole plasma. These events develop on a fast time scale ( $\simeq$  ms), decrease the plasma performance and can damage components of the tokamak, which make it indispensable to study their very nature.

### 1.1.3. Plasma heating

As noted before in 1.1.2, the coil in the central celenoid serves also to heat the plasma. Owing to the plasma resistivity  $\mu$ , the Ohmic heating power density is

$$p_{ohmic} = \mu j^2. \quad (1.1.6)$$

The plasma resistivity, however, decreases with increasing plasma temperature as  $T^{-3/2}$  and the maximum current density  $\mathbf{j}$  is limited by MHD stability (see chapter 2). The plasma temperature reached by Ohmic heating is not sufficient to start and sustain a fusion reaction. Thus, additional plasma heating is is required.

One method of additional plasma heating consists of injecting energetic particles into the plasma by means of neutral beams of hydrogen or deuterium. The neutral particles travel unaffected by the magnetic field until they collide with ions from the plasma, which will ionize them. The resulting ions and electron are henceforth confined by the magnetic field and deposit their energy via further collisions to the rest of the plasma. The beam absorption depends essentially on the orbits of the created highly energetic particles within the plasma.

A second method of additional heating is the injection of high energetic electromagnetic waves into the plasma. Once the wave has coupled to the plasma, its energy is absorbed at fairly high rate at the resonance frequency such as the ion or electron cyclotron frequencies, lower hybrid frequency and higher harmonics of these frequencies.

#### 1.1.4. Power plant concept and improved plasma scenarios

In a fusion plant the plasma temperature is supposed to be maintained by energy transfer from the, by the fusion process created,  $\alpha$ -particles to the combustibles D and T. The magnetic field has to confine the charged  $\alpha$ -particles long enough so that they can transfer their energy via collisions and equilibrate their energy with the bulk plasma before leaving the plasma. In contrast to the  $\alpha$ -particles, the neutrons leave the plasma without any interaction and should be absorbed in a blanket surrounding the reactor vessel to breed the Tritium from Lithium, equation (1.1.3). The heat is carried away by a suitable coolant and used to drive vapor steam turbines.

A power balance gives an estimate for the plasma parameters required for a fusion power plant and culminates in the triple product or Lawson criteria [1]

$$nT\tau_E > 5 \times 10^{21} \text{ m}^{-3}\text{keV s}, \quad (1.1.7)$$

where  $T$  and  $n$  are the plasma temperature and density and  $\tau_E$  the energy confinement time. High plasma power, represented by the dimensionless parameter  $\beta_t$ ,

$$\beta_t = \frac{\langle p \rangle}{B_{tor}^2/2\mu_0}, \quad (1.1.8)$$

where  $p = nT$  and  $\langle . \rangle$  denotes the volume average, can be achieved by auxiliary heating and by energy transfer from the  $\alpha$ -particles. The dependence of equation (1.1.7) on the energy confinement time gives reason to develop so-called improved plasma scenarios, such as high-confinement mode (H-mode) or plasmas with internal transport barriers (ITB), in which transport quantities decrease significantly minimizing the power loss of the plasma.

In the case of H-mode, an external transport barrier with a steep pressure gradient arises at the very edge of the plasma reducing the internal particle and heat transport to almost neoclassical quantities. This leads to an improvement in confinement, the so called H-factor [2], by 2 – 3 times. However, this improved plasma scenario gives rise to resistive or ideal MHD modes developing in the steep pressure gradient region of the

Parameter	Symbol	Value
Major radius	$R_0$	0.88 m
Minor radius	$a$	0.25 m
Aspect ratio	$\epsilon^{-1} = R_0/a$	$\approx 3.5$
Vessel internal full width	$R_{max} - R_{min}$	0.56 m
Vessel internal full height	$z_{max} - z_{min}$	1.54 m
Toroidal vessel resistance	$\Omega_{tor}$	45 m $\Omega$
Toroidal field on axis	$B_0$	$\leq 1.54$ T
Plasma current	$I_P$	$\leq 1.2$ MA
ECH-heating	$P_{X2}$	$\leq 2.8$ MW
	$P_{X3}$	$\leq 1.4$ MW

**Table 1.1.:** Main TCV machine parameters

barrier. The so called edge-localized modes (ELM's, see subsection 2.2.1) represent, with its fast ejection of energetic particles, a potential danger to plasma facing components of the reactor vessel.

ITB scenarios feature high core confinement combined with a non-negligible self-generated current fraction, the so called bootstrap current, while operating at high normalized pressure and moderate current. This regime suggest a potential route to the steady-state mode of operation desirable for fusion power plants.

## 1.2. Tokamak à configuration variable

### 1.2.1. The Tokamak

This thesis work was carried out on the *Tokamak à Configuration variable* (TCV), a medium size elongated machine. It started operation in 1992 with the main aim to investigate the effect of plasma shape on confinement and stability. It was designed to produce a large variety of plasma shapes. In addition, TCV is equipped with a powerful electron cyclotron resonance heating system, which enables to heat the plasma at the second and third harmonic of the electron cyclotron frequency. The main machine parameters are listed in table 1.1.

TCV's plasma shaping is achieved by 16 independently controlled poloidal field coils which are mounted in two vertical stacks on both sides of the plasma outside the vacuum

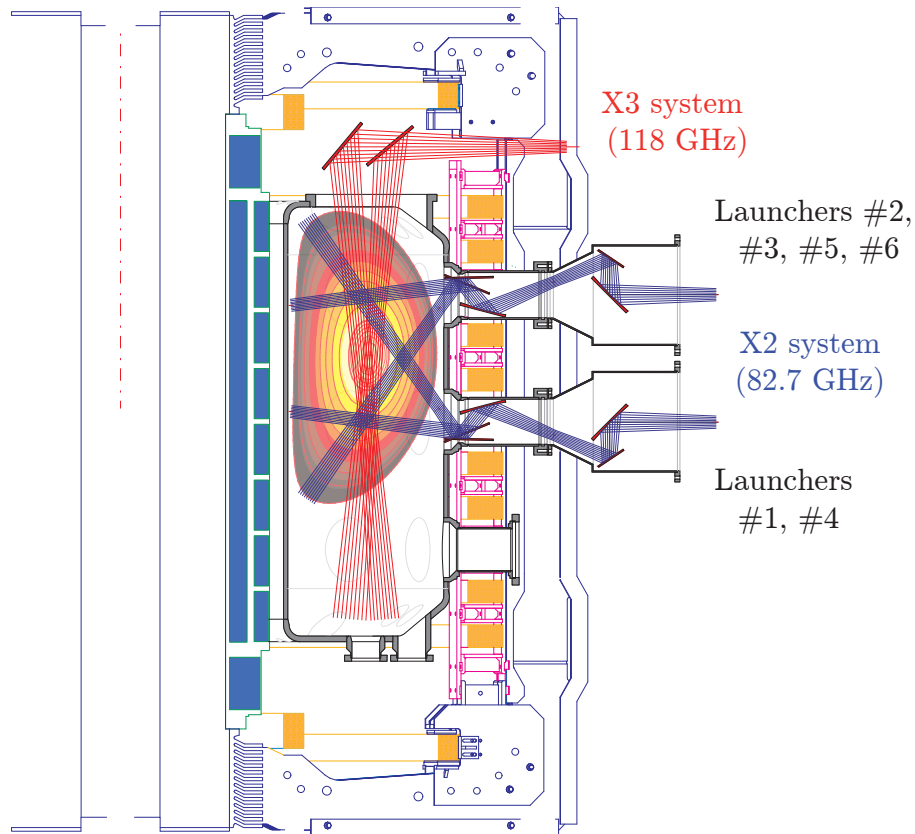


**Figure 1.2.:** TCV plasma heating system: The X2 launcher are placed on the two equatorial (L1, L4) and four upper lateral ports (L2, L3, L5, L6). Two degrees of freedom in the launcher mirror angles allow a wide range of poloidal (ECH) and toroidal angles (ECCD). The X3-launcher is mounted on the top of the machine and has two degrees of freedom to optimize the injection angle radially and poloidally, whereas the toroidal angle is fixed to  $0^\circ$ .

chamber. It has the flexibility to operate at high plasma elongation  $\kappa \leq 2.8$ , high positive and negative triangularity  $-0.77 \geq \delta \leq 0.86$ , high squareness  $\lambda \leq 0.5$ , in pear and doublet shape and in various upper and lower single null and double null divertor configurations.

### 1.2.2. Electron cyclotron heating

TCV is equipped with a very flexible electron cyclotron heating (ECH) and current drive (ECCD) system. It consists of six 82.7 GHz gyrotrons for heating at the second harmonic of the electron cyclotron frequency, and three 118 GHz gyrotrons for heating at the third harmonic (figure 1.2) [3]. The polarization of each beam can be modified and is usually set for propagation as an extraordinary wave (X2-, X3-mode).

The X2-system allows to heat and drive current in plasmas with a density up to the cut-off density for the X2-mode propagation,  $n_{e,\text{cut-off},X2} = 4.25 \times 10^{19} \text{ m}^{-3}$ . There are two launcher (L1, L4) mounted in equatorial ports and four launcher (L2, L3, L5 and L6) in upper lateral ports. Each launcher has two steering axes, whose combination allows a huge variety of poloidal and toroidal injection angles. The nominal power of each gyrotron is 465 kW. The gyrotrons for L1, L2 and L3 and the gyrotrons for L4, L5 and L6 are powered by two individual power supplies which feature the possibility of power ramps.

The gyrotrons of the X3-system are combined in one launcher at the top of the vessel and heat plasmas with a density up to the cut-off density for the X3-mode propagation,  $n_{e,\text{cut-off},X3} = 11.5 \times 10^{19} \text{ m}^{-3}$ . The microwave beam is injected nearly tangentially to the resonant surface to maximize the beam absorption. The launcher mirror can be moved radially and steered poloidally to optimize the injection angle and the relative position of the beam path in respect to the resonant layer. The nominal power of each gyrotron is 480 kW. All three gyrotrons are powered by the same power supply which does not support power ramping. However, half the power of one or three gyrotrons can be attained using power modulations with 50 % duty cycle [4].

During this thesis work, the EC-heating system has been extensively used. One has to mention that for the case of heating with X3, uncertainties in the calculation of the absorption coefficient by TORAY-GA [5] can become non-negligible. As the injection of the X3-heating beam is along the resonance line to maximize the first-pass absorption, small deviations from the optimal launcher angle and position leads to large variations in the computed power absorption coefficient  $\eta_{\text{abs}}$ . An error in the absolute calibration of the launcher angle  $\theta_{X3}$  by only  $\pm 0.5$  deg. or of the launcher radial position  $R_{X3}$  by  $\pm 0.5$  cm can lead to changes of  $\eta_{\text{abs}}$  in the range of 0 – 75%.

During the experiments, the beam absorption was maximized by keeping an optimal  $R_{X3}$  fixed and sweeping  $\theta_{X3}$  by few degrees observing the response on the central soft X-ray emission. The optimal launcher parameters were kept throughout the experiment, however, uncertainties in the launcher calibration could impede the determination of the total absorbed power.

### 1.2.3. Selected diagnostics

The following section will shortly present the main diagnostics used for the results presented in this thesis.

### **Magnetic probes**

Magnetic probes and flux probes are installed at four separate toroidal locations, which are toroidally separated by  $90^\circ$  [6]. One poloidal array consists of 38 probes installed behind the graphite protection tiles. These probes measure the poloidal component of the magnetic field tangential to the vessel wall.

3 sets of 8 probes on the high field side (HFS) and 17 probes on the low field side (LFS) are installed in form of toroidal bands at the vessel midplane, 35 cm above and below, which allow the measurement of the toroidal mode number  $n \leq 16$ .

### **Thomson scattering**

The Thomson scattering system measures electron temperature ( $T_e$ ) and density ( $n_e$ ) profiles. It measures the light emitted from electron excited by high energetic laser light. A spectral analysis of the scattered light permits the reconstruction of the bulk electron velocity distribution and thus the bulk electron temperature and density [7]. The Thomson scattering installed on TCV comprises three pulsed, Q-switched, solid state Nd:YAG lasers with a beam energy of  $\leq 1.5$  J and pulse duration of 10 – 15 ns [8]. The lasers emit in the near-infrared at the wavelength of  $1064 \mu\text{m}$ , each with a repetition frequency of 20 Hz. The electron temperature and density are measured at 35 different local positions along the beam path. More details are given in chapter 3.

### **Far-infrared interferometry (FIR)**

The FIR interferometer is of Mach-Zehnder type and provides line integrated electron density  $n_{el}$  along 14 vertically aligned chords [9]. A continuous wave  $\text{CO}_2$  laser excites the light emission of a  $\text{CH}_2\text{F}_2$  filled cavity at the wave length of  $214.6 \mu\text{m}$ . The laser beam is then divided into a reference beam, which is frequency shifted by a rotating grating, and 14 probe beams passing the plasma at different radial positions. When the probe beams pass through the plasma, the difference in refractive index will cause a phase delay with respect to the reference beam. Since the reference beam is frequency shifted, the phase delay can directly be obtained from a comparison of the detector signals (He cooled InSb bolometers with 5kHz bandwidth) at the difference frequency (beat frequency). For the wavelength and polarization of the FIR beams, the refractive index of the plasma is directly related to the electron density. Therefore, the system will provide continuous measurements of the line-integrated density along 14 chords.

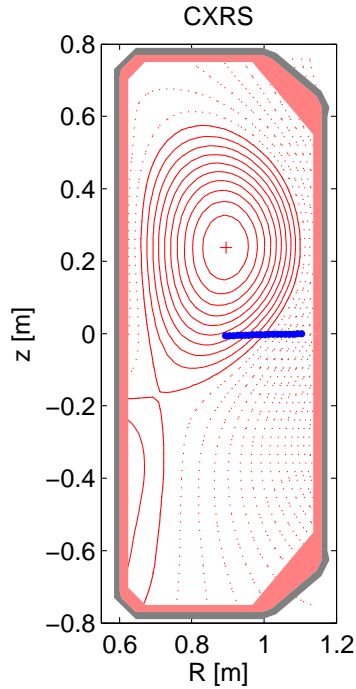


**Figure 1.3.:** Line of sights of the CXRS diagnostic indicated as blue dashed line for a standard H-mode discharge, whose magnetic poloidal flux surfaces are shown in red.

At the chosen frequency, beam refraction is negligible up to very high line integrated densities of  $n_{el} \sim 2 \times 10^{20} \text{ m}^{-2}$  and measurements are typically made at a precision of  $\delta n_{el} \sim 5 \times 10^{17} \text{ m}^{-2}$  [8]. The system is fully automated and part of the basic and essential diagnostic set in operation for each TCV shot. The measurement along the central chord is used for real time control of the plasma density.

### Change exchange spectroscopy (CXRS)

TCV is equipped by a Charge eXchange Recombination Spectroscopy (CXRS) diagnostic. The analysis of the momenta of a charge exchange line emitted when an impurity ion interacts with a neutral atom yields impurity temperature, density and fluid velocity. The diagnostic observes the CVI line (529.1 nm), emitted when a charge exchange reaction takes place between a  $\text{C}^{6+}$  atom in the plasma and a neutral  $\text{H}^0$ , injected by a low power diagnostic neutral beam (DNBI) at the vessel mid-plane, figure 1.3. For TCV, carbon is the main impurity and can be considered thermalized with the main ion species (deuterium). The CCD detector (Xcam Ltd., back-illuminated e2v CCD57-10) of the diagnostic has a typical integration time of 10 – 100 ms, depending on the carbon concentration in the vacuum vessel. The typical spatial resolution is  $\sim 1 \text{ cm}$ .



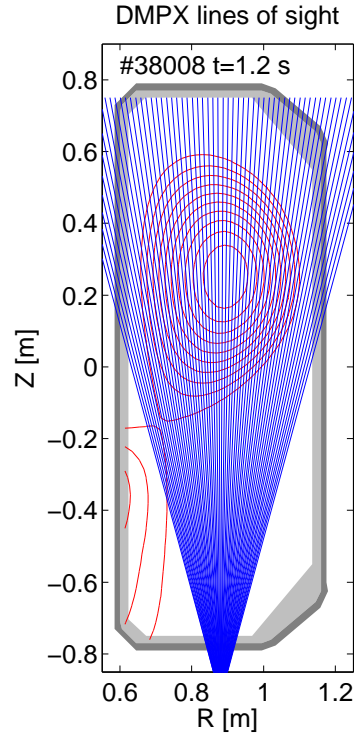


**Figure 1.4.:** Line of sights of the DMPX diagnostic indicated as blue lines for a standard H-mode discharge, whose magnetic poloidal flux surfaces are shown in red.

The arrangement of the DNBI and CXRS diagnostic allows full profile measurement of the ion temperature and density only in plasmas with their magnetic axis located at the vessel mid-plane. In the case of H-mode discharges, usually situated in the upper half of the vacuum vessel, the diagnostic measures only the plasma edge up to a normalized poloidal flux radius of  $\rho \sim 0.8$ .

### Duplex Multiwire Proportional X-ray counter (DMPX)

Soft X-ray emission from a hot plasma with energy below 50 keV is typically composed out of Bremsstrahlung, electron-ion recombination and line emission. The Duplex Multiwire Proportional soft X-ray counter (DMPX) is a 64-channel soft X-ray detector located underneath TCV and viewing the plasma vertically. The detector is made up of two superimposed wire-chambers sensitive to soft X-ray emission with energy between 3 – 30 keV. The DMPX has high resolution in time and space: the acquisition rate is 200 kHz and, at the equatorial plane of TCV vacuum vessel, the mean distance separating two lines-of-sight is of 7.9 mm.

### 1.3. Motivation for the thesis

The H-mode pedestal, a narrow region of reduced turbulent transport at the plasma edge, sets the boundary conditions for core plasma performance. Understanding the physics of the pedestal dynamics and predicting its performance in future devices is the key to reduce the uncertainties associated with the realization of burning plasma conditions. For next step tokamaks, such as ITER, H-mode operation at the maximum possible pedestal pressure is needed. However, the H-mode pedestal with its high pressure gradient is subject to periodic relaxation processes driven by MHD (ELMs) causing high energy losses. ELMs considerably degrade the plasma performance and, with their associated high power exhaust, pose serious problems to plasma facing components. Today's research is concentrated on the understanding of ELM physics, development of predictive models for ELM losses, regimes with suppressed ELM activity and ELM control.

The main study of this work relates to the ELM physics in H-mode plasmas on TCV. It combines the aspect of (1) diagnosing the pedestal, (2) the investigation of the influence of pedestal properties on macroscopic plasma quantities, e.g. energy confinement and transport, (3) the role of plasma shaping and heating on the pedestal and ELM characteristics, and (4) addresses the behavior of pressure and current driven instabilities in the pedestal region.

The powerful ECR heating system of TCV permits efficient heating of H-mode plasmas and gives the unique possibility to study the influence of electron heating on pedestal and plasma parameters. The capability of TCV for plasma shaping is well suited for MHD analysis, since the MHD stability can strongly depend on the plasma geometry, and for investigating new divertor concepts, e.g. the snowflake divertor.

## 1.4. Outline of the thesis

The thesis work is structured as following:

- Chapter 1: A brief introduction to nuclear fusion and the tokamak concept as possible future fusion device is given. The TCV tokamak with its ECRH system, control system and diagnostics is presented.
- Chapter 2: This chapter describes the analysis tools used throughout the thesis work. It explains the computation of the plasma equilibria by the CHEASE code, introduces the H-mode and ELMs. The MHD theory, its basic assumptions and validity are shortly presented. Emphasize is given on the numerical calculations of the MHD stability by the KINX code and the explanation of the calculation scheme.
- Chapter 3: This chapter is devoted to the Thomson scattering diagnostic. The upgrades of the diagnostic hardware towards measurements of transport barriers are explained and the method of synchronization of the diagnostic with MHD events in realtime is described. The improvements in the data analysis are discussed. Measurements of the electron and ion pedestal in H-mode plasmas are presented.
- Chapter 4: A brief introduction to the snowflake (SF) magnetic divertor is given. The realization of SF diverted discharges on TCV is presented. MHD stability limits in the pedestal region of H-mode plasmas with SF divertor are discussed and experimental results are shown and interpreted.
- Chapter 5: This chapter is devoted to the investigation of the role of the H-mode pedestal on energy confinement and ELM energy losses. The study includes H-mode discharges with variable heating power, ELM characteristics and plasma shapes. Pedestal scalings are tested against models and the MHD stability limits of the pedestal are analyzed for a variety of discharges.
- Chapter 6: The temporal evolution of the electron temperature, density and pressure profiles during an ELM cycle is analyzed for three different heating powers. The results are interpreted in the frame of ideal MHD.
- Chapter 7: In this chapter, conclusions are drawn on the presented work.

- Appendices A-D: In these chapters, additional material is given. This comprises the used code settings, convergence studies of the KINX code for the problems treated in this work, details from MHD stability calculations for the snowflake diverted H-mode and the electron profile measurements during an ELM cycle.

## 2. Selected chapters of Tokamak physics

In this chapter, an introduction is given to the physical models and descriptions used throughout this work. The ideal MHD description of a plasma and its application to analyze stability is briefly described. In addition, a short summary to the present understanding of H-mode is given.

### 2.1. Ideal MHD

A brief description of the ideal MHD, its assumptions, validity and basic predictions is outlined in the following. We want to refer to text books [1, 10] for a more detailed explanation.

#### 2.1.1. Assumptions and validity

The MHD equations are derived from the Boltzmann equations by calculating moments and introducing physical variables, such as density and velocity. Each moment equation contains the next higher moment thus forming an infinite set of fluid equations. A complete description of a plasma is achieved by coupling this set of fluid equations with the Maxwell equations. The full derivation of the MHD equations itself can be found for example in [10] and is beyond the scope of this work.

The description of a plasma can be considerably simplified by the following approximations: (1) The plasma is assumed to be fully ionized and composed of electrons and ions of hydrogen or isotopes. (2) The displacement current and net charges are neglected in Maxwell's equations (low frequency limit  $\epsilon_0 \rightarrow 0$ ). (3) The plasma is assumed to be

macroscopically quasi-neutral ( $n_i = n_e = n$ ). These assumptions have as consequence that phase velocities of electromagnetic waves have to be much slower than the speed of light and the characteristic thermal velocities are limited to non-relativistic velocities. Quasi-neutrality requires that the macroscopic charge separation, which can develop in the low frequency approximation, is rapidly compensated by electrons, i.e. the characteristic frequencies are much lower than the electron plasma frequency and characteristic lengths are much longer than the Debye length. A *single fluid MHD description* of a plasma is obtained by introducing fluid variables, such as the mass density  $\rho$ , fluid velocity  $\mathbf{v}$ , and current density  $\mathbf{j}$ , and combining the equations for electrons and ions under the assumption that the electron mass is negligible ( $m_e \rightarrow 0$ ). Nevertheless, the closure of the set of single-fluid equations together with Maxwell equations requires a further assumption on the pressure tensor.

The *ideal MHD model* is derived from the assumption that a plasma is dominated by collisions. This means that the electron and ion distribution functions are nearly Maxwellian, which give rise to an isotropic pressure  $p$ . The condition is satisfied when considerations are limited to macroscopic phenomena, where the characteristic times have to be sufficiently long to allow the collisions to make the distribution function nearly Maxwellian. Resistive terms are neglected in Ohm's law with the assumption that resistive diffusion is sufficiently small. This imposes an upper limit on the collisionality, but can also be expressed as a lower limit of the macroscopic characteristic length scales. Therefore, the simplification of Ohm's law implies that resistive diffusion is small and that the ion Larmor radius is much smaller than the macroscopic plasma dimension. The *ideal MHD equations* are then

$$\frac{\partial \rho}{\partial t} = -\nabla \cdot (\rho \mathbf{v}) \quad (2.1.1)$$

$$\rho \left( \frac{\partial \mathbf{v}}{\partial t} + (\mathbf{v} \cdot \nabla) \mathbf{v} \right) = -\nabla p + \mathbf{j} \times \mathbf{B} \quad (2.1.2)$$

$$\mathbf{E} = -\mathbf{v} \times \mathbf{B}, \quad (2.1.3)$$

where  $\mathbf{E}$  and  $\mathbf{B}$  are electric and magnetic fields. The set of equations is closed by assuming adiabatic behavior

$$\frac{\partial p}{\partial t} + \mathbf{v} \cdot \nabla p = -\gamma p \nabla \cdot \mathbf{v} \quad (2.1.4)$$

with  $\gamma = 5/3$  being the adiabatic coefficient.

The assumptions required for the formulation of the ideal MHD equations define the formal *validity range of the ideal MHD model* and lead to the three basic requirements:

- high plasma collisionality,
- macroscopic scale length of the plasma must be much larger than the ion Larmor radius,
- large plasma size, so that resistive diffusion is negligible.

In tokamak experiments and fusion plasmas, the first condition is never satisfied due to the high plasma temperatures and “relatively” low operational densities. The second condition is valid in the description of macroscopic MHD phenomena, but is not necessarily satisfied when describing MHD modes with a narrow mode structure, as it is the case for ELMs. The usually very low resistive current diffusion in tokamak plasmas satisfies the third condition.

Nevertheless, during many years of fusion research, the ideal MHD theory has proven to give accurate predictions of macroscopic plasma behavior, since the incorrectly treated parts, namely the transport of parallel momentum and energy, are of little importance in equilibrium and stability calculations.

### 2.1.2. Tokamak equilibrium

The cornerstone of MHD theory of toroidal systems is the Grad-Shafranov equation, which describes the two-dimensional equilibrium of a toroidal axisymmetric plasma. This equation provides the basis for subsequent stability analysis.

#### Grad-Shafranov equation

The time independent form of the ideal MHD equations, i.e.  $\partial/\partial t = 0$ , can be used to calculate an equilibrium configuration. According to equation (2.1.2), a static equilibrium, where the velocities are set to zero ( $\mathbf{v} = 0$ ), requires

$$\nabla p = \mathbf{j} \times \mathbf{B}. \tag{2.1.5}$$

From this equation one can show that there are no pressure gradient along magnetic field lines and that the magnetic field lines lie nested on surfaces of constant pressure, referred

to as magnetic flux surfaces. Using the definition of the poloidal flux,

$$\psi = \int_{A_{tor}} \mathbf{B} \cdot d\mathbf{A}, \quad (2.1.6)$$

where  $A_{tor}$  is an arbitrary toroidal cross section of a flux surface, and Maxwell's equation, the Grad-Shafranov equation is derived [10],

$$\Delta^* \psi = -\mu_0 R^2 p'(\psi) - T(\psi) T'(\psi), \quad (2.1.7)$$

where  $p' = \partial p / \partial \psi$  is the pressure derivative,  $\Delta^* = R \frac{\partial}{\partial R} \left( \frac{1}{R} \frac{\partial}{\partial R} \right) + \frac{\partial^2}{\partial Z^2}$  the elliptic operator in cylindrical coordinates and  $T(\psi) = R B_\varphi$  with  $B_\varphi$  the toroidal magnetic field. Equation (2.1.7) is a nonlinear elliptic differential equation and must, in general, be solved numerically. However, the problem is ill posed, since  $p'$  and  $TT'$  must be given as function of  $\psi$ , whose spatial coordinate is not known until equation (2.1.7) is solved and consequently iterative schemes have to be used.

On TCV, the free-boundary Grad-Shafranov solver LIUQE [11] solves the equilibrium iteratively by using a series of polynomials for  $p'$  and  $TT'$  and fitting those to the measurements of the magnetic probes in least-square sense. Having knowledge of the plasma kinetic pressure profile, e.g. measured by Thomson scattering and CXRS, and the current density profile, either from direct measurements or from resistivity calculations, allows for a more accurate and self-consistent plasma reconstruction.

### Pressure profile

Measurements of the electron pressure profile on TCV by Thomson scattering can provide an additional constraint for an equilibrium reconstruction. The ion contribution to the pressure profile is either obtained from CXRS measurements or from scaling of the electron pressure. In the case of H-mode discharges, which are usually performed in the upper half of the TCV vacuum vessel, the CXRS diagnostic only provides edge profile measurements. Therefore, in this work, the full ion pressure profile  $p_i$  was usually scaled from the electron pressure with help of a formula obtained from transport simulations by PRETOR for the ohmic discharge phase on TCV [12],

$$p_i = 0.07 n_{el,e19}^{0.8} q_{95}^{0.6} p_e \frac{2}{Z_{eff}}, \quad (2.1.8)$$

where  $n_{el,e19}$  is the line-integrated density,  $q_{95}$  the safety factor,  $p_e$  the electron pressure and  $Z_{eff}$  the effective ion charge.



### Current density profile

The parallel ohmic current density profile  $j_{\parallel,ohm}$  can be either obtained from the equilibrium reconstruction or from resistivity calculations by Ohm's law. In this work,  $j_{\parallel,ohm}$  was taken from LIUQE yielding a monotonic  $q$ -profile.

In the toroidal geometry, a fraction of particle is trapped due to the magnetic field geometry. They execute banana orbits and, in the presence of a density gradient, carry a current parallel to the magnetic field. This current is caused by the momentum transfer between passing and trapped particles induced by collisions, which adapts their velocities accordingly. From the difference in velocity between passing and trapped particles, a net current arises, the so-called *bootstrap current*.

In this work, the bootstrap current was computed by the CHEASE code employing the Sauter model [13] (valid in the banana regime) with the assumption  $\partial \ln n_e / \partial \psi = \partial \ln n_i / \partial \psi$  and equal ion and electron temperature ( $T_i = T_e$ ),

$$\langle \mathbf{j} \cdot \mathbf{B} \rangle_{BS} = T(\psi)p \left[ A_1 \frac{\partial \ln n_e}{\partial \psi} + R_{pe} (A_1 + A_2) \frac{\partial \ln T_e}{\partial \psi} \right] \quad (2.1.9)$$

$$+ (1 - R_{pe}) \times \left( 1 + \frac{A_3}{A_1} \alpha \right) A_1 \frac{\partial \ln T_i}{\partial \psi} \Bigg], \quad (2.1.10)$$

where  $A_1$ ,  $A_2$ ,  $A_3$  and  $\alpha$  are functionals,  $n_e$  and  $n_i$  electron and ion density and  $R_{pe} = p_e/p$  the ratio between electron and total pressure. For standard values of the coefficients  $A_1$ ,  $A_2$ ,  $A_3$  and  $\alpha$ , it was found that density gradients are more efficient in driving bootstrap current. The parallel bootstrap current density reads then  $j_{\parallel,BS} = \langle \mathbf{j} \cdot \mathbf{B} \rangle_{BS} / \langle \mathbf{B} \cdot \nabla \phi \rangle$ , where  $\phi$  is the toroidal flux.

In general, taking into account the set of pressure and current density profiles ( $j_{\parallel,ohm} + j_{\parallel,BS}$ ) and the plasma boundary obtained from LIUQE, a more accurate and self-consistent equilibrium can be computed, e.g. by the fixed-boundary code CHEASE [14].

## 2.2. High confinement mode

In high confinement mode (H-mode) it was found that energy confinement approximately doubles to that found in low confinement mode (L-mode), which is due to the formation of an edge transport barrier in the presence of sufficient plasma heating. When the

barrier forms, it produces an increase in density over the whole plasma on the timescale of a confinement time. The H-mode operation is accompanied by the appearance of edge localized modes (ELMs) leading to a periodical relaxation of the edge pressure profile. These modes are instabilities driven by the steep gradients at the plasma edge and produce large particles and heat blasts escaping from the plasma. Not only the energy confinement is influenced by these modes, also they exhibit a potential danger for plasma facing components.

The phenomenology of ELMs has been numerously reviewed in literature [15–17]. Here, a short summary of the terminology and general physical understanding is given.

### 2.2.1. Phenomenology of edge localized modes

ELMs are repetitive instabilities and the ELM cycle is characterized by a quiet phase during which transport across the H-mode edge barrier is small, so that edge density and temperature gradients can gradually build up. When the pressure gradient reaches a stability limit, a phase of magnetic turbulence and associated enhanced radial transport sets in, which is terminated only after the collapse of the density and temperature profiles in the edge region. The duration of the refuel and reheat phase in between ELM crashes is directly related to the ELM losses.

More detailed descriptions about the current understanding of ELMs can be found in [15, 16], a more theoretical interpretation in [16, 18], and simulations of the pedestal stability for TCV H-mode discharges in [19–21]. In the following, we want to summarize the definitions and observations for different ELM types and introduce the terminology used in this work.

#### Type-I ELMs

The stability limit associated with type-I ELMs is linked to the edge pressure and edge pressure gradient and is approximately represented by a hyperbolic curve in  $n$ - $T$  space. They appear to be connected with values of the normalized local edge pressure gradient,  $\alpha \equiv -2\mu_0 R_0 (q^2/B_0^2) dp/dr$  near the limit of coupled low or intermediate- $n$  kink (peeling)-ballooning modes, where  $q$  is the safety factor,  $p$  the plasma pressure,  $R_0$  the major radius and  $B_0$  the toroidal magnetic field.

The ELM repetition frequency  $f_{ELM}$  increases with the energy flux  $P_{sep}$  through the

separatrix as

$$\frac{df_{ELM}}{dP_{sep}} > 0. \quad (2.2.1)$$

Spatially resolved measurements of the electron temperature  $T_e$  have shown that in some cases  $T_e$  drops even inside half of the major radius within a few milliseconds after the ELM event.

### Type-III ELMs

Type-III ELMs are found below a certain critical temperature at an edge pressure at or below that of type-I ELMs. The critical edge temperature for type-III ELMs appears to be independent of density at high edge density (resistive type) and can follow a  $n \times T \approx const.$  tendency at low density (ideal type).

The ELM repetition frequency decreases with the energy flux through the separatrix:

$$\frac{df_{ELM}}{dP_{sep}} < 0. \quad (2.2.2)$$

### Large ELMs

In TCV and COMPASS-D, at  $P_{tot} \gg P_{thr}$ , where  $P_{tot}$  is the total plasma power, another class of ELMs was found which exhibits larger energy and particle losses than what is usually observed for type-III ELMs. These ELMs are sometimes referred to as “large” ELMs [16]. In TCV, these ELMs slow down and increase in amplitude with increasing heating power and the pedestal pressure gradient is found to be limited by ideal ballooning. The ELM characteristics seem to be related to that of type-III ELMs at low collisionality.

### L-H transition

It was found that the Alfvén drift wave instability (ADW) plays an essential role in the edge plasma physics and represents the threshold for the L-H transition. The stability theory shows that, with increasing plasma pressure, the Alfvén waves mix with electron drift waves and suppress the unstable long wavelength perturbations, which are dominant in the transport. Analysis of the turbulent transport coefficients yields a scaling for the edge electron temperature  $T_e$  at the L-H transition [22],

$$T_e(a - \Delta x) [eV] = 32.6 A^{-1/5} s^{3/5} n_{el,e19}^{-3/10} B_0^{3/5} I_{MA}^{3/5} a_m^{-6/5} \Delta x_{cm}, \quad \nu^* > 1 \quad (2.2.3)$$

$$T_e(a - \Delta x) [eV] = 23.3 A^{-1/2} s n_{el,e19}^{-1} B_0 I_{MA} a_m^{-2} \Delta x_{cm}, \quad \nu^* < 1, \quad (2.2.4)$$

where  $a$  the plasma minor radius,  $\Delta x$  the width of the pedestal,  $A$  the plasma surface,  $s$  the magnetic shear,  $n_{el,e19}$  the line-integrated density,  $B_0$  the vacuum toroidal magnetic field,  $I_{MA}$  the plasma current and  $\nu^*$  the plasma collisionality.

The power threshold for L-H transition in TCV is given by [23],

$$P_{thr} = 1.42 n_{el,e20}^{0.58} B_0^{0.82} a^{0.81} R_0^1. \quad (2.2.5)$$

For  $P_{sep} \approx P_{thr}$ , repetitive L-H-L transitions occur.

### 2.2.2. Confinement and transport in H-mode

The H-mode exhibits global energy confinement values about a factor of two better than L-mode. Part of this is due to the formation of the edge transport barrier, another part of this improvement is due to a reduction in local transport throughout the plasma after the L-H transition. Experiments comparing L- and H-mode local transport rates under similar conditions have shown reductions in the electron thermal diffusivity, ion thermal diffusivity and angular momentum diffusivity, with the reduction in the electron thermal diffusivity being especially prominent. To quantify the enhancement of energy confinement with respect to L-mode in this work, we use the ITER-IPB98(y,2) scaling [2]:

$$\tau_E = \frac{W_e}{P_{tot}} \quad (2.2.6)$$

$$\tau_{IPB98(y,2)} = 5.62 \times 10^{-2} I_{MA}^{0.93} B_0^{0.15} n_{e19}^{0.41} P_{MW}^{-0.69} R^{1.97} \kappa_a^{0.78} (a/R_0)^{0.58} M_{amu}^{0.19} \quad (2.2.7)$$

$$H_{IPB98(y,2)} = \frac{\tau_E}{\tau_{IPB98(y,2)}}, \quad (2.2.8)$$

where  $W_e$  the electron plasma energy,  $P_{tot}$  the total heating power,  $I$  is the plasma current,  $B_0$  the vacuum toroidal magnetic field,  $n_{e19}$  line average density,  $R$  the major radius,  $\kappa_a = area/\pi a^2$  with  $a$  the minor radius, and  $M$  the average ion mass. The thermal diffusivity, attributed to H-mode, seems to be consistent with gyro-Bohm scaling,

$$\chi_{gB} = 3.25 T_{e,keV}^{3/2} B_0^{-2} M_{amu}^{0.5} Z^{-2} a^{-1} \text{ m}^2/\text{s}, \quad (2.2.9)$$

where  $T_e$  is the electron temperature and  $Z$  the ion charge [24]. Confinement studies of core and pedestal energy as function of the magnetic geometry have lead to the following

scalings of the pedestal pressure  $p_{e,ped}$  [25]:

$$p_{e,ped} \propto IB_0/a \times (B_0 R^{1.25})^{-0.1} \quad (2.2.10)$$

$$p_{e,ped} \propto \frac{I (mT_{e,ped})^{0.5}}{qa^2 (1 + \kappa^2)} \quad (2.2.11)$$

$$p_{e,ped} \propto I^{1.7} B_0^{0.4} V^{-0.5} P^{0.2} m^{0.5} \left( \frac{q_{95}}{q_{cyl}} \right)^{1.67} \quad (2.2.12)$$

where  $m$  is the ion mass,  $\kappa$  the plasma elongation,  $q_{95}$  the safety factor at 95% normalized poloidal flux radius and  $q_{cyl} = (2\pi B_0 a^2 \kappa) / (\mu_0 I R)$  the cylindrical safety factor.

### 2.2.3. Scaling of pedestal height and width

It is desirable to have a predictive capability for the pedestal pressure height and maximum gradient to identify MHD critical gradients. The pedestal pressure  $P_{ped}$  can be expressed as

$$P_{ped} = \left( \frac{dP}{dr} \right)_{crit} \Delta_{r,ped}, \quad (2.2.13)$$

where  $(dP/dr)_{crit}$  is the critical pressure gradient inside the pedestal region and  $\Delta_{r,ped}$  the pedestal width. As for the critical pressure gradient, a simple analytical formula for the ideal ballooning critical gradient [26] is given by

$$\left( \frac{dP}{dr} \right)_{crit} = \frac{1}{2\mu_0} \frac{1}{R} \left( \frac{RB_\theta}{a} \right)^2 \left( \frac{2}{1 + \kappa^2} \right). \quad (2.2.14)$$

Here,  $R$ ,  $\kappa$ ,  $B_\theta$  and  $\mu_0$  are major radius, elongation, poloidal magnetic field and permeability in the vacuum. This expression is only a simplified analytical formula for the critical pressure gradient limited by the infinite- $n$  ballooning instability. Recent theoretical, numerical and experimental studies have shown that with increasing plasma shaping, ballooning and external kink modes decouple due to the effect of the magnetic well and the critical pressure gradient is dominated by intermediate  $n$ 's [18, 19, 27, 28]. In this situation, the expression of equation (2.2.14) is significantly modified. Examination of the International Pedestal Database gives suggestions of these modifications [29].

A previous study [28] indicated that the maximum stable pressure gradient is only weakly dependent on width over a range of conditions,  $\nabla p_{crit} \propto \Delta_{r,ped}^{-1/4}$  and thus  $P_{ped} \propto \Delta_{r,ped}^{3/4}$ . The increase in the pedestal height with increasing width is somewhat less than linear because the typical unstable modes have eigenmodes with finite spatial extent and respond to the whole pedestal profile and not just the highest local pressure gradient.

Due to the weak dependence of the critical pedestal pressure gradient on the pedestal width, relatively large uncertainties in the width measurement result in only small uncertainties in the modeled pressure gradient. Since the measurement of pedestal height is more accurate than pedestal gradient or width, and the pedestal gradient can be obtained from pedestal height and width, various scalings of the pedestal pressure width have been proposed thus far based on experiments and theories. In the following, the basic assumptions are shortly presented; more details can be found in the literature [26, 30, 31].

### Width scaling based on magnetic and flow shear stabilization

This model assumes that the turbulence that drives the transport with gyro-Bohm scaling is stabilized by the magnetic and flow shear  $\gamma_{\mathbf{E} \times \mathbf{B}}$  in the pedestal region. It assumes that the maximum growth rate associated with this drift turbulence scales as  $\gamma_{max} \propto (c_s/\Delta) s^{-2}$ , where  $\Delta$  is the pedestal width in normalized poloidal flux,  $c_s$  the ion sound velocity and  $s$  the magnetic shear. The turbulence is suppressed when the  $\mathbf{E} \times \mathbf{B}$  shearing rate is equal to or larger than the maximum growth rate  $\gamma_{\mathbf{E} \times \mathbf{B}} \geq \gamma_{max}$ . The pedestal width is found to be

$$\Delta = C_1 \rho s^2 \quad (2.2.15)$$

with  $\rho$  the ion gyro radius and  $C_1$  some constant.

### Width scaling based on flow shear stabilization

In this model, the  $\mathbf{E} \times \mathbf{B}$  suppression of long wavelength modes is assumed to be relevant for establishing the edge transport barrier. The local growth rate is related to the connection length between the bad curvature region, on the outer side of the torus, and the good curvature region, on the inner side of the torus, in the pedestal region and reads  $\gamma_{local} \sim c_s / (qR)$ , where  $R$  is the major radius and  $q$  the safety factor. It is assumed that the turbulence is suppressed when  $\gamma_{\mathbf{E} \times \mathbf{B}} \geq \gamma_{local}$ . The pedestal width is found to be

$$\Delta = C_2 \sqrt{\rho R q}, \quad (2.2.16)$$

where  $C_2$  is some constant.

### Width scaling based on diamagnetic stabilization

For this model, the ideal ballooning mode growth rate is approximated by  $\gamma_b \approx [2c_s^2 / (L_p R)]^{1/2}$ , where  $L_p = -p / (dp/dr)$  is the pressure gradient scale length. It is assumed that the

pedestal width is approximately equal to  $V_{*i}/\gamma_b$ , where  $V_{*i} = \rho^2\omega_{ci}/L_{pi}$  is the ion diamagnetic velocity. Assuming further that  $L_p \sim L_{pi} \sim \Delta$ , one finds

$$\Delta = C_3\rho^{2/3}R^{1/3}, \quad (2.2.17)$$

where  $C_3$  is some constant.

### Width scaling based on neutral penetration

Neutral particles, which usually come from the scrape of layer (SOL) region, can penetrate inside the separatrix and affect the H-mode by modifying the particle, momentum and energy balance of the main plasma. From the neutral particle diffusion coefficient one finds the neutral penetration length  $\Delta x$  for steady-state neutral density proportional to the pedestal density  $n_{ped}^{-3/2}$ . In this model, the width of the barrier is assumed to be the length that neutral particles penetrate into the plasma and hence

$$\Delta = C_4 \frac{10^{27}}{n_{ped}^{3/2}} \quad (2.2.18)$$

where  $n_{ped} = n_i$  is the pedestal density and  $C_4$  some constant.

### Width scaling based on ion orbit loss

In Shaing's model based on ion losses [32], the predicted width of the pedestal is  $\Delta \propto \sqrt{\epsilon\rho_\theta}/\sqrt{s_{orbit}}$ , where  $\epsilon = a/R$  is the inverse aspect ratio,  $\rho_\theta$  the ion poloidal gyro radius and  $s_{orbit}$  a term due to the squeezing of the banana orbits by the electrical field. Assuming that  $s_{orbit}$  is constant, the scaling of the pedestal width is

$$\Delta = C_5\sqrt{\epsilon\rho_\theta} \approx C_5\epsilon^{-1/2}q\rho/\kappa_{95} \quad (2.2.19)$$

with  $\kappa_{95}$  the elongation at the 95% normalized poloidal flux radius and  $C_5$  some constant.

### Width scaling based on normalized poloidal pressure

In this model, the scaling of the pedestal width is based on a model proposed by Osborne [33]. Its argument is based on the onset of strong electromagnetic kinetic ballooning mode (KBM) turbulences near a critical value of normalized pressure gradient, which leads to the expectation of a strong dependence of the pedestal width in normalized poloidal flux space  $\Delta_\psi$  on the normalized plasma pressure  $\beta_\theta$  at the top of the pedestal.

Furthermore, the model describes a weak or no dependence of the width on other normalized parameters, such as the toroidal or poloidal gyroradius or the plasma collisionality. The scaling reads

$$\Delta_\psi = C_6 \beta_\theta^\gamma, \quad (2.2.20)$$

where  $C_6$  is some constant. The exponent  $\gamma$  was found to range in between 0.4 – 0.5.

### Empirical scalings

An empirical model treating the ionization length of neutrals into the pedestal [34] is given by

$$\Delta_r/R_0 = C_7 \left( \frac{dn_e}{dr} \right)^{-1/2}, \quad (2.2.21)$$

where  $\Delta_r$  is the pedestal width in real space,  $R_0$  the major radius and  $C_7$  some constant.

Another scaling of the normalized pedestal width  $\Delta_r/R_0$  as function of the pedestal electron temperature  $T_e$  [35] is given by

$$\Delta_r/R_0 = C_8 \frac{T_{e,ped}^{0.46}}{B_\theta^{0.51}}, \quad (2.2.22)$$

with a constant  $C_8$ . Both scaling were found to satisfy the DIII-D results [30]. The combination of both scalings reads

$$\Delta_r/R_0 = C_{9,1} \sqrt{\frac{n_{e,ped} T_{e,ped}}{\nabla n_{e,ped}} \frac{1}{B_\theta^{0.5}}} = C_{9,2} \sqrt{\frac{\beta_\theta B_\theta^{3/4}}{\nabla n_{e,ped}}}, \quad (2.2.23)$$

where  $C_{9,1}$  and  $C_{9,2}$  are some constants.

## 2.3. Ideal MHD stability analysis

In this section, a brief description of the ideal MHD stability analysis is given; a more detailed can be found in [10]. The numerical codes used to compute equilibria and ideal MHD stability are presented. The method and organization of these codes to compute stability maps of the pedestal region is described.

### 2.3.1. Normal mode formulation and eigenvalue problem

A plasma equilibrium is MHD stable, when the forces that act on the system are completely balanced. The force balance is changed by the occurrence of plasma perturbations,



which is inevitable in a real system. The evolution of the equilibrium depends then on the behavior of these forces, which can either restore the initial equilibrium state or enhance the perturbations. MHD instabilities arise on the ideal MHD time scale, typically in the order of milliseconds, and usually cause significant degradation or even complete destruction of the plasma confinement.

We want to study the *linear response of an equilibrium state*  $\rho_0$ ,  $\mathbf{j}_0$  and  $\mathbf{B}_0$  to a perturbation described by the vector displacement  $\xi$  of a fluid element. The linearized and integrated form of equations (2.1.1, 2.1.3, 2.1.4) reads

$$\rho_1 = \nabla \cdot (\rho_0 \xi) \quad (2.3.1)$$

$$\mathbf{Q} \equiv \mathbf{B}_1 = \nabla \times (\xi \times \mathbf{B}_0) \quad (2.3.2)$$

$$p_1 = -\gamma p_0 \nabla \cdot \xi - \xi \cdot \nabla p_0. \quad (2.3.3)$$

The perturbed quantities on the right hand side of the linearized momentum equation (2.1.2),

$$\rho_0 \ddot{\xi} = \nabla p_1 + \mathbf{j}_1 \times \mathbf{B}_0 + \mathbf{j}_0 \times \mathbf{B}_1 \quad (2.3.4)$$

can be replaced by using equations (2.3.1, 2.3.2, 2.3.3) to obtain a single vector equation for the displacement  $\xi$ ,

$$\rho_0 \ddot{\xi} = \mathbf{F}(\xi), \quad (2.3.5)$$

where  $\mathbf{F}$  is the force operator

$$\mathbf{F}(\xi) = \nabla (\gamma p_0 \nabla \cdot \xi + \xi \cdot \nabla p_0) + \frac{1}{\mu_0} [(\nabla \times \mathbf{B}_0) \times \mathbf{Q} + (\nabla \times \mathbf{Q}) \times \mathbf{B}_0] \quad (2.3.6)$$

The coefficients in  $\mathbf{F}$  do not depend on time and thus allow to formulate a *normal mode problem* using the Fourier ansatz  $\xi(\mathbf{x}, t) = \hat{\xi}(\mathbf{x})e^{i\omega t}$ , which leads to the eigenvalue equation

$$-\omega^2 \rho_0 \hat{\xi} = \mathbf{F}(\hat{\xi}). \quad (2.3.7)$$

The operator  $\mathbf{F}$  is self-adjoint [10]; its eigenvalues  $\omega^2$  are real. A positive eigenvalue  $\omega^2 > 0$  corresponds to a pure oscillations and is hence considered stable, whereas  $\omega^2 < 0$  implies a solution which grows exponentially with the rate  $\gamma = \sqrt{-\omega^2}$ , thence unstable.

### 2.3.2. Extended energy principle

Equation (2.3.7) has a direct relation with the change of potential energy  $\delta W$  of the system associated with the perturbation  $\xi = \xi(\mathbf{x})^1$ . Multiplication of equation (2.3.7) by

---

<sup>1</sup>The hat notation of  $\xi$  has been dropped.

$\xi^*$  and integration over the plasma volume yields the *conservation of energy*

$$\omega^2 K(\xi^*, \xi) = \frac{\omega^2}{2} \int \rho_0 |\xi|^2 dV = -\frac{1}{2} \int \xi^* \mathbf{F}(\xi) dV = \delta W(\xi^*, \xi) \quad (2.3.8)$$

$$\omega^2 = \frac{\delta W(\xi^*, \xi)}{K(\xi^*, \xi)}, \quad (2.3.9)$$

where  $K(\xi^*, \xi)$  is proportional to the kinetic energy of the plasma.  $\delta W$  can be interpreted as the work done against the force  $\mathbf{F}(\xi)$ , when the plasma displaces by  $\xi$ . The sign of  $\delta W$  determines thence the stability, since  $\delta W < 0$  implies  $\omega^2 < 0$ . The energy principle states that for any allowable test function  $\xi$ , for which  $\delta W$  becomes negative, is sufficient for instability.

Taking appropriate *boundary conditions* into account, the potential energy  $\delta W$  can be separated into a plasma (P), a surface (S) and a vacuum (V) contribution,

$$\delta W = \delta W_P + \delta W_S + \delta W_V, \quad (2.3.10)$$

where the individual contributions are given by [10]

$$\delta W_P = \int_P dV \left[ \underbrace{\frac{|\mathbf{Q}|^2}{\mu_0}}_{>0} + \underbrace{\gamma p_0 |\nabla \cdot \xi|^2}_{>0} + \underbrace{\mathbf{j} \cdot (\xi \times \mathbf{Q})}_{\geq 0} + \underbrace{(\nabla \cdot \xi) (\xi \cdot \nabla p_0)}_{\geq 0} \right] \quad (2.3.11)$$

$$\delta W_S = \int_S dS |\mathbf{n} \cdot \xi|^2 \mathbf{n} \cdot \left[ \nabla \left( p_0 + \frac{B_0^2}{2\mu_0} \right) \right] \quad (2.3.12)$$

$$\delta W_V = \frac{1}{2} \int_V dV \frac{|\hat{B}_1|^2}{\mu_0}, \quad (2.3.13)$$

with  $\hat{B}_1$  denoting a perturbation of the vacuum field.

The surface component  $\delta W_S$  usually vanishes unless currents flow on the surface of the plasma-vacuum boundary. The term  $\delta W_V$  is identical to the perturbed magnetic energy in the vacuum region. The presence of a ideal conducting wall close to the plasma surface is stabilizing, whereas a large vacuum region is destabilizing.

The terms in  $\delta W_P$  have the following physical interpretation. The  $|\mathbf{Q}|^2$  term represents the required energy to bend magnetic field lines and is stabilizing. The  $\gamma p_0 |\nabla \cdot \xi|^2$  term represents the energy required to compress the plasma and is stabilizing. The third and fourth term are proportional to  $j_{\parallel}$  and  $\nabla p$  and can be positive or negative and, if destabilizing, are sometimes referred to *current- and pressure-driven modes*.

### 2.3.3. Basic types of instabilities and numerical approach

The terminology of current- and pressure-driven modes and their numerical computation is briefly explained in the following.

#### The external kink mode

Current-driven modes can even exist in zero-pressure force-free plasmas with parallel current. Among these current-driven modes, the modes with long parallel wavelengths and macroscopic perpendicular wavelengths ( $k_{\parallel}/k_{\perp} \ll 1$ ,  $k_{\perp}a \sim n \sim 1$ , where  $n$  is the toroidal mode number) are the most dangerous and are called kink modes.

In this work, the KINX code [36] was extensively used to solve the ideal MHD stability problem in order to test plasma equilibrium stability against external kink modes. The code provides the option to compute either the growth rate of the mode by using the full description of the kinetic energy in flux coordinates, or to find only the stability index, i.e. the sign of the lowest eigenvalue, by using a reduced norm of the kinetic energy  $K$ , as it is for example given by equation (2.3.8). The results of the code compare well with those of ELITE, MISHKA and GATO [37].

The code decomposes the normal plasma displacement  $\xi_r = \xi \cdot \nabla\psi$  into its harmonics by using trigonometric basis functions,

$$\xi_r = \sum_{m,n} \xi_{m,n}(\psi) e^{i(m\theta+n\phi)}, \quad (2.3.14)$$

with  $n$  the toroidal and  $m$  the poloidal mode number. In this frame, the helicity of the magnetic field lines coincides with the helicity of the dominant  $(m, n)$  contribution of the perturbation. The Fourier modes  $\xi_n e^{in\phi}$  with different toroidal mode number  $n$  are decoupled and equation (2.3.9) becomes an 2-dimensional eigenvalue problem for each  $\xi_n$ , which yields a continuous spectrum of stable solutions and cluster points as unstable ones.

When using a sufficiently fine-meshed equilibrium, the KINX code features  $N^{-2}$  convergence of the mode growth rate as function of the grid size, where  $N$  is the number of grid points. The growth rate  $\gamma_{\infty}$  for an infinite dense mesh can be then extrapolated by

$$\gamma_{\infty} = \left( \frac{\gamma_1}{N_2} - \frac{\gamma_2}{N_1} \right) \times \left( \frac{1}{N_2} - \frac{1}{N_1} \right)^{-1} \quad (2.3.15)$$

from the eigenvalues  $\gamma_1$  and  $\gamma_2$  obtained from equilibria with grid size  $N_1$  and  $N_2$ . Convergence studies of the growth rate obtained from KINX, for the H-mode equilibria with

various shapes studied in this work, can be found in appendix B. The study showed that grid sizes of  $N_\psi \times N_\chi = 256 \times 256$  and  $320 \times 320$  are sufficient to yield a good convergence of  $\gamma$  for single null and snowflake diverted discharges, respectively.  $N_\psi$  and  $N_\chi$  correspond to the number of radial and poloidal grid points.

### The ballooning mode

The most important pressure-driven instabilities are the interchange and ballooning modes. Former modes are usually stabilized for  $q > 1$  and high magnetic shear  $s = (r/q)(dq/dr)$  by the average curvature of the toroidal magnetic field; their stability is given by the Mercier criterion [10].

Latter modes destabilize for high pressures and thus determine one set of criteria which limits the maximum achievable value of  $\beta$ . The mode is concentrated in the unfavorable curvature region in the low field side of the magnetic surfaces and can lead to more unstable situations than the simple interchange perturbation. Magnetic shear can be helpful in stabilizing ballooning modes, yet the most effective way to stabilize given magnetic field profiles is to keep  $\beta$  below some critical value [10]. The most unstable modes have long parallel and short perpendicular wavelengths ( $k_{\parallel}/k_{\perp} \ll 1$  and  $k_{\perp}a \sim n \gg 1$ ).

The CHEASE equilibrium code solves the ballooning mode criteria in the limit of an infinite toroidal mode number  $n$ , where the potential energy reads

$$\delta W_P(n \rightarrow \infty) = \frac{1}{2} \int_{-\infty}^{+\infty} \left\{ c_1 \left| \frac{\partial \xi_r}{\partial \chi} \right|^2 + c_2 |\xi_r|^2 \right\} J d\chi. \quad (2.3.16)$$

$\xi_r$  is the radial component of the displacement vector, as noted before, and  $\chi$  is a generalized poloidal angle in straight field line coordinates. The quantities appearing in equation (2.3.16) are given in the literature [14, 38]. In general, the ballooning stability is computed by truncating the integral in equation (2.3.16). It often, but not always, turns out that  $\chi = 0$  is the most unstable case. Therefore, it is standard practice to use a rather moderate integration interval, e.g.  $\chi = [-10\pi, 10\pi]$ .

### Diamagnetic stabilization

Instabilities with short perpendicular wavelengths that exhibit a narrow radial mode structure will be subject to finite ion Larmor effects. For these instabilities, finite diamagnetic drift frequency effects must be taken into account, especially if one wants

to treat the edge plasma region between the separatrix and the high density side of the pedestal in H-mode. Extensions to the ideal MHD theory have been formulated to investigate the finite gyroradius stabilizing effect of ion diamagnetic drift frequency,  $\omega_{*i} = (m/r) (T_i/e_i B_0) (d \ln p_i/dr) \propto 1/p_i$ , on linear ideal MHD eigenmodes [27, 39]. Here,  $T_i$ ,  $e_i$  and  $p_i$  are temperature, charge and pressure of the thermal ions of the plasma,  $B_0$  is the equilibrium magnetic field,  $r$  is the radial coordinate, and  $m$  is the poloidal mode number.

In these models, the growth rate  $\gamma_{MHD}$  of an ideal MHD mode, such as finite- $n$  ballooning or low- $n$  kink (peeling) mode, is compared with  $\omega_{*i}$ . The mode is stabilized by ion diamagnetic effects, if  $\gamma \leq \omega_{*i}/2$  is satisfied. For the H-mode pedestal it was found that for low enough plasma density the  $\omega_{*i}$  stabilization can lead to a second zone of ballooning stability, in which all the ballooning modes are stable for any value of the pressure gradient. One example is the MISHKA-D code, which includes these effects [27].

Although a rough estimate, a practical formula including effects of  $\omega_{*i}$  stabilization is given by Huysmans [27] for the maximal unstable toroidal mode number  $n_{max}$  and reads

$$n_{max} \cong \frac{\epsilon^2 L_p}{q \rho_i}, \quad (2.3.17)$$

where  $\epsilon = r/R_0$  with  $r$  the radius of the magnetic surface and  $R_0$  the major radius,  $L_p = L_{pi} = |d(\ln p_i)/dr|^{-1}$  the characteristic ion pressure gradient scale length,  $\rho_i = \sqrt{T_i M_i} / (e_i B_0)$  the ion Larmor radius with ion temperature  $T_i$  and mass  $M_i$ , the vacuum toroidal field  $B_0$ , and  $q = (r B_t) / (R_0 B_p)$  the safety factor with  $B_t$  and  $B_p$  the toroidal and poloidal magnetic field.

In this work, the corresponding values in equation (2.3.17) are taken at the flux surface where the pedestal gradient is maximal and  $L_{pi}$  is assumed to be equal to  $L_{pe}$ .

### 2.3.4. General organization of the calculations

The organization of the calculations is presented as following: First, a general description about the coupling of the individual codes is given, which explains the computation of the ideal MHD stability limits of a plasma equilibrium. Secondly, the method to compute the stability limits of an H-mode edge pedestal is described. When computing the stability map of the edge pedestal, general task consists of scanning the pedestal pressure gradient and bootstrap current fraction.

### **Ballooning and external kink mode stability**

An initial plasma equilibrium is created, either set artificially or taken from the LIUQE equilibrium reconstruction and kinetic and current profiles, and is given as input to the CHEASE code. A self-consistent equilibrium is computed and tested against ballooning stability. Additional informations, such as flux surface averaged quantities, bootstrap current density etc. can be extracted by a Perl-script. The CHEASE-equilibrium is passed via an interface to the CAXE equilibrium code [40], which recalculates the equilibrium on an optimized flux mesh for KINX calculations. Then, the KINX stability calculations are performed by iteration on the initial guess of the mode growth rate; the lowest eigenvalue is obtained as output.

The computations were performed on a Intel<sup>®</sup> Core 2 Duo or Core i7 CPU. A typical calculation cycle CHEASE-CAXE-KINX takes less than 5 minutes and depends on the grid sizes and stability of the mode. Initially stable configurations require more time, because in this case the initial eigenvalue guess has to pass all the way from the initial value to the lowest absolute preset value.

### **Edge pedestal stability map**

The analysis of the edge stability requires an accurate description of the pressure and current density profiles in the pedestal region. The slightest misalignment of the bootstrap current with respect to the edge pressure gradient can change stability significantly. Particular care needs to be taken to ensure that the ratios between the pressure gradient at the separatrix and the maximum pressure gradient are kept constant. As consequence, due to the alignment of the bootstrap current with the pressure gradient, the ratio between bootstrap current density at the separatrix and maximum bootstrap current must be also constant. This makes it possible to compare stability properties of a series of equilibria with different pedestal pressure gradient and bootstrap current density. The following generalized recipe was followed to compute the stability map of the edge pedestal:

1. An initial self-consistent equilibrium is created with CHEASE from an artificial or experimental plasma shape, pressure gradient  $p'$  and current density  $j_{||}$  profile.
2. The Heaviside function  $H(x) \simeq 1/[1 + e^{-2kx}]$  is constructed from the pedestal parameters, where  $k = 1/2\delta$  with the pedestal width  $\delta$ , and  $x = \rho - (\rho_0 - \delta)$  with the location  $\rho_0$  of the pedestal center (see figure 2.1). The  $p'$  profile from the initial

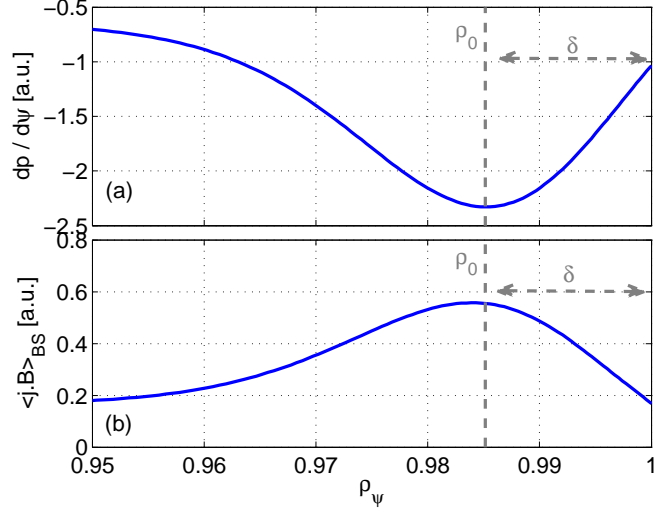


**Figure 2.1.:** Schematic representation of the barrier position  $\rho_0$  and width  $w$  for (a) the pressure profile derivative  $dp/d\psi$  and (b) the bootstrap current density parallel to the magnetic field  $\langle \mathbf{j} \cdot \mathbf{B} \rangle_{BS}$  (flux surface averaged).

equilibrium is rescaled,  $p'_{new} = p' \times [1 + (A - 1) H / \max(H)]$ , to obtain an adapted pressure gradient profile.

3. The collisionless bootstrap current  $j_{BS}$  is computed by CHEASE based on  $p'_{new}$  using the formulas given by Sauter [13] (see subsection 2.1.2), assuming equal temperatures  $T_i = T_e$ . Only the edge bootstrap current density  $j_{BS,edge}$ , i.e. for  $\rho \gtrsim 0.97$ , is used for further calculations.
4. A self-consistent equilibrium is computed by CHEASE based on the scaled pressure derivative profile  $p'_{new}$  and  $j_{||,new} = j_{||} + B \times j_{BS,edge}$ , where  $B$  is a preset scaling factor of the edge bootstrap current. The total plasma current is kept constant.
5. Ideal MHD-stability analysis is performed:
  - Calculation of the ballooning stability criteria by CHEASE.
  - Computation of the growth rate of external kink modes for various  $n$ 's with CAXE-KINX (reduced energy norm) on two different grid sizes and using equation (2.3.15) to extrapolate the growth rate of the mode for a infinite dense grid.

The stability map is scanned with help of the two scaling factors  $A$  and  $B$  for the pressure derivative and bootstrap current density profile in the edge, respectively. To obtain a

sufficiently high resolved stability map, 20 – 25 values each for  $A$  and  $B$  are needed. The stability of external kink modes was usually computed for the toroidal mode numbers  $n = \{1, 3, 5, 8, 10, 15, 20, 30, 40\}$  for each grid point in the stability diagram. The results of each code are saved in serial in a central text file and are further processed for analysis in MATLAB<sup>®</sup>.

UNIX shell scripts control the computation cycle with the possibility to recover, if the automatic preparation of a self-consistent equilibrium by CHEASE failed. Since the computation of the mode growth rates for various  $n$ 's is time-consuming and certain modes appear only in a narrow parameter range, a configuration file allows to set-up regions of interest in the stability map beforehand, for which the computation of growth rates is carried out or skipped. The total computation time strongly depends on the grid size of the stability map, total number of toroidal mode numbers, the grid size of the equilibrium and stability codes, and the choice of regions of interest. A typical computation time is around 3 – 7 days on a Intel<sup>®</sup> Core 2 Duo or Core i7 CPU.



## 3. Thomson scattering diagnostic

The theory of light scattering by electrons in a magnetized plasma and its practical application as Thomson scattering diagnostic is beyond the scope of this thesis, but can be found in numerous textbooks [7, 41]. In this chapter the basic principles of Thomson scattering and its realization as diagnostic on TCV are briefly discussed. The upgrade of this diagnostic with regard to higher spatial resolution for the measurements of high electron pressure gradients associated with transport barrier as in eITB and H-mode discharges, is presented. Further, the interpretation of the scattered signal by non-linear fitting to evaluate electron temperature and density is described. Finally, the possibility of laser triggering in synchronization to MHD events like ELMs is discussed.

### 3.1. Theory of Thomson scattering

Under the influence of an electric field  $\mathbf{E}_i$  with angular frequency  $\omega_i$ , free electrons can be excited to oscillate at the same frequency. In the non-relativistic limit, they will emit radiation in a dipole pattern in directions different from that of the incident wave. If the photon energy is much smaller than the rest energy of the electron, this effect is called Thomson scattering. Basically, this effect can be described by classical, non-relativistic electrodynamics. A relativistic correction becomes significant in the scattering spectrum when electron thermal energies exceed a fraction of a percent of their rest mass, i.e.  $T_e > 1$  keV.

### 3.1.1. Non-relativistic dipole approximation

In the dipole approximation for the non-relativistic limit, the scattered electrical field by a *single electron* is derived from the Maxwell equations and can be expressed as

$$\mathbf{E}_s = \frac{r_e}{R} [\hat{\mathbf{s}} \times (\hat{\mathbf{s}} \times \mathbf{E}_i)] \quad (3.1.1)$$

where  $\hat{\mathbf{s}}$  is the direction in which the scattered signal is detected,  $R$  the distance to the charge and

$$r_e = \frac{e^2}{4\pi\epsilon_0 m_0 c^2} = 2.82 \times 10^{-15} \text{ m}. \quad (3.1.2)$$

the classical electron radius. The operator  $\hat{\mathbf{s}} \times \hat{\mathbf{s}} \times \equiv \hat{\mathbf{s}}\hat{\mathbf{s}} - \mathbf{I}$  in (3.1.1) represents the polarization tensor in dipole approximation. The scattered power per unit solid angle  $\Omega_s$  is given by

$$\frac{dP}{d\Omega_s} = R^2 c \epsilon_0 |E_s|^2 = r_e^2 \sin^2 \phi c \epsilon_0 |E_i|^2, \quad (3.1.3)$$

with  $\phi$  the angle between  $\hat{\mathbf{s}}$  and  $\mathbf{E}_i$ . The differential scattering cross section, the ratio of  $dP/d\Omega_s$  to the incident power per unit area  $c \epsilon_0 |E_i|^2$ , is defined as

$$\frac{d\sigma}{d\Omega_s} = r_e^2 \sin^2 \phi. \quad (3.1.4)$$

The integral of this expression over all solid angles, where  $d\Omega_s = 2\pi \sin \phi d\phi$ , gives the total Thomson scattering cross section

$$\sigma = \frac{8\pi}{3} r_e^2 = 6.65 \times 10^{-29} \text{ m}^2. \quad (3.1.5)$$

The scattered field of *many electrons* can be calculated by superposing the electrical field contributions of all electrons in the observation volume, which requires information on the relative phase of each contribution as well as the amplitude. In a plasma, a test electron is surrounded by a cloud of other charged particles. This charged cloud will lead to a screening of the electrical field of the test electron within a typical distance, the Debye-length,

$$\lambda_D = \sqrt{\frac{\epsilon_0 e T_e}{n_e e^2}} \quad (3.1.6)$$

with  $T_e$  in eV. A test electron has a shielding cloud of charge  $+e$  consisting purely of electron holes. The thermal ions do not contribute to the shielding, because they move much slower than the electrons. If the scattered fields of electron and shielding cloud are *incoherent*, the phase difference from both scattered fields will be large, i.e.  $|\mathbf{k}| \lambda_D \gg 1$ .

Assuming that the scattering induces only a small change in the wavelength of incident and emitted wave,  $|\mathbf{k}_i| \approx |\mathbf{k}_s|$ , a phase correlation parameter  $\alpha$  can be written as

$$\alpha = \frac{\lambda_i}{4\pi\lambda_D \sin(\theta/2)}, \quad (3.1.7)$$

with  $\theta = \pi - \phi$  the angle between  $\mathbf{k}_s$  and the axis of the observation optics.

For the Thomson scattering on TCV, with scattering angles of  $60^\circ \leq \theta \leq 120^\circ$  and laser wave length  $\lambda_i = 1064$  nm, the condition of incoherent scattering, i.e.  $\alpha \ll 1$ , is well satisfied. For the most unfavorable case of phase correlation, i.e. low temperature  $T_e \sim 10$  eV, high density  $n_e \sim 10^{20} \text{ m}^{-3}$  and  $\theta \sim 60^\circ$ , one obtains  $\alpha \sim 1/14$ .

In order to calculate the total incoherently scattered power from an assembly of electrons within a specified volume element  $d\mathbf{x}d\mathbf{v}$  in phase space  $(\mathbf{x}, \mathbf{v})$ , one needs to know the position and velocity of each electron for every time. For this purpose, equation (3.1.1) is evaluated in Fourier space for the far field approximation. The scattered field from one electron becomes

$$\mathbf{E}_s(\omega_s) = \frac{r_e e^{i\mathbf{k}_s \cdot \mathbf{x}}}{2\pi x} 2\pi\kappa \mathbf{\Pi} \cdot \mathbf{E}_i \delta(\mathbf{k} \cdot \mathbf{v} - \omega), \quad (3.1.8)$$

using  $\kappa = |d(\mathbf{k} \cdot \mathbf{v} - \omega)/d\omega_s| = |1 - \hat{\mathbf{s}} \cdot \mathbf{v}/c|$ . The scattered field of this electron has a single frequency

$$\omega_s = \omega_i + \mathbf{k} \cdot \mathbf{v} = \omega_i + (\mathbf{k}_s - \mathbf{k}_i) \cdot \mathbf{v}, \quad (3.1.9)$$

which is the double Doppler-shifted frequency of the input wave. The shift arises from the electron motion with respect to the source of the incident wave  $\mathbf{k}_i \cdot \mathbf{v}$  and from its motion with respect to the observation point  $\mathbf{k}_s \cdot \mathbf{v}$ .

The total incoherently scattered power spectrum is equal to the number of particles in the element  $\int f d\mathbf{x}d\mathbf{v}$  with distribution function  $f$ . If the electrons are in thermal equilibrium,  $f = f(\mathbf{x}, \mathbf{v})$  is given by the Maxwellian distribution function at temperature  $T_e$ , and we can write

$$\frac{d^2 P}{d\Omega_s d\omega_s} = r_e^2 \int_V \langle S_i \rangle \int |\mathbf{\Pi} \cdot \hat{\mathbf{e}}|^2 \kappa f(\mathbf{x}, \mathbf{v}) \kappa \delta(\mathbf{k} \cdot \mathbf{v} - \omega) d\mathbf{v} d\mathbf{x} \quad (3.1.10)$$

where  $V$  is the scattering volume from which the scattered radiation is observed and  $\langle S_i \rangle$  the mean incident Poynting vector usually expressed as  $P_i/A$ , the total incident power divided by the total input beam area.

### 3.1.2. Relativistic effects and spectral density function

At the electron temperature values achieved in TCV,  $1 \text{ eV} \leq T_e \leq 15 \text{ keV}$ , it is essential to treat the Thomson scattering process relativistically. The relativistic corrections affect the polarization of the scattered radiation and the scattered spectrum.

The polarization operator  $\mathbf{\Pi}$  in equation (3.1.1) becomes dependent on  $\beta = \mathbf{v}/c$  when the relativistic equations of motion are introduced. This changes the orientation of the incident field vector seen by the electron. A small fraction of the scattered light, in the order of  $\beta^2 = eT_e/mc^2$ , will be polarized in a direction orthogonal to the incident polarization. For TCV's typical high temperature plasmas, where  $T_e \sim 10 \text{ keV}$ , the depolarization factor reaches values of  $\sim 2\%$ .

The scattered spectrum is modified by the effect of the relativistic aberration, where uniformly emitted radiation in the rest frame of the electron becomes a light cone in forward direction in the frame of a stationary observer. This implies that we observe preferentially greater scattering intensity from electrons moving towards the observation point. Additionally, scattering from relativistic plasma will modify the Doppler effect and shift the spectrum towards the blue. In case the relativistic corrections are neglected in the interpretation, the asymmetry in the spectrum leads to an over-estimation of  $T_e$  by approximately  $(1 - eT_e/m_0c^2)^2 \sim 4\%$  for the above used value of  $T_e$  and scattering angle of  $\theta = 90^\circ$ .

A simple analytic form of the relativistic Thomson scattering spectrum was derived by Selden [42], in which  $\mathbf{k}$  and  $\omega$  are replaced by equivalent and more accessible variables  $\theta$  and  $\lambda_s$ . For  $100 \text{ eV} \leq T_e \leq 100 \text{ keV}$ , the relativistic spectral density function reads

$$S(T_e, \epsilon, \theta) = \frac{1}{\lambda_i} a(\zeta) \frac{e^{-2\zeta B(\epsilon, \theta)}}{A(\epsilon \theta)}. \quad (3.1.11)$$

where

$$\epsilon = \frac{\lambda_s}{\lambda_i} - 1, \quad \zeta = \frac{m_e c^2}{2eT_e}, \quad (3.1.12)$$

$$A(\epsilon, \theta) = (1 + \epsilon^3) [2(1 - \cos \theta)(1 + \epsilon) + \epsilon^2]^{1/2}, \quad (3.1.13)$$

$$B(\epsilon, \theta) = \left[ 1 + \frac{\epsilon^2}{2(1 - \cos \theta)(1 + \epsilon)} \right] - 1, \quad (3.1.14)$$

$$a(\zeta) = \sqrt{\frac{\zeta}{\pi}} \left( 1 - \frac{15}{16\zeta} + \frac{345}{512\zeta^2} + \dots \right). \quad (3.1.15)$$

The scattered spectral power can then be written as

$$\frac{dP_s}{d\lambda_s d\Omega} = P_i n_e L r_e^2 S(T_e, \epsilon, \theta), \quad (3.1.16)$$

with the laser input power  $P_i$ , the electron density  $n_e$  and the length  $L$  of the observation volume.

Assuming a known (Maxwellian) velocity distribution function, and a given geometry ( $\theta$ ), the free parameter in  $S$  is  $T_e$ . The total scattered intensity is directly proportional to density. Measuring the scattered intensity in a number of spectral channels gives access to  $T_e$  and  $n_e$ . The  $Te$  measurement requires only a relative calibration of the spectrometer, whereas  $n_e$  relies on absolute calibration of the system.

Major advantages of a Thomson scattering system are that (1) it measures local quantities due to well defined observation volumes, (2) it provides instantaneous measurements due to a laser pulse in nanosecond range and (3) the interpretation of the measured signals is unambiguous, since they represent a velocity distribution.

## 3.2. The Thomson scattering system on TCV

The small total Thomson scattering cross section, equation (3.1.4), indicates very low values for the incoherent scattered signal. As a rough estimate for TCV, using representative values for the size of the observations volume,  $L = 13$  mm, the solid angle,  $\Delta\Omega_s \approx 1.5 \times 10^{-2}$  sr, and the electron density,  $n_e \approx 1 \times 10^{19}$  m<sup>-3</sup>, and assuming the optical throughput of the detection system to be 100%, only a fraction of  $n_e L r_c^2 \Delta\Omega_s \approx 1.5 \times 10^{-14}$  of the incident photons will reach the detector. This estimate illustrates the severe requirements on the high power light source and the need for an efficient and sensitive detection system. This implies the careful adaption of the observation optics to the needs of the experiment and an elaborated and reliable analysis of the acquired data.

### 3.2.1. Laser system and beam path

As light source three commercially available high power Q-switched Nd:YAG-laser, model Quanta-Ray PRO 290 from Spectra-Physics, are used. They consists of an oscillator and amplifier unit and emit at a wavelength of 1064 nm with a repetition frequency of 20 Hz. The nominal output energy of one laser unit is 1.5 J with a typical pulse length of 10 – 15 ns. The beam diameter at the exit of the laser unit is  $\sim 10$  mm, its beam divergence  $< 1$  mrad.

The lasers are located in a room separated from TCV, where the beams of the three individual lasers are grouped in an horizontal plane on a optical table. The beam bundle

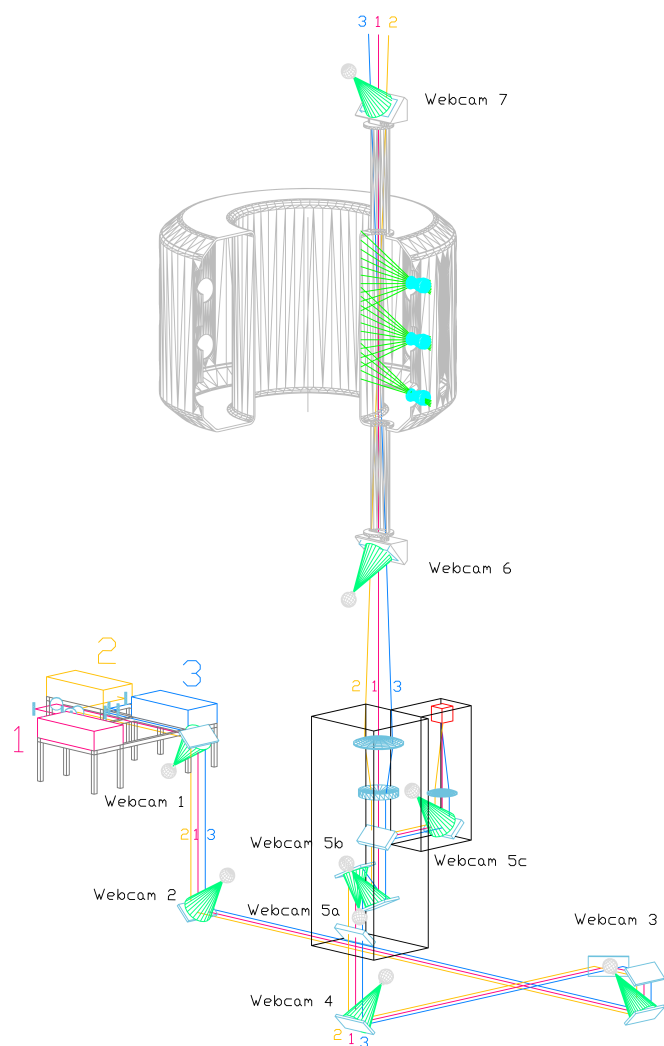


**Figure 3.1.:** Laser beam path of the TS-system on TCV: Three laser beams (red,yellow,blue) are conducted by multiple mirrors from the laser room to a box underneath TCV. In the box, each beam is independently aligned and after focusing send to the vacuum vessel. A fraction of light scattered from a glass surface is directed to an integrating sphere and used to monitor the laser pulse energy. Individual reflecting mirrors and the Brewster windows are monitored by web-cams.

is then guided by means of five steering mirrors from the laser room to an box underneath TCV, where six individual mirrors, two for each laser beam, align the individual beams for their passage through the vessel. The linear polarized laser beams, with the electrical field parallel to the toroidal magnetic field, enter and leave the TCV vacuum vessel via windows oriented at Brewster's angle, figure 3.1.

To stay well below the damage threshold of the optical components ( $\sim 1$  GW/cm) in the beam path, the beam diameter is increased by a Galilean telescope in the laser room, which consists of a defocusing and focusing lens, and refocused by a second double lens telescope to the midplane of the TCV vessel.

Along the beam path, commercially available web-cams, with their IR-filters removed, are installed for monitoring and alignment purposes. The fraction of scattered laser light from the mirror or lens surfaces is sufficient to allow for surveillance of the surface treatments of these components as well as the beam alignment during TCV operations.

#### 3.2.2. Collection optics and fiber bundles

The scattered light from the vertical laser beams is collected by wide angle camera lenses installed on three horizontal ports of TCV (setup in 2006). The lenses are positioned behind vacuum windows, which are protected by automatic shutters from coating during boronization and glow discharges. The optical axes of the camera lenses and the laser chords are arranged such that the scattering plane is perpendicular to the toroidal field, figure 3.2(a).

The wide angle camera lenses have been specially designed for this application. Their f-number is adapted to the numerical aperture of the fibers. The scattered light is projected to the highly transmissive fiber bundles (CeramOptec, Optran WF 1000/1100), which consist of 8 or 9 single quartz glass, large core fibers ( $\varnothing = 1$  mm). Mounted in line, figure 3.2(b), their front ends define the scattering volume dimension. At the polychromator end, fiber bundles with rectangular and circular sections are used with the 3-channel and 4-channel versions, respectively.

#### 3.2.3. Polychromators and detectors

The small Thomson scattering cross-section together with the short-pulse operation of the Nd:YAG-laser require fast and sensitive detectors in the visible and near infrared spectral range. Silicon avalanche photodiodes (APD) have become a widely used detector type due to their favorable quantum efficiency of between  $\rho = 0.8$  at  $\lambda = 960$  nm and  $\rho = 0.2$  at  $\lambda = 1060$  nm and to their high internal gain factors ( $M \sim 100$ ) at a noise equivalent power (NEP) of the order of  $10^{-13}$  W/ $\sqrt{\text{Hz}}$ . The sharp drop in the efficiency towards longer wavelengths in the infrared limits their application to the use of shorter wavelengths than the used laser wavelength.

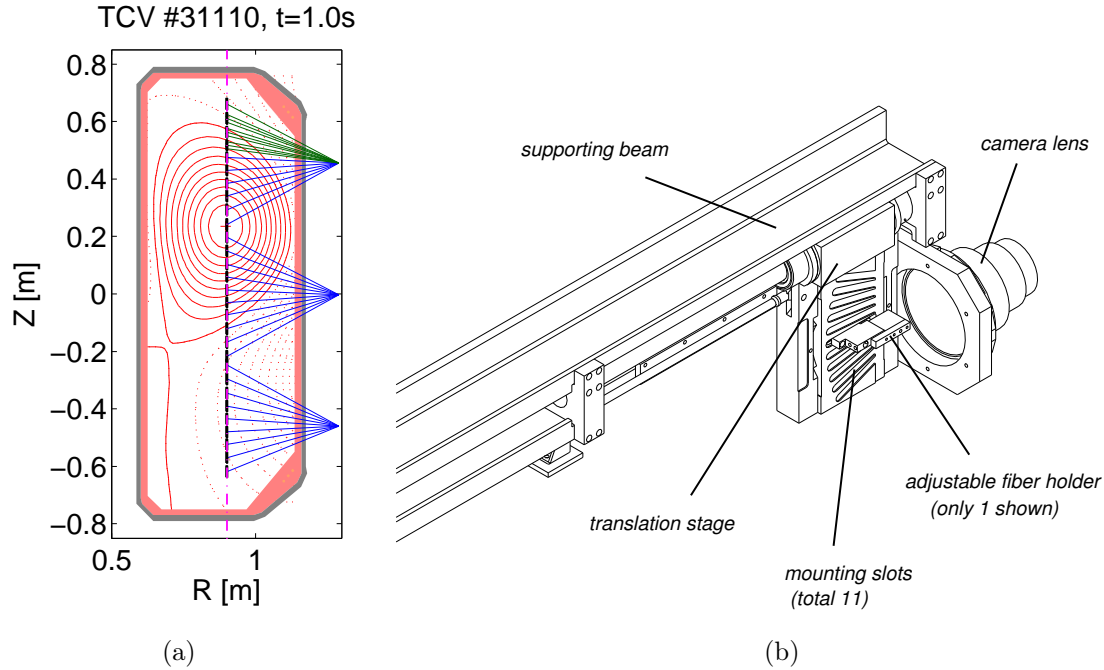


**Figure 3.2.:** (a) Setup of the viewing chords of the TCV-TS system in 2006 covering the full vessel cross section. The vertical dash-dotted magenta line shows the path of the laser beam. The viewing chords represent different observation volume lengths:  $\Delta z \approx 38$  mm (blue) and  $\Delta z \approx 13$  mm (green). (b) Support structure for the optical fibers and camera lens.

The TS system consist of two different types of polychromators, one version with 3 spectral channels using APDs (RCA, model C30974E) with a electrical bandwidth  $B$  of 20 MHz as detectors. Each detector incorporates a preamplifier such that responses of up to 370 kV/W at 900 nm are achieved when the diodes are operated close to their maximum bias voltage, which is typically 340 – 380 V at room temperature. These polychromators are employed in the TS-EDGE system.

The second version of polychromators, used in the TS-MAIN system and shown in figure 3.3, features 4 spectral channels using APDs (RCA, model CD1787) with a electrical bandwidth of 50 Hz. Their temperature is stabilized by a Peltier thermo-electric circuit to a value of  $13.2 \pm 0.1^\circ$  C.

A disadvantage of APDs is the strong dependency of their responsivity on the diode temperature. Heat dissipation in the preamplifier leads to a gradual rise in the detector temperature and a consequent decrease in its response. To monitor the detector response, each one is irradiated with short light pulses from a LED diode before and after the plasma



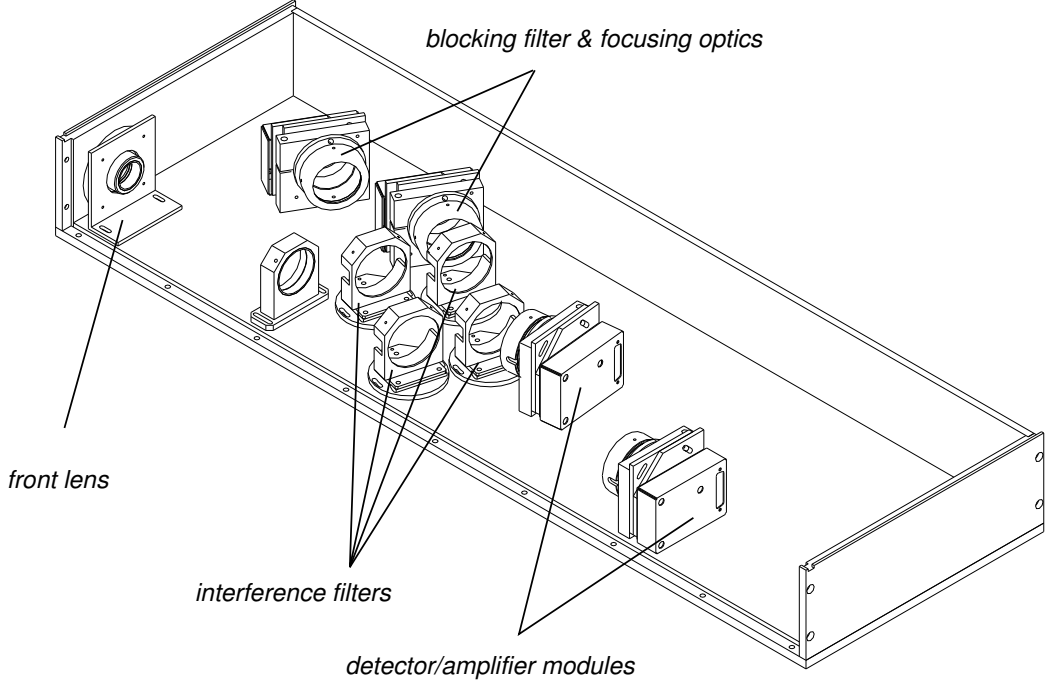


**Figure 3.3.:** Schematic view on the 4-channel filter polychromator.

discharge. Variations in sensitivity are measured by comparing the signal from a given detector with a reference. This information can be used to disable faulty detectors in the latter analysis of the signals.

The signal-to-noise ratio of a APD detection circuit in the case of a narrow-band detection system is given by [43]:

$$\frac{S}{N} = \left( \frac{i_s}{i_n} \right)^2 = \frac{(RP_0)^2}{B(NEP \cdot R)^2}, \quad (3.2.1)$$

where  $P_0$  is the average value of the intensity of light incident on the detector and  $R$  the responsivity of the APD, which includes the internal gain factor. A more realistic estimation, which is used to estimate the temperature resolution capability of each polychromator in section 3.3.2, is given by

$$\frac{S}{N} = \frac{(\tau RP_0)^2}{B(\gamma_{NEP} NEP \cdot R)^2 + 2e_0 B \cdot \tau R (P_{scat} + \gamma_{brems} P_{brems})}, \quad (3.2.2)$$

which takes into account the spectral transmission  $\tau$  of the optical system, photon statistics in the scattered signal  $P_{scat}$  and background radiation  $P_{brems}$ , a noise enhancement factor  $\gamma_{brems}$  to include line radiation from recombination processes in the plasma and high background radiation in the case of strong additional EC-heating, and the excess noise factor  $\gamma_{NEP}$  for additional noise multiplication.

### 3.3. Optimization for the measurement of transport barriers

The TS system was initially designed to cover a wide variety of possible plasma equilibria [8]. The scattered light was collected at 35 observation volumes (spatial channels) distributed along the laser beam to cover the full vertical height of the vacuum vessel. During this thesis work, the system has been reconfigured in order to match needs for measurements with high spatial resolution with the following goals: (1) Resolve gradients associated with eITBs in the plasma core. (2) Keep a set of channels for measurements of the H-mode pedestal (ETB). (3) Expand the  $T_e$  range of the edge channels. Some of the following general considerations concerning spatial resolution apply to both ITBs and ETBs.

Part of the viewing optics were regrouped and re-attributed to the regions of interest covering now only the middle and upper poloidal part of the vessel. One has to note that these modifications were subject to several boundary conditions. The available laser power, the desired minimum detectable electron density and the optical throughput of the detection system imposed conditions on the choice of the size of the scattering volume and hence the spatial resolution of the system. Further restrictions on the operational regime were imposed by the application of strong EC-heating leading to a substantial increase in background light and hence a severe decrease in signal-to-noise ratio ( $S/N$ ). In this section, the technical considerations and compromises to optimize the TS system for the measurement of transport barriers are presented.

#### 3.3.1. Optimization of the viewing optics for the high resolution measurement of transport barriers

In the past there were several reasons to believe that the electron temperature and density gradients in eITB, measured by the TS-system, were limited by the spatial resolution of the system. The following subsection is a short summary of the experimental observations and theoretical simulations suggesting the need of improvements towards higher spatial resolution. The hardware modifications are presented and measurements of the gradients in  $T_e$  and  $n_e$  in fully non-inductive eITB discharges are discussed.

width $\delta$	original $R_0/L_x$	$R_0/L_x$ after profile convolution			
		$\Delta z = 40$	$\Delta z = 20$	$\Delta z = 13$	$\Delta z = 4.5$
60	30	<b>26</b>	29	30	30
40	45	35	42	43	45
30	60	41	<b>53</b>	57	60
20	90	47	70	<b>79</b>	88
10	180	52	94	122	168
7	250	53	101	137	<b>220</b>
5	350	53	104	148	280

**Table 3.1.:** Limits of measurable normalized gradient  $R_0/L_x$ : Width of the gradient region  $\delta$  [mm], length of the scattering volume  $\Delta z$  [mm] determining the spatial resolution and the normalized gradient  $R_0/L_x$  after profile convolution. The maximum achievable  $R_0/L_x$  for an error of  $\leq 20\%$  is labeled in bold.

### Profile convolution

In order to study profile gradients characterized by a width that is comparable to the effective size of the TS observation volume, it is necessary to address the effect of gradient smoothing due to limited spatial resolution. To quantify the effect, a convolution procedure has been applied, which uses a simple box-shaped function of width  $\Delta z$  as the instrumental profile, figure 3.4(a). The results are presented in table 3.1, showing the normalized gradient  $R_0/L_x$  before and after smoothing, where  $R_0 = 0.88$  m is the major radius and  $L_x$  the gradient scale length of a quantity  $x$ . As seen from the simulation, significant smoothing (ratio  $> 1.2$ ) will occur if the width  $\delta$  of the original profile is approximately  $\Delta z$ . The value  $\Delta z = 4.5$  mm corresponds to the “effective” spatial resolution of the TS-EDGE system *after mapping on the mid-plane*, but depends on the flux expansion and thus on the particular shape of the plasma cross section.

It was found that the former standard spatial resolution of  $\Delta z = 40$  mm of the TS-MAIN system, *along the laser beam path*, was not sufficient to resolve normalized gradients  $R/L_x$  in eITBs exceeding values of 25 – 30 without altering the results considerably. Several options for  $\Delta z$  were analyzed and are shown in figure 3.4(b). A good compromise between S/N, range of measurable  $R/L_x$ , availability of polychromators and financial costs, suggested to double the spatial resolution, i.e.  $\Delta z = 20$  mm.

One has to keep in mind that the operation of deconvolution is only defined for linear

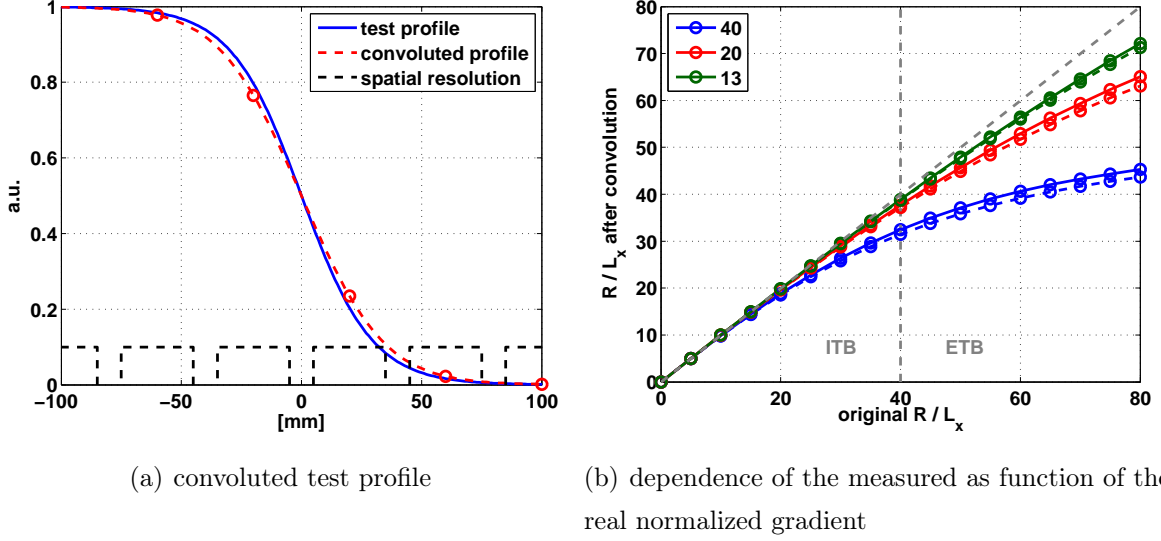


**Figure 3.4.:** (a) Convolution of a test profile,  $R/L_x = 30$ , with the box response function for low spatial resolution,  $\Delta z = 40$  mm. (b) Dependence of  $R/L_x$  after the convolution as function of the real  $R/L_x$  for  $\Delta z = 40, 20, 13$  mm and different response function representations: box as solid line and Gaussian as dashed line.

systems. Temperature and density profiles from Thomson scattering are obtained as the result of non-linear operations. The recorded signals from a given observation volume may be regarded as a linear superposition, but the relation to the relevant parameters - density and temperature - is non-linear. Therefore, deconvolution of a smoothed profile cannot be used to recover the original.

### Cross-check with soft X radiation profile from DMPX

On TCV, the Thomson scattering is the only system to measure directly the electron temperature in EC-heated discharges. The electron cyclotron emission (ECE) system suffers from signal pollution by suprathermal electrons during periods of EC-heating. However, valuable information about the temperature profile can be deduced from the plasma soft X ray emissivity measured by the Duplex Multiwire Proportional X-ray counter (DMPX). Inversion of the line integrated DMPX measurements by the Fisher algorithm [44] yields spatial emissivity profiles which can be approximated as

$$g_{\text{soft X}} \propto Z_{\text{eff}} n_e^2 T_e^{\alpha(T_e)}. \quad (3.3.1)$$

Figure 3.5 shows that the profile reconstruction of the DMPX signals indicates a

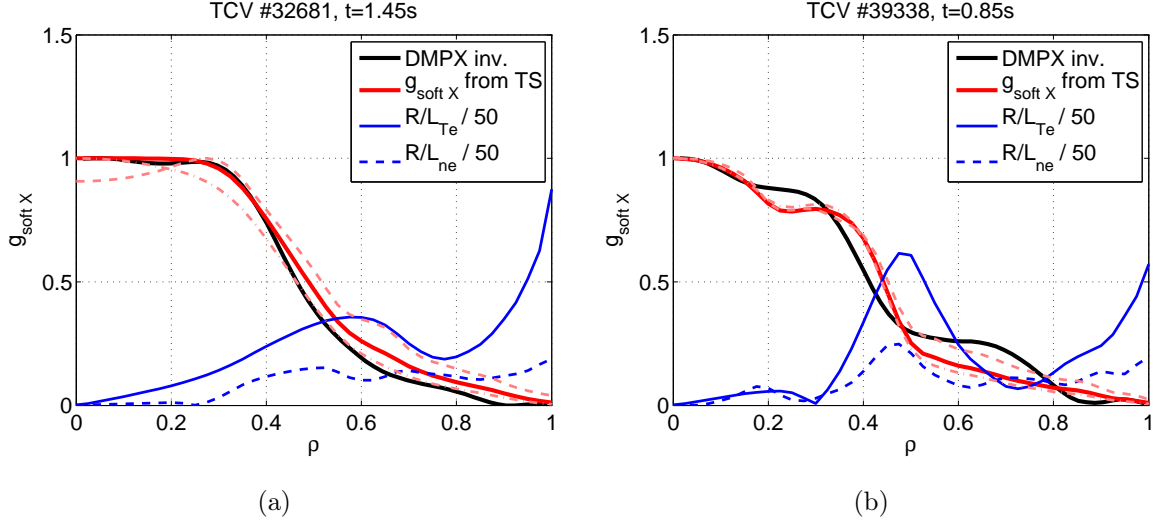


**Figure 3.5.:** Comparison of the soft X emissivity profile from an eITB, (a) low spatial resolution  $\Delta z = 40\text{ mm}$  and (b) after the upgrade to high spatial resolution  $\Delta z = 20\text{ mm}$ . The black line is the cubic spline fit of the soft X-ray emissivity profile measured by DMPX (normalized). The red line is the cubic spline fit of the normalized soft X-ray emissivity with  $\alpha = 0.35$  computed from the TS measurements. The light red dashed and dash-dotted line represent the soft X-ray emissivity profile computed with  $\alpha = 0.1$  and  $0.5$ , respectively. The blue solid and dashed line represent the normalized gradients  $R/L_{T_e}$  and  $R/L_{n_e}$  from the  $T_e$  and  $n_e$  profiles, respectively.

higher gradient in  $T_e$  and/or  $n_e$  as could be resolved by the former low spatial resolution with  $\Delta z = 35 - 40\text{ mm}$  of the TS system.

One has to keep in mind that the inversion process of the soft X-ray emissivity profile yields no unique but a class of possible solutions in terms of temperature and density making an absolute quantification of profile shape difficult. Furthermore, the DMPX profiles can be also polluted by contributions from impurities and variations in  $\alpha(T_e)$  as function of the plasma radius are difficult to estimate.

### Predictions from theory

Gyrokinetic studies of the stationary density gradient  $(R/L_{n_e})_{\text{stat}}$  in eITB discharges have shown that relatively large values of  $10 - 15$  can be sustained [45]. In the regime of low or negative magnetic shear, which is inherent with these plasma scenarios, the trapped electron mode (TEM) leading to an outward particle flux is strongly stabilized,

such that the density profile is coupled to  $T_e$  via the thermodiffusive pinch,  $(R/L_{ne})_{stat} \sim 0.45 R/L_{Te}$ , and  $T_e$  is tailored by local changes in the  $q$  profile. Due to this coupling, theoretical values of  $R/L_{ne} \sim 20$  were reported suggesting the existence of an inward pinch in reverse shear eITB scenarios. These results were interpreted to be either an effect of neoclassical inward thermodiffusion in the absence of anomalous activity, suppressed by negative magnetic shear, or an effect of another mechanism whose physics is still linked to turbulence. The latter micro-instability should lead to weaker radial energy transport and to an inward thermodiffusion pinch localized near the  $s = 0$  region. Temperature gradient modes are a possible candidate for the last mechanism for typical values of  $R/L_{Te}$  reached in TCV [46, 47].

These numerical predictions underlined the necessity to improve the spatial resolution capability of the system. More accurate measurements of  $R/L_{Te}$  and  $R/L_{ne}$  could give valuable information for future data modeling and the analysis of the underlying physics.

#### Arrangement of spatial channels

The modification and re-attribution of the viewing chords were determined by the necessity to keep the ability to diagnose various plasma scenarios. There are several possibilities to place the channels with different spatial resolution to cover certain parts of the plasma cross section. The mounting plate comprises 10 slots that can be used for different sets of fiber bundles. The available sets of fibers were bundles with  $2 \times 4$  fibers for high-resolution core channels, where one bundle feeds two polychromators, and bundles with  $3 \times 3$  fibers for high-resolution edge channels, where one bundle feeds three polychromators. Several regions of interest, as the location of the eITB barrier or the H-mode edge pedestal, were identified and had to be taken into account.

Figure 3.6 presents the general layout of the viewing chords with the color coding for the length  $\Delta z$  of the observation volume blue/magenta/green = 35 – 39/16 – 19/12 mm, respectively. The chords of the TS-MAIN system were arranged such that measurements of high spatial resolution,  $\Delta z = 16 – 19$  mm, can be done in eITB discharges with the magnetic axis at  $z \geq 0$  m. The position of the TS-EDGE chords (green) with high spatial resolution of  $\Delta z = 12$  mm for the measurement of the H-mode pedestal was adapted to the needs of the respective H-mode experiment.

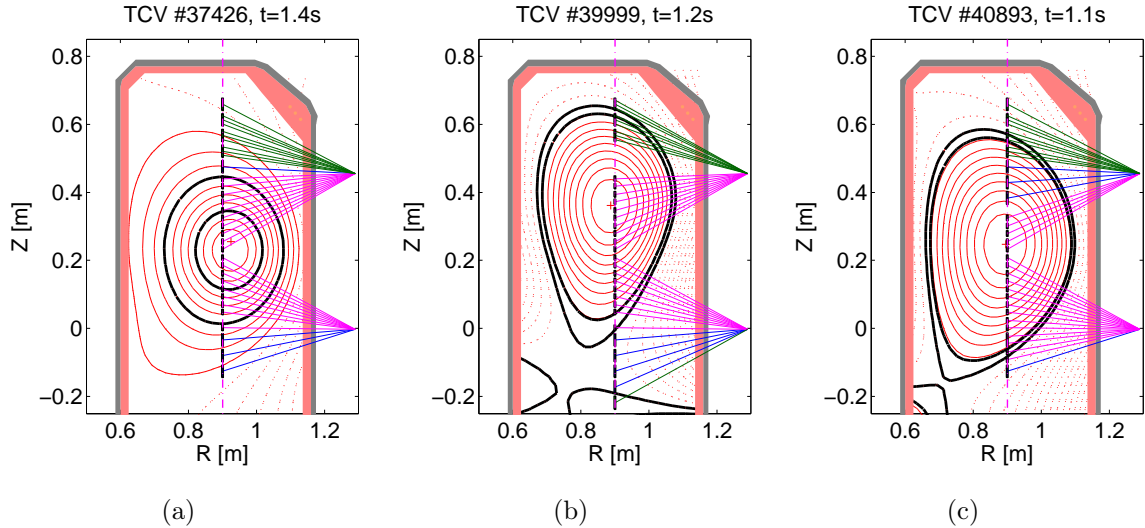


**Figure 3.6.:** Optimization of the TCV-TS viewing chords for various plasma scenarios covering only the mid and upper part of the TCV vessel cross-section: (a) high spatial resolution in the core (magenta chords) and low edge resolution (blue) for eITB measurements in 2008, (b) high core resolution and TS-EDGE (green) adapted for snowflake diverted H-mode discharges in 2009-2010 and (c) high core resolution and TS-EDGE adapted for single-null diverted H-mode discharges in 2010. Black lines show the plasma flux surface region.

### Fiber splitting

As discussed before, there were several limitations of different nature to the hardware modifications towards higher spatial resolution. The best compromise of all constraints, which also involved as little hardware modifications as possible to ensure backwards compatibility, suggested to install modified fiber bundles on the former fixations of the observation optics. For this purpose, fiber bundles (CeramOptec, WF 1000/1100N) consisting of  $2 \times 4$  single quartz glass ( $\varnothing = 1$  mm) were purchased that are composed of one single head facing the plasma and then split into two branches to feed the scattered light into two different polychromators, figure 3.7.

The limitation of the number of available polychromators made it necessary to re-attribute the viewing chords such that only plasmas in the upper half of the plasma vessel are covered.

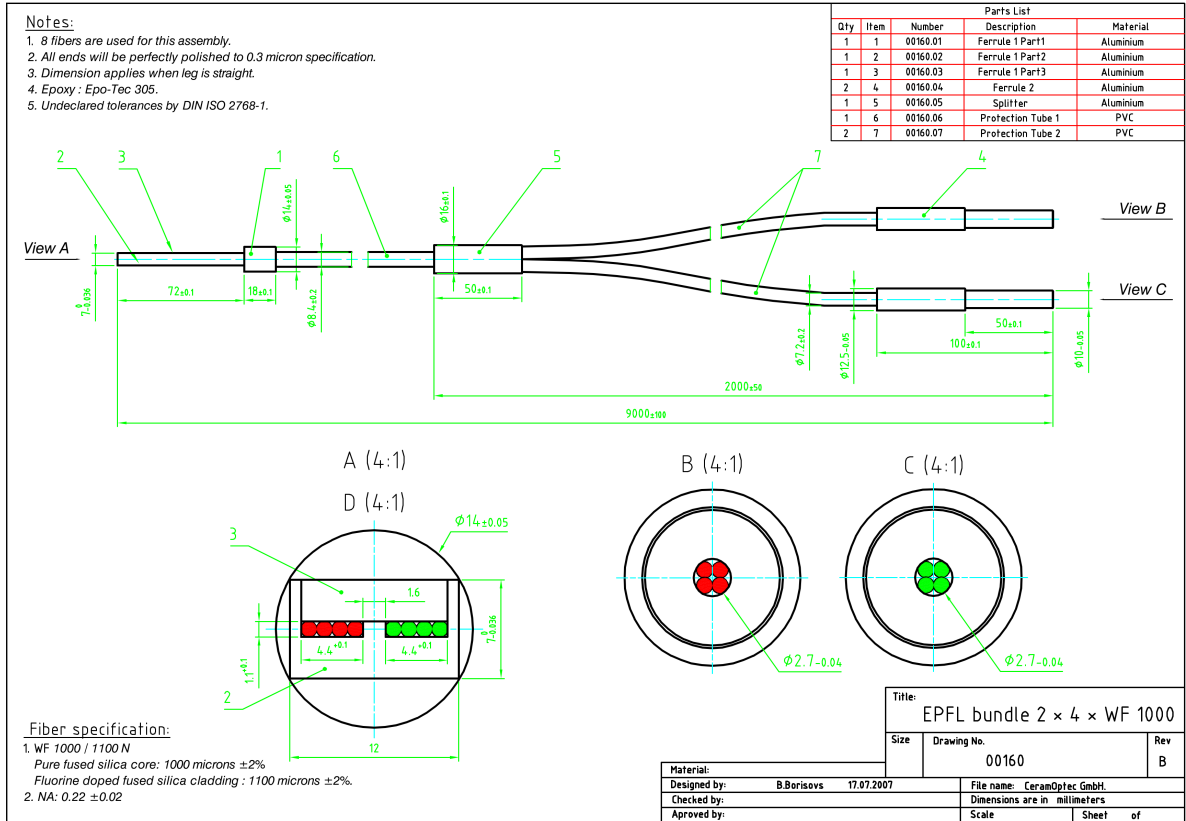


**Figure 3.7.:** Technical design of the fiber bundles: The compact front piece facing the plasma is composed of  $2 \times 4$  fibers, view A, which split into two separate bundles and feed the scattered light into two different polychromators, view B and C.

### Results from eITB measurements

The comparison of the  $T_e$  and  $n_e$  gradient measurements from comparable eITB discharges after and before the hardware upgrade shows that there was indeed profile smoothing by the limited spatial resolution. For the comparison, a series of fully non-inductive eITB discharges was repeated under similar conditions. In order to enlarge the parameter space, a scan in density for line-integrated densities of  $n_{e,lin} = (6 - 12) \times 10^{18} \text{ m}^{-2}$  and EC-heating power of  $P_{ECH} = 500 - 750 \text{ kW}$  was done, varying the bootstrap current contribution to the total current in the range of 35 – 50%. For TCV, the highest reported normalized gradients measured by low spatial resolution were  $R/L_{T_e} = 20 - 25$  and  $R/L_{n_e} = 9 - 12$  [48]. The new measurements, whose results are shown in figure 3.8, revealed about 20% higher  $T_e$  and almost identical  $n_e$  gradients, suggesting  $(R/L_{n_e})_{stat.} \sim c_1 R/L_{T_e}$  with  $c_1 = 0.25 - 0.45$ .

The profiles hint that there could be even higher gradients in  $n_e$  comparable to those as



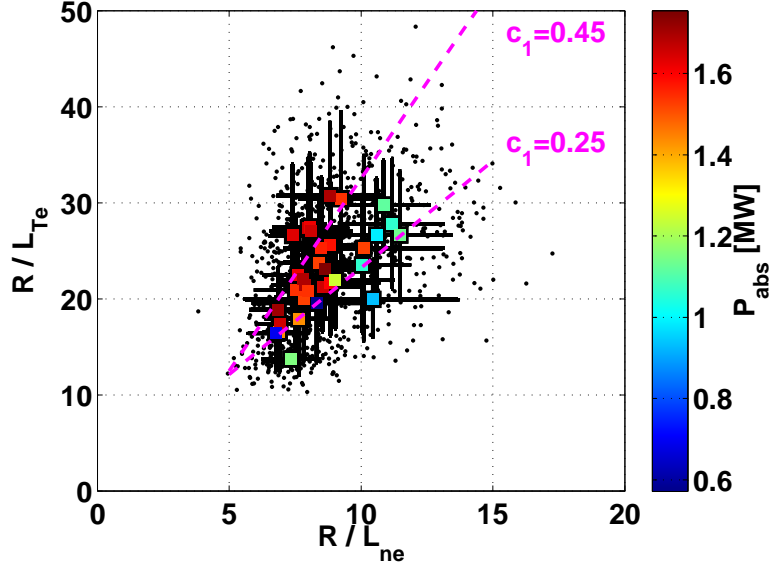


**Figure 3.8.:** Gradient measurements in eITB discharges:  $R/L_{Te}$  as function of  $R/L_{ne}$  in fully non-inductive eITB discharges, averaged over the stationary phase of the discharge. Black dots represent all gradients from the profiles fitted by splines.

spectral channel	edge		core	
	$\lambda_{\text{center}}$ [nm]	FWHM [nm]	$\lambda_{\text{center}}$ [nm]	FWHM [nm]
F1	1054	6	1041	20
F2	1041	20	1012	38
F3	1012	38	950	85
F4	950	85	810/830	160

**Table 3.2.:** Interference filter characteristics for the polychromators of the TS-MAIN system

predicted by theory [45]. These profiles correspond to times shortly before the appearance of MHD events, such as infernal modes, that degrade considerably the transport barrier. A more thorough scan in parameters will be needed to throw more light on this issue. Furthermore, eITB discharges with central counter-current drive leading to even higher gradients in  $T_e$  and  $n_e$  should be investigated for this purpose. However, this was beyond the scope of this thesis work.

spectral channel	default		high $T_e$	
	$\lambda_{\text{center}}$ [nm]	FWHM [nm]	$\lambda_{\text{center}}$ [nm]	FWHM [nm]
F1	1054	6	1041	20
F2	1041	20	1012	38
F3	1012	38	950	85

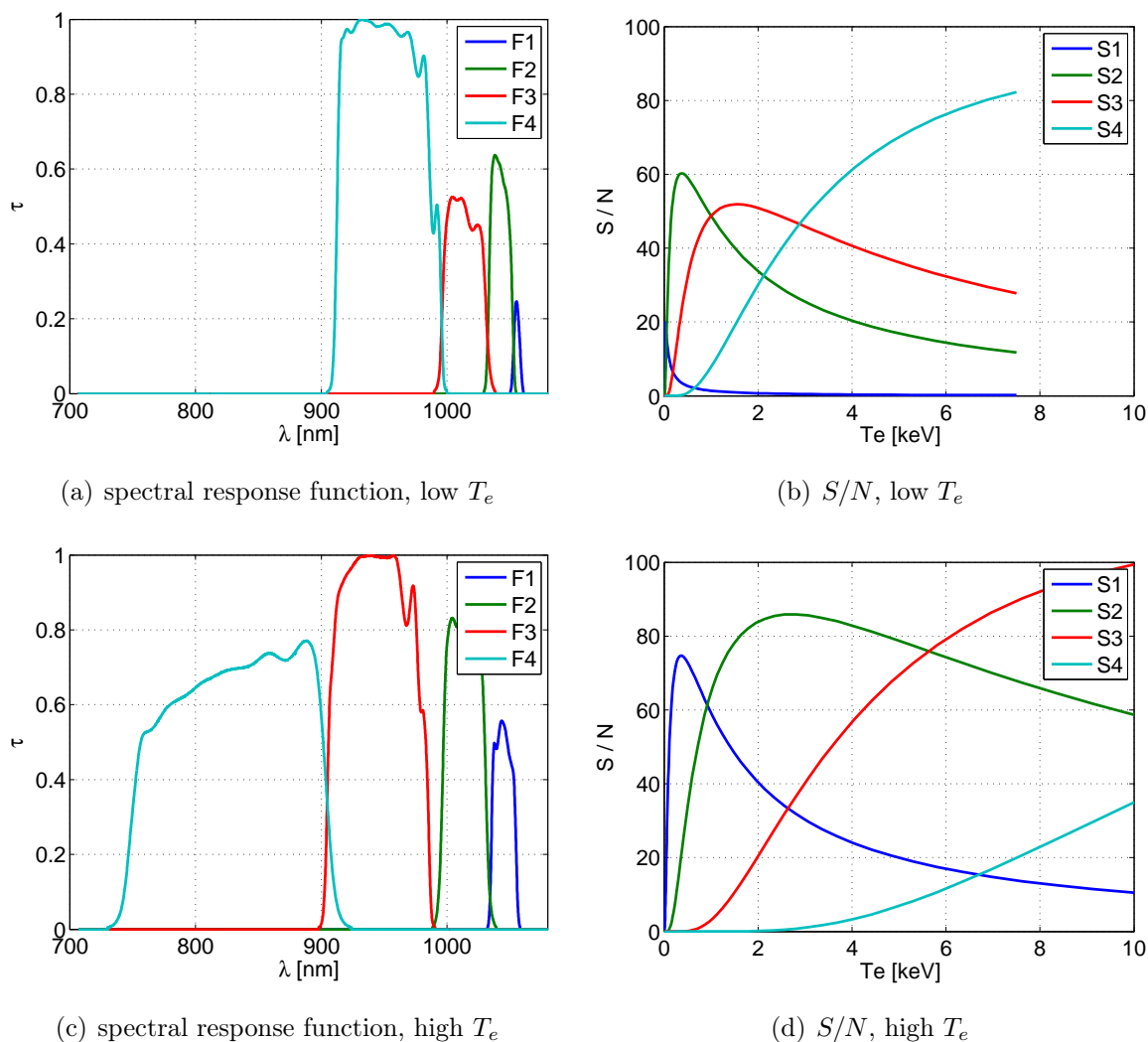
**Table 3.3.:** Interference filter characteristics for the polychromators of the TS-EDGE system

### 3.3.2. Optimization of the polychromators for high temperature measurements

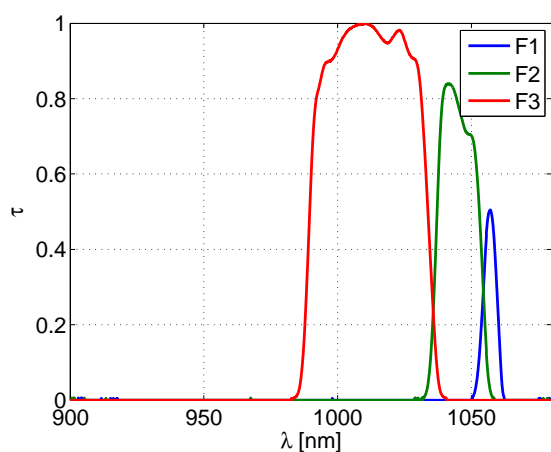
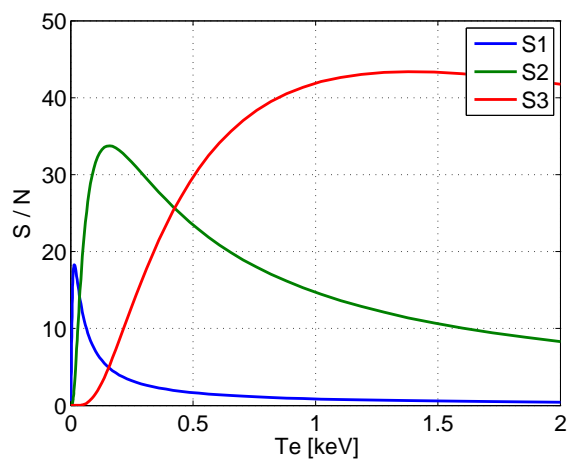
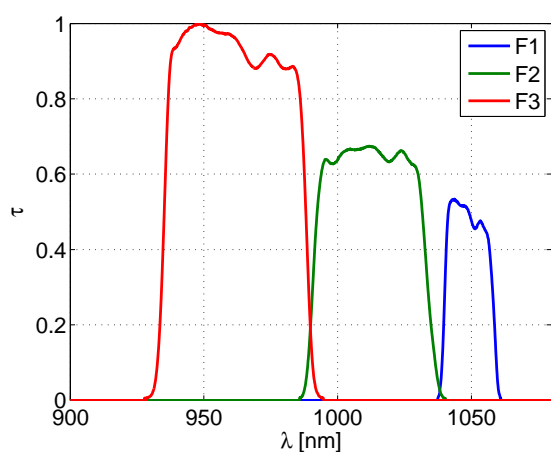
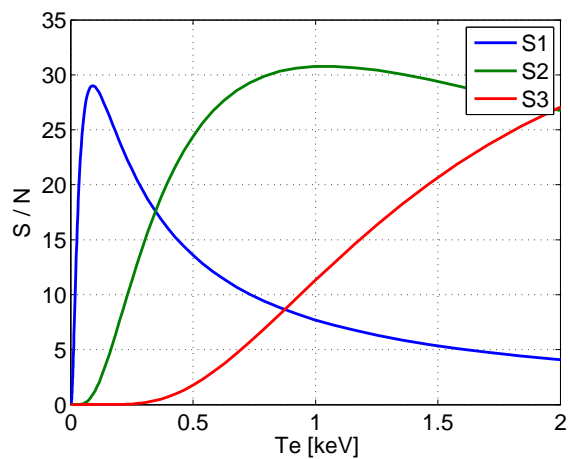
The spectral filter settings of both polychromator types, the 3-channel and 4-channel model, were modified to meet the measurement requirements of high  $T_e$  in additional heated H-mode discharges and eITB. Table 3.2 lists the combination of wide band filters that have been chosen for the 4-channel model to cover a range of  $T_e$  from 10 eV  $\rightarrow$  7.5 keV at the plasma edge and a range of  $T_e$  from 150 eV  $\rightarrow$  25 keV in the plasma core. The relative filter transmission of the two different setups and the estimation of the signal-to-noise ratio for each spectral filter, computed with equation (3.2.2) and  $\gamma_{\text{brems}} = 200$  and  $\gamma_{\text{NEP}} = 5$ , is presented in figure 3.9.

Table 3.3 lists the combination of wide band filters that have been chosen for the 3-channel model to cover a range of  $T_e$  from 25  $\rightarrow$  1 keV or 50  $\rightarrow$  2.5 keV.

The spectral filter setting and an approximation of the signal-to-noise ratio using  $\gamma_{\text{brems}} = 20$  and  $\gamma_{\text{NEP}} = 10$  in  $T_e$  are shown in figure 3.10.



**Figure 3.9.:** Spectral response function and  $S/N$  approximation for the 4-channel polychromator: spectral response function for (a) low and (c) high  $T_e$ , approximation of the signal-to-noise ratio for each spectral filter as function of  $T_e$  for (b) low and (d) high  $T_e$

(a) spectral response function, low  $T_e$ (b)  $S/N$ , low  $T_e$ (c) spectral response function, high  $T_e$ (d)  $S/N$ , high  $T_e$ 

**Figure 3.10.:** Spectral response function and  $S/N$  approximation for the 3-channel polychromator: spectral response function for (a) low and (c) high  $T_e$ , approximation of the signal-to-noise ratio for each spectral filter as function of  $T_e$  for (b) low and (d) high  $T_e$

### 3.4. Improvements in the data processing

The calculation of electron temperature  $T_e$  and density  $n_e$  from the scattered signals requires that the emission spectrum can be described by a known function of these two parameters. The measured signals refer to the scattered light intensity in the different spectral channels of a polychromator. The full emission spectrum can be reconstructed by use of equation (3.1.16).  $T_e$  and  $n_e$  can be obtained by either a straight-forward comparison of signal ratios in the individual filters, section 3.4.1, or a more elaborated non-linear fitting of the signals in least-square sense, section 3.4.2. In this section the improvements in the data analysis and treatment are discussed.

#### 3.4.1. Ratio evaluation method

A simple and fast method to obtain  $T_e$  from a set of signals measured in different spectral channels uses signal ratios from pre-calculated look-up tables. This method is known as ratio evaluation method (REM). Using equation (3.1.16), the scattered power collected by the detector  $j$  of a polychromator  $m$  reads

$$P_{jm} = P_i r_e^2 L_m \Delta\Omega_m n_{e,m} \int_{-\infty}^{\infty} \tau_{jm}(\lambda) S(T_{e,m}, \theta_m, \lambda) d\lambda, \quad (3.4.1)$$

where  $\Delta\Omega_m$  represents the solid angle, under which the collection optics is seen by the observation volume. The absolute spectral transmission  $\tau_{jm}$  between observation volume and detector element includes the imaging lens, polarizer, fiber bundles and the complete imaging and filter optics in the polychromator and includes the spectral variation of the detector sensitivity. For the analysis of the individual channel signals, an effective spectral transmission  $\tau_{mj}^*$  is used instead of  $\tau_{jm}$ . It represents a normalized spectral responsivity for the spectral channels in each polychromator with the maximum set to unity.

The ratio of the scattered signals in two neighboring channels is derived from equation (3.4.1) and reads

$$R_q = \frac{E_{jm}}{E_{km}} = \frac{\int \tau_{jm}^*(\lambda) S(T_{e,m}, \theta_m, \lambda) d\lambda}{\int \tau_{jk}^*(\lambda) S(T_{e,m}, \theta_m, \lambda) d\lambda}. \quad (3.4.2)$$

These ratios  $E_{jm}/E_{km}$  can be pre-computed as function of  $T_e$  and stored as conversion functions in form of look-up tables, since the spectral response functions are known from the polychromator calibration. Thus, the determination of the electron temperature  $T_{e,q}$  from a signal ratio becomes a simple table look-up in the calculated conversion functions.

Under experimental conditions, however, equation (3.4.1) is an idealization, since it does not account for errors in signals, calibration etc. A more realistic representation is

$$R_q^* = \frac{E_{jm}^*}{E_{km}^*} = \frac{\int (\tau_{jm}^* \pm \delta\tau_{jm}^*) (S_m \pm \sigma_{bg}) d\lambda \pm \Delta S_{en,jm}}{\int (\tau_{jk}^* + \delta\tau_{jk}^*) (S_k \pm \sigma_{bg}) d\lambda \pm \Delta S_{en,jk}}, \quad (3.4.3)$$

where  $\delta\tau^*$  is a calibration error of the spectral response function of each filter,  $\sigma_{bg}$  represents the fluctuation in the contribution from plasma radiation and  $\Delta S_{en}$  is caused by electronic noise of the detector. These uncertainties can lead to errors in  $T_{e,q}$  in case of an inaccurate calibration or strong fluctuation in a particular wavelength range or when electronic noise dominates, i.e. for cases with low  $S/N$  ratio.

An average  $T_{e,avg}$  is obtained from channels where the signals have a reasonable  $S/N$ , usually  $> 3$ . The weighted average electron temperature is based on the following expression, where each  $T_{e,q}$  comes from a different probability distribution with variance  $(\Delta T_{e,q})^2$ :

$$T_{e,avg} = \frac{\sum_q w_q T_{e,q}}{\sum_q w_q}, \quad w_q = \frac{1}{(\Delta T_{e,q})^2}, \quad (3.4.4)$$

The uncertainty of  $T_{e,q}$  are evaluated as following:

- The plasma background which is composed by Bremsstrahlung and line radiation. Since every measurement is a single event in 100 ns-time scale, it can be perturbed by fast-time scale fluctuation in the plasma background radiation  $\sigma_{bg}$  and in the detector itself  $\Delta S_{en,j}$ . A second measurement without laser pulse is shortly done after the Thomson scattering measurement to provide an estimate of this background radiation. A single-event  $S/N$  ratio can be evaluated, whose uncertainty on scattered signals in the spectral channels can be written as

$$\Delta S_j = \sqrt{\left(\int \sigma_{bg} d\lambda\right)^2 + \Delta S_{en,j}^2}. \quad (3.4.5)$$

To avoid under and overestimation of the signal error, different methods have been tested to quantify the background light fluctuations. It was found that a moving average or robust LOESS<sup>1</sup> filter yields to a more reliable signal error estimation than a simple analysis of the standard deviation of the fluctuation level, since it

---

<sup>1</sup>LOcally wEighted Scatterplot Smoothing (LOESS) combines the simplicity of linear least squares regression with the flexibility of nonlinear regression by fitting polynomials to localized subsets of the data to build up a function that describes the deterministic part of the variation in the data, point by point.

fails in discharges where parameters change significantly [49]. Since the moving average is prone to “outliers” and includes no time information in the averaging process, the robust LOESS filter (RLOESS) was chosen. We represent the filtered fluctuation level by  $\Delta S_j^*(t) = \text{rloess}\{\Delta S_j(t)\}$ . For numerical issues, an additional offset is added, such that  $\Delta S_j^{**}(t) = \Delta S_j^*(t) + 0.05S_j(t) = \Delta E_j$

- Having the knowledge of the ratio  $S/N = E_j^*/\Delta E_j$  for each spectral channel, the upper and lower limits of the signal ratios from two different channels  $p$  and  $q$  are evaluated as:

$$R_q^{max,min} = \frac{E_p^* \pm \Delta E_p}{E_q^* \mp \Delta E_q} \quad \text{for } q \neq p. \quad (3.4.6)$$

- Estimation of the error of each  $T_{e,q}$  becomes:

$$\Delta T_{e,q} = 0.5 [T_e(R_q^{max}) - T_e(R_q^{min})]. \quad (3.4.7)$$

The error in  $T_{e,avg}$  is also determined in the sense of weighted averaging and reads:

$$\Delta T_{e,avg} = \sqrt{\frac{1}{\sum_q w_q}}, \quad w_q = \frac{1}{(\Delta T_{e,q})^2}, \quad (3.4.8)$$

Having computed an average electron temperature, one can reconstruct the spectral emission function. The surface underneath the curve is proportional to the electron density. By using the absolute calibration of the system, one obtains  $n_e$  based on  $T_{e,avg}$ . Therefore, any error in the evaluation of  $T_{e,avg}$  will be also reflected in  $n_e$ .

One has to underline that this method may lead to biased results when channels with low  $S/N$  have to be excluded from the analysis [49]. Channels with a low signal level cannot be used to compute a electron temperature, but provide additional information to boundary conditions of the spectral emission function. These boundary conditions can be used in a more sophisticated model to reduce uncertainties in the evaluation of  $T_e$  and  $n_e$ .

### 3.4.2. Robust non-linear least-square fitting approach

Consistency checks, i.e. reverse calculation of synthetic signals for each spectral channel based on the  $n_e$  and  $T_e$  values obtained from the forward analysis, have shown occasional but significant deviations from the acquired signals in plasma discharges with unfavorable parameters for the diagnostic. These deviations appear in discharges with strong heating

and low density, where  $S/N$  is low, and have the highest impact on the measurements with the 3-channel polychromator. For this reason a least-square fit method (LSQM) using the signals from all spectral channels was found to be a better candidate for the computation of reliable  $T_e$  and  $n_e$ . Furthermore, an approach in least-square sense gives better possibilities to treat “outliers” more efficiently.

For the interpretation and fitting of the scattered spectrum, a Levenberg-Marquardt algorithm [50] was modified such that it includes M-estimators [51], closely related to the method of maximum-likelihood. For data with probability density function pdf( $z$ ), the method requires to minimize the functional

$$S(\mathbf{a}) = - \sum_{i=1}^n \log\{\text{pdf}(z_i)\} = \sum_{i=1}^n \rho(z_i),$$

in solving

$$\sum_i \frac{y_i - f(x_i; \mathbf{a})}{\sigma_i^2} \frac{\partial f}{\partial a_j} w(z_i) = 0$$

with  $\rho(z)$  the maximum likelihood estimator, the weight function  $w(z) = (1/z) (d\rho(z)/dz)$ , the residual  $z_i = (y_i - f(x_i; \mathbf{a})) / \sigma_i$ , the parameter vector  $\mathbf{a}$  of the fit function  $f$  and  $x_i$  the individual signals. In standard theory of least-square fitting, the estimator is  $\rho(z) = 1/2z^2$  and thus the weight function is simply a constant. In the robust least-square fitting approach  $\rho(z)$  is represented by a more complex analytical function overweighting data with small residual and vice versa, which decreases the effect of “outliers” on the final fit result. The latter approach has, however, high requirements on the convexity of the M-estimator in order to ensure good convergence for several reasons:

- convexity guarantees the stability with respect to the input
- no parameter graduation and/or annealing is necessary

The developed fitting algorithm implements four commonly used M-estimators, namely the Cauchy-, Tukey biweight-, Green- and Huber estimator [50–52]. The best estimator was chosen by optimizing the three criteria:

- Comparison of the number  $F$  of fit divergence from standard and robust least-square fitting.
- Comparison of the fitted  $T_e$  obtained from REM, standard and robust least-square fitting to identify the normalized number of fit artifacts  $N_{\text{artifact}}/N_{\text{tot}}$  by an empir-



	$F_{robust}/F_{std.}$	$N_{artifact}/N_{tot}$	$R_{robust}/R_{std.}$
Huber	1.04	0.12	1.02
Cauchy	0.90	0.23	1.08
Tukey-biweight	0.88	0.08	1.11
Green	0.95	0.01	1.07

**Table 3.4.:** Properties of M-estimators: Normalized fit divergence  $F_{robust}/F_{std.}$ , number of outliers  $N_{artifact}/N_{tot}$  and signal residual  $R_{robust}/R_{std.}$  for different M-estimators

ical formula. We judge the result  $T_{e,robust}$  to be a fit artifact, if

$$\frac{|T_{e,robust} - T_{e,std.}|}{|T_{e,std.} - T_{e,REM}|} > 1.$$

- Comparison of the fit residuals  $R = |E_{exp} - E_{th}|$  from standard and robust least-square fitting to verify efficiency of signal weighting, where  $E_{exp}$  is the acquired and  $E_{th}$  the reverse-calculated signal in a spectral channel based on the fitted  $T_e$ .

Table 3.4 presents averages of the result from the analysis of the TS data from  $\sim 630$  TCV discharges. Greens’s estimator, represented by the analytical formula

$$\rho(z) = \log\{\cosh(z)\} \tag{3.4.9}$$

$$w(z) = \tanh(z)/z, \tag{3.4.10}$$

turned out to be the best compromise for good fit convergence, accuracy and CPU time. Figure 3.11 shows a comparison of the results obtained from the REM and LSQM. The results from REM are computed using the standard deviation analysis to quantify the fluctuation level; results from LSQM include RLOESS-filtering and Green’s estimator.

A sketch of the work-flow of the new data analysis algorithm is presented in figure 3.12. The data is read from the acquisition modules of the diagnostic. In the data pre-treatment step, the fluctuation level and  $S/N$  ratio is computed and low signal levels are masked for REM. The REM computes  $T_e$  and  $n_e$  as starting parameters of the LSQM. After removal of “outliers” in  $T_e$ , an approximate value for the global minimum is sought on a non-equidistant grid in least-square sense. The grid is chosen such that it is relatively coarse but mesh-packed in the vicinity of the initial parameters in order to minimize computational effort. The least-square iterations are initialized with this “global” minimum and minimize the  $\chi^2$  cost function. If the fit did not converge, it is re-initialized with

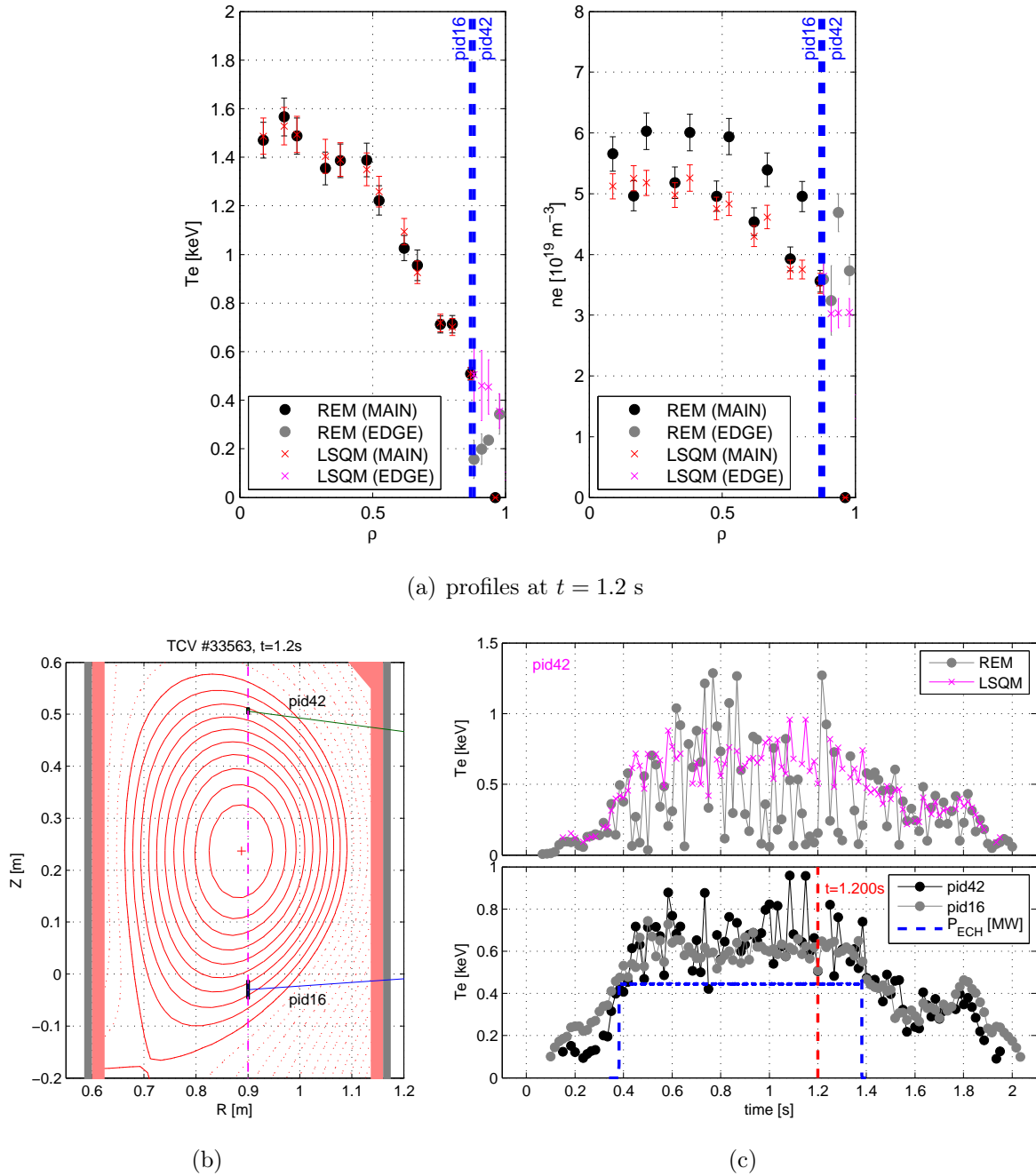


**Figure 3.11.:** Comparison of results from REM and LSQM for polychromator 16 (MAIN) and 42 (EDGE): (a)  $T_e$  and  $n_e$  profiles at  $t = 1.2$  s from REM and LSQM, (b) observation volumes and flux contours of both polychromators on same flux surface, (c)-top  $T_e$  from REM and LSQM for polychromator 42 and (c)-bot.  $T_e$  from LSQM for both polychromators with power trace from the X3-gyrotrons

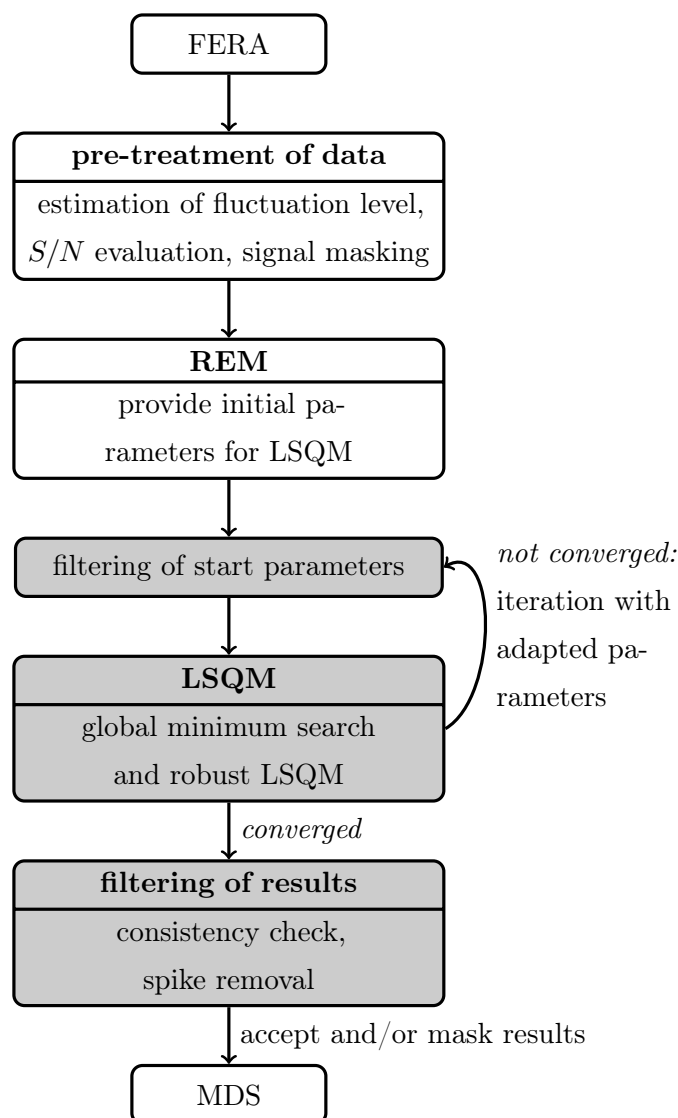


**Figure 3.12.:** Work-flow sketch of the LSQM algorithm: The raw data is loaded from the FERA acquisition modules and pre-treated. REM provides the initial parameters for the LSQM. After spike removal and global minimum search, the  $\chi^2$  cost function is minimized and the fit results are checked for consistency. Finally, the data and a status mask containing additional informations about the individual spectral filter signals is written to the MDS database.

adapted starting parameters, otherwise the results are verified for consistency with the raw signals. For this purpose, synthetic signals are recomputed using the results from LSQM. If two or more out of three or four<sup>2</sup> synthetic signals match the raw signals within error bars, the fit result is accepted, otherwise masked. The fit results and the data mask containing  $S/N$  ratio and fit information for each time and spectral filter are eventually written to the TCV shot file. The whole procedure was optimized such that a total of 1000 – 4000 fits per shot, including data loading and storage, are performed in less than 10 s on one core of an Intel<sup>®</sup> Xeon<sup>®</sup> CPU E5430.

### 3.5. Calibration of the Thomson scattering system

The analysis of the scattered signals relies on the calibration of the system that must provide the relative spectral response function of the polychromator channels and the absolute sensitivity of the complete system. The relative spectral response functions can be measured separately, while the absolute calibration has to be performed with the complete system in experimental conditions. The following section presents the processes of calibration. Finally, a cross-calibration of the TS system with the interferometry measurements is described.

#### 3.5.1. Laboratory calibrations

The spectral response function, as already discussed in section 3.3.2, describes the response of the detection system to a radiation source of constant spectral emissivity. During the calibration process of the polychromators, the response function is measured by illuminating the polychromator input including the fiber bundle with a radiation source of known spectral emissivity and recording the detector output as a function of wavelength. The response function are normalized such that the maximum value of the three or four functions for a given polychromator is equal to unity. This calibration is relatively time consuming and is only carried out when optical components in the polychromator and/or the fiber bundles are modified.

During this thesis work all 35 polychromators were re-calibrated following the two methods described above. A more detailed description and thorough analysis of error sources and absolute calibration errors can be found in Franke's thesis work [8].

---

<sup>2</sup>The total number of signals depends on the number of detectors in a polychromator.

### 3.5.2. In-situ calibrations

As discussed in section 3.4,  $T_e$  measurements are based on signal ratios and therefore require only relative calibration of the spectral channels. For the measurement of  $n_e$ , however, the absolute sensitivity of the detection system, including optics, polychromators, amplifiers and data acquisition, must be known. Thus, an absolute calibration must be carried out under identical conditions to those of a Thomson scattering measurement.

Rotational Raman scattering from nitrogen gas in the vacuum vessel is routinely used for the absolute calibration. The excitation of the gas by the laser light results in a multitude of spectral lines on both sides of the excitation wave length, the Stokes and anti-Stokes branch. Only wavelength in the anti-Stokes branch are covered by spectral channels of the polychromators closest to the laser wavelength. A full Raman scan comprises scattering measurements at 3 – 4 different gas pressures in the interval of 0 – 75 mbar. The spectral channel sensitivity and a possible stray light contribution is determined by a linear regression of the acquired Raman scattering signals as function of the gas pressure [8].

Raman scattering calibrations of the system are frequently repeated, e.g. after modifications of optical components in the beam path or of the vertical position of viewing chords or after realignment of the laser beams.

### 3.5.3. Cross-diagnostic calibration

During TCV operations, mechanical stress on the mounts of optical components in the beam path and thermal expansion effects due to changes in the ambient temperature can lead to a misalignment of the laser beams that leads to the loss of calibration. The beam misalignment can be analyzed by the installed web-cams and manually corrected between two discharges. The absolute calibration, however, is not always recovered and recalibration becomes necessary.

The FIR interferometer, introduced in section 1.2.3, provides a second measurements of  $n_e$  at TCV. Profiles of  $n_e$  can be obtained by inversion of the line-integrated measurements, e.g. by Fisher regularization or singular value decomposition (SVD) method. One has to keep in mind that the 14 observation channels of the FIR interferometer are insufficient to yield a unique profile reconstruction on a radial grid with 41 equidistant points used when interpreting the TS profiles - or in other word, the inversion is largely underdetermined. To partly overcome these drawback, a profile inversion by SVD was

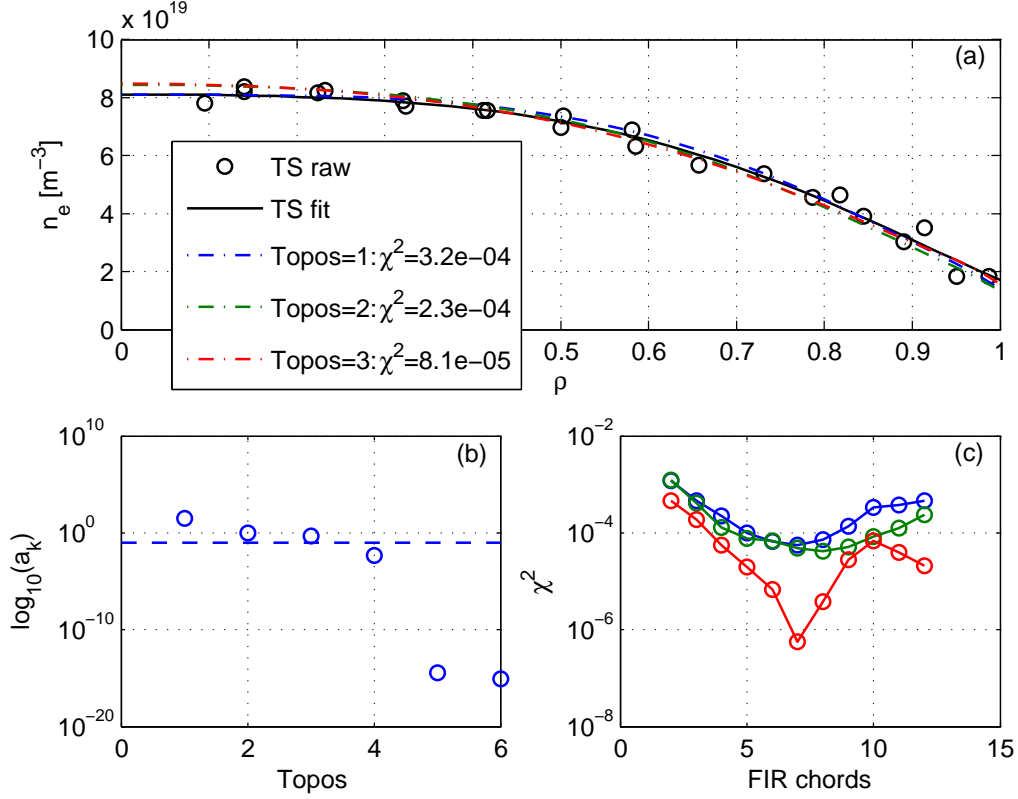


**Figure 3.13.:** Interferometer measurement inversion by SVD: (a) The black solid line represents the polynomial fit of TS  $n_e$  raw data  $\circ$ , together with dash-dotted  $n_e$  profiles from FIR inversion by SVD for basis functions based on the linear combination of 1 – 3 topos. (b) Logarithmic singular value of each topos. (c)  $\chi^2$  from each FIR chord and the corresponding line-integrated  $n_e$  from the inverted profile as function of the FIR chord.

developed [53]. Furthermore, this method can be only applied on L-mode profiles, where profile gradients are small and well reproduced by the inversion procedure.

The SVD method expands the local  $n_e$  profiles from the FIR interferometer measurements into a limited series of orthogonal basis functions, topos, formed from the SVD of TS measurements, which are obtained at much lower sampling rate than the interferometer data. Because these basis functions are formed from a polynomial fit of the local measurement of  $n_e$  in the same plasma, they are well adapted to the class of density profiles to be reconstructed. Using this expansion, the inversion of the interferometer data is reduced to solving an overdetermined set of equations. Therefore, the local  $n_e$  can be approximated as  $n_e(\rho, t) \cong \sum a_k(t)\tau_k(\rho)$ , where  $\tau_\rho$  are the topos retained and the coefficients  $a_k(t)$  are determined by interferometry. These profiles are then time averaged

to reduce effects of sawteeth and resampled on the TS times. Correction factors for  $n_e$  for each TS observation channel are computed by comparing the averaged local FIR and TS density; the standard deviation gives the individual errors.

Figure 3.13 shows an example of reconstructed  $n_e$  profiles from FIR interferometry that are represented by the linear combination of the first three topos and used to recalibrate the sensitivity of each TS observation chord. Studies have shown that a maximum of 3 – 4 topos is sufficient to reconstruct an appropriate profile, when plasma configurations with smooth  $n_e$  profiles (L-mode) are chosen. The relative error of each  $n_e$  correction factor normally stays below 10%, however, uncertainties quickly increase because of:

- low S/N ratio in FIR signals
- bad reference profiles from TS for SVD method
- no or few data in individual TS channels
- poor coverage of the plasma edge by the FIR channel

## 3.6. Measurement and interpretation of the pedestal profiles

Several improvements of the TCV Thomson scattering edge system (TS-EDGE) have permitted measurements of the pedestal height and gradient of electron density and temperature profiles near the separatrix during ELMy H-mode. This section gives a short introduction and few examples about the measurement of the edge pedestal and the interpretation of the profiles in terms of pedestal height, width and gradient.

### 3.6.1. Measurement of the electron contribution by Thomson scattering and its interpretation

The TS-EDGE system measures the electron temperature  $T_e$  and density  $n_e$  edge profiles in the upper part of the TCV plasma vessel. During the stationary ELMy phase of the discharge, the plasma position is moved vertically by circa  $\pm 1$  cm around its initial position. This  $z$ -movement sweeps the plasma in front of the TS-EDGE viewing chords in order to improve the coverage of the edge pedestal by the diagnostic. This method

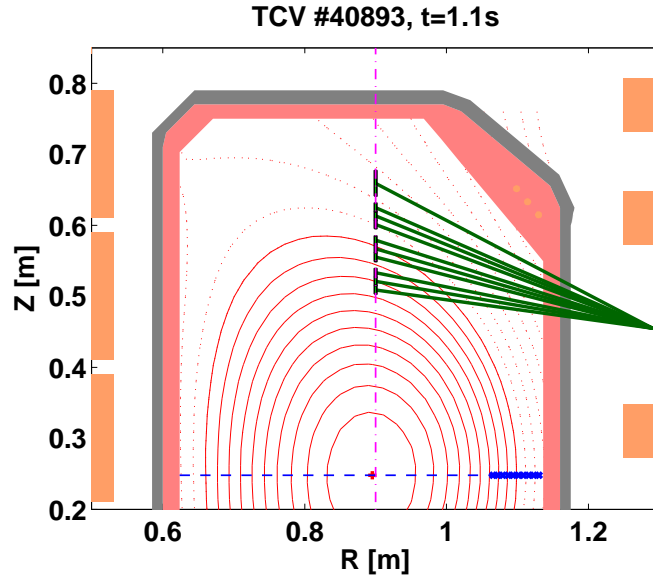


**Figure 3.14.:** TCV vessel cross section and viewing chords of TS-EDGE: The TS-EDGE viewing optics, dark green, measuring the electron temperature and density profiles at the plasma edge along the vertical laser beam depicted as magenta dash-dotted line. For data fitting and interpretation, the observation volumes, blue crosses, are mapped onto the radial coordinate along the plasma midplane, blue dashed line.

provides a profile measurement without radial gaps, which would be the case for a fixed plasma  $z$ -position, and hence decreases uncertainties in the fitting process.

The spatial profiles of  $T_e$  and  $n_e$  are measured along the vertical laser beam that intersects the plasma at the radial position of  $R = 0.9$  m. For the interpretation of this data in tangible quantities and for comparison with other tokamaks, the data is mapped onto radial coordinates in the plasma midplane, where gradients are largest. Figure 3.14 shows the cross section of the TCV vessel and an example of the configuration of the TS-EDGE viewing chords; the observation volumes mapped onto radial coordinates at the plasma midplane are also represented.

After mapping, temperature and density profiles close to the separatrix are fitted by the analytical expression [35]

$$F = a_5 - a_1 \tanh X - a_1 a_4 \frac{X e^{-X}}{e^X - e^{-X}}, \quad (3.6.1)$$

where  $X = (R - a_2) a_3^{-1}$  is a normalized radial coordinate. The parameters provide a simple description of the edge pedestal properties, namely  $height = a_1 + a_5$ ,  $width = 2a_3$



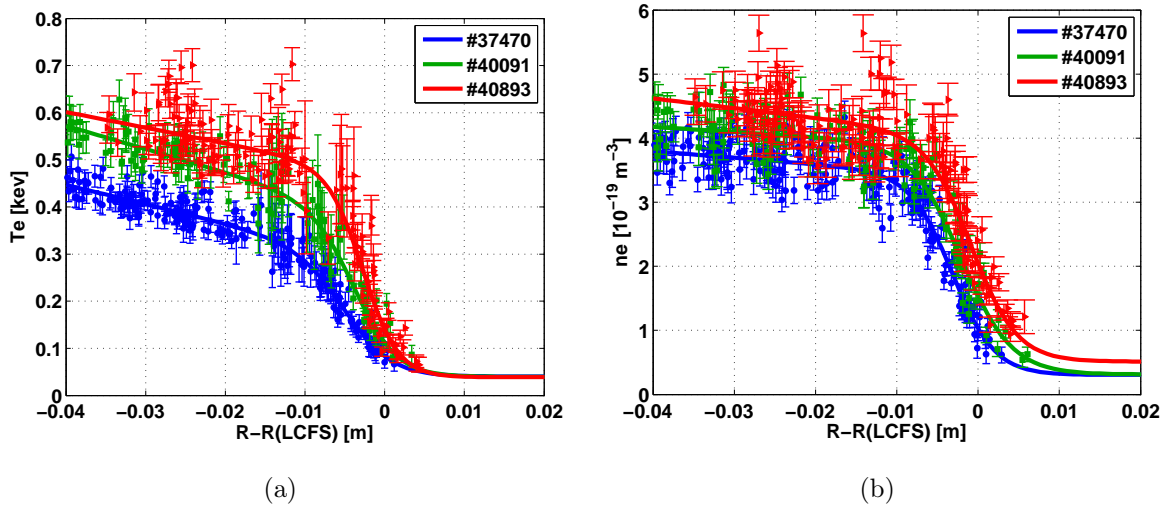


**Figure 3.15.:** Examples of H-mode pedestal profile measurements by TS-EDGE: (a) Electron temperature edge profile measurement with error bars during the inter-ELM phase and pedestal fit for different ECH powers and (b) the corresponding electron density measurements and profiles fits. The data is mapped onto a radial coordinate at the plasma midplane, where  $R - R(\text{LCFS})$  represents the radial position in respect to the radial location of the separatrix. The corresponding plasma parameters are listed in table 3.5.

and  $gradient = a_1 a_3^{-1}$  at the location of steepest slope. This analytical function provides a good description of the H-mode pedestal profile when restricting the interval to the range from  $-4$  cm inside to  $+2$  cm outside the separatrix.

Figure 3.15 shows examples of  $T_e$  and  $n_e$  measurements of the pedestal for three different ECH powers in H-modes with identical shape and plasma parameters. The data is mapped and fitted by equation (3.6.1) on a normalized radial coordinate at the midplane. The plasma parameters and pedestal properties of the chosen examples are listed in table 3.5.

### 3.6.2. Measurement of the ion temperature by CXRS

The diagnostic neutral beam injector (DNBI) provides the diagnostic neutral beam used by the charge-exchange recombination spectroscopy (CXRS) to measure plasma ion temperature and impurity (carbon) density. The DNBI beam is injected radially at the TCV vessel midplane thus constraining CXRS measurements at this position. The standard H-mode scenario at TCV, however, permits reproducible discharges only in the upper

	#37470	#40091	#40893
$I_p$ [kA]	370	370	370
$q_0$	$\sim 0.9$	$\sim 0.9$	0.9
$q_{95}$	$\sim 2.4$	$\sim 2.4$	2.3
$\langle n_e \rangle$ [ $10^3 \text{m}^{-3}$ ]	$\sim 3.6$	$\sim 3.4$	$\sim 3.7$
ELM type	III	III	I
$P_{ECH}$ [kW]	-	$\sim 340$	$\sim 930$
$\eta_{abs}$	-	X3 $\sim 70\%$	X3 $\sim 75$ & O2 $\sim 20\%$
$T_{e,ped}$ [eV]	$325 \pm 30$	$392 \pm 47$	$477 \pm 38$
$\Delta_{Te}$ [mm]	$11.8 \pm 0.7$	$10.7 \pm 0.9$	$8.8 \pm 0.7$
$R/L_{Te}$	$132 \pm 31$	$132 \pm 50$	$194 \pm 45$
$n_{e,ped}$ [ $10^{19} \text{m}^{-3}$ ]	$3.69 \pm 0.26$	$3.88 \pm 0.27$	$4.02 \pm 0.20$
$\Delta_{ne}$ [mm]	$10.5 \pm 0.5$	$12.4 \pm 0.8$	$11.0 \pm 0.6$
$R/L_{ne}$	$162 \pm 29$	$138 \pm 29$	$139 \pm 22$

**Table 3.5.:** Plasma parameters of the pedestal profile measurement examples: Plasma current  $I_p$ , safety factor  $q_0$  and  $q_{95}$  at normalized poloidal flux radius  $\rho = \sqrt{\psi_N} = \{0, 0.95\}$ , line-integrated density  $\langle n_e \rangle$ , absorbed ECH power  $P_{ECH}$  with absorption coefficient  $\eta_{abs}$  by TORAY-GA [5], electron temperature pedestal height  $T_{e,ped}$ , width  $\Delta_{Te}$  and normalized gradient  $R/L_{Te}$  and, respectively, electron density pedestal parameters from profile fitting by equation (3.6.1) of the TS-EDGE measurements.

half of the TCV vessel. This is due to an asymmetry in the poloidal field distribution of the machine and the plasma stabilization by the wall, which makes it difficult to maintain a stationary H-mode discharge with the magnetic axis close to the vessel midplane. For that reason, the measurements of the whole radial ion profile in H-mode was not possible, only edge measurements in the divertor region with normalized poloidal flux radius  $\rho = \sqrt{\psi_N} \geq 0.8$  were feasible.

Figure 3.16 shows the ion temperature measured by CXRS of the H-mode edge pedestal for the shot #40091 during the stationary ELMy phase. Features of expelled ions by an ELM event are visible in the individual  $T_i$  profiles due to the long integration time, 60 ms, of the CXRS detector. This integration time exceeds the ELM cycle duration several times, hence providing only an averaged  $T_i$  profile.

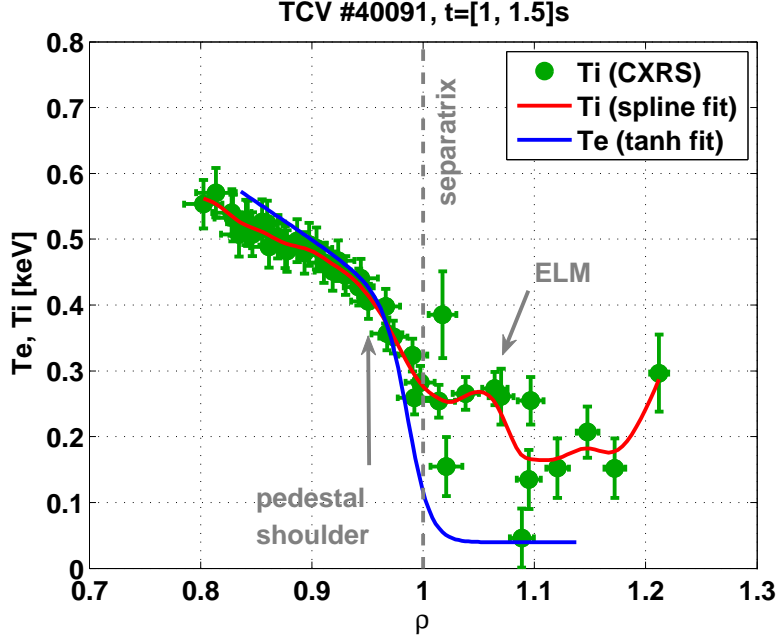


**Figure 3.16.:** Pedestal ion temperature measurement by CXRS:  $T_i$  measurements, green, of the discharge #40091 during the stationary ELMy H-mode phase showing features of expelled ions by an ELM; the corresponding spline fit depicted in red. For comparison, the  $T_e$  profile, fitted by equation (3.6.1).

### 3.6.3. Dependence of ion temperature as function of electron temperature in the pedestal region

Measurements of the ion temperature  $T_i$  in the pedestal region could be obtained for the ECH power steps (nominal power)  $P_{ECH} = \{0.5, 1.0, 1.5, 2.0\}$  MW, but no measurements were done for pure ohmically heated discharges. Nevertheless, we want to investigate for which range of pedestal electron we can assume  $T_i \approx T_e$ . Since the energy transfer from electrons to ions is  $Q_e \propto n^2 (T_e - T_i) / T_e^{3/2}$  [1], we expect a decoupling of both species when lowering the plasma density and/or increasing  $T_e$  by EC-heating.

Figure 3.17 shows  $T_i$  as function of  $T_e$  in the pedestal region for different ECH power and at different radii  $\rho = \{0.80, 0.85, 0.90, 0.95\}$ . The  $T_i$  profiles from CXRS, which are available for  $\rho \geq 0.8$  in these plasma types, were fitted by splines. Similar, the  $T_e$  profiles were spline fitted and values at different radial positions were taken from the  $T_i$  and  $T_e$  fits. We observe that  $T_i = T_e$  is a good approximation for  $\rho > 0.85$  and hence at the position of the upper pedestal shoulder  $\rho_{ped} \sim 0.95$ . Normalized ion temperature gradients  $R/L_{T_i}$  could not be estimated from the CXRS measurements for the two reasons: (1)

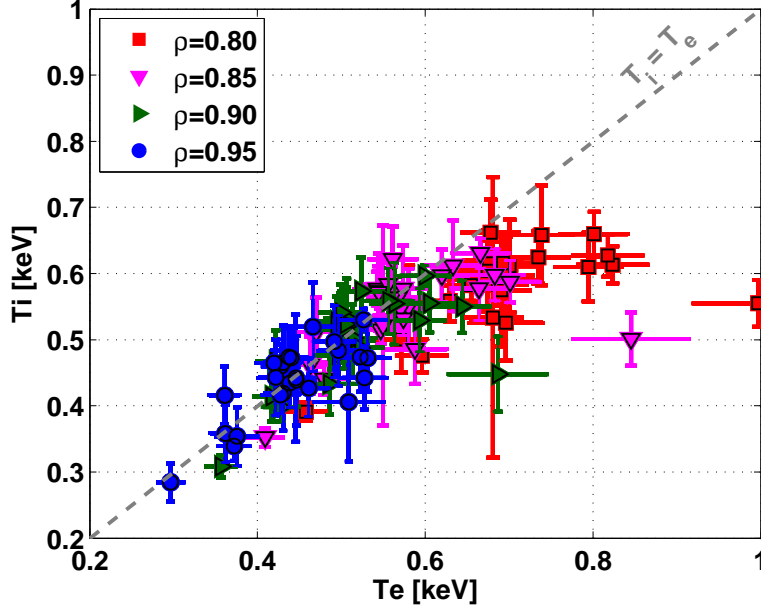


Figure 3.17.: Ion temperature versus electron temperature at the pedestal: abc

The programmed vertical plasma movements for improving the TS-EDGE measurements considerably smoothed the  $T_i$  pedestal gradient. (2) Due to the high integration times of the detectors in the CXRS spectrometer, only  $T_i$  averaged over several ELM cycles could be obtained.

Measurements of the pedestal ion profile in other machines (DIII-D [30, 54], NSTX [55], ASDEX-Upgrade [56], JT60 [30]) showed that  $T_{i,ped} \geq T_{e,ped}$  and  $\nabla T_{i,ped} \simeq \nabla T_{e,ped}$ . For the ion density  $n_i$ , we assume quasi-neutrality and a single impurity  $C^{6+}$  and obtain

$$n_i = n_e \frac{Z_{imp} - Z_{eff}}{Z_{imp} - 1} \quad (3.6.2)$$

$$n_{imp} = (n_e - n_i) / Z_{imp}, \quad (3.6.3)$$

where  $Z_{eff}$  is the effective charge,  $Z_{imp}$  the charge of the impurity and  $n_{imp}$  the density of the impurity. For typical TCXV H-modes with ECH, we find  $Z_{eff} \sim 3$  and hence  $n_i/n_e \sim 3/5$ .

### 3.7. Synchronized laser triggering on ELMs

The investigation of H-mode edge profile properties during an ELM cycle requires diagnostics with sufficiently high acquisition rates. Especially the conditions shortly before the ELM crash are of particular interest, since they enter for example in MHD stability

calculations of the edge pedestal. On TCV, the TS system is the only diagnostic able to provide  $T_e$  and  $n_e$  of the edge pedestal with high spatial resolution. Unfortunately the low repetition frequency of 20 Hz of the lasers does not allow to trace the profile evolution in time during an ELM cycle. In discharges with low input power, the ELM frequency of  $f_{\text{ELM}} \sim 100 - 300$  Hz is sufficiently high to obtain profile measurements relatively close to the ELM event. However, in strongly EC-heated discharges, where  $f_{\text{ELM}} \sim 50$  Hz and becomes comparable with the laser frequency, the probability of measuring a profile shortly before an ELM is very small. In order to obtain a reliable profile nonetheless, identical discharges have to be repeated many times. To partly overcome this drawback of low sampling rate of the TS system, a real time (rt) algorithm was developed to synchronize the laser trigger with ELM events.

This section presents technical details about the trigger cycle of the TS lasers, the implemented real time algorithm, results from the synchronized laser triggering and an approach of magnetic triggering of ELMs to control and/or stabilize their frequency.

### 3.7.1. PC-based multi-channel controller

On TCV, the signals of many diagnostic, e.g. photodiodes, soft X-ray emission and line-integrated density from interferometry, are acquired by D-tAcq 196 Compact-PCI (C-PCI) acquisition modules<sup>3</sup>. One module acquires up to 96 differential channels of 16bit data per card and stores data for post-shot analysis. These cards are combined in a C-PCI crate to provide acquisition of hundreds of channels and also have the capability to send acquired data to the memory of a host PC for data processing in realtime (rt). The default clock rate of the crate is set to 10 kHz, limited by the number of treated channels, although the individual D-tAcq modules can work at frequencies up to 100 kHz, leaving less computational time for algorithms.

Linux is used as the rt PC operating system. Simulink<sup>®</sup> and the rt workshop for embedded targets have been integrated with the D-tAcq drivers to facilitate rapid development and testing of algorithms. The rt workshop generates and compiles C code from the Simulink block diagrams which is then sent to the real time PC over the network. This platform gives the unique possibility to easily develop algorithm to control plasma parameters and properties [57], trigger diagnostics on MHD events, reconstruct the magnetic equilibrium etc. in real time.

---

<sup>3</sup>D-tAcq Solutions Ltd. <http://www.d-tacq.com/>

### 3.7.2. Modes of operation and laser triggering

The TS system comprises three repetitively pulsed Nd:YAG laser units connected to individual controller units which set the operational parameters and select the mode of operation and the trigger mode. The controller units are connected via RS-232 interface to a second controller (TCV-slave), which receives trigger pulses and laser settings from the TCV control system. The TCV-slave generates the timing pulses for external triggering of the lasers, supervises the operation of the lasers, e.g. interlocks, and controls the external laser shutters as part of the security system.

In external trigger mode operation, trigger pulses for flash lamps and Q-switch are provided by the slave and sent to the laser power supplies via 50  $\Omega$  coaxial cable. The slave triggers on the positive edge of pulses with rectangular waveform of amplitude 2.5  $\rightarrow$  6 V and  $>$  500 ns duration sent by the TCV clock. If the trigger is accepted by the TCV-slave, a TTL<sup>4</sup> trigger is sent to the laser unit and the laser fires.

#### Simultaneous triggering

This mode of operation is used to increase the total laser pulse energy for scattering measurements. Since the three laser beams are combined in a narrow fan focused into the TCV vessel, they appear to the observation optics collecting the scattered light as one single beam with tripled energy. In this mode the timing sequence is determined by the parameters of laser unit #1, which serves as master in this case. Common trigger pulses are sent to all laser units; adapted length of the coax-cables ensures laser synchronization with minimum jitter.

#### Burst mode

In this mode of operation, the lasers are triggered independently from each other and are fired one after the other within a small time interval ( $\Delta t \geq 1$  ms). After one burst of laser pulses, the time interval until the next burst is fixed by the repetition rate of the lasers. This mode of operation is of particular interest, since it allows to measure profiles (maximal 3) within a very short time interval, which can give insight into transitory effects in the profiles.

---

<sup>4</sup>Logic 0 (“low”): 0 – 0.8 V, logic 1 (“high”): 2 – 4.75/5.25 V

### Synchronization with TCV events

To extend the capability of the system to measure TCV events, the slave is equipped with a separate input for external synchronization signals conform to TTL standard. If the signal happens to fall within a specified time window before the preset trigger time, the trigger is accepted and a laser pulse is generated after a fixed delay of about  $200\mu\text{s}$ . The length of this synchronization time window is limited by the laser hardware to  $\sim 10\%$  of the natural repetition period of 50 ms of the lasers.

The trigger timings and delays for default and synchronized trigger mode are:

- default trigger, i.e. when no synchronized trigger is sent or accepted:

$$T = T_{\text{clock}} + \Delta T_1 + T_{\text{sync-win}} + \Delta T_{\text{FL-Qsw}}, \quad (3.7.1)$$

where  $T_{\text{clock}}$  is the time vector of the TCV clock,  $\Delta T_1$  a user defined delay,  $\Delta T_{\text{sync-win}}$  the synchronization time window and  $\Delta T_{\text{FL-Qsw}}$  the delay of the Q-switch.

- synchronized trigger, i.e. when the trigger is accepted:

$$T = T_{\text{ext}} + \Delta T_{\text{FL-Qsw}}, \quad (3.7.2)$$

where  $T_{\text{ext}}$  is an external trigger derived from a TCV event.

A sketch of the timing scheme for synchronized triggering is shown in figure 3.18. In combination with burst mode operation of the lasers, where the individual lasers are fired within a short time period ( $\sim 2 - 3$  ms), and a suitable pre-trigger, this option provides enhanced probability for synchronization with fast repetitive events, like ELMs or sawtooth activity.

#### 3.7.3. Triggering on ELMs

For synchronized laser triggering on ELMs, aiming at measurements before and after the same ELM event by operating the lasers in burst mode, the vertical  $D_\alpha$  signal from the photodiodes, acquired by a D-tAcq module in the crate, is used as observer. The signal is transferred on the CPU unit on which the rt algorithm is executed.

In the algorithm, the observer signal is filtered to reduce noise effects. The low-frequency background in the observer signal is suppressed. In the next step, the MHD

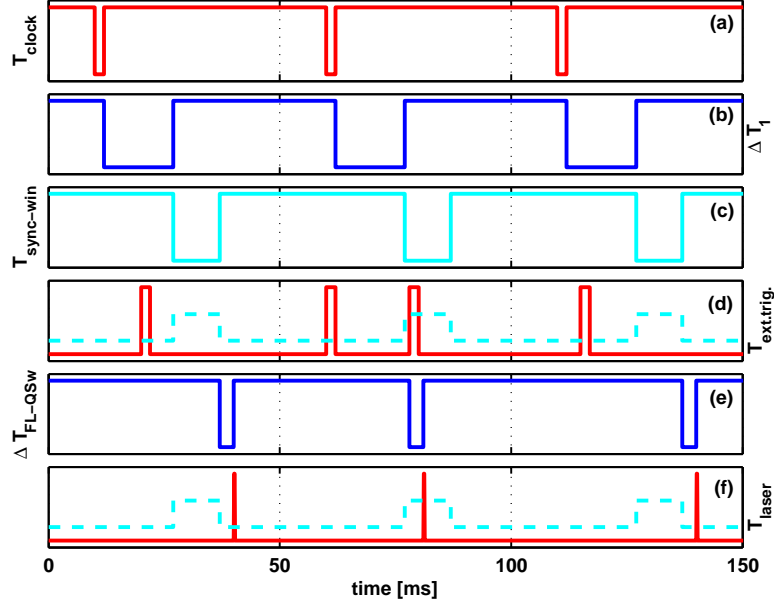


**Figure 3.18.:** Timing scheme for external triggering: (a) Master clock pulses, (b) user-defined delay  $\Delta T_1$  that initializes (c) the synchronization window. (d) The external trigger, (e) a pre-set delay time and (f) the laser pulse.

event is identified by analyzing the time derivative of the observer signal applying threshold detectors. A local and averaged event frequency is generated. The local event frequency results from two events, latter is composed by the local frequency and the former event history by applying a lowpass filter. If the times of the MHD events in the discharge and the event frequency happen to satisfy predefined parameters, the detected event will be identified as ELM and further examined. If the algorithm has identified the event as ELM, the next future ELM time is computed and it is verified, if this next ELM happens to fall in the predefined synchronization window of the lasers. If this is the case, a TTL trigger pulse is send to the laser slave by the digital output of the D-tAcq module, otherwise the lasers are triggered by the D-tAcq at its default time.

Usually the lasers are operated in burst mode; the time intervals between the three individual lasers are defined by the user before the discharge, but remains the same during the rt control. In the post-shot phase, only a selected set of traces from the algorithm is saved to MDS, since all informations can be retrieved by manually rerunning the algorithm in off-line mode. The algorithm is conceived such that it can be also used to trigger the diagnostic on sawtooth oscillations. A simplified scheme of the working principle of the algorithm is shown in figure 3.19.

The probability to trigger the diagnostic synchronized to an ELM event within a 2 ms



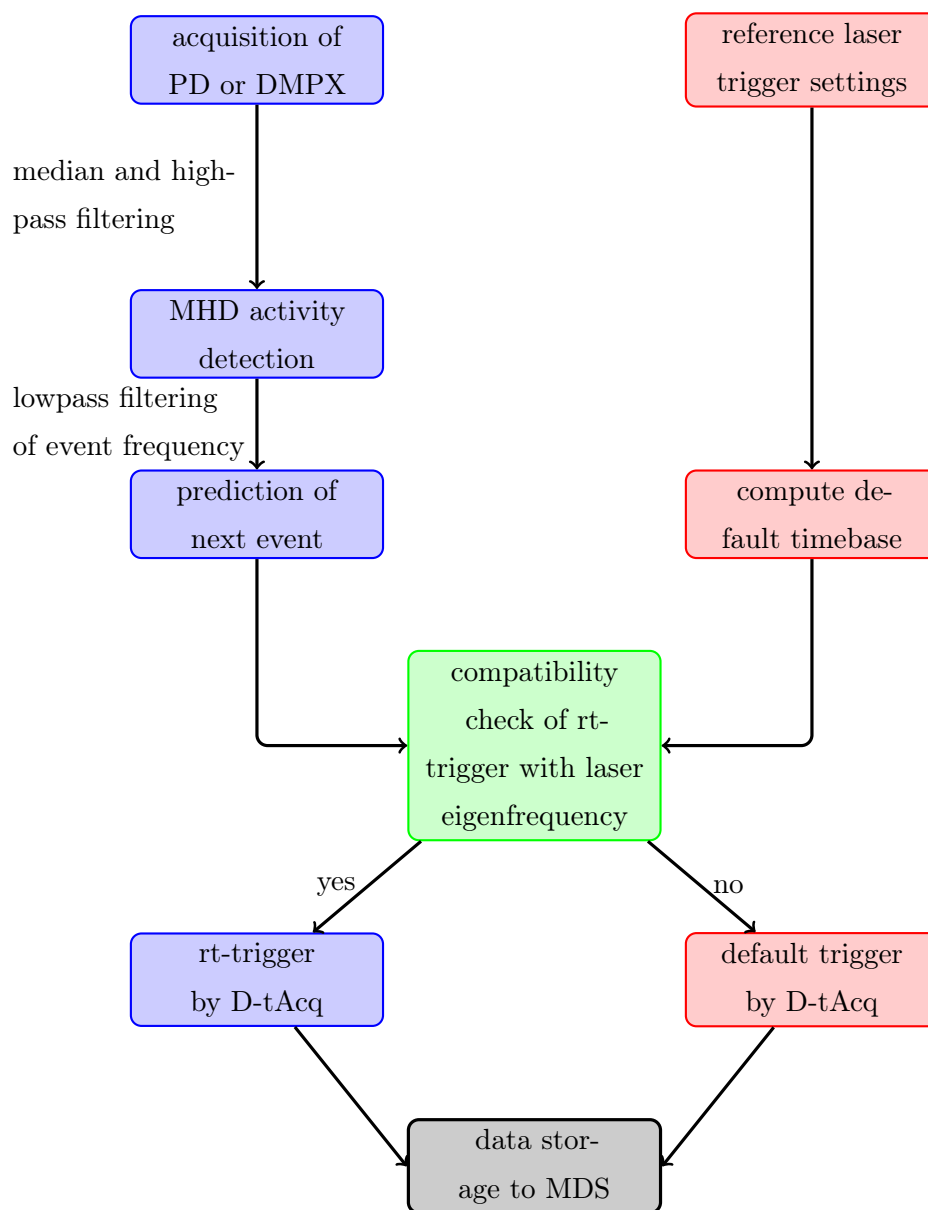


**Figure 3.19.:** Sketch of the rt laser control algorithm: Red items correspond to the control of the TS diagnostic; blue items represent the treatment of the observer signal. For every rt trigger on a MHD event, its compatibility with the laser settings is verified, green item. In the post-shot processing the data is written to the TCV shot file, gray item.

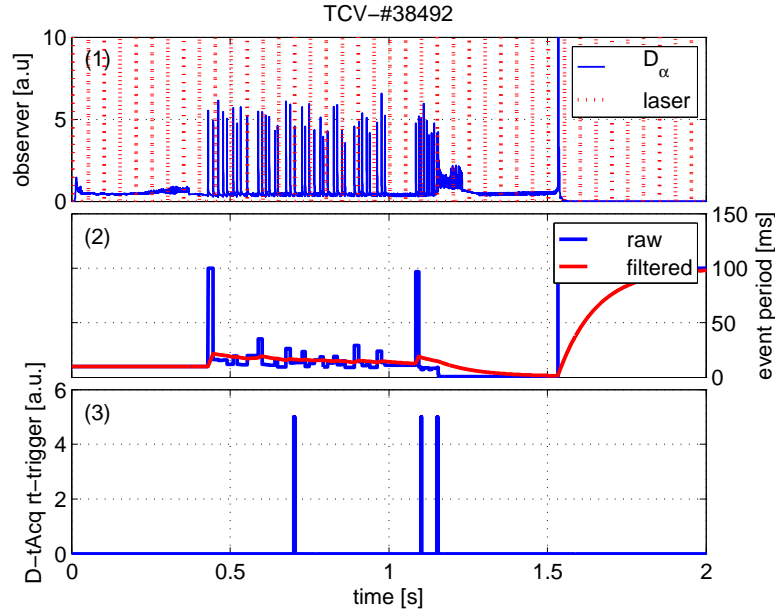


**Figure 3.20.:** Results from rt laser control in ELMy H-mode: (1)  $D_\alpha$  observer and default laser times, (2) real and filtered ELM period, (3) accepted rt trigger sent to laser.

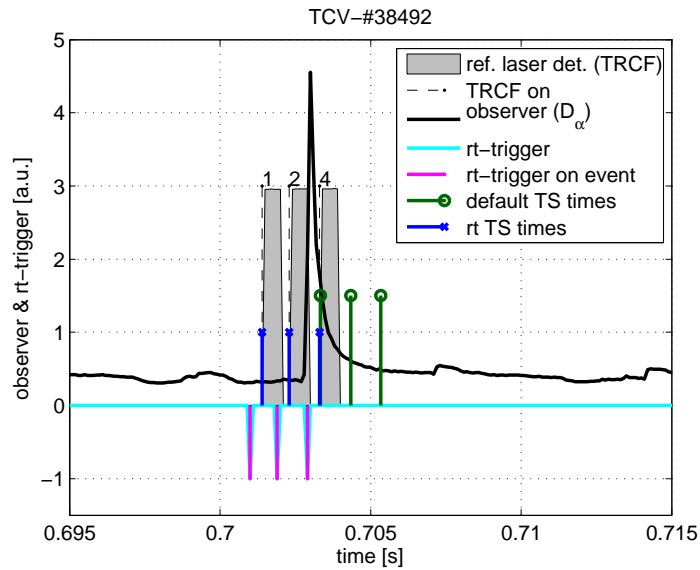


**Figure 3.21.:** Shift of the TS laser pulse (blue) away from its default trigger (green) closer towards the ELM crash. 400  $\mu$ s after the rt trigger from the d-tAcq (magenta), the laser light is registered by a reference detector (TRCF, gray box) at the entrance to the TCV vessel. The laser unit is coded in binary, the time delay between the three individual laser pulses is 1 ms.

time window is  $\sim 10 - 25\%$ , if the time delay between the individual lasers is chosen to be 1.5  $\rightarrow$  2.5 ms. The probability of a successful trigger strongly depends on the initial

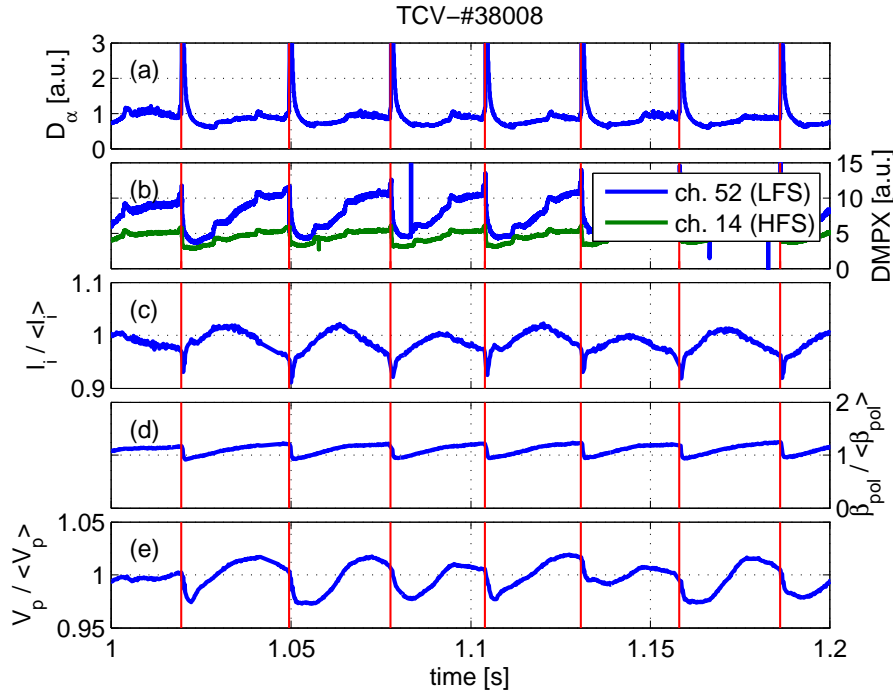
phase shift between the ELM event and laser pulse, ELM frequency and regularity, the number of laser pulses during the stationary ELMy phase of the discharge, the time delay between the individual lasers and the maximum length of the synchronization window  $\Delta T_{\text{sync-win}}$ . It was found that the natural laser frequency can not be changed by more than 5%, i.e.  $\Delta T_{\text{sync-win}} \leq 2.5$  ms, instead of the 10% as given by the manufacturer. This restricts the success rate of the synchronized triggering considerably.

Figure 3.20 shows the result from the rt trigger control during the ELMy phase of an H-mode discharge. The ELM frequency is computed from the spikes in the  $D_\alpha$  observer signal and then low-pass filtered to provide a stable estimate for the next ELM event. The rt synchronization of the laser on ELMs was activated in the time interval  $0.40 \rightarrow 1.55$  s. Figure 3.21 shows an example of laser synchronization with the ELM crash. The rt algorithm moves the trigger pulses away from their default times towards the time of the event. Shortly after the trigger is sent, the laser light is registered on a reference detector (TRCF).

The usual delay between a trigger sent by the D-tAcq and the time when the laser light is registered by the TRCF is  $400 \mu\text{s}$ . This delay is composed by a refresh delay of  $100 \mu\text{s}$  due to the internal clock rate of the C-PCI crate at 10 kHz,  $\sim 50 \mu\text{s}$  of latency in data transfer from the host PC running the algorithm to the DAC output, the laser Q-switch delay  $\Delta T_{\text{FL-Qsw}} = 160 \mu\text{s}$  and the delay of  $50 - 100 \mu\text{s}$  of the TRCF module at a clock rate of 10/20 kHz. Taking this delay into account, the algorithm has to either detect a precursor long before the ELM appears or predict the next ELM crash  $\sim 0.5$  ms before it actually happens in order to fire the laser shortly before the event.

Up to the present day, only the prediction of next ELM events based on their former history is implemented which requires ELMs with fairly regular frequency. Since the ELM frequency depends on many parameters as for example EC-power coupling or density, it is difficult to do an accurate estimate for the time of the next event thus decreasing the probability to fire the lasers at the right time. Magnetic triggering [58–60] has been tested to lock the ELM frequency to an imposed vertical plasma oscillation in order to improve the predictions of the rt algorithm. The results are presented in section 3.7.4.

For the future, additional observer would be needed to improve the capability of the algorithm to predict ELMs. The detection of a toroidal mode of low or medium  $n$  as type-I ELM precursor in the signals of the magnetic probes could be one possibility, although they do not exist always [16, 17] and might be too difficult to detect in realtime. Another



**Figure 3.22.:** Some plasma parameters during ELM cycle: (a)  $D_\alpha$  trace from the vertical photodiode, (b) soft-X ray radiation from DMPX looking at the plasma edge (channel 52 LFS, channel 12 HFS), (c) normalized internal inductance  $l_i$ , (d) normalized  $\beta_{pol}$  and (e) normalized plasma volume. Traces (b)-(e) are normalized by their median, traces (c)-(d) are from the LIUQE equilibrium reconstruction at 5 kHz.

issue is that the diagnostic needs a trigger sufficiently early with respect to the time of the next ELM, since  $\sim 500 \mu\text{s}$  of time delay have to be taken into account.

Another approach based on plasma property changes on relatively “long” time scales during the ELM cycle would be more promising. Figure 3.22 shows traces from the equilibrium reconstruction by LIUQE and soft-X ray emission of the plasma edge (on HFS and LFS) measured by the DMPX for a type-I ELMy H-mode with strong additional EC-heating. The plasma volume variation during an ELM cycle resembles a  $n = 0$  like global ballooning mode which tends to saturate and eventually invert the trend at 7–9 ms before the ELM event occurs. At the same time soft-X ray radiation from the edge measured by the DMPX and  $D_\alpha$  emission increase. This observation suggest that the gradual increase in plasma volume due to the extensive heating, in this case the plasma shape control is feed-forward, is inverted by loss of energy confinement due to increased transport across

the edge barrier. The internal inductance <sup>5</sup> undergoes a similar cycle; its maximum is attained  $\sim 13$  ms before the ELM crash. After the maximum  $l_i$  is passed the current profile relaxes hence increasing the edge current fraction. High edge current density is favorable to trigger external kink modes which are the common explanation of the type-I ELM event.

Since the energy confinement time  $\tau_E$  and internal inductance  $l_i$  are linked by  $\tau_E \propto I_p l_i$  [61], a observer combining information from both plasma energy losses and internal inductance, for example from a real time equilibrium reconstruction or independent  $l_i$  observer, seems promising to give a better prediction of the next ELM event. However, this was out of the scope of this thesis work.

### 3.7.4. ELM pacing

Magnetic triggering of ELMs was reported first from TCV in ohmic plasmas showing type-III ELMs [58]. This method, showing successful locking of the ELM frequency to an imposed vertical plasma oscillation, was also demonstrated in the type-I ELM regime in ASDEX Upgrade [59]. Therefore, this method seemed to be a good candidate to stabilize the ELM frequency and improve the probability in predicting the next ELM event by the rt algorithm.

For the plasma movement required, a series of pulses were added to the reference signal for vertical position control. Frequency and amplitude of the pulses (drive) were varied for different heating power to find locking of ELMs to the magnetic perturbations. The pulse length of the vertical displacement was 1 ms; the displacement was a down-up movement with  $|dz/dt|$  being largest in the upwards direction. The ELM pacing experiments were conducted during the stationary ELMy H-mode phase, where plasma parameters were kept constant. The shown experimental results were obtained from a series of similar discharges.

Experiments, in which the drive frequency  $f_{\text{drive}}$  was varied by  $\sim 25\%$  around the natural ELM eigenfrequency  $f_{\text{ELM}}$ , showed that some locking appears only when  $f_{\text{drive}} \approx f_{\text{ELM}}$ . A scan in drive amplitude  $\delta z_{\text{drive}}$  with  $f_{\text{drive}} \approx f_{\text{ELM}}$  showed no direct dependency of the capability to trigger an ELM on  $\delta z_{\text{drive}}$ . The ELM is “triggered” with relatively small probability 2 – 5 ms after the pulse, independently of its amplitude. These results

---

<sup>5</sup>measure of the peakedness of the current profile, defined as  $l_i = \int dV B_p^2 / [V B_p^2(a)]$  with  $\langle B_p(x) \rangle = \oint_x dl B_p / \oint_x dl$  and  $0 \leq x = [V(x)/V(a)]^{1/2} \leq 1$

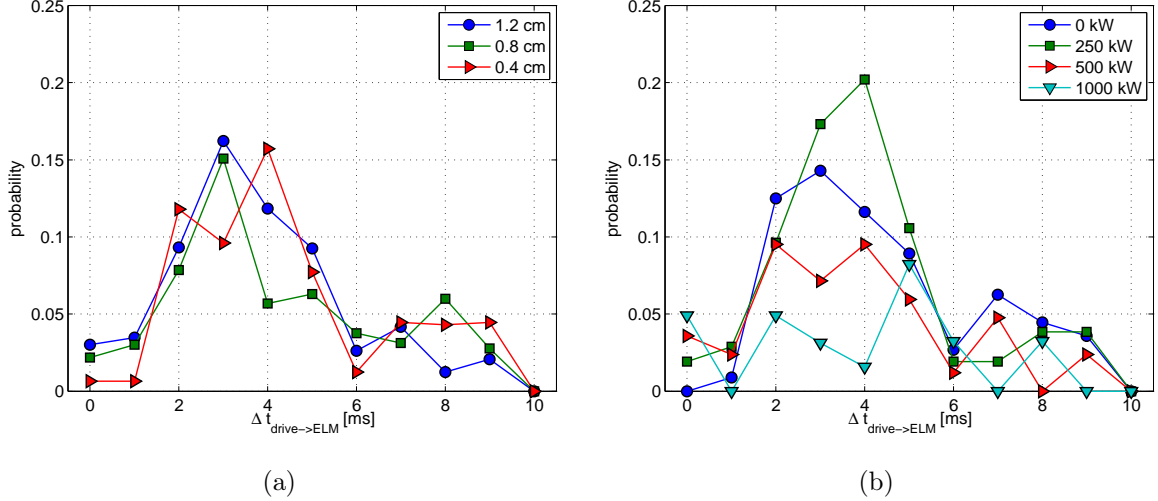


**Figure 3.23.:** (a) Histogram of the probability to trigger an ELM for the drive amplitudes  $\delta z_{\text{drive}} = \{0.4, 0.8, 1.2\}$  cm. (b) Histogram of the probability to trigger an ELM for the different nominal EC-heating powers  $P_{\text{ECH}} = \{0, 250, 500, 1000\}$  kW. The histogram was computed from the set of data, where  $\delta z_{\text{drive}} = \{0.8, 1.2\}$  cm.

are presented in figure 3.23(a), a histogram showing the probability of a triggered ELM as function of the time between drive and ELM pulse for  $\delta z_{\text{drive}} = \{0.4, 0.8, 1.2\}$  cm and nominal EC-heating power  $P_{\text{ECH}} = 0 - 500$  kW.

Figure 3.23(b) shows the results from magnetic triggering of ELMs with  $\delta z = \{0.8, 1.2\}$  cm and  $f_{\text{drive}} \approx f_{\text{ELM}}$  for  $P_{\text{ECH}} = \{0, 250, 500, 1000\}$  kW with 50 – 65% absorption computed by TORAY-GA [5]. The histogram depicts the probability to trigger the ELM as function of the drive-ELM delay. We find  $\Delta t_{\text{drive} \rightarrow \text{ELM}} \approx 2 - 5$  ms and the probability decreases roughly with  $P_{\text{ECH}}$ . For the highest heating power,  $P_{\text{ECH}} = 1$  MW, no correlation between drive and ELM can be found.

Figure 3.24 shows an example where the ELM frequency locked to the drive during a time interval of  $\sim 400$  ms. The magnetic perturbations are applied during the stationary H-mode phase of the discharge, i.e. in the time interval  $t = 0.65 - 1.40$  s. After a initial phase  $0.65 \leq t \leq 1.05$  s in which  $f_{\text{ELM}}$  appears to be perturbed by the drive, the ELMs lock to the drive and their frequency is stabilized. However, the ELM crashes follow the drive with a relatively large delay of  $\Delta t_{\text{drive} \rightarrow \text{ELM}} = 4 - 5$  ms and keep also a fairly regular frequency once the magnetic triggering is stopped. In other cases the relation between the occurrence of an ELM after a magnetic perturbation is less clear; there are even examples where  $f_{\text{ELM}}$  is rather destabilized than stabilized by the magnetic

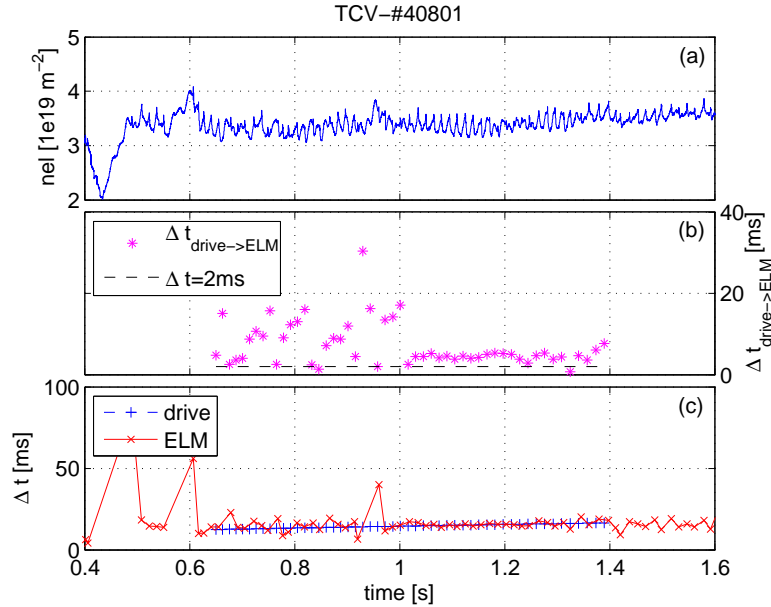


**Figure 3.24.:** Example of successful locking of the ELM frequency to the imposed vertical plasma oscillation: (a) line-integrated density from interferometry, (b) delay  $\Delta t_{\text{drive} \rightarrow \text{ELM}}$  and (c) drive (blue) and ELM (red) periods  $\Delta t$ .

perturbations. The reason for this behavior is not yet clear and should be investigated in future experiments. Therefore, the magnetic triggering was abandoned for all further H-mode studies.

### 3.8. Conclusion

During this thesis work, the TS system was successfully upgraded to the needs of measurements of transport barriers in eITB and H-mode discharges. The hardware upgrades were carried out keeping the flexibility of the system to adapt to various discharge scenarios. The interpretation of the scattered signal was highly improved leading to a better accuracy in  $T_e$  and  $n_e$  and allowing for measurements even in extreme situations where  $S/N$  is very low.

Results from measurements of the normalized gradients  $R/L_{T_e}$  and  $R/L_{n_e}$  in fully non-inductive eITB discharges confirmed profile smoothing by the former low spatial resolution of the system. With the upgrade towards higher spatial resolution, the profile simulations and experiments are now in better agreement. These results show that measurements are not anymore influenced by the diagnostic itself.

Measurements of the electron and ion temperature in the H-mode pedestal region suggest approximately equal temperatures for both species.

The synchronization of the diagnostic trigger with MHD events as a new method to trigger the Thomson scattering lasers, taking into account all its inherent limitations, has been tested successfully. Some suggestions were given for further improvements in the prediction of ELMs. ELM pacing by magnetic perturbations to stabilize and/or control their frequency was tested to improve the probability of triggering the diagnostic on an ELM event. However, these experiments did not yield conclusive results and hence require further investigations.



## 4. The snowflake divertor

The reduction of heat flux on plasma facing components (PFCs) in a tokamak is a crucial issue for future large nuclear fusion experiments. In diverted plasma configurations, energy and particle losses are channeled primarily into the divertor region through the scrape-off layer (SOL). However, high power flux on the relatively small divertor strike region causes overheating of the divertor PFCs which may undergo destructive erosion. In the case of H-mode, the reference scenario of ITER, plasma energy loss attributed to ELMs may exceed the maximal tolerable power load of these components.

The “snowflake” (SF) divertor configuration [62, 63] was proposed as a possible solution to reduce the plasma-wall interaction by changing the divertor’s poloidal magnetic field topology. This configuration also exhibits increased magnetic shear in the edge region predicted to improve the pedestal stability and to influence ELM activity [18]. The first realization of a SF magnetic divertor was experimentally demonstrated on TCV [64].

In this chapter, an overview on the SF experiments in L- and H-mode on TCV is given. The ideal MHD stability limits of the edge pedestal are computed for a set of SF equilibria. Sensitivity studies are presented to study the effect of edge magnetic shear and plasma shaping on the stability limits. Finally, experimental results of SF diverted type-I ELMy H-mode are presented and discussed.

### 4.1. Snowflake divertor magnetic configuration

This section gives a short introduction to the SF divertor, its physical properties and its advantages compared to a standard single-null divertor. Further, a SF experiment in L-mode is shortly presented.

### 4.1.1. Properties of the snowflake divertor

By using a set of poloidal field coils, one can create a divertor in which the poloidal magnetic field null in the divertor region is of second order ( $\nabla^2\psi = 0$ , where  $\psi$  is the poloidal magnetic flux), not of first order ( $\nabla\psi = 0$ ) as in the usual single-null (SN) divertor [62]. The separatrix in the vicinity of the null point splits the poloidal plane into six sectors which generates a hexagonal snowflake-like shape. This arrangement, shown in figure 4.1, is supposed to spread the heat load over a much broader area than in the case of a standard divertor. Also the edge magnetic properties are substantially altered [63]:

- The flux expansion near the null-point becomes about two times larger in TCV.
- The connection length of the open field lines from the equatorial plane to the divertor plate increases by factor of about 2.5 for TCV parameters.
- The safety factor and the magnetic shear in the edge of the plasma becomes much larger for finite current density at the edge. However, in the case of H-mode, this effect is partly neutralized by the bootstrap current fraction resulting from the pressure gradient near the edge, as demonstrated in subsection 4.2.2.
- In the open field line region, the elongation of the flux tubes near the null-point increases leading to a reduction of plasma turbulence in the divertor legs and the scrape-of-layer (SOL). In TCV, the elongation of the flux tubes is increased by a factor of  $\sim 2.5$ , when compared to a SN configuration [64].

### 4.1.2. L-mode experiments on TCV

The snowflake divertor plasma was created starting from a SN configuration with both strike points on the central column. The high field side (HFS) strike points are then subsequently moved towards the low field side (LFS) producing the SF configuration. Perturbing the exact SF configuration by shifting the plasma column away from the null point or towards it, while keeping divertor currents and plasma current constant, produces the SF+ and SF- configuration. The SF+ configuration exhibits vertically aligned X-points, whereas the SF- is represented by two X-points aligned in a horizontal plane [64].

The magnetic equilibria of the SF configurations are reconstructed by LIUQE [11] using the magnetic measurements. The reconstructed equilibria are shown in figure 4.1.

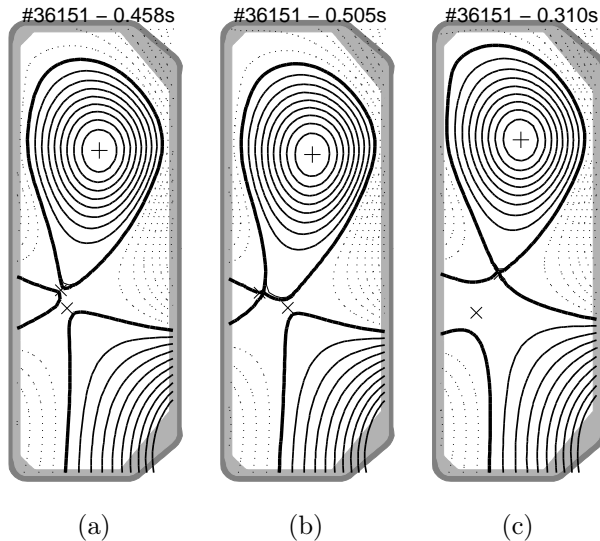


**Figure 4.1.:** Magnetic equilibrium reconstruction of snowflake diverted discharge in L-mode #36151: (a) SF, (b), SF minus (SF-) and (c) SF plus (SF+).

The plasma current was  $I_p = 230$  kA, the line integrated density  $n_{el} \sim 3.5 \times 10^{19} \text{ m}^{-2}$ , central electron temperature  $T_e(0) \sim 0.65$  keV, safety factor  $q_0 \sim 0.8$  and  $q_{95} \sim 3.5$ , plasma elongation  $\kappa \sim 1.6$  and triangularity  $\delta \sim 0.2$ .

The vertical stability, i.e. the  $n = 0$  mode, where  $n$  is the toroidal mode number, was computed for all configurations by using the KINX code [36] and imposing a conformal and perfectly conducting wall with wall radius  $r_w$ . The conformal wall radius is defined as  $r_w = r_{wall}/a_{min}$ , where  $a_{min}$  is the plasma minor radius and  $r_{wall}$  the radius of the wall with a shape conformal to the plasma contour. The growth rate  $\gamma(N_\chi, N_\psi)$  was computed as function of the conformal wall radius on a grid of  $N_\chi \times N_\psi = 160 \times 160$  and  $N_\chi \times N_\psi = 192 \times 192$  grid, where  $N_\chi$  is the number of poloidal and  $N_\psi$  the number of “radial” grid points. The obtained growth rates were then extrapolated for infinite grid size ( $N \rightarrow \infty$ ) assuming  $1/N^2$  convergence of  $\gamma(N)$  in KINX (section B.1, appendix B). Figure 4.2 shows  $\gamma(N \rightarrow \infty)$  as function of  $r_w$ . All growth rates converge to asymptotic values for  $r_w > 5$ , the so-called no-wall limit, which is usually used to approximate resistive effects not taken into account by ideal MHD codes.

The numerical values of  $\gamma$ , together with the central Alfvén wave frequency  $\omega_A$ , are given in table 4.1 for  $r_w = 10$ . No major differences in the growth rate of the  $n = 0$  mode are found between the configurations. Thus, the SF configuration has no drawbacks in terms of vertical stability when compared with a SN divertor. The growth rates of all

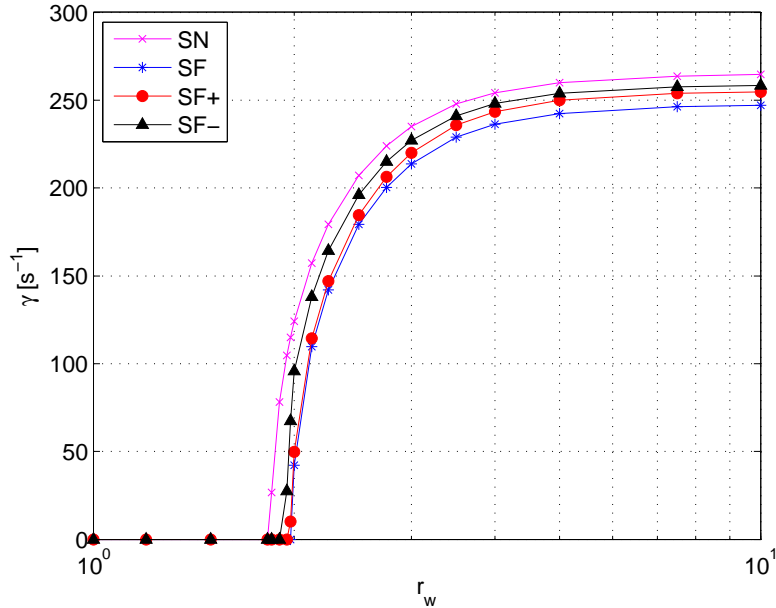


**Figure 4.2.:** Vertical stability of snowflake diverted discharge #36151 (L-mode): Growth rate  $\gamma$  of the  $n = 0$  ideal MHD mode as function of the normalized conformal wall radius  $r_w$ .

configuration	$\omega_A$ [ $10^6 \text{ s}^{-1}$ ]	$\gamma$ [ $\text{s}^{-1}$ ]
SN	1.30	265
SF	1.28	245
SF+	1.32	250
SF-	1.26	260

**Table 4.1.:** Growth rate  $\gamma$  of the  $n = 0$  ideal MHD-mode for  $r_w = 10$  (no-wall limit) and the central Alfvén wave frequency  $\omega_A$ .

configurations are well below the threshold of the TCV control system, which is able to stabilize plasmas with open loop growth rates up to  $4400 \text{ s}^{-1}$  [65].

## 4.2. Ideal MHD stability properties of snowflake diverted H-mode

In this section, the ideal MHD stability of the edge pedestal is studied with equilibria modeling TCV discharges that were purely ohmically heated and exhibited type-III ELMs. The influence of the bootstrap current on the safety factor and magnetic shear profile is

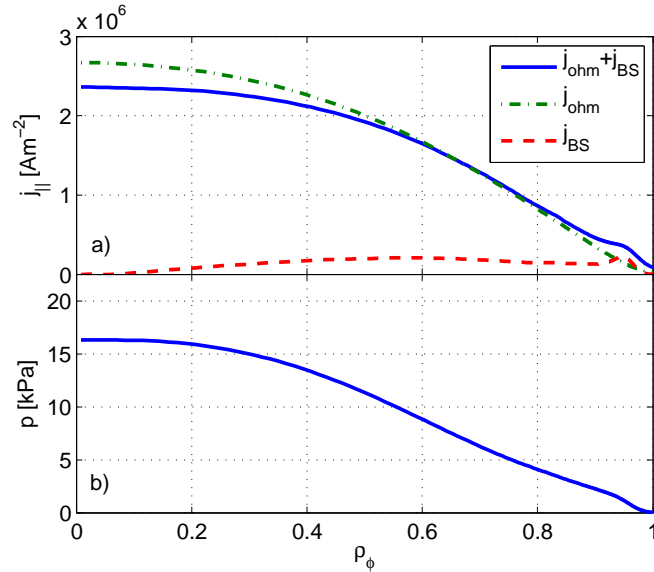


**Figure 4.3.:** Current density and pressure profile for synthetic snowflake-diverted H-mode equilibria: a) Ohmic and bootstrap current density as function of the normalized toroidal flux radius  $\rho_\phi = \sqrt{\phi_N}$ . The profiles  $j_{ohm}$  and  $j_{ohm} + j_{BS}$  are scaled to the same total plasma current,  $I_p = 320$  kA. b) Total pressure profile taken from a SN type-III ELMy H-mode (#32715).

quantified for the pedestal region. Finally, the stability limits of the SF-configurations are compared and discussed.

#### 4.2.1. Construction of the equilibria

As discussed before, the SF divertor has several advantages when being employed in H-mode discharges. One of them is that the MHD stability of the pedestal region is supposed to improve by higher magnetic shear. In order to investigate possible improvements of MHD-stability in H-mode, equilibria were constructed using the plasma boundary of the SF discharge (#36151,  $I_p = 230$  kA,  $n_{el} \sim 3.2 \times 10^{19} \text{ m}^{-2}$ ) in L-mode. The electron pressure profile was taken from a type-III ELMy H-mode (#32715,  $I_p = 370$  kA,  $n_{el} \sim 3.5 \times 10^{19} \text{ m}^{-2}$ ) in SN configuration with high ohmic heating power. So far, no reliable pedestal data were available from type-I ELMing discharges. Figure 4.3 shows the ohmic and bootstrap current density and the total pressure profile as function of the normalized toroidal flux radius  $\rho_\phi = \sqrt{\phi_N}$ .

The ohmic current density was taken from the LIUQE reconstruction of the reference H-mode discharge. The electron pressure profile was obtained from Thomson scattering

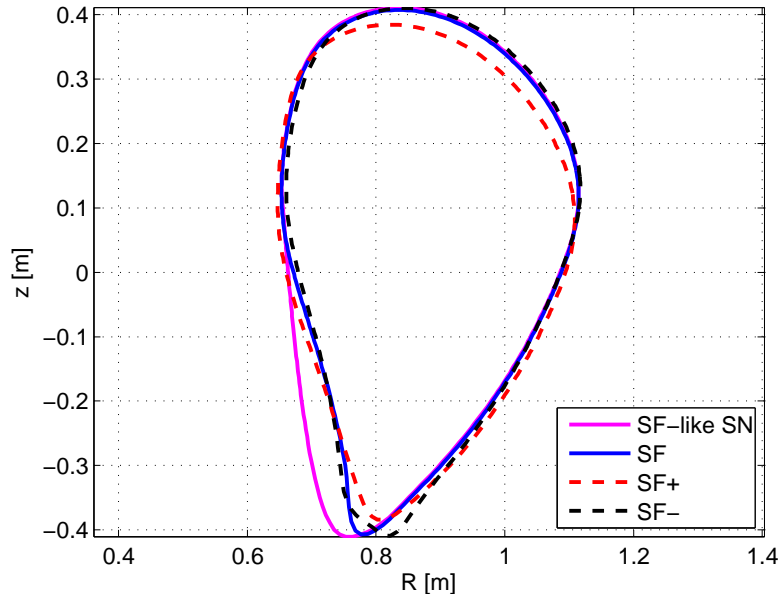


**Figure 4.4.:** Plasma boundary of the SF-like SN and SF equilibria: Shown is the constructed SF-like SN plasma boundary, and the SF+, SF- and SF boundary from discharge #36151.

data of the same discharge including the edge pedestal fit by a modified tanh-function [35], equation (3.6.1). The ion pressure profile was obtained by scaling the electron pressure with a fixed ratio  $p_e/p_{tot} = 0.7$  obtained from equation (2.1.8), which was found to be a good approximation for ohmic H-mode discharges in TCV. The ion density profile was obtained by scaling the electron density profile using  $Z_{eff} = 2.5$  and  $C^{6+}$  as single impurity, equation (3.6.2). The value of  $Z_{eff}$  was obtained from soft X-ray measurements and conductivity calculations for the discharge #32715. The ion temperature profile is then derived from ion pressure and density. This approximation agreed with ion temperature measurements by Charge eXchange Recombination Spectroscopy (CXRS) for a similar shot. The bootstrap current was computed with Sauter's model [13] based on the kinetic profiles. Finally, self-consistent equilibria were computed using the CHEASE equilibrium code. The total plasma current was re-scaled to 320 kA, a value given by the limitation of the current in the TCV plasma shaping coils in the case of a SF configuration.

In order to have a better comparability of the results from the pedestal stability analysis with those of a SN configuration, a synthetic SN configuration (SF-like SN) was constructed as follows: (1) The HFS part of the boundary, below  $z = 0$  m, was cut off till the double X-point magnetic divertor. (2) The X-point was constructed by keeping the LFS boundary unchanged. (3) The former cut off region was reconstructed including

configuration	$\delta$	$\kappa$	$l_i$	$q_0$	$q_{95}$
SF-like SN	0.30	1.73	0.72	1.2	5.3
SF	0.30	1.73	0.75	1.2	8.8
SF+	0.24	1.60	0.82	1.0	5.2
SF-	0.25	1.79	0.80	1.0	7.7

**Table 4.2.:** Shape and plasma parameters from the SF-like SN and SF equilibria: Plasma triangularity  $\delta$ , elongation  $\kappa$ , plasma inductance  $l_i$ , safety factors  $q_0$  and  $q_{95}$ .

the X-point by keeping the boundary angles unchanged. To stay consistent with the SF configurations, the total plasma current of the SN configuration was renormalized to  $I_p = 320$  kA. The shape and some plasma parameters of the synthetic equilibria are given in table 4.2, the plasma boundaries are shown in figure 4.4.

#### 4.2.2. Impact of bootstrap current on edge magnetic shear

In the SF configuration, safety factor  $q$  and magnetic shear  $s$  in the pedestal region are expected to be than in a SN configuration [63]. However, a finite current density in the pedestal region will reduce this increase in  $q$  and  $s$ . In reality, we have to take into account a finite edge current fraction due to the bootstrap current  $j_{BS}$  resulting from the steep pressure gradient in the H-mode edge barrier. The  $q$  and  $s$  profiles with and without including the bootstrap current were computed using the CHEASE code [14] and are presented in figure 4.5 as function of the normalized toroidal flux  $\rho_\phi = \sqrt{\phi_N}$ . We have to note that a finite edge current density may change the angle of the plasma boundary close to the X-point(s) [66, 67]. This effect was neglected, since CHEASE is a fixed-boundary code that cannot compute this self-consistently.

The comparison of the  $q$ -profiles between SN and SF, 4.5(a), yields a ratio of  $q_{SF}/q_{SN} \sim 2.2$  between  $q$  of the SF and SF-like SN at the separatrix, when the bootstrap current is not included, and to  $q_{SF}/q_{SN} \sim 1.6$ , when it is included. A similar behavior is observed for the shear profiles, when  $j_{BS}$  is taken into account. The overall change of edge  $q$  and  $s$  by including  $j_{BS}$  is larger for the SF configuration. In the case of SF+ and SF-, figure 4.5(b), the differences in the ratios  $q_{SF-}/q_{SF+} \sim 1.6$  w/o. and  $\sim 1.5$  with  $j_{BS}$  is somewhat less pronounced. In this case, the decrease in  $q$  and  $s$  when adding the  $j_{BS}$  is more important in the SF- configuration.

When comparing  $q$  and  $s$  of all configurations, one observes that the SF+ configura-

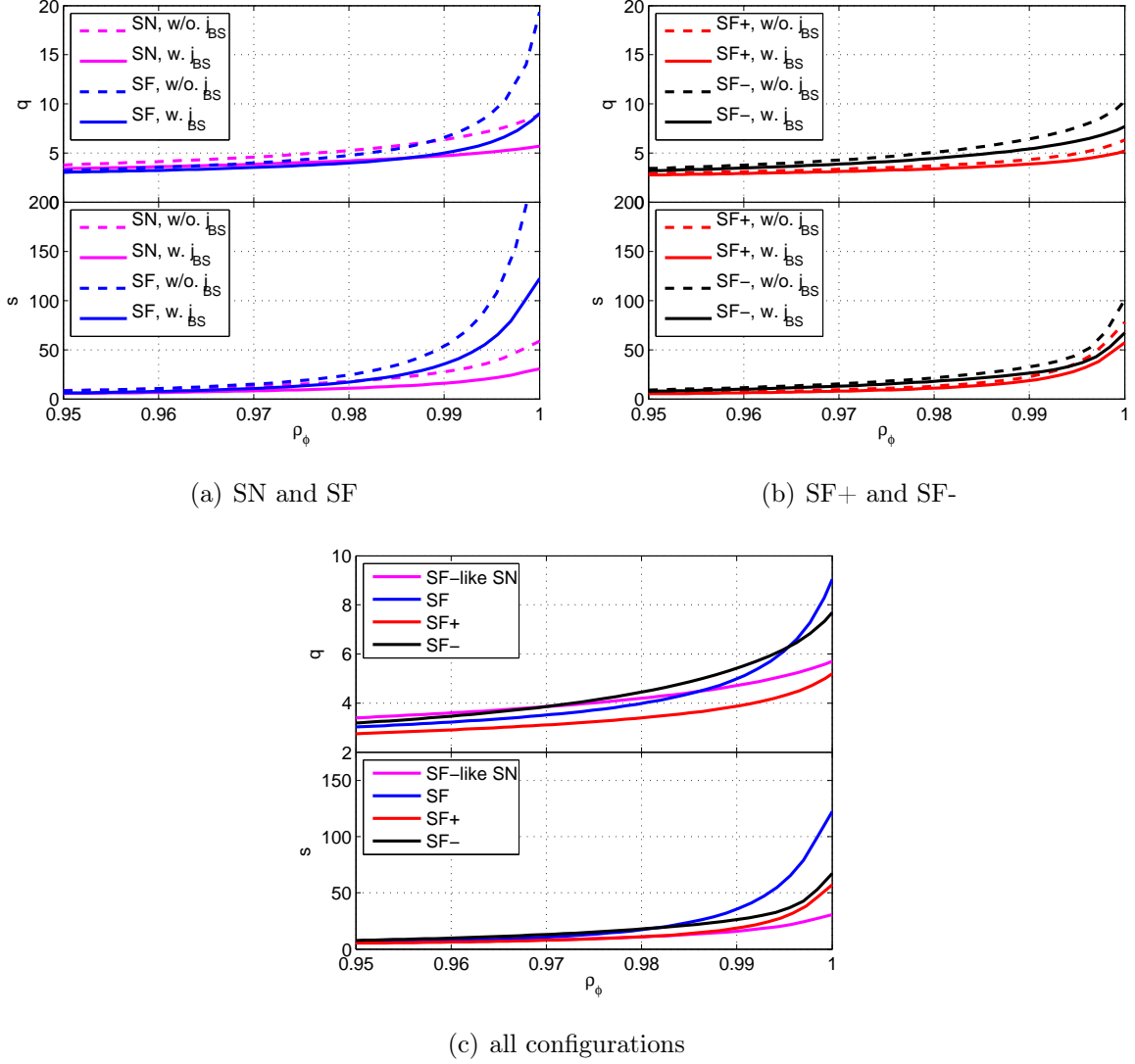


**Figure 4.5.:** Safety factor  $q$  and magnetic shear  $s$  from the SF-like SN and SF equilibria as function of  $\rho_\phi$ : (a) SN and SF configuration with (solid line) and without (dashed line) bootstrap current, (b) SF+ and SF- configuration with and without bootstrap current and (c) all equilibria with the bootstrap current included.

tion exhibit an overall lower  $q$ . This is explained by the fact that its plasma surface is smaller compared to the other configurations while having the same total plasma current (compare with figure 4.4).

In terms of improved edge pedestal stability, high magnetic shear is desirable to stabilize coupled kink-ballooning modes [18, 68]. We remark that the SF and SF- configuration are more likely to provide high edge magnetic shear. However, in terms of actively control-



ling the position of the two X-points during the plasma discharge, these two configurations are the most difficult to handle.

### 4.2.3. Ideal MHD stability analysis of the edge pedestal region

The analysis of ideal MHD stability in the pedestal region was carried out with a conformal and perfect conducting wall with  $r_w = 1.2$ , instead of the TCV wall. This eliminates effects of plasma-wall distances, being different for the various configurations, on mode stabilization and hence ensures better comparability of the MHD-stability limits. By choosing the conformal wall, we expect current-driven modes to be slightly more stable than in the case of the TCV wall. In the equilibria, the maximum pressure gradient was fixed at  $\rho_{0,\psi} = \sqrt{\psi_N} = 0.984$ , where  $\rho = \sqrt{\psi_N}$  and the width of its peak was  $\Delta_\rho = 0.015$ . The bootstrap current profile was aligned with the pressure gradient profile, so that the ratios  $j_{edge}/j(\rho_{0,\psi}) \approx 0.32$  and  $p'_{edge}/p'(\rho_{0,\psi}) \approx 0.32$  were constant. All equilibria were renormalized to a total plasma current of  $I_p = 320$  kA, a feasible value for H-mode operation in TCV with such configurations.

For the stability diagram, we use the definition  $\alpha \equiv -\mu_0 p' V' \sqrt{V/(2\pi^2 R)}/2\pi^2$  [35] for the normalized pressure gradient at the point of its maximum in the pedestal, where prime denotes  $d/d\psi$ ,  $p$  is the total pressure,  $V$  is the plasma volume,  $R$  the major radius and  $\psi$  the poloidal flux. The normalized current density  $J_{||}/\langle J \rangle$  is taken at the position where the pressure gradient is maximal.  $\langle J \rangle$  is the total plasma current normalized to the plasma cross sectional area. The method explaining the computation of the stability map is described in subsection 2.3.4 of chapter 2. For the sake of clarity, only a condensed form of the stability limits is shown here, figure 4.6. We refer the reader to subsection C.1 in appendix C, where all stability maps are given in detail.

The MHD-stability limit for each configuration is given by a solid or dashed line with the respective color coding. In the gray region, all configurations become MHD-unstable. From the experimental point of view, a pure SF configuration is difficult to sustain and may eventually form a SF+ or SF- configuration. For that purpose, the region in which the different SF configurations are marginal stable is represented in blue-gray color. The points with a diagonal line as error bar correspond to the experimental values of  $\alpha$  in type-III H-mode. The large error bar reflects uncertainties in the measurement of the electron pedestal pressure gradient and the determination of the total pressure gradient.

We observe that in general the SF configurations may improve stability, probably due

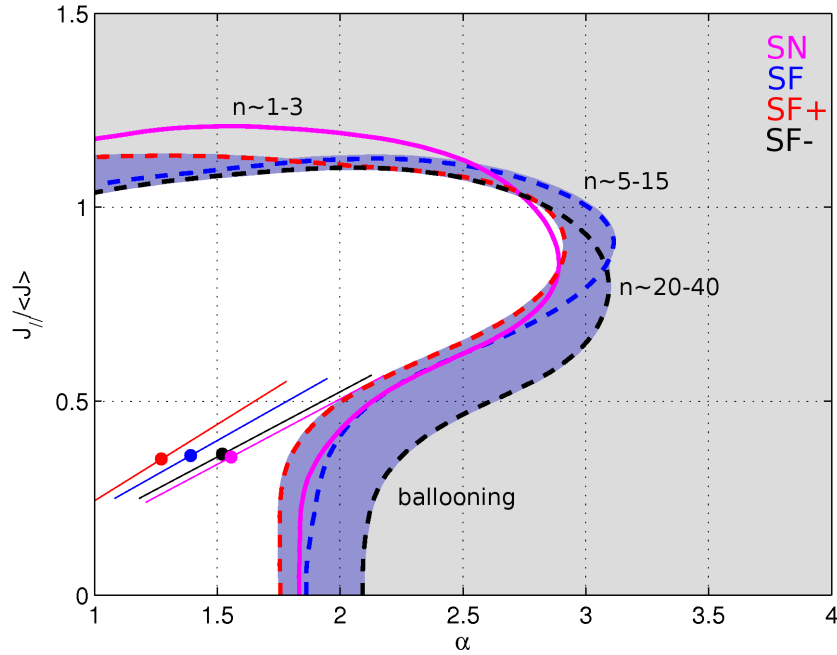


**Figure 4.6.:** Comparison of the edge pedestal stability of the SF-like SN and SF equilibria: Shown are the stability limits of the SN, SF, SF+ and SF- configuration. Colored lines depict the stability limits of each configuration. In the gray region, all configurations are MHD-unstable. Some representative mode numbers  $n$  are given for unstable external kinks.

to their higher magnetic shear in the pedestal region. Surprising is the better stability of the SF-, especially against ballooning modes, when compared to the true SF configuration. In the following, a more detailed analysis of the most unstable modes is given.

### Ballooning modes

The ballooning limits for the SN and SF configuration are comparable within certain uncertainties due to the computation grid. This is due to the fact that pressure-driven modes are less affected by magnetic shear than current-driven modes [18]. For the stability of ballooning modes, the plasma boundary shape plays a more important role. Since the last closed flux surface (LCFS) of both configurations and the length of magnetic field lines in the bad curvature are comparable, only small differences in the ballooning limit are expected.

The  $n \rightarrow \infty$  stability of the SF+ configuration is somewhat difficult to compare with the other configurations, since triangularity and elongation, table 4.2, are reduced, hence destabilizing pressure and current-driven modes [18]. In general, we can only

conclude that its stability limit is not too different from a SN configuration, which is not surprisingly considering the fact that, among all SF configurations, the SF+ magnetic divertor region resembles the most a SN configuration. The SF- has a critical normalized pressure gradient  $\alpha_{crit}$ , which is  $\sim 15\%$  higher compared to the SF and SF-like SN in the zero-bootstrap current limit. This difference originates from a somewhat larger value of  $dV/d\psi$  in the expression for  $\alpha$  reflecting the fact that the magnetic divertor region is very distinct and the poloidal flux  $\psi$  changes only little across the entire region whilst volume does<sup>1</sup>.

### Low- $n$ external kinks

The  $n = 1$  global kink mode becomes more unstable in the SF than in the SN which is connected to the plasma current and  $q$ -profile, figure 4.7. In the case of the SF, the proximity of the  $q = 4$  rational surface to the separatrix, figure 4.7(b), leads to a destabilization of the  $m/n = 4/1$  mode, whereas in the SN this rational  $q$  surface does not exist at the chosen current density, figure 4.7(a). We note that the shear reversal in the pedestal region of the SF takes place at slightly higher  $J_{||}/\langle J \rangle$  than in the SN, which results from the fact that the magnetic shear in the SF is in general higher.

In the SF+, the global kink mode  $n = 1$  is more unstable than in the SN configuration. This is due to the fact that the equilibrium is renormalized to the same plasma current with a somewhat smaller volume, hence leading to smaller values of  $q$ . The mode spectrum of the SF+, figure 4.7(c), shows a destabilization of the  $m/n = 3/1$  mode in the vicinity of the inflection point in the  $q$ -profile, i.e.  $q'' = 0$  (shear reversal). The external kink modes with low  $n$  are also more destabilized in the SF-, figure 4.7(d), which results from shear reversal at a lower value of  $J_{||}/\langle J \rangle$ .

In general, we note that the stability limits of the low- $n$  modes are strongly governed by the shear reversal. The proximity of the inflection point  $q'' = 0$  to a rational  $q$ -surface generally leads to a destabilization of modes related to this  $q$ -surface.

---

<sup>1</sup>Comparison with the cylindrical representation  $\alpha_{cyl} \equiv -2\mu_0 R_0 (q^2/B_0^2) dp/dr$ , where  $R_0$  is the major plasma radius,  $q$  the safety factor,  $B_0$  the toroidal field and  $dp/dr$  the pressure gradient, yields the same tendencies.

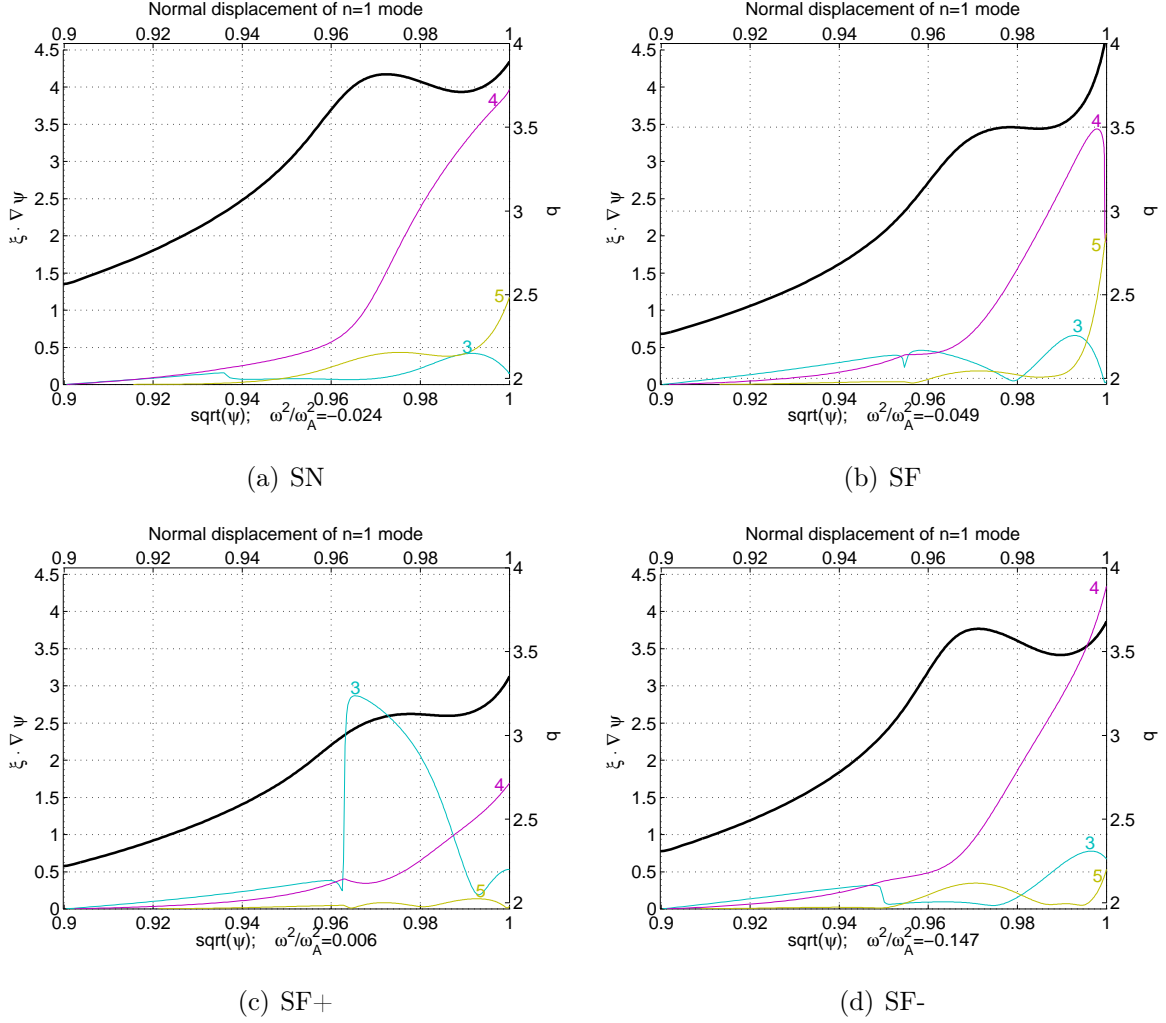


**Figure 4.7.:** Mode structure versus the poloidal flux radius for  $n = 1$  of (a) the SF-like SN, (b) SF, (c) SF+ and (d) SF- configuration. The first three modes with the largest normal displacement are shown and labeled by their poloidal mode number  $m$ . The  $q$ -profile is plotted as bold black line. The equilibria were computed with  $\alpha \approx 1.4$ , corresponding to the experimental value of the normalized pressure gradient  $\alpha_{exp}$ , and  $J_{\parallel} / \langle J \rangle = 1.3$ .

### Medium- and high- $n$ external kinks

The destabilization of the medium and high- $n$  modes appears at higher  $\alpha$  in the case of the SF compared to the SN, so that the MHD-stable region is expanded to higher pressure gradients. This effect is mainly due to increased edge magnetic shear in this configuration and agrees well with the literature, where coupled kink-ballooning modes are stabilized at higher magnetic shear [18, 68].

Regarding the medium and high- $n$  stability limits of the SF+ and SF- configurations, which have both similar magnetic shear profiles in the pedestal region, the SF+ resembles more the SN while the SF- is clearly more SF-like. This is comprehensible since the magnetic divertor topology of the SF+, two vertically aligned X-points, is closer to a SN than to a SF-configuration. Additionally, medium- and high- $n$  are certainly more unstable due to a decreased  $\delta$  and  $\kappa$  in this configuration. The SF- gains in stability of medium- and high- $n$  current-driven modes in respect to the SN due to its increased magnetic shear.

The results of the MHD-stability calculations show that some improvements in pedestal stability can be achieved by employing a snowflake divertor. Furthermore, no major disadvantages of this configuration in respect to vertical stability or low- $n$  mode destabilization was found, which encourages to give experimental evidence. However, this analysis assumed that kinetic profiles are identical in all configurations and that the edge barrier is located at the same radial position and has a fixed width. If the ELM characteristics and/or energy confinement and transport properties are in some sense different for each configuration, this assumption may not hold anymore and needs experimental verification. Furthermore, improved shaping of a SN discharge may lead to the same stability enhancement as seen for the SF.

### **4.3. Dependence of pedestal stability on plasma parameters**

The interpretation of the pedestal stability requires a thorough investigation of the sensitivity of such an analysis on various plasma parameters. In the following, we will study the influence of the radial position of the maximum pedestal pressure gradient, which is inherent to the equilibrium, on the pedestal stability. Further, we want to investigate if plasma shaping, which is accessible to external control, can further improve pedestal stability. We will carry out this analysis for the SF, but, in general, these results are universally valid.

### 4.3.1. Procedures to modify equilibrium

In order to investigate the dependence of the edge pedestal stability upon plasma shaping and radial position of the edge barrier, a series of equilibria was constructed, where only one single quantity was changed at a time.

For the purpose of studying the sensitivity of the analysis on shape, the upper plasma boundary of LCFS has been modified in the following way:

1. The upper plasma boundary of the snowflake was fitted with the analytical formulas

$$R = R_0 + a [1 + \lambda \cos(\theta)] \cos(\theta + \delta \sin(\theta) - \lambda \sin(2\theta)), \quad (4.3.1)$$

$$Z = Z_0 + \kappa a \sin(\theta), \quad (4.3.2)$$

where  $\delta$  is the triangularity,  $\kappa$  the elongation,  $\lambda$  the squareness,  $a$  the minor radius and  $(R_0, Z_0)$  the radial and vertical position of the magnetic axis.

2. One of the obtained shaping parameter was changed and the upper LCFS was reconstructed with the formulas from above. The new plasma boundary was then combined with the lower and unchanged part of the LCFS.
3. A self consistent plasma equilibrium was computed with CHEASE; the total current was renormalized to a fixed value.

The radial position of the barrier was adapted by rescaling the  $p'$  and  $j_{||}$  profiles from the reference discharge #32715 as function of the radial normalized poloidal flux coordinate  $\rho = \sqrt{\psi_N}$ . This modification has also an impact on the plasma core, but is negligible for the changes of  $\Delta\rho_{0,\psi} \leq 4 \times 10^{-3}$  used in these studies. Effects of the edge current density on the plasma boundary shape close to the X-point(s) are neglected.

### 4.3.2. Radial position of the maximum pressure gradient

As noted before, a higher value of magnetic shear in the edge region of the plasma is supposed to suppress coupled kink-ballooning modes [18, 68]. This gives the motivation to investigate the role of the edge magnetic shear on the ideal MHD-stability limits and to compare between SN and SF. For that purpose, the radial position of the maximum pressure gradient and thus also bootstrap current is artificially varied. Note that in the experiment, the barrier position cannot be directly controlled but will be defined by plasma parameters and the equilibrium.

$\rho_{0,\psi}$	$j_{edge}/j_0$	$p'_{edge}/p'_0$	$q_{SN}$	$q_{SF}$	$s_{SN}$	$s_{SF}$
0.980	0.15	0.13	4.2	4.3	14	21
0.984	0.31	0.32	4.5	4.7	17	28
0.988	0.51	0.52	4.7	5.1	20	35
0.992	0.74	0.75	5.2	6.2	25	55

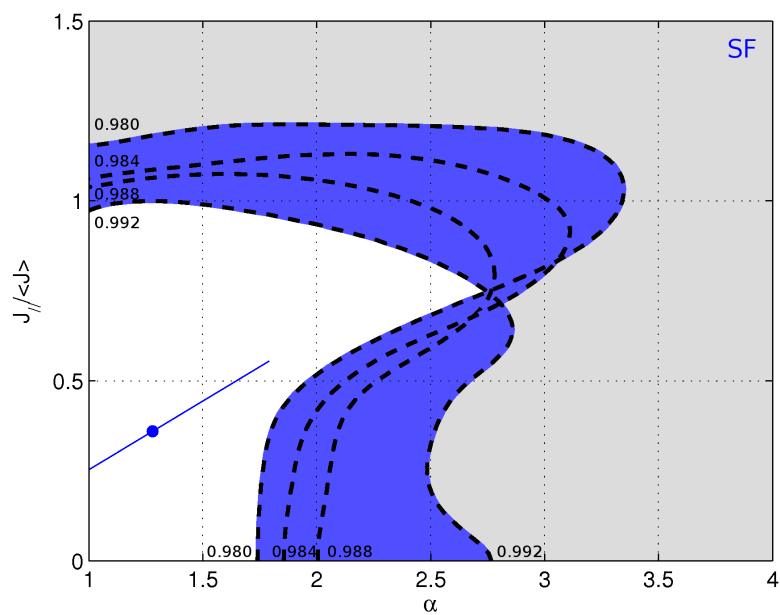
**Table 4.3.:** Some parameter of the MHD-stability analysis with varying radial position of the maximum pressure gradient:  $j_{edge}/j_0$  is the ratio between the parallel current density at the separatrix and at the radial position of maximum pressure gradient,  $p'_{edge}/p'_0$  the ratio between pressure gradients at the same radial positions, safety factor  $q$  and magnetic shear  $s$  for SN and SF.

Another reason for this study is to quantify the sensitivity of the stability analysis on the radial position of the edge barrier, since uncertainties in the determination of this position can easily appear due to uncertainties in the equilibrium reconstruction [67] and profile fitting procedure [69].

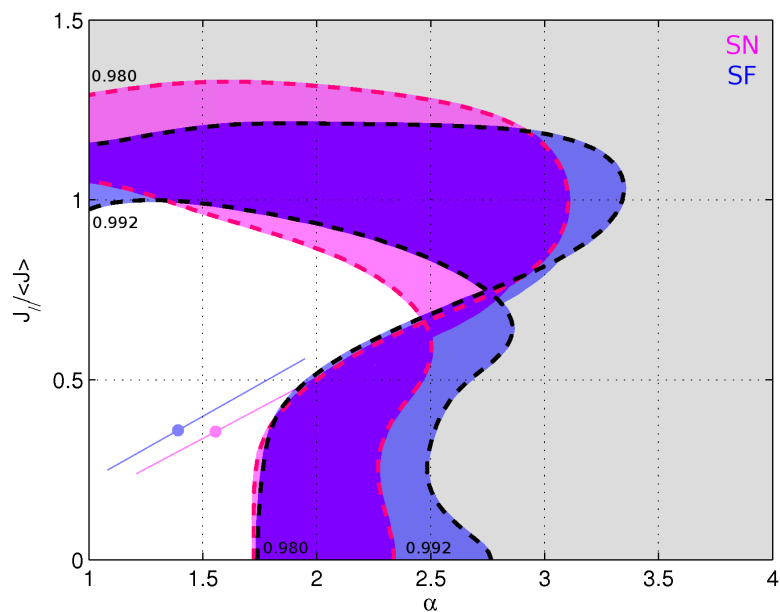
For this purpose, the reference current density and pressure gradient profiles as function of  $\rho_\psi$  were mapped on a rescaled  $\rho_\psi$ -axis, hence marginally stretching or compressing the profiles. In the following step, the equilibrium was computed by CHEASE and its total current rescaled to  $I_p = 320$  kA. The ideal MHD-stability limits were computed for the different radial positions of the maximum pressure gradient  $\rho_{0,\psi} = \{0.980, 0.984, 0.988, 0.992\}$ . For the sake of clarity, only a general representation of the results is given here, figure 4.8. The detailed stability maps for each radial position can be found in section C.2 of appendix C.

The gray region represents the MHD-unstable zone regardless of  $\rho_{0,\psi}$  or the configuration. The blue-colored region with black dashed lines as boundary depicts the variation of the stability limits as function of  $\rho_{0,\psi}$  for the SF, respectively, the magenta tube with red dashed for the SN.

Table 4.3 gives the ratios between the parallel current density  $j_{edge}/j_0$  and the pressure gradient  $p'_{edge}/p'_0$  at the separatrix and at the radial position of maximum pressure gradient. Further, the safety factor  $q$  and magnetic shear  $s$  are given for SN and SF configurations. In the following, we want to summarize the differences between the individual MHD-stability diagrams.



(a) SF



(b) SN and SF

**Figure 4.8.:** Ideal MHD-stability limits of the pedestal as function of the radial position  $\rho_{0,\psi}$  of the maximum pressure gradient: (a) Pedestal stability of the SF as function of  $\rho_{0,\psi} = \{0.980, 0.984, 0.988, 0.992\}$ . (b). Comparison of the MHD limit of SF and SF-like SN for the extrema  $\rho_{0,\psi} = \{0.980, 0.992\}$ .



$\rho_{0,\psi}$	$q_{\text{SF}}(q'' = 0)$	$q_{\text{SN}}(q'' = 0)$
0.980	3.4	3.7
0.984	3.5	3.8
0.988	3.7	3.9
0.992	3.8	4.0

**Table 4.4.:** Inflection point ( $q'' = 0$ , shear reversal) in the safety factor  $q$  profile for the radial positions  $\rho_{0,\psi}$  of the edge barrier in the SN and SF equilibria.

### Ballooning modes

The ballooning stability boundary is shifted towards higher  $\alpha$ 's for all configurations when the radial position of the maximum pressure gradient  $\rho_{0,\psi}$  increases, even for the ideal ballooning limit, where  $J_{||}/\langle J \rangle = 0$ . This effect is due to the sufficiently large  $q$  in the edge region close to the separatrix, which increases the magnetic well and, therefore, stabilizes pressure-driven instabilities.

### Low- $n$ external kinks

The stability limits of the global kink mode  $n = 1$  do change by about 30%. The limiting value of  $J_{||}/\langle J \rangle$  for the  $n = 3, 5$  modes is decreasing with increasing  $\rho_{0,\psi}$  for both SN and SF, which is the result of an increase of edge current. The mode structure exhibits modes with large amplitudes appearing in the proximity of the rational surfaces  $q = 3$  and 4, where the magnetic shear is low. Table 4.4 gives the positions of the inflection points in the  $q$ -profiles taken from the equilibria with  $\alpha = \alpha_{exp}$  and  $J_{||}/\langle J \rangle = 1.3$ .

### Medium- and high- $n$ external kinks

A general effect, being valid for SN and SF, is the destabilization of medium- and high- $n$  external kink modes when increasing  $\rho_{0,\psi}$ . By increasing the parallel current density close to the separatrix, one destabilizes these modes that close the access to the second ballooning stable region. The medium- and high- $n$  modes are more stable in the case of the SF for all  $\rho_{0,\psi}$  which results from the overall higher magnetic shear compared to the SN (see table 4.3).

In summary, the results of the stability analysis strongly depend on the radial position

of the maximum pressure gradient at the edge; small uncertainties in this position have large effects. Therefore, a comparison between different configurations should be done with identical profiles, if only the relative changes linked to the magnetic configuration are of interest. We also conclude that the snowflake configuration has general advantages in edge pedestal stability when compared to a single-null configuration. The pedestal stability benefits from the somewhat higher magnetic shear in the SF, however, it remains open whether the kinetic profiles in the SN and SF are comparable or if they exhibit essential differences that may diminish the pedestal stability enhancement in the SF configuration.

### 4.3.3. Upper triangularity and upper squareness

Plasma shaping is known to increase the  $\beta$ -limit and to stabilize certain classes of ideal and resistive MHD instabilities [10]. Local changes in plasma triangularity and/or squareness were found to influence the stability of ballooning and medium- and high- $n$  kink modes [19, 70]. Here, we investigate the influence of these local changes of plasma shape on the pedestal stability. These effects are expected to be valid also for SN configurations, as reported in [20] or demonstrated in section 5.3, and give indications by how much the plasma shape of a SN configuration has to be altered to obtain similar stability limits as found for the SF.

The ideal MHD-stability limits of the pedestal were computed for a set of different upper triangularities  $\delta_{top} = \{-0.25, 0, 0.25, 4\}$  and upper squareness  $\lambda_{top} = \{-0.15, 0.15, 0.30\}$  in SF configuration. Once more, the detailed MHD-stability diagrams can be found in the appendix C, section C.3 and C.4. A schematic representation of the MHD-stability analysis for  $\delta_{top}$  and  $\lambda_{top}$  are shown in figure 4.9 and 4.10, respectively. The colored lines depict the stability limits of each configuration while the gray region represents the MHD-unstable zone for all configurations. The mode numbers of unstable external kinks are given in the corresponding color to  $\delta_{top}$  or  $\kappa_{top}$ . In the following, the differences in the ideal MHD-stability limits are shortly discussed.

#### Ballooning modes

Positive upper triangularity improves the stability of pressure-driven modes, which is related to the Mercier criterion. It is related to the fact that for such cross sections a magnetic field line has a relatively large fraction of its trajectory located in the favorable

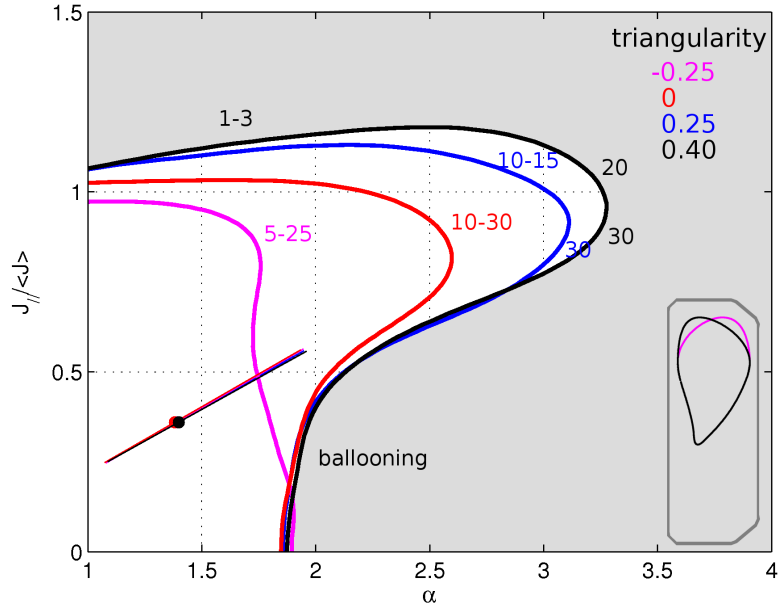


**Figure 4.9.:** Sensitivity of the MHD-stability limits of the pedestal upon upper triangularity  $\delta_{top}$ : Schematic representation of the ideal MHD stability limits of the SF configuration for  $\delta_{top} = \{-0.25, 0, 0.25, 0.4\}$ .

curvature region on the high field side (HFS). Thus, decreasing the triangularity increases the effective length of field lines in the bad curvature region and destabilizes the pressure-driven modes. For such a case, an increase in the current density is required to reduce the magnetic shear to a low value and to give access to the second ballooning stable region [10].

The ballooning stability reacts only little on changes in upper squareness. Only for high positive squareness, where field lines cover a somewhat longer distance in the bad curvature region, noticeable destabilization takes place.

### Low- $n$ external kinks

The stability of low- $n$  external kink modes for both  $\delta_{top}$  and  $\lambda_{top}$  is rather limited by  $J_{||}/\langle J \rangle \sim 1$ , hence less susceptible to shaping [19]. The stability limit of  $n = 1$  is reduced in the cases of  $\delta_{top} = -0.25$  and  $\delta_{top} = -0.15$ , where modes appear in the mode structure at  $q \sim 4$  and 5 close to the separatrix.

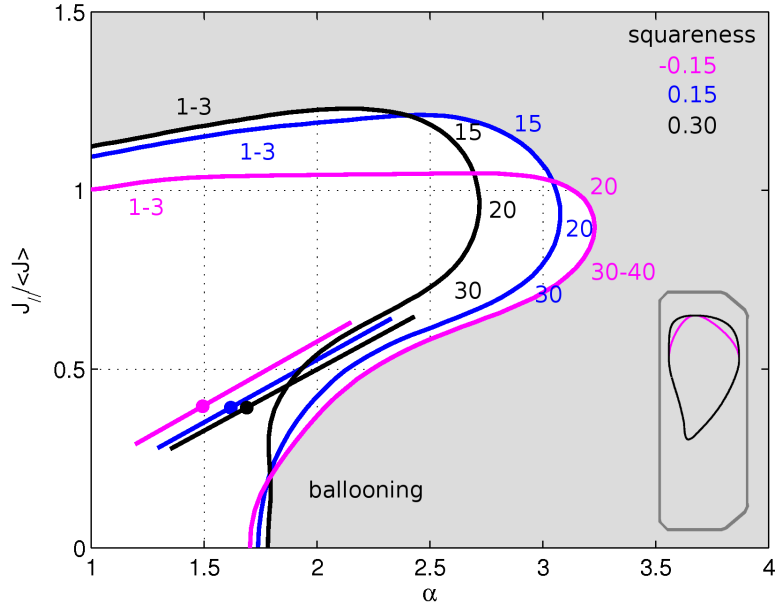


**Figure 4.10.:** Sensitivity of the MHD-stability limits of the pedestal upon upper squareness  $\lambda_{top}$ : Schematic representation of the ideal MHD stability limits of the SF configuration for  $\lambda_{top} = \{-0.15, 0.15, 0.3\}$ .

### Medium- and high- $n$ external kinks

Increasing  $\delta_{top}$  or decreasing  $\lambda_{top}$  improves the stability of external kink modes, mainly medium- and high- $n$ . We observe that  $\delta_{top}$  has a larger influence on the medium- and high- $n$  modes than  $\lambda_{top}$ . At low value of  $\delta_{top}$ , the external kink and ballooning mode couple at finite  $n$  and close access to the second stability region. Since the strength of the coupling is a function of  $n$ , the second stability gap opens more easily for higher  $n$  modes when shaping improves [18].

A change in squareness can be also seen as a modification of triangularity both on the high field and low field side of the torus, so that a decrease in  $\lambda_{top}$  has as consequence an increase in  $\delta_{top}$  on HFS and LFS. Since the stability of external kink modes is more susceptible to changes of the plasma boundary at the LFS, it is not surprisingly that stability limits are modified by squareness in a similar manner as by triangularity.

### 4.3.4. Elongation

As for shaping of the plasma cross section at high triangularity and low squareness, increased plasma elongation  $\kappa$  can stabilize certain classes of MHD instabilities and in-

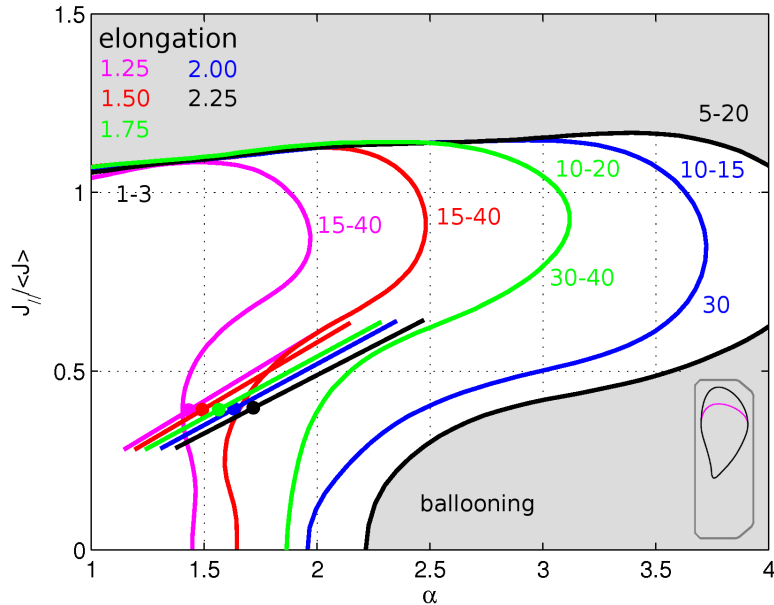


**Figure 4.11.:** Sensitivity of the MHD-stability limits of the pedestal upon elongation: Ideal MHD stability limits of the SF for  $\kappa = \{1.25, 1.50, 1.75, 2.00, 2.25\}$ .

increases the  $\beta$ -limit, although very large values of  $\kappa$  may imply saturation of  $\beta$  [10]. Further, transiting from one SF-configuration to another during a plasma discharge may eventually alter the plasma elongation due to changes in the divertor region. For that purpose, it is necessary to investigate how sensitive the MHD stability limits of the pedestal are to plasma elongation.

The ideal MHD-stability limits were computed for a set of different elongations  $\kappa = \{1.25, 1.50, 1.75, 2.00, 2.25\}$  in SF configuration. For these equilibria, however, the plasma current was not renormalized to one value but was increasing with  $\kappa$  such that  $q_{95}$  was kept approximately constant. Again, the detailed MHD-stability diagrams can be found in the appendix C, section C.5. A schematic representation of the MHD-stability is shown in figure 4.11. Colored lines depict the stability limits of each configuration while the gray region represents the MHD-unstable zone for all configurations. The mode numbers of unstable external kinks are given in the corresponding color to  $\kappa$ . We want to shortly discuss the differences in the ideal MHD-stability limits in the following.

### Ballooning modes

It is evident that an increase in  $\kappa$  strongly improves the ballooning stability. A combination of elongation and positive triangularity is, according to the Mercier criterion,

stabilizing for  $n \rightarrow \infty$  modes [6, 10]. This is related to the fact that for this plasma shape a magnetic line has a relatively large fraction of its trajectory located in the favorable curvature region on the inside of the torus.

### **Low- $n$ external kinks**

As in the former cases with modified triangularity or squareness, the stability limit of low- $n$  external kinks is set by  $J_{\parallel}/\langle J \rangle \sim 1$  and does not change significantly as function of  $\kappa$ .

### **Medium- and high- $n$ external kinks**

Medium- and high- $n$  external kink modes are strongly stabilized by increased  $\kappa$ . The magnetic well increases with increasing  $\kappa$ , hence suppressing short-wavelength radial pressure-driven instabilities. This leads, at finite  $n$ , to a decoupling of external kink and ballooning modes providing access to the second ballooning stable region.

In summary, the MHD stability of the pedestal is highly sensitive on the plasma shaping parameters. Already small changes in one shaping parameter can have strong influences on the critical pressure gradient in the pedestal region, if it is limited by ideal MHD. The stability limit of current-driven modes is most sensitive to triangularity and elongation, whereas ballooning stability is more sensitive to elongation. In experiments, particular attention is required to maintain shaping parameters as close as possible when comparing the individual SN and SF-configuration.

## **4.4. Snowflake experiments**

This section is dedicated to the snowflake diverted type-I ELMy H-mode experiments on TCV [71]. It presents experimental results from a discharge in H-mode which transits from a SN to a SF+ configuration. The edge pedestal properties from Thomson scattering measurements are presented for both configurations. Safety factor and magnetic shear are computed including the collisional bootstrap current density based on the kinetic profiles. Finally, the stability of the edge pedestal from experiment is analyzed in the frame of ideal MHD.

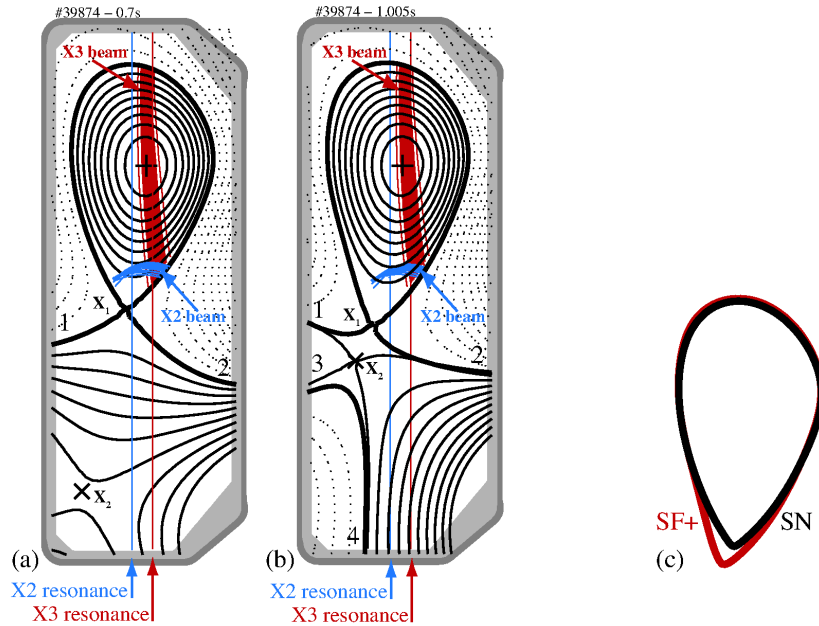


**Figure 4.12.:** (a) SN and (b) SF+ configuration in H-mode: The ECH-X3 beam, injected from the top of TCV, is shown in red together with the location of the resonance layer. The ECH-X2 beam, injected from the low-field side, is presented in blue. The null-points are marked as  $X$ 's, the strike-points enumerated. (c) Comparison of the LCFS of the SN (black) and the SF+ (red) configuration.

#### 4.4.1. H-mode experiments on TCV

The SF+ configuration with its two vertically aligned X-points was chosen to demonstrate SF diverted H-mode on TCV [64]. This choice was made because the plasma shape of the SF+ resembles most the SN shape. Additional fine-tuning of the SN and SF+ shapes provided a good matching of the LCFS, thus minimizing influences of plasma shape on the pedestal stability. Furthermore, out of the three possible SF configurations, it is the easiest to achieve under experimental conditions on TCV.

The SF+ and its equivalent SN configuration are shown in Fig. 4.12(a) and (b), respectively. In the two scenarios, the  $\mathbf{B} \times \nabla \mathbf{B}$  ion-drift is directed towards the X-point. The plasma current was  $I_p = 300$  kA at a toroidal magnetic field of 1.43 T. The plasma was heated with 1.5 MW of ECH: 1 MW injected at the 3<sup>rd</sup> electron cyclotron harmonic (X3) from the top of TCV and 0.5MW injected from the low-field side (LFS) at the 2<sup>nd</sup> harmonic (X2). The absorbed fraction computed by the ray tracing code TORAY-GA [5] was 75% for the X3, primarily in the core region, and 100% for the X2, localized near the plasma edge. Differences between the two shapes are only significant in the null

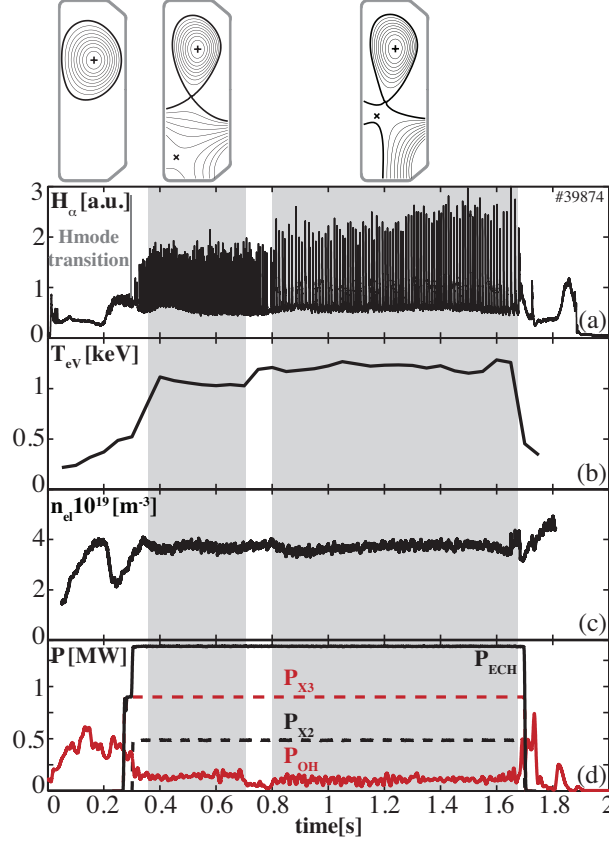


**Figure 4.13.:** Plasma parameters of SN and SF+ configuration in H-mode: (a)  $H_\alpha$  edge emission detected by a wide-angle filtered photodiode at the top of the vessel; (b) volume averaged electron plasma temperature  $T_{eV}$ ; (c) line averaged electron plasma density  $n_{el}$ ; (d) ohmic power  $P_{OH}$  (red solid line), ECH-X2 power  $P_{X2}$  (black dashed line), ECH-X3 power  $P_{X3}$  (red dashed line), and total ECH power  $P_{ECH}$  (black solid line).

point region where the larger flux expansion of the SF+ configuration results in a small modification of the plasma separatrix geometry. For comparison, the LCFS of the two configurations are shown in Fig. 4.12(c).

At the transition from SN to SF, which is visible in figure 4.13 by a change in the  $H_\alpha$  signal, the X-point  $X_2$  is moved towards the main X-point  $X_1$  by changing the currents in the poloidal coils. At the same time, the divertor recycling signal  $H_\alpha$  is significantly changed, figure 4.13. The ELM frequency  $\nu_{ELM}$  is 2-3 times lower and the ELM energy loss normalized by the total plasma energy increases by  $\sim 30\%$ . The energy confinement increases which, for constant input power, results in an increase of volume-integrated electron temperature  $T_{eV}$  by  $\sim 15\%$ , whilst the line-integrated density is kept constant.



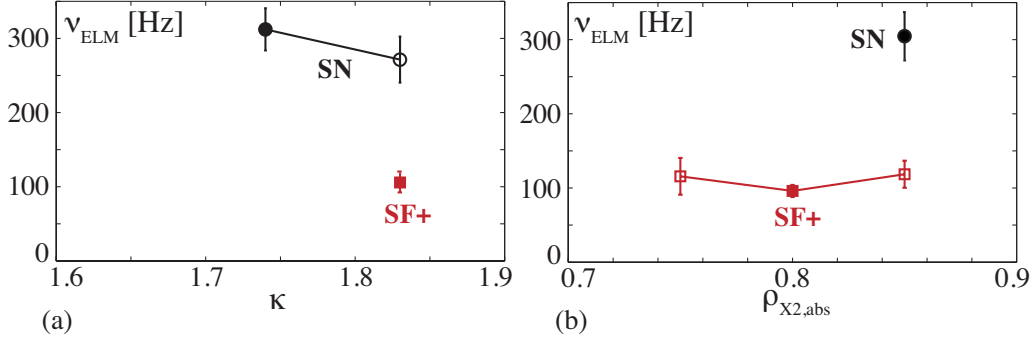


**Figure 4.14.:** ELM frequency variation as a function of (a) the plasma elongation and (b) the position of the X2 absorption for the SN (black) and the SF+ (red) configurations. The solid points represent the reference scenario.

Experiments investigating the dependence of ELM frequency and amplitude upon plasma elongation and ECH deposition location revealed that, within the uncertainty range, the difference of ELM behavior between both configurations is indeed due to the different null-point topology and not to the change in plasma elongation, figures 4.14(a) and (b).

#### 4.4.2. Edge pedestal properties

The temperature and density pedestal profiles were measured by Thomson scattering for the SN and the SF+ configurations. The edge profile data was taken from the last 20% ( $\sim 2$  ms for SF,  $\sim 1$  ms for SN) of the time interval before the ELM crash and fitted by a modified-tanh function, equation (3.6.1), and is shown in figure 4.15(a). No significant difference in the pedestal profiles is visible, except for a slightly steeper temperature gradient just inside the pedestal region and a slightly larger density pedestal width of the SF+ configuration. The pedestal quantities from profile fitting by equation (3.6.1) are given in table 4.5. We notify that the measured normalized pedestal gradient  $R/L_x$  exceeds the limits set by the spatial resolution of the edge Thomson scattering system (compare with table 3.1 in subsection 3.3.1). Therefore, the measured gradients are already affected by smoothing.

The safety factor and magnetic shear (here  $s = (\rho_{\text{vol}}/q) (dq/\rho_{\text{vol}})$ , where  $\rho_{\text{vol}}$  is the normalized radius calculated as  $\sqrt{V(\psi)/V_{\text{tot}}}$ ) is computed for the two configurations using CHEASE and is shown in Fig. 4.15(b). Inclusion of the collisional edge bootstrap current, calculated from the electron temperature and density profiles [13], decreases the edge safety factor from  $q_{\text{SF+}} = 7.5 \rightarrow 4.5$  and the edge magnetic shear from  $s_{\text{SF+}} = 124 \rightarrow 43$

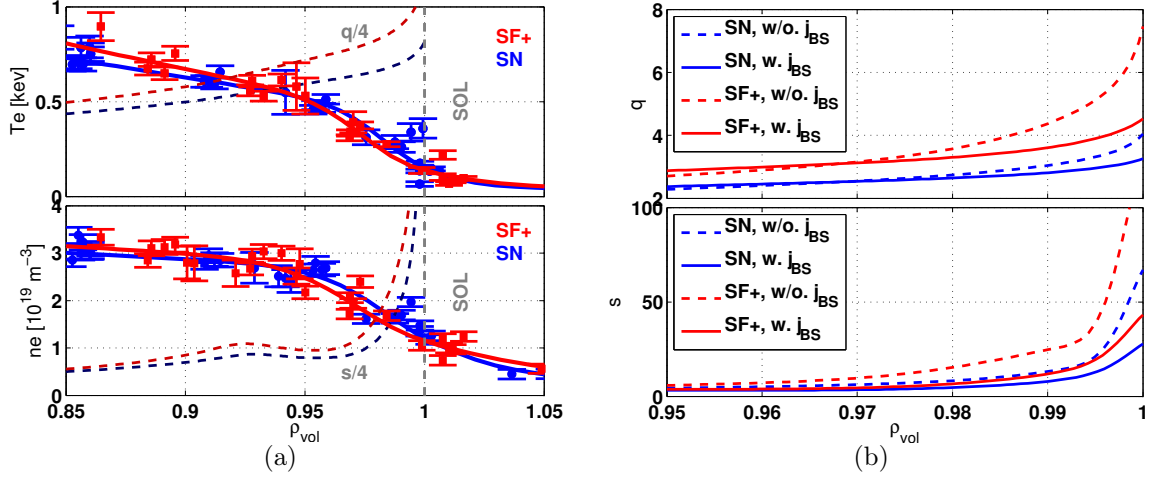


**Figure 4.15.:** (a) Electron temperature  $T_e$  and density  $n_e$  profiles for SN (blue) and SF+ (red) configuration as function of normalized radius  $\rho_{vol}$ . For comparison, the  $q/4$ - and  $s/4$ -profile including the edge bootstrap current calculated from the profiles are shown as dashed lines. (b) Safety factor  $q$  and magnetic shear  $s$  from equilibrium with ohmic profile only (dashed line) and including the bootstrap current (solid line) versus  $\rho_{vol}$  for SN (blue) and SF+ (red) configuration.

	SN	SF+
$T_{e,ped}$ [eV]	$465 \pm 40$	$480 \pm 80$
$\Delta T_e$ [mm]	$5.8 \pm 0.6$	$6.1 \pm 0.4$
$R_0/L_{Te}$	$290 \pm 50$	$275 \pm 45$
$n_{e,ped}$ [ $10^{19} \text{ m}^{-3}$ ]	$2.7 \pm 0.2$	$2.8 \pm 0.2$
$\Delta n_e$ [mm]	$8.6 \pm 0.6$	$9.8 \pm 0.6$
$R_0/L_{ne}$	$190 \pm 30$	$165 \pm 30$

**Table 4.5.:** Pedestal profile quantities of the SN and SF+ configuration: Electron temperature pedestal height  $T_{e,ped}$ , width  $\Delta T_e$  and normalized gradient  $R_0/L_{Te}$  and, respectively, the quantities of the electron density pedestal, where  $R_0 = 0.88$  m is the major radius.

for the SF+, and also decreases  $q_{SN} = 4.0 \rightarrow 3.3$  and  $s_{SN} = 67 \rightarrow 28$  for the SN. The SF+ configuration has  $\sim 1.4$  times higher magnetic shear and safety factor just inside the plasma separatrix and a slightly lower bootstrap current fraction.

The experimental profiles confirm the trends of assumptions taken earlier, which were presented in subsection 4.2.2. We remind that edge safety factor and edge magnetic shear,

when the bootstrap current is included, were  $q_{SF+} = 5.2$  and  $s_{SF+} = 57$  and  $q_{SN} = 5.7$  and  $s_{SN} = 31$  for the model equilibria. Although the absolute values differ, especially for the safety factor, the qualitative results are similar.

#### 4.4.3. MHD stability of the edge pedestal

An analysis of the stability of the plasma edge was undertaken to assess the nature of the ELMs for the two configurations. For the ideal MHD analysis, a conformal and perfectly conducting wall with  $r_w = 1.2$  was chosen to ensure good comparability of the results for the two configurations. The mode stability was computed on a grid with size  $N_\chi \times N_\psi = 320 \times 320$ ; the growth rate  $\gamma$  was extrapolated for infinite grid size assuming inverse quadratic convergence in  $\gamma$  as function of the grid size [36]. Figure 4.16 shows the MHD stability diagrams in the space of normalized parallel current density in the pedestal ( $J_{\parallel}/\langle J \rangle$ ) versus the normalized pressure gradient  $\alpha \equiv \mu_0 p' V' \sqrt{V/(2\pi^2 R_0)}/(2\pi^2)$  [72], where prime denotes  $d/d\psi$ .

The ballooning unstable region is marked by red crosses, its boundary by a thick solid red line. The external kink modes are represented by solid cyan lines with toroidal mode numbers  $n$ , added. High- $n$  external kink modes are stabilized by diamagnetic effects (section 2.3.3); the maximal number for unstable toroidal modes is  $n_{max} \sim 20$  for the SF+ and  $n_{max} \sim 25$  for the SN calculated by equation (2.3.17). The black square and cross represents the operational point obtained from the equilibrium including the bootstrap current density under the assumption of  $T_i = T_e$ . The ion temperature has been measured by Charge eXchange Recombination Spectroscopy (CXRS) near the plasma edge for similar discharges (see subsection 3.6.3). The ion density is scaled from  $n_e$  by equation (3.6.2) with  $Z_{eff} = 3$  from conductivity calculations and  $C^{6+}$  as single impurity. The uncertainties in the parameters of the operational point (square) are indicated by horizontal and vertical bars. The horizontal error bar is determined by progression of the uncertainty in the measurement of the edge electron pressure gradient into the total pressure gradient using above assumptions for the ion contribution. The vertical error bar represents the uncertainty in the bootstrap current estimation. The uncertainty in the ion contribution can only be estimated, since no appropriate ion pressure gradient measurements are available till today. The horizontal dashed line represents the limit for local reversal of the magnetic shear  $s$  near the edge. A diagonal dash-dotted line refers

configuration	$q_0$	$q_{95}$	$\kappa$	$\delta_{top}$	$\delta_{bot}$
SN	$\sim 1$	$\sim 2.3$	1.7	0.16	0.22
SF	$\sim 1$	$\sim 2.6$	1.8	0.16	0.28

**Table 4.6.:** Safety factor  $q$  and shape parameters elongation  $\kappa$ , upper and lower triangularity  $\delta_{top}$  and  $\delta_{bot}$  for SN and SF+ phase of discharge #39874.

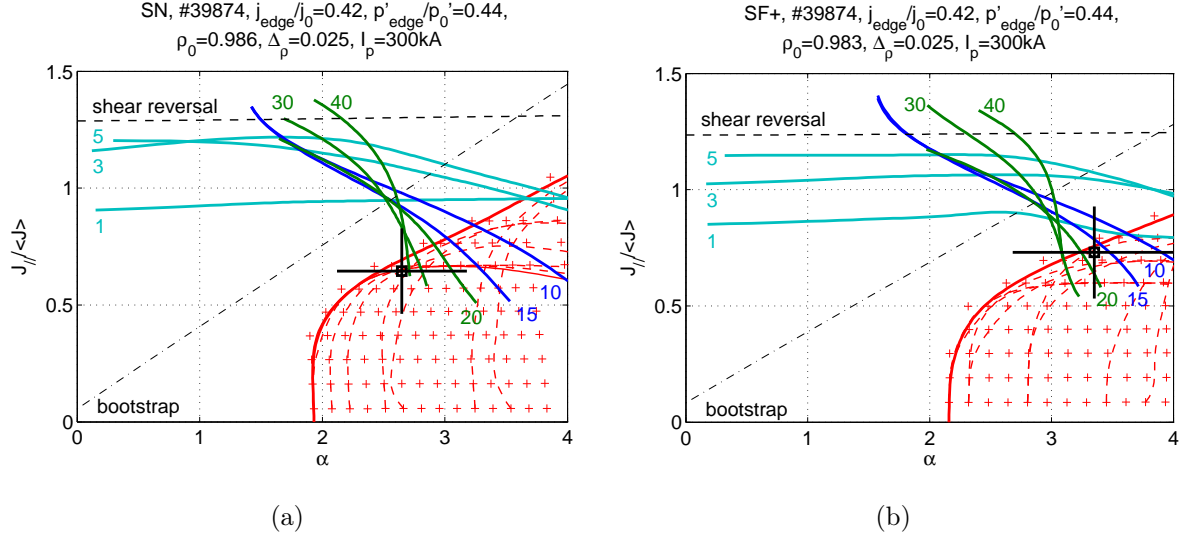


**Figure 4.16.:** Ideal MHD-stability maps of the edge pedestal for (a) the SN and (b) the SF+ phase of discharge #39874.

to the collisionless bootstrap current. Some representative plasma parameters of the SN and SF+ phases of discharge #39874 are given in table 4.6.

Figures 4.16(a) and 4.16(b) show that the second stability region is slightly larger for the SF+ configuration, i.e. coupled kink-ballooning modes at intermediate-high toroidal mode numbers are more stable, whereas low- $n$  modes are less stable. This is a general feature of SF configurations and was also confirmed when calculating the stability diagram with identical profiles (compare with subsection 4.2.3). The experimental point of the SF+ has  $\sim 20\%$  higher normalized pressure gradient ( $\alpha_{max}^{SN} \cong 2.6$  and  $\alpha_{max}^{SF+} \cong 3.1$ ). Furthermore, the ideal ballooning limit  $\alpha_{crit}$ , i.e. where  $J_{||}/\langle J \rangle = 0$ , is shifted towards higher  $\alpha$ 's for the SF+ ( $\alpha_{crit}^{SN} \cong 1.94$  and  $\alpha_{crit}^{SF+} \cong 2.16$ ). These differences are mainly caused by an increase in the term  $dV/d\psi$  in the expression for  $\alpha$ , which is due to the null-point topology. In the SF+, the poloidal magnetic field changes less quickly in a relatively large volume in the null-point region than in the SN.

It remains unclear if the improvement in edge stability of the SF+ is sufficient to

explain the difference in ELM characteristics between the two configurations. It may partly explain the increases in plasma energy and ELM energy loss which has been also observed in plasmas with stronger shaping, where the second ballooning stable region is also enlarged [25, 70, 73, 74]. However, it cannot give an explanation for the fundamental change in ELM frequency. It is also possible that small differences in the pedestal electron pressure gradient of both configurations are smoothed by the limited spatial resolution of the edge Thomson scattering diagnostic. Further improvements in the spatial resolution of the edge Thomson scattering system and measurement of the ion contribution are required to obtain a more accurate information about the edge pedestal.

## 4.5. Conclusion

In this chapter we addressed the MHD stability of the pedestal region in the SF diverted H-mode. The analysis of a set of equilibria revealed that an enhancement of pedestal stability is indeed possible in a SF configuration due to increased edge magnetic shear.

A study was performed to investigate the sensitivity of the analysis on the radial position of the maximum pressure gradient. It was found that the MHD limits strongly depend on the barrier position, whose exact determination from the experiment point of view is particularly challenging. In general, due to its higher magnetic shear in the edge, the snowflake remains the more stable configuration when radially shifting the edge barrier.

Plasma shaping has significant effects on the stability of the pedestal and needs to be taken into account when comparing different configurations. One may also want to use shaping to optimize the configuration in terms of pedestal characteristics, stability and ELM behavior.

Measurements in H-mode conditions revealed that there are no significant differences in the pedestal quantities between the SN and SF+ configuration. Even if the absolute values measured may suffer from smoothing, a comparison is still possible, since significant differences would be visible. More accurate measurements would be needed for verification.

The MHD stability calculations predict slightly more favorable limits for the pressure gradient in the case of the SF+. While a higher ELM energy loss in the SF+ may be explained by this result, it remains unclear what causes the fundamental change in ELM frequency.

# 5. H-mode scenarios in TCV

In this chapter we investigate the H-mode scenarios in TCV. The general H-mode pedestal and profile behavior is studied in a machine with dominant electron heating. A general survey of all the parameters, for which a possible scaling is extractable, is presented.

The ELM regimes are analyzed, the transition between type-III to type-I ELMs is described. The operational boundary of each ELM regime is shown and verified by ideal MHD stability simulations of the edge pedestal. Further, we analyze the edge pedestal properties as pedestal height, width and gradient and their influences on global plasma parameters and confirm the scaling of the pressure pedestal width as a function of normalized poloidal pressure. Finally, the dependence of pedestal properties upon plasma shaping is investigated and verified by ideal MHD stability calculations for the pedestal region.

We will note where results are obtained in agreement or disagreement with previous publications and where data is not sufficient to test the current view.

## 5.1. H-mode regimes with type-III, large and type-I ELMs

On TCV, the L- to H-mode transition can be achieved by Ohmic heating alone. A stable ELMy H-mode discharge is sustained by ohmic power only within a narrow parameter space: the line-integrated density  $n_{el} \sim 2.5 - 4.5 \times 10^{19} \text{ m}^2$ , ohmic power  $P_{ohm} \approx 500 \text{ kW}$ , safety factor  $2 < q_{95} < 4$  (at 95% normalized poloidal flux radius), plasma elongation  $1.6 \leq \kappa \leq 1.8$  and triangularity  $0.2 \leq \delta \leq 0.5$ .

In the past, the lack of additional heating power limited initially the operational space, but also made a study of pedestal and ELM properties as a function of heating power

Parameter	SN	SF-like SN and SF+
$I_p$ [kA]	330 – 480	230 – 320
$q_0$	0.7 – 1.1	0.7 – 1.5
$q_{95}$	1.8 – 2.3	1.9 – 2.7
$n_{el}$ [ $10^{19}\text{m}^{-2}$ ]	2.6 – 5.4	1.9 – 6.7
$n_{e,ped}$ [ $\text{m}^{-3}$ ]	2.4 – 4.7	1.5 – 5.4
$T_e(0)$ [keV]	0.8 – 3.2	0.7 – 4.5
$T_{e,ped}$ [keV]	0.2 – 0.7	0.2 – 0.8
$P_{ECH,nom.}$ [MW]	0 – 2.0	0 – 2.9
$\nu_{ped}^*$	0.35 – 2.70	0.12 – 10
$\kappa$	1.50 – 1.90	1.65 – 1.95
$\delta$	0.15 – 0.62	0.17 – 0.26
$\delta_{top}$	–0.30 – 0.40	0.13 – 0.22
$\delta_{bot}$	0.55 – 0.85	0.16 – 0.36
$\lambda_{top}$	0 – 0.15	0

**Table 5.1.:** H-mode plasma parameters for single null (SN), snowflake plus (SF+) and SF-like SN configurations: Plasma current  $I_p$ , safety factor  $q_0$  and  $q_{95}$ , line-integrated electron density  $n_{el}$ , central electron temperature  $T_e(0)$ , pedestal electron density  $n_{e,ped}$ , temperature  $T_{e,ped}$  and collisionality, nominal EC-heating power  $P_{ECH,nom.}$ , plasma shaping parameters elongation  $\kappa$ , total  $\delta$ , upper and lower triangularity  $\delta_{top}$  and  $\delta_{bot}$  and upper squareness  $\lambda_{top}$ .

impossible. With the availability of electron cyclotron heating at the 3rd harmonic, which can efficiently heat the high density H-mode discharges, a more thorough investigation of the H-mode properties in presence of plasma heating became possible.

This section addresses the classification of observed ELM types, discusses the role of the heating power on ELM energy loss, on pedestal properties and on the operational boundary and verifies pedestal scaling models. The analysis is based on H-mode discharges with a parameter space listed in table 5.1. In the following, we make a distinction between SN and SF or SF-like configurations for the reason that latter had, besides X3-heating, additional X2-heating in the plasma edge at the normalized poloidal flux radius  $\rho_{abs} \approx 0.9 - 0.95$ . This feature is unique to these configurations because of their edge density below the X2 cut-off and their vertical position being advantageously for

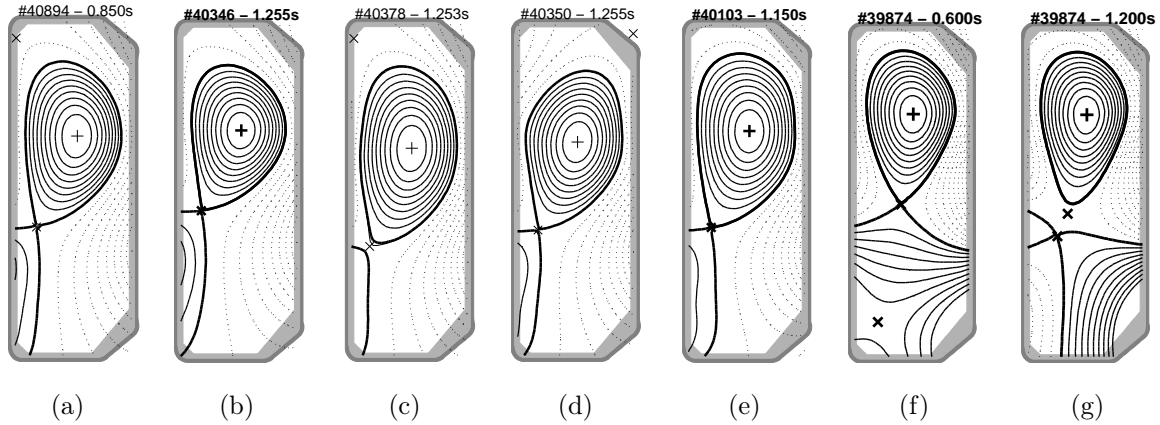


**Figure 5.1.:** H-mode plasma shapes and their symbolic representation in figures: (a) standard single null (SN) configuration with elongation  $\kappa \sim 1.7$ , upper triangularity  $\delta_{top} = 0.23$  and upper squareness  $\lambda_{top} = 0$  [■]. (b) SN with  $\kappa \sim 1.5$  [■] and (c) with  $\kappa \sim 1.9$  [■], where  $\delta_{top} = 0.23$  and  $\lambda_{top} = 0$ . (d) SN with  $\delta_{top} = -0.25$  [◄], (e) with  $\lambda_{top} = 0.15$ , (f) Snowflake-like single-null (SF-like SN) [•] and (g) snowflake plus (SF+) [▼].

the mid-plane X2-launcher. For the figures, the following identification of the magnetic configurations is kept throughout the chapter, if more than one configuration is shown at the same time: ■ single-null (SN) with  $\delta_{top} > 0$  and  $\kappa = 1.5 - 1.9$ , ◄ SN with  $\delta_{top} < 0$  and  $\kappa = 1.7$ , ▼ snowflake plus (SF+) and • snowflake-like single-null (SF-like SN).

### 5.1.1. Influence of the input power on the ELM characteristics

On TCV, the typical type-III ELM frequency is  $f_{ELM} \sim 100 - 300$  Hz with ELM power loss normalized to the total plasma energy  $\Delta W_{ELM}/W_{tot} \sim 7 - 2\%$  using the diamagnetic loop, respectively, figure 5.2. This class of ELMs occurs for heating power  $P_{tot} < 0.8$  MW, where  $P_{tot} = P_{ohm} + P_{ECH}$  with  $P_{ohm}$  the ohmic and  $P_{ECH}$  the absorbed EC-heating power. Observation of their frequency as a function of  $P_{tot}$  show a slowdown when increasing  $P_{tot}$  while their ELM amplitude increases. This is consistent with the accustomed definition  $df_{ELM}/dP_{sep} < 0$  [15], where  $P_{sep}$  is the power crossing the separatrix (see subsection 2.2.1). Above this power threshold one enters the region where large ELMs occur with  $f_{ELM} \sim 100 - 35$  Hz and  $\Delta W_{ELM}/W_{tot} \sim 8 - 25\%$ , where an increase in heating power leads to a decrease in ELM frequency. Further increase in heating power accelerates the ELM frequency, ranging between 35–300 Hz, and decreases the normalized ELM power loss  $\Delta W_{ELM}/W_{tot} \sim 25 - 10\%$ , respectively, which is consistent with the definition



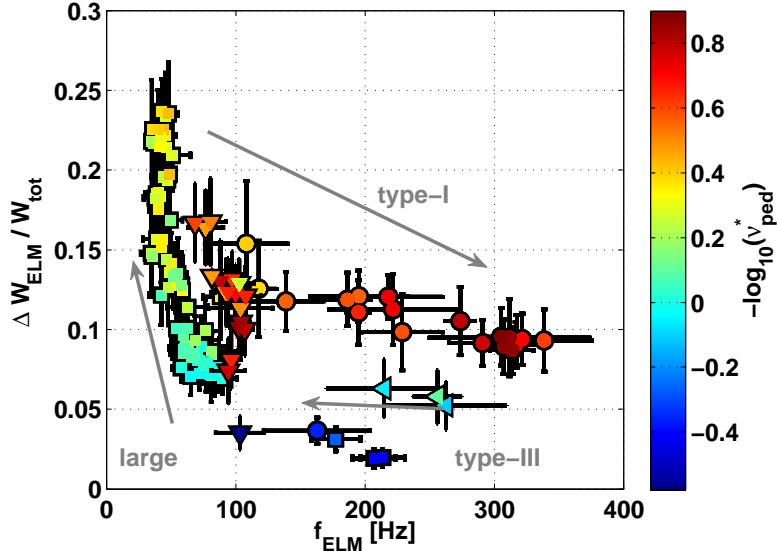


**Figure 5.2.:** ELM energy loss versus ELM frequency: ELM energy loss  $\Delta W_{ELM}$  normalized by total plasma energy  $W_{tot}$  versus the ELM frequency  $f_{ELM}$ , resolved by the logarithmic collisionality  $\nu_{ped}^*$  at the pedestal top.

$df_{ELM}/dP_{sep} > 0$  of type-I ELMs. Figure 5.3 shows examples of the divertor recycling signal,  $D_\alpha$  emission, for H-mode discharges with different EC-heating power. Also given is the time averaged ELM frequency  $f_{ELM}$  and the ELM energy loss normalized to the total plasma energy  $\Delta W_{ELM}/W_{tot}$ .

The ELM frequency is plotted in figure 5.4 as a function of the reciprocal normalized pedestal collisionality  $\nu_{ped}^*$ , which is a rough measure of the heating power  $P_{tot}$ . The normalized pedestal collisionality is defined by  $\nu_{ped}^* = 10^{-14} Z_{eff} R_0 n_{e,ped} T_{e,ped}^{-2}$  [75], where  $Z_{eff} = 3$  and  $n_{e,ped}$  and  $T_{e,ped}$  are electron density and temperature at the top of the pedestal.

We observe the typical type-III ELM behavior below a total absorbed power threshold of approximately 0.8 MW. The strong variations in  $f_{ELM}$  in this region may be ascribed to different plasma properties, shapes, SN and SF+ divertor. When exceeding the power threshold, a speed-up of  $f_{ELM}$  is observed, followed by a separation in ELM behavior of the SF+ and SF-like SN divertor configuration.

Interesting is the clear separation between SF+ and SF-like SN configuration while heating power increases. The ELMs are less frequent in the SF+ than in a comparable SN configuration. This seems to be linked to the improved edge pedestal stability properties of the SF+ configuration caused by higher magnetic shear in the edge [21, 71]. Pedestal measurements by Thomson scattering in comparable SF+ and SF-like SN discharges,

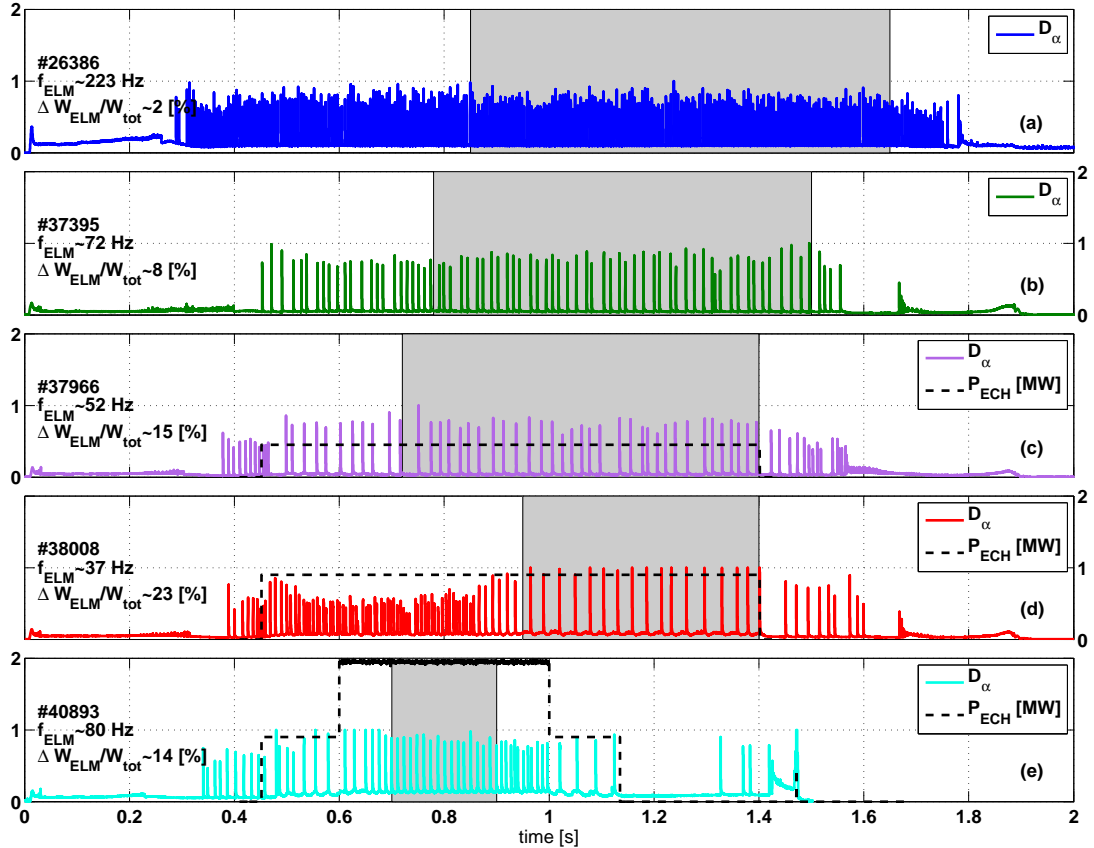


**Figure 5.3.:** Examples of normalized  $D_\alpha$  emission: a) resistive type-III ELMs (unfavorable ion  $\mathbf{B} \times \nabla \mathbf{B}$  drift), b) type-III ELMs close to ideal ballooning limit, c) type-III ELMs with additional EC-heating of  $P_{ECH} \sim 0.5$  MW (X3-only), d) large ELMs at  $P_{ECH} \sim 1.0$  MW (X3-only, change in ELM frequency and amplitude for  $t < 0.9$  s is caused by an increase in density) and e) type-I ELMs at  $P_{ECH} \sim 2.0$  MW (X3+O2). The gray box represents the time interval in which averaged ELM frequency  $f_{ELM}$  and relative ELM energy loss  $\Delta W_{ELM}/W_{tot}$  were computed.

however, did not reveal significant differences in the edge pedestal height, width and gradient (see subsection 4.4.2) requiring further studies to clarify this issue.

Another way to represent the data is to plot the ELM energy loss normalized to the total plasma energy,  $\Delta W_{ELM}/W_{tot}$ , and the fractional power loss per ELM,  $\Delta W_{ELM} \times f_{ELM}/P_{tot}$  as a function of the pedestal collisionality, figure 5.5. The relative ELM energy loss increases gradually with decreasing pedestal collisionality, figure 5.5(a). Large ELMs occur at  $\nu_{ped}^* \sim 1$  ( $-\log(\nu_{ped}^*) \sim 0$ ) indicating the region of transition between type-III and type-I ELMs. The ELM amplitude decreases for  $\nu_{ped}^* < 0.5$  ( $-\log(\nu_{ped}^*) > 0.3$ ). No

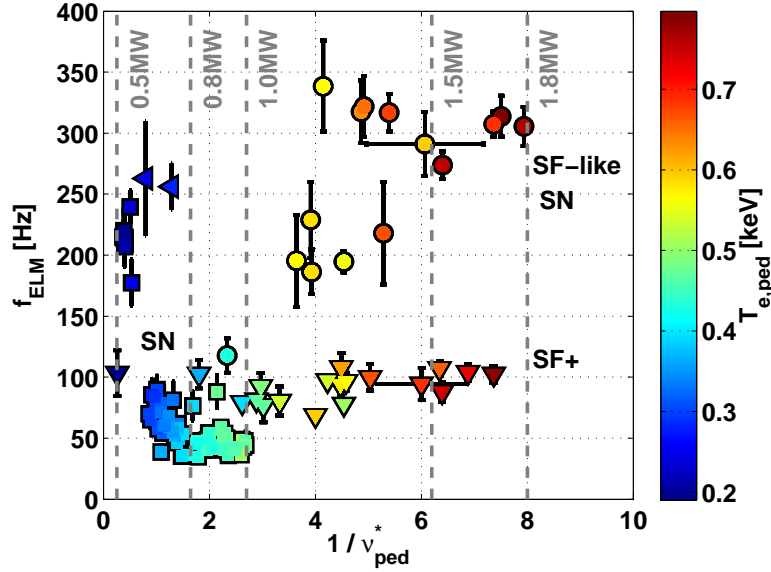


**Figure 5.4.:** ELM frequency versus reciprocal collisionality: ELM frequency  $f_{ELM}$  averaged over the stationary ELM phase of each discharge; collisionality  $\nu_{ped}^*$  computed from the edge pedestal fit of  $T_e$  and  $n_e$  of the stationary ELM phase, resolved by the pedestal top electron temperature  $T_{e,ped}$ . Grey dashed line represent approximately the absorbed ECH power. At low  $\nu_{ped}^*$ , i.e. high ECH power, we observe the typical type-I ELM behavior, however, more pronounced in the SF-like SN than SF+ configuration.

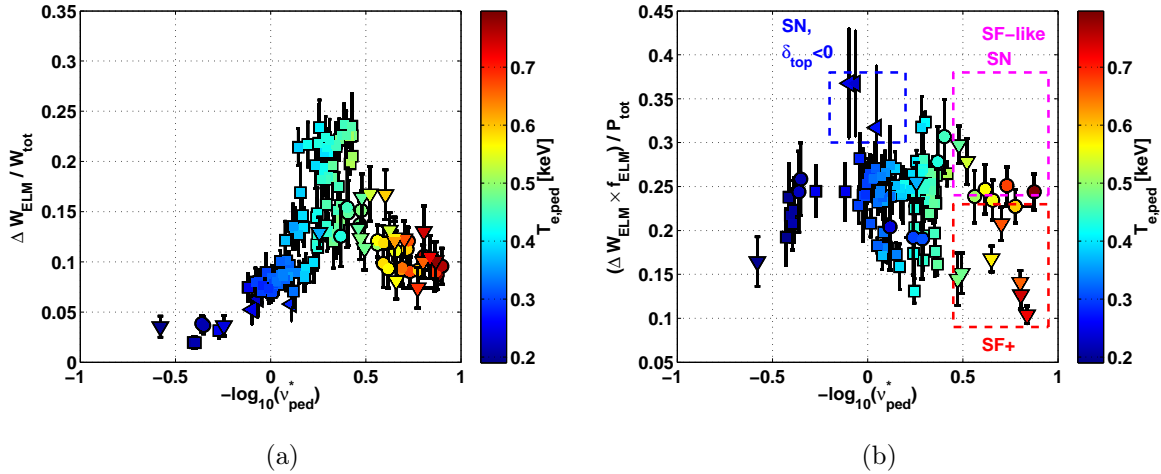


**Figure 5.5.:** Fractional power loss per ELM: (a) Energy loss per ELM normalized to the total plasma energy and (b) fractional power loss per ELM,  $\Delta W_{ELM} \times f_{ELM} / P_{tot}$ , versus the logarithmic pedestal collisionality, resolved by the electron temperature  $T_{e,ped}$  at the pedestal top.

striking difference can be seen between the two magnetic configurations, SF+ and SF-like SN.

The fractional power loss per ELM, figure 5.5(b), remains approximately constant at  $\sim 25\%$  over a large range of  $\nu_{ped}^* = 0.5 - 4$ . Note that the large scatter in the data is introduced by the normalization of the ELM power loss by the absorbed total power  $P_{tot} = P_{ohm} + P_{ECH}$ , where uncertainties are large for  $P_{ECH}$ . For low pedestal collisionality,  $\nu_{ped}^* < 0.5$ , we observe a separation of SF+ and SF-like SN discharges. Discharges with SN divertor remain at ratios of  $\sim 25 - 35\%$ , while SF+ diverted discharges have a reduced power loss per ELM, ranging between  $\sim 10 - 25\%$ . This behavior is due to the very different ELM frequency of both configurations at high ECH power, whilst the ELM size in both configurations is somewhat comparable.

The ELM frequency increases gradually with power in the case of the SN, while it increases only little or even saturates at  $\sim 100$  Hz in the case of the SF+. Therefore, the normalized ELM power loss in the SF+ is lowered by  $10 - 15\%$  with respect to the SN at the same total absorbed power (see also figure 5.4). The reason for this behavior is still unclear.

### 5.1.2. Operational boundary in pedestal region in ELMy H-mode plasmas

The classification of ELM behavior as a function of the pedestal properties, i.e. in the space of pedestal density  $n_{e,ped}$  and pedestal  $T_{e,ped}$ , provides some insight into the operational domain. The electron temperature and density profiles were measured by Thomson scattering. The inter-ELM edge profiles of the whole stationary ELMy phase were averaged and fitted by a modified hyper-tangent function, equation (3.6.1). The pedestal heights are shown in figure 5.6 together with the ideal MHD stability limits of the pedestal region described by  $p_{e,ped} \sim const.$  contours obtained from an approximation of the critical normalized pressure gradient  $\alpha$  for large- $n$  ballooning and intermediate- $n$  kink modes.

The normalized pressure gradient is obtained from edge pedestal stability calculations (see subsection 5.3.3). The critical values for ballooning stability,  $\alpha_b = 2.75$ , and intermediate- $n$  kink stability for SN,  $\alpha_{k,SN} = 4.0$ , and SF+,  $\alpha_{k,SF} = 4.9$ , configuration have been found to represent well the chosen class of plasma parameters ( $\kappa \sim 1.7$ ,  $\delta_{top} > 0$ ,  $\lambda_{top} \sim 0$ ,  $q_{95} \sim 2.5$ ). In order to compute the stability limit contour in the  $n - T$  space, the cylindrical approximation  $\alpha_{cyl} \equiv -2\mu_0 R_0 (q^2/B_0^2) dp/dr$  was used, where  $R_0$  is the

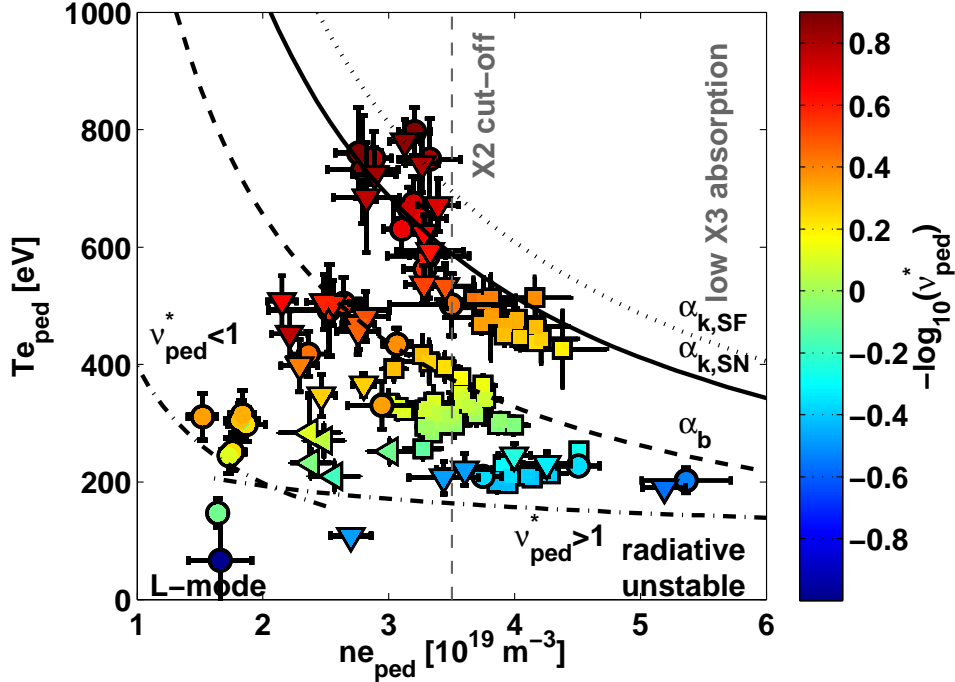


**Figure 5.6.:** Operational boundary in pedestal region: The H-mode threshold, Alfvén drift wave stability, is shown as dashed-pointed line. The limit of the critical normalized pressure gradient for ballooning modes,  $\alpha_b$ , is represented by the dashed line. External kink mode stability limits,  $\alpha_k$ , are depicted by the solid line for SN and by the dotted line for SF+ and SF-like SN shots.

major plasma radius,  $q$  the safety factor,  $B_0$  the toroidal field and  $dp/dr$  the pressure gradient. We assume  $p_e \approx p_i$  and use for the sake of generality  $q = 2.5$ ,  $B_0 = 1.43$  T and  $dp/dr \approx p/\Delta_r$  with  $\Delta_r = 10$  mm as width of the pedestal. Note that these assumptions do not necessarily hold for all discharges, as will be shown in subsections 5.1.3 and 5.1.4.

The Alfvén drift wave stability boundary, equations (2.2.4) and (2.2.3), is shown as dash-dotted line for both approximations,  $\nu_{ped}^* \geq 1$ . Below this boundary, discharges remain in L-mode, at the boundary we observe L-H mode dithering. Above the boundary, type-III ELMs occur, whose pedestal temperature is low ( $T_{e,ped} \sim 200$  eV). They are characterized by their high ELM frequency  $f_{ELM} \sim 180 - 300$  Hz with relatively low normalized power loss per ELM  $\Delta W_{ELM}/W_{tot} \sim 2 - 5\%$ . These discharges are distinguished by  $P_{tot} \gtrsim P_{thresh}$ , which is often the case for ohmic discharges where the ion  $\mathbf{B} \times \nabla \mathbf{B}$  drift points away from the X-point.

In configurations with favorable ion drift, i.e. ion drift towards the X-point, and ohmic heating, where  $P_{tot} > P_{thesh}$  and  $T_{e,ped} \sim 250 - 400$  eV, we enter the region

where the pedestal pressure gradient is limited by ideal ballooning modes, represented as  $\alpha_b$  (see also section 6.3). The ELMs are of type-III with  $f_{ELM} \sim 70 - 100$  Hz and  $\Delta W_{ELM}/W_{tot} \sim 8 - 12\%$ . Adding additional ECH power increases further  $T_{e,ped}$  to values ranging in between  $400 - 500$  eV, approaching the external kink stability limit. The ELM frequency decreases to  $\sim 40$  Hz, their amplitude increases up to values of  $\Delta W_{ELM}/W_{tot} \sim 20 - 25\%$  (large ELMs). Further increasing the ECH power, type-I ELMs occur, where the pedestal is limited by current-driven modes represented as  $\alpha_{k,SN}$ . The ELM frequency increases with power,  $f_{ELM} \sim 40 \rightarrow 350$  Hz, and their amplitude decreases,  $\Delta W_{ELM}/W_{tot} \sim 25 \rightarrow 10\%$ .

The edge temperature for type-III ELMs appears to be independent of the density at high values of pedestal density,  $n_{e,ped} \geq 3.5 \times 10^{19} \text{ m}^{-3}$ , and follows a  $n \times T = const.$  curve at low density. This may be explained by change in the underlying physics due to the transition from resistive to ideal type-III ELMs at lower collisionality.

The limit of  $p_{ped}$  associated with type-I ELMs generally correspond to a hyperbolic curve in  $n - T$  space [17] and is represented by the  $\alpha_{k,SN}$ -limit in figure 5.6. We observe that the increase of  $n_{e,ped}$  accompanies the decrease of  $T_{e,ped}$ , as effect of the increasing collisionality, so that the pedestal pressure  $p_{e,ped}$  and hence the kinetic energy stored in the pedestal are kept constant. This is due to the fact that the limitation of  $p_{ped}$  is imposed by the destabilization of type-I ELMs.

### 5.1.3. Properties of the electron pedestal parameters

We want to study the impact of additional EC-heating on the pedestal height, width and maximum gradient. Since we have to face important uncertainties in the determination of the absorbed X3-power (see subsection 1.2.2), we use pedestal temperature and collisionality as a measure of total input power. The absorbed X3-power increases with increasing temperature and is maximal at central electron densities of  $4 - 6 \times 10^{19} \text{ m}^{-3}$  (corresponds to  $n_{e,ped} \sim 3 - 4.5 \times 10^{19} \text{ m}^{-3}$ ). Here, we concentrate on the electron temperature and density pedestal only and want to describe their trends, independently of their underlying physics, as polynomial of 1st order and as power law. A more complete analysis including physical models is presented in subsection 5.1.4, where the scaling of the pressure pedestal width with the normalized poloidal pressure  $\beta_\theta$  [33] is analyzed. The following analysis includes pedestal measurements from 115 H-mode discharges in single-null configuration with various plasma shaping, whose plasma parameters are given in table 5.1. Note that

the SF-like SN and SF configurations are excluded from this analysis because of the fact that pedestal properties may be affected by the X2-heating in the pedestal region.

### Electron temperature pedestal

Figure 5.7 shows the normalized electron temperature pedestal width  $\Delta_{T_e}/R_0$  and maximum pedestal gradient  $\nabla_{T_e}$  as a function of the electron pedestal temperature height  $T_{e,ped}$  and density height  $n_{e,ped}$ , where  $R_0$  is the major radius. Figures 5.7(a) and 5.7(b) indicate that  $\Delta_{T_e}/R_0$  scales differently for low and high pedestal collisionality  $\nu_{ped}^*$ . We observe the following tendencies:

- for  $\nu_{ped}^* > 0.6$  ( $-\log(\nu_{ped}^*) < 0.2$ ),  $\Delta_{T_e}/R_0$  increases weaker than linearly as a function of  $T_{e,ped}$  ( $1/L_{T_e}$  increases faster than  $T_{e,ped}$ ) and decreases weakly as a function of  $n_{e,ped}$
- for  $\nu_{ped}^* < 0.6$  ( $-\log(\nu_{ped}^*) > 0.2$ ),  $\Delta_{T_e}/R_0$  decreases strongly as a function of  $T_{e,ped}$  (fast increase in  $1/L_{T_e}$ ) and increases as a function of  $n_{e,ped}$
- $\Delta_{T_e}/R_0$ 's of the discharges with negative upper triangularity ( $\delta_{top} < 0$ ) are clearly separated from discharges with  $\delta_{top} > 0$

Figures 5.7(c) and 5.7(d) show the same bifurcation in  $\nabla_{T_e}$  for the two different collisionality regimes  $\nu_{ped}^* \gtrless 0.6$  as was found for  $\Delta_{T_e}/R_0$ :

- for  $\nu_{ped}^* > 0.6$  ( $-\log(\nu_{ped}^*) < 0.2$ ),  $\nabla_{T_e}$  increases weaker than linearly as a function of  $T_{e,ped}$  ( $1/L_{T_e}$  decreases weakly) and is a linear function of  $n_{e,ped}$
- for  $\nu_{ped}^* < 0.6$  ( $-\log(\nu_{ped}^*) > 0.2$ ),  $\nabla_{T_e}$  strongly increases with  $T_{e,ped}$  ( $1/L_{T_e}$  increases) and strongly decreases with  $n_{e,ped}$ , i.e.  $1/L_{T_e}$  is maximal at low collisionality

The results from the polynomial and power law scaling of  $\Delta_{T_e}/R_0$  and  $\nabla_{T_e}$  as a function of  $T_{e,ped}$  and  $n_{e,ped}$  for  $\nu_{ped}^* \gtrless 0.6$  are listed in table 5.2.

### Electron density pedestal

Figure 5.8 shows the normalized electron density pedestal width  $\Delta_{ne}/R_0$  and maximum pedestal gradient  $\nabla_{ne}$  as a function of  $T_{e,ped}$  and  $n_{e,ped}$ . Figures 5.8(a) and 5.8(b) show that  $\Delta_{ne}/R_0$  scales similarly for low and high pedestal collisionality  $\nu_{ped}^*$ :  $\Delta_{ne}/R_0$  increases

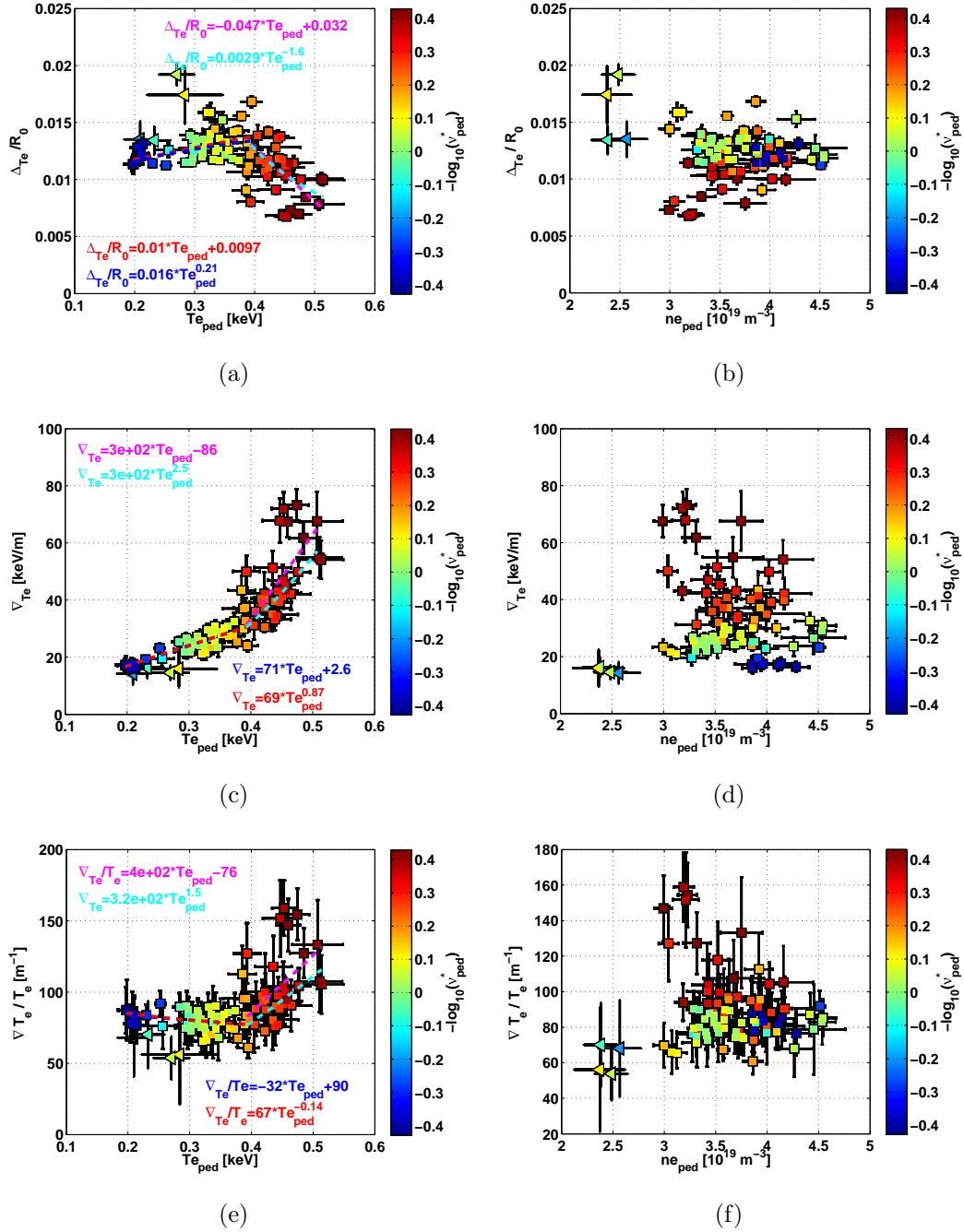


**Figure 5.7.:** Electron temperature pedestal properties: Normalized temperature pedestal width  $\Delta/R_0$  as a function of (a) pedestal temperature height  $T_{e,ped}$  and (b) pedestal density height  $n_{e,ped}$ . Maximum temperature pedestal gradient  $\nabla_{Te}$  as a function of (c)  $T_{e,ped}$  and (d)  $n_{e,ped}$ . The inverse temperature gradient scale length  $\nabla T_{e,ped}/T_{e,ped}$  as function of (e)  $T_{e,ped}$  and (f)  $n_{e,ped}$ .



	$\nu_{ped}^*$	linear regression	power law
$\Delta_{T_e}/R_0(T_{e,ped})$	$> 0.6$	$+0.10T_{e,ped} + 0.01$	$0.015T_{e,ped}^{0.2}$
$\Delta_{T_e}/R_0(T_{e,ped})$	$< 0.6$	$-0.05T_{e,ped} + 0.03$	$0.003T_{e,ped}^{-1.6}$
$\Delta_{T_e}/R_0(n_{e,ped})$	$0.3 - 3.0$	n.a.	n.a.
$\nabla_{T_e}(T_{e,ped})$	$> 0.6$	$+70T_{e,ped} + 3$	$70T_{e,ped}^{0.9}$
$\nabla_{T_e}(T_{e,ped})$	$< 0.6$	$+300T_{e,ped} - 90$	$300T_{e,ped}^{2.5}$
$\nabla_{T_e}(n_{e,ped})$	$0.3 - 3.0$	n.a.	n.a.
$\nabla T_{e,ped}/T_{e,ped}(T_{e,ped})$	$> 0.6$	$-32T_{e,ped} + 90$	$70T_{e,ped}^{-0.15}$
$\nabla T_{e,ped}/T_{e,ped}(T_{e,ped})$	$< 0.6$	$400T_{e,ped} - 80$	$320T_{e,ped}^{1.5}$
$\nabla T_{e,ped}/T_{e,ped}(n_{e,ped})$	$0.3 - 3.0$	n.a.	n.a.

**Table 5.2.:** Temperature pedestal width  $\Delta_{T_e}/R_0$  and gradient  $\nabla_{T_e}$  as a function of pedestal temperature  $T_{e,ped}$  and density  $n_{e,ped}$ . Dependencies are fitted by 1st order polynomials and power law for  $\nu_{ped}^* \geq 0.6$ . Errors in the fit coefficients are below 10%.

weakly or is constant as a function of  $n_{e,ped}$  ( $1/L_{ne}$  increases) and increases as a function of  $T_{e,ped}$ . The data does not satisfy the model which predicts that  $\Delta_{ne}$  is proportional to the characteristic neutral penetration depth and that the relation  $\Delta_{ne} \propto 1/n_{e,ped}^{3/2}$ , equation (2.2.18), should be approximately obeyed. Figures 5.8(c) and 5.8(d) show the dependence of  $\Delta_{ne}/R_0$  and  $\nabla_{ne}$  as a function of  $n_{e,ped}$  and  $T_{e,ped}$ :

- $\nabla_{ne}$  increases either linearly or more than linear with  $n_{e,ped}$  ( $1/L_{ne}$  increases)
- $\nabla_{ne}$  generally decreases with  $T_{e,ped}$ :
  - discharges with negative upper triangularity have small  $\nabla_{ne}$  indicating deterioration of the pedestal
  - discharges in unfavorable ion drift directed away from the X-point exhibit stronger density gradients than in favorable ion drift which is due to their high  $n_{e,ped}$  and relatively small  $\Delta_{ne}/R_0$
  - $\nabla_{ne}$  may be nearly constant for  $\nu_{ped}^* \sim 0.6 \rightarrow 2.0$  ( $-\log(\nu_{ped}^*) \sim 0.2 \rightarrow -0.4$ ) and standard parameters ( $\delta_{top} > 0$ , favorable ion  $\mathbf{B} \times \nabla \mathbf{B}$  drift) and slightly decreasing for  $\nu_{ped}^* < 0.6$

The polynomial and power law scaling of  $\Delta_{ne}/R_0$  and  $\nabla_{ne}$  as a function of  $T_{e,ped}$  and  $n_{e,ped}$  for  $\nu_{ped}^* \sim 0.3 \rightarrow 3.0$  are listed in table 5.3.

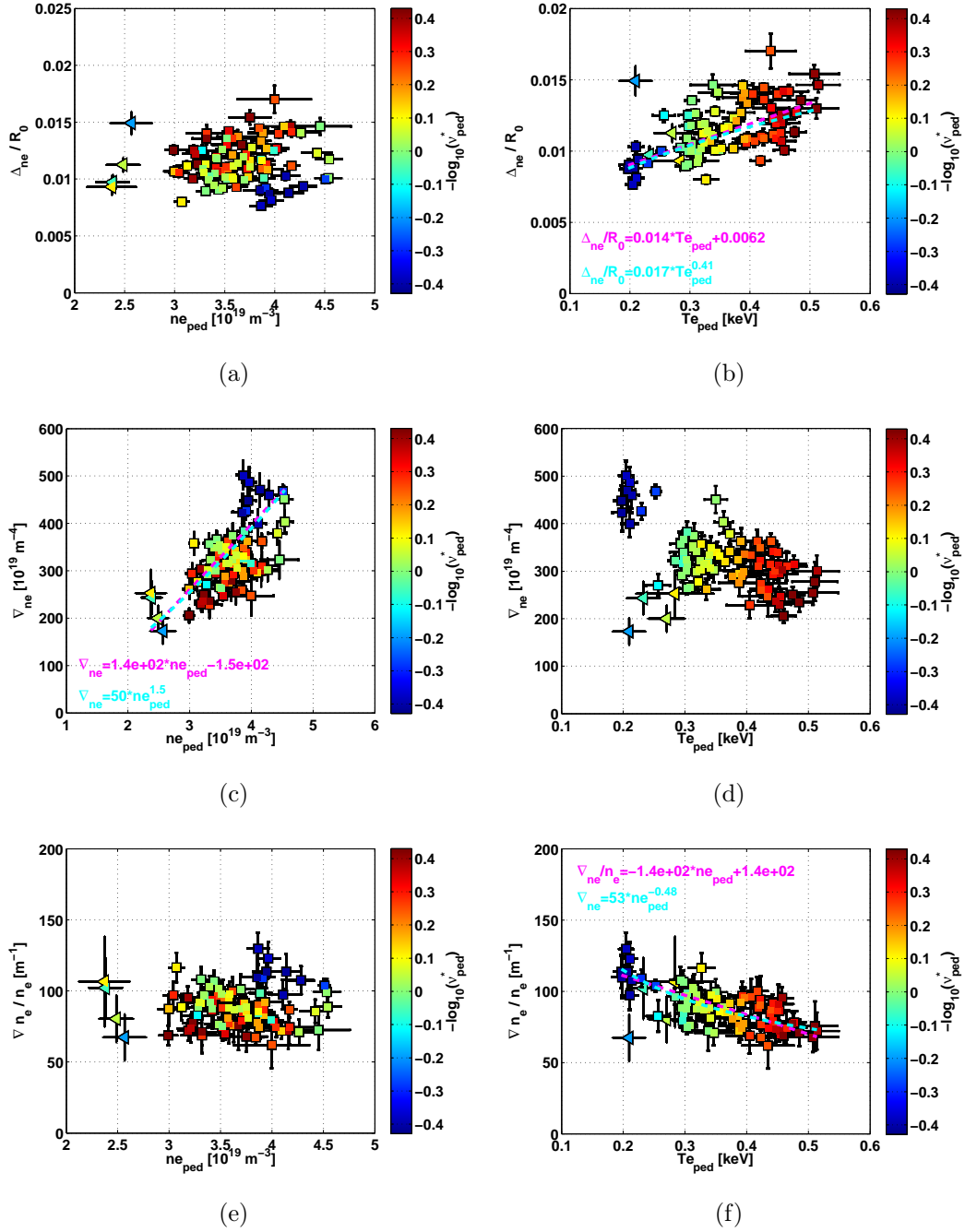


**Figure 5.8.:** Electron density pedestal properties: Normalized density pedestal width  $\Delta/R_0$  as a function of (a) pedestal temperature height  $T_{e,ped}$  and (b) and pedestal density height  $n_{e,ped}$ . Maximum density pedestal gradient  $\nabla_{ne}$  as a function of (c)  $T_{e,ped}$  and (d)  $n_{e,ped}$ . The inverse density gradient scale length  $\nabla_{ne,ped}/n_{e,ped}$  as function of (e)  $n_{e,ped}$  and (f)  $T_{e,ped}$

	$\nu_{ped}^*$	linear regression	power law
$\Delta_{ne}/R_0(n_{e,ped})$	0.3 – 3.0	n.a.	n.a.
$\Delta_{ne}/R_0(T_{e,ped})$	0.3 – 3.0	n.a.	n.a.
$\nabla_{ne}(n_{e,ped})$	0.3 – 3.0	$+140n_{e,ped} - 160$	$50n_{e,ped}^{1.5}$
$\nabla_{ne}(T_{e,ped})$	0.3 – 3.0	n.a.	n.a.
$\nabla n_{e,ped}/n_{e,ped}(n_{e,ped})$	0.3 – 3.0	$-140n_{e,ped} - 150$	$50n_{e,ped}^{-0.5}$
$\nabla n_{e,ped}/n_{e,ped}(T_{e,ped})$	0.3 – 3.0	n.a.	n.a.

**Table 5.3.:** Density pedestal width  $\Delta_{ne}/R_0$  and gradient  $\nabla_{ne}$  as a function of pedestal temperature  $T_{e,ped}$  and density  $n_{e,ped}$  fitted by 1st order polynomials and power law. Errors in the fit coefficients are below 10%.

The bifurcation of the trends in the  $T_e$  pedestal takes places in the range of  $\nu_{ped}^* \sim 0.6 \rightarrow 0.8$  where the transition from the type-III to type-I ELM regime occurs (see subsection 5.1.2, figure 5.6). In contrary, the density pedestal seems to be less affected by this transition or more generally by the pedestal collisionality. Only in the case of  $\nabla_{ne}$  we have indications of different behavior for discharges with  $\delta_{top} < 0$  and high pedestal collisionality (unfavorable ion  $\mathbf{B} \times \nabla \mathbf{B}$  drift).

In general, the pressure pedestal width  $\Delta_p$  is expected to scale with the ion Larmor radius as  $\Delta_p/R_0 \propto \rho_i^\gamma$ , where  $\gamma = \{1, 1/2, 2/3\}$  is an exponent different for the respective model (see also chapter 2, subsection 2.2.3). Since we have  $\rho_i \propto T_i^{1/2}$  at constant toroidal magnetic field, the pedestal width should increase with the pedestal temperature, which is observed for the case of the electron density profile. In DIII-D H-mode discharges, both in the initial ELM-free and in the later inter-ELM phase, it was found that  $\Delta_{ne} \propto T_{e,ped}^{1/2}$  [69, 76], however, with the width measured in normalized poloidal flux. The exponent  $\sim 2/5$  found for the TCV discharges is rather close to 1/2.

One would expect that the above mentioned arguments should also explain to some extent the behavior of the electron temperature width. This could be partly true for  $\nu_{ped}^* > 0.6$ , however, an inverse trend of  $\Delta_{Te}$  as a function of  $T_{e,ped}$  is seen for  $\nu_{ped}^* < 0.6$ . It is not clear whether this effect can be only attributed to the transition from type-III to type-I ELM regime at  $\nu_{ped}^* \sim 0.6$ , or if transport properties across the pedestal change significantly at the same time. A possible explanation could be that cooling of the pedestal at the very edge by re-ionization of neutrals has an impact on the temperature

pedestal width, and that it is more visible at higher  $T_{e,ped}$ . Experiments with a more thorough scan of pedestal collisionality would be needed to clarify this issue, but were beyond the scope of this work.

As observed above,  $n_e$  and  $T_e$  are not independent from each other and, therefore, make it necessary to investigate the scaling of the pressure pedestal width rather as function of the pedestal pressure than its components.

#### 5.1.4. Scaling of the pedestal width

Electromagnetic gyrofluid and gyrokinetic simulations [77, 78] have found the onset of very strong electromagnetic turbulence near a critical value of the normalized pressure gradient. This turbulence persists even when the ideal ballooning mode enters the second stable regime that provides a mechanism for constraining the edge gradient.

Several models treating the scaling of the pedestal height and width as a function of plasma parameters were developed to predict the limiting pressure gradient. Their underlying physics is shortly discussed in subsection 2.2.3. Here, we want to test the model developed by Osborne [33] and find how the pedestal width  $\Delta_\psi$ , where  $\psi$  represents the normalized poloidal flux  $\psi_N$ , scales with the normalized poloidal pressure. We rewrite equation (2.2.20) for the sake of clarity:

$$\Delta_\psi = C\beta_{\theta,ped}^\gamma, \quad (5.1.1)$$

where  $\beta_{\theta,ped} = 2\mu_0 p_{ped} / \langle B_{\theta,ped} \rangle^2$  is the local normalized poloidal pressure,  $\langle B_\theta(\psi) \rangle = \oint_\psi dl_\theta B_\theta / \oint_\psi dl_\theta$  the flux surface averaged poloidal field,  $p_{ped} \approx 2n_{e,ped}T_{e,ped}$ . The position of the barrier in normalized flux coordinates is given by  $\psi_{ped} = 1 - \Delta_\psi$ .

We alter equation (5.1.1) such that we replace  $\beta_{ped}$  by a simplified expression,

$$\beta_{\theta,ped,X} \equiv 2\mu_0 p_{ped} / B_{\theta,X}^2, \quad (5.1.2)$$

where  $B_{\theta,X} = \mu_0 I_p / L_p$  is an averaged poloidal magnetic field at the separatrix with perimeter  $L_p$  in the poloidal cross-section [35]. The main reason for re-defining equation (5.1.1) is the reduction of uncertainties caused by the  $\langle B_\theta \rangle^2$  term. The poloidal magnetic field is computed from the equilibrium reconstruction LIUQE [11], which does not take into account the bootstrap current in the pedestal region. Another advantage of this choice is a better comparability of the results with calculations of the edge pedestal stability [21].

For reduction of errors, the total 3870 time slices of SN diverted discharges in the database are averaged in the time interval of the stationary phase of each discharge thus

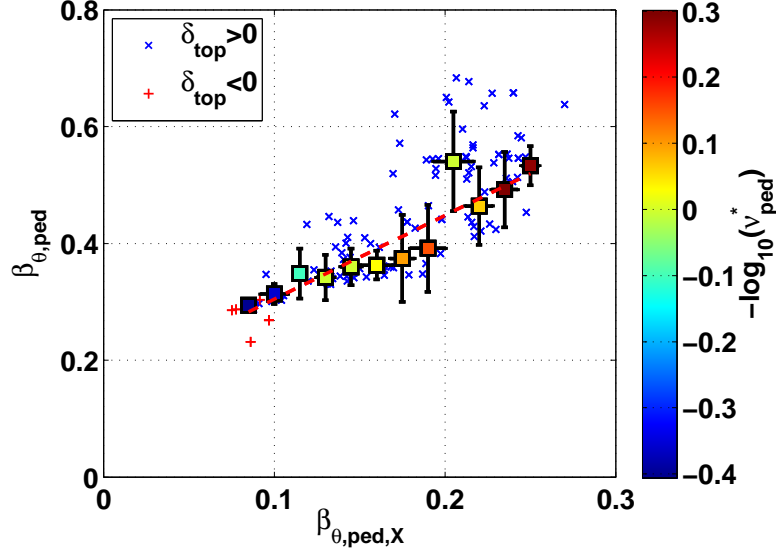


**Figure 5.9.:** Normalized poloidal pressure  $\beta_{\theta,ped}$  at the pedestal top as a function of a simplified normalized poloidal pressure  $\beta_{\theta,ped,X}$  at the pedestal top with the relation  $\beta_{\theta,ped} \simeq 2.34\beta_{\theta,ped,X}$  from linear regression, dashed red line.

providing values averaged over the whole ELM cycle. SF and SF-like SN discharges are not included in the analysis because of their X2-heating close to the edge pedestal top. The edge profiles measured by Thomson scattering in the inter-ELM phase were fitted for each shot. All further quantities are derived from these averages, encompassing the data of 115 discharges, and are plotted using cross and plus signs. The data is binned according to values of the abscissa and weighted averaging is employed on the data in each individual bin. Horizontal error bars reflect the width of the bins, vertical error bars reflect the data scatter in the bin normalized by the individual error bar. The averaged plot data is color-coded using the quantity indicated next to the color bar.

Figure 5.9 shows  $\beta_{\theta,ped}$  plotted versus  $\beta_{\theta,ped,X}$ , the raw data as blue cross ( $\delta_{top} > 0$ ) and red plus ( $\delta_{top} < 0$ ) and the averaged values binned in  $\beta_{\theta,ped,X}$ . Linear regression of the dependence yields the relation  $\beta_{\theta,ped} = (2.34 \pm 0.25)\beta_{\theta,ped,X}$ . Note that there is a large scatter in  $\beta_{\theta,ped}$  for  $\beta_{\theta,ped,X} > 0.2$ , where plasma collisionality is low and the bootstrap current becomes important. This effect may be attributed to an underestimation of the  $\langle B_\theta \rangle^2$  term in equation (5.1.1) by LIUQE.

Figure 5.10 shows the averaged data from 115 experimental discharges and their in  $\beta_{\theta,ped,X}$  binned averages. The solid red line shows an optimal fit, the dashed colored lines show the variation of the fit for  $\gamma = \{1/4, 1/3\}$  with the same constant  $C_X$ . The green dash-dotted line,  $\gamma = 1$ , shows a linear dependence  $\Delta_\psi \propto \beta_{\theta,ped,X}$  for reference. From

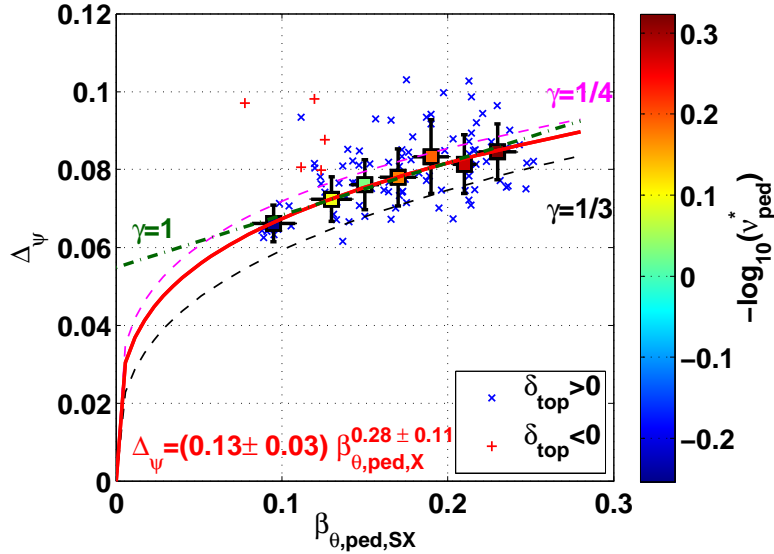


**Figure 5.10.:** Pedestal width  $\Delta_\psi$  plotted as a function of the normalized poloidal pressure  $\beta_{\theta,ped,X}$  at the pedestal top. The obtained functional dependency  $\Delta_\psi = 0.13\beta_{\theta,ped,X}^{0.28}$ , excluding data from discharges with negative upper triangularity, is shown as solid red line; the range of possible fit exponents with fixed constant is represented by colored dashed lines. A linear dependency,  $\Delta_\psi \propto \beta_{\theta,ped,X}$ , is plotted as green dash-dotted line.

fitting of the averaged pedestal width  $\Delta_\psi$  by the formula  $\Delta_\psi = C_X \beta_{\theta,ped,X}^\gamma$ , we obtain  $C_X = 0.13 \pm 0.03$  and  $\gamma = 0.28 \pm 0.11$ .

The fitted exponent from the TCV data set is smaller than the range of  $\gamma = 2/5 - 1/2$  that was found for the H-mode database of DIII-D [31, 35, 79] and  $\gamma = 1/2$  from ASDEX Upgrade (AUG) [80]. This may result from the fact that the only additional heating source for H-mode discharges in TCV is electron cyclotron heating at the 3rd harmonic (X3), whereas the main heating of DIII-D and AUG is by neutral beam injection (NBI). The result also indicates that this kind of work may be influenced by the heating scheme and, on ITER, the conclusions may not be valid. Another uncertainty in the result may arise from the fact that only the electron pressure profiles were used. The assumption of  $p_{ped} = 2n_{e,ped}T_{e,ped}$  may not hold anymore at high  $T_{e,ped}$  and low  $n_{e,ped}$ , i.e. low values of collisionality.

One has to note that the pressure pedestal width in discharges with  $\delta_{top} < 0$  is approximately  $\sim 25\%$  larger than in those with  $\delta_{top} > 0$  at the same  $\beta_{\theta,pol,X}$ . This is mainly due to an increase of the width of the electron temperature pedestal, which is shown in more detail in subsection 5.1.3. This result is consistent with former studies [73]

which report that the measured pedestal width is below the scaling predictions at high triangularity and above the scaling at low triangularity, indicating an inverse dependence on triangularity. For this reason and to keep similar plasma shapes, as were used in the analysis of the DIII-D and AUG shots, discharges with  $\delta_{top} < 0$  remain disregarded in the following analysis, but are included in the figures for comparison.

We expect that the constant  $C_X$  is somewhat too large with respect to published values, since we used  $\beta_{\theta,ped,X}$  instead of  $\beta_{\theta,ped}$ . Applying the formerly obtained relation  $\beta_{\theta,ped} = (2.34 \pm 0.25) \beta_{\theta,ped,X}$ , leads to  $C = 0.10 \pm 0.03$ , which agrees within some uncertainty with  $C = 0.076$  found for the DIII-D discharges [79] and  $C = 0.11$  for the AUG discharges [80]. Onjun [26] finds values for  $C$  ranging between 0.05 – 0.10 depending on the model and whether or not an approximation of the bootstrap current is included. For AUG, it should be noted that the pedestal width cannot be distinguished from a linear dependence in  $\beta_{\theta,ped}$  [80]. This could be also the case for the TCV data and must be verified in the following.

Next, we explore whether other dependencies of the edge pedestal width play a role, after the dependence on  $\beta_{\theta,ped,X}^\gamma$  is accounted for. This should also reveal the parameters space in which the model is satisfied. We define a normalized pedestal width  $F = \Delta_\psi / (0.13\beta_{\theta,ped,X}^{0.28})$  and expect  $F \sim 1$ , if there are no other dependencies. In figure 5.11, the measured value of normalized width is plotted as a function of the normalized toroidal (Fig. 5.11(a)) and poloidal (Fig. 5.11(b)) gyro radius. No significant dependence of the normalized width  $F$  is found on either  $\rho^* = \rho/a$  or  $\rho_{\theta,ped}^*/a$  [81], where

$$\rho = 4.57 \times 10^{-3} \sqrt{M_D T_{e,ped} [keV]} / (Z_{eff} a [m] B_0 [T]) \quad (5.1.3)$$

$$\rho_{\theta}^* = q_{95} \rho^* / \kappa_{95} \quad (5.1.4)$$

with the unit ion mass  $M_D$ , the minor radius  $a$ , the toroidal field  $B_0$ , the safety factor  $q_{95}$ , the plasma elongation  $\kappa_{95}$  and the effective ion charge  $Z_{eff} = 3$ . The results compare with those of DIII-D [79]. For  $\rho^* \gtrsim 0.013$ , a slight deviation from  $F \sim 1$  is visible, which suggest that a scaling  $\Delta_\psi \propto \rho^\alpha$  with some exponent  $\alpha$  becomes important, as mentioned in subsection 2.2.3. The quality of the data and the small range in  $\rho^*$ , however, does not allow further interpretation.

We further note that the measured value  $F$  is found to be essentially independent of density for  $n_{e,ped} \gtrsim 3.3 \times 10^{19} \text{ m}^{-3}$ , figure 5.11(c). Similarly, we find that  $F$  is also approximately independent of the normalized collisionality, figure 5.11(d). However, at very low collisionality,  $\nu_{ped}^* < 0.4$ , deviations from the scaling become visible. The same

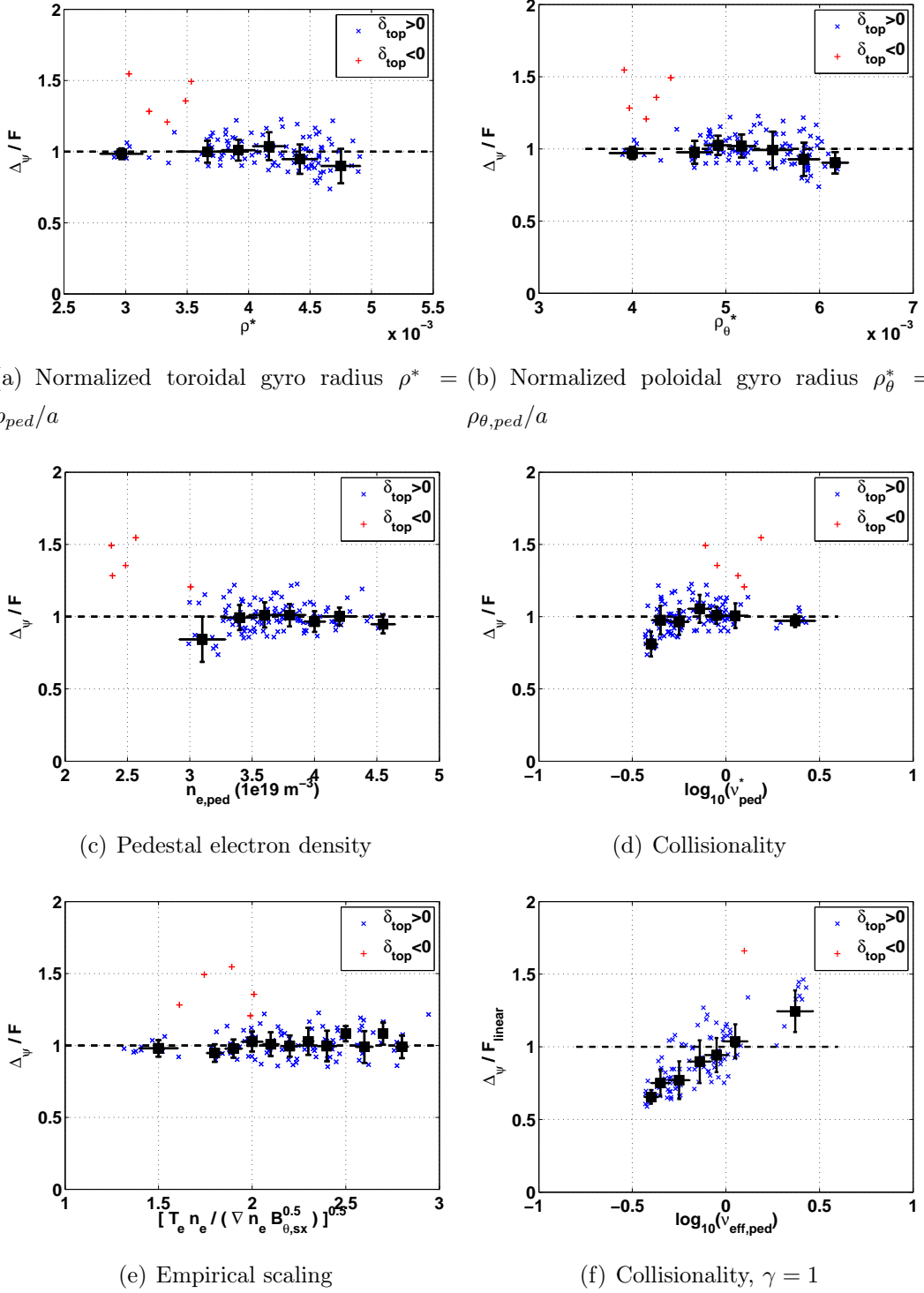


**Figure 5.11.:** Normalized pedestal width  $F = \Delta_\psi / \left( 0.13 \beta_{\theta,ped,X}^{0.28} \right)$ , plotted as a function of (a) normalized toroidal gyro radius  $\rho^*$ , (b) normalized poloidal gyro radius  $\rho_{ped}^*$ , (c) pedestal electron density  $n_{e,ped}$ , collisionality  $\nu_{ped}^*$  at the pedestal top for (d)  $\gamma = 0.28$  and (f) for  $\gamma = 1$  and (e) an empirical scaling given by equation (2.2.23).



discharges correspond to the set of data for which  $\Delta_\psi/F$  deviates from unity as a function of  $n_{e,ped}$  and for which  $\Delta_\psi$  stays below the scaling, figures 5.9 and 5.10. Further experiments have to be done to clarify if this effect is physical or if it is simply due to large uncertainties in the data. Figure 5.11(f) shows  $\Delta_\psi/F_{linear}$  versus  $\nu_{ped}^*$  assuming linear scaling  $\Delta_\psi \propto \beta_{\theta,ped,X}$ . The strong linear deviation indicates an overestimation of  $\beta_{\theta,ped,X}$ , i.e.  $\gamma$  needs to be smaller than unity to hold the requirements. Similar deviations are visible when plotting  $\Delta_\psi/F_{linear}$  against the other quantities presented here (not shown for simplicity of reading).

Finally we cross-check the pedestal width scaling for empirically found scaling laws, as explained in subsection 2.2.3. Scaling of the pedestal width  $\Delta_\psi$  as a function of  $(\nabla n_{e,ped})^{-1/2}$ , equation (2.2.21), could be identified, but did not conform to the scaling of the normalized width  $\Delta_\psi/F$ . The model assuming pedestal width scaling proportional to  $T_{e,ped}^{0.46}/B_\theta^{0.51}$  yields ambiguous results not allowing any conclusions. The combination of both empirical scalings, equation (2.2.23), is presented in figure 5.11(e) which reveals that  $F$  is also a good representation for this case. Further on, the density pedestal width shows correlation with  $B_{\theta,ped,X}$  as  $\Delta_{ne,r} \propto B_{\theta,ped,X}$  which has been also found on AUG [80].

## 5.2. Influence of the pedestal on energy confinement and transport

In this section we want to examine the influence of the pedestal properties in TCV H-mode plasmas on the energy confinement and on central electron temperature and density. We investigate the density peaking, crucial for efficient future fusion power plants, in the presence of EC-heating over a wide range of collisionality and outline the pedestal transport scaling.

### 5.2.1. Energy confinement

From the viewpoint of thermal energy stored in the core plasma  $W_{core}$  and, in general, of energy confinement in H-mode discharges, a higher pedestal stored energy  $W_{ped}$  is required [82]. The ELM energy loss  $\Delta W_{ELM}$ , however, usually increases with high pedestal stored energy [83]. Since the ELM is essentially a relaxation of the steep pressure gradient that occurs at the pedestal, it can be expected that  $\Delta W_{ELM}$  is a significant fraction of  $W_{ped}$ . Here, we examine the variation of  $\Delta W_{ELM}$  as a function of pedestal parameters

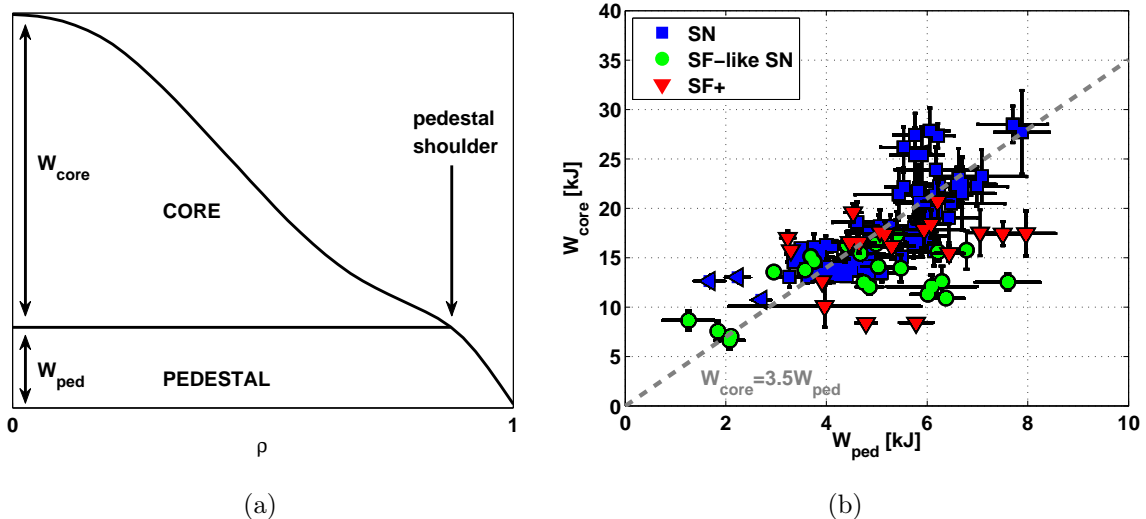


**Figure 5.12.:** (a) Schematic representation of the thermal energy stored in the pedestal plasma  $W_{ped}$  and in the core plasma  $W_{core}$ . (b)  $W_{core}$  plotted as a function of  $W_{ped}$  for SN, SF-like SN and SF+ configuration. The dashed grey line assumes a linear relation between  $W_{core}$  and  $W_{ped}$ , which seems valid for SN configurations (blue markers).

by assuming that  $\Delta W_{ELM}$  can be expressed as  $\Delta W_{ELM} = W_{ped} f(\nu_{ped}^*, \rho^*, \beta_\theta, \dots)$ . Figure 5.12(a) shows a schematic representation of the definitions used for  $W_{ped}$  and  $W_{core}$ .

First, we want to verify that  $W_{core}$  is indeed proportional to  $W_{ped}$ . In figure 5.12(b),  $W_{core}$  is plotted as a function of  $W_{ped}$ ; for TCV we find the relation  $W_{core} \sim 3.5 \times W_{ped}$  for a large range of  $W_{ped}$ . There is some scatter in the data of discharges with SN configuration due to different plasma shapes, e.g. varying plasma elongation or negative upper triangularity. The SF-like SN and the SF+ configurations deviate from this tendency at higher pedestal energy,  $W_{ped} > 4$  kJ, which may explain the behavior  $T_{e,ped} \neq f(n_{e,ped})$  in figure 5.6. This may be due to off-axis X2-heating being applied besides the usual central X3-heating. The additional X2-power raises the pedestal temperature and thus pedestal energy without affecting much the plasma core energy leading to a perturbation between the proportionality between  $W_{core}$  and  $W_{edge}$ .

Figure 5.13(a) shows the variation of the ELM energy  $\Delta W_{ELM}$  against the pedestal energy  $W_{ped}$ , resolved by the logarithmic pedestal collisionality. In JT-60U and ASDEX (AUG) it was found that  $\sim 10\%$  of the pedestal energy is released by a typical type-I ELM [84]. This value is largely exceeded in TCV. The smallest ELMs have normalized energy losses in the range of  $\Delta W_{ELM}/W_{ped} \sim 20 - 40\%$ , where the pedestal collisionality

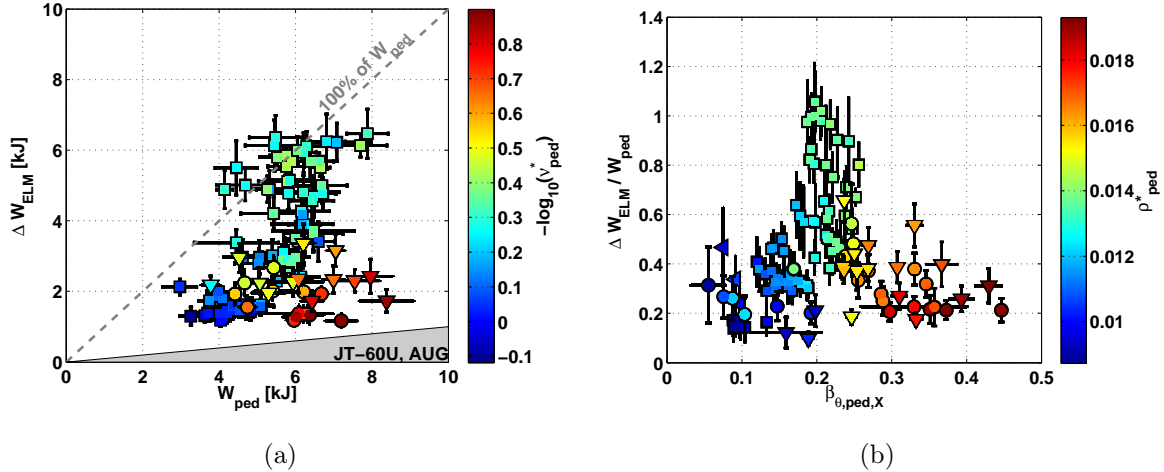


**Figure 5.13.:** ELM energy loss versus pedestal stored energy and poloidal beta: (a) Relation between the energy loss per ELM,  $\Delta W_{ELM}$ , as a function of the pedestal energy  $W_{ped}$ , resolved by the logarithmic pedestal collisionality. The dashed line corresponds to 100% of the pedestal energy which is released by one ELM. The gray shaded region represents the rescaled parameter space for JT-60U and ASDEX Upgrade (AUG) and corresponds to  $\Delta W_{ELM}/W_{ped} = 10\%$ . (b) Normalized ELM energy loss  $\Delta W_{ELM}/W_{ped}$  as a function of the normalized poloidal pressure in the pedestal  $\beta_{\theta,ped,X}$  with the normalized pedestal ion Larmor radius  $\rho_{ped}^*$  as additional parameter (color-coded).

is found to be  $\nu_{ped}^* > 1$  or  $< 0.2$ . In the region of transition between type-III to type-I ELMs, i.e.  $\nu_{ped}^* \sim 0.6$ , large ELMs occur that exhaust nearly 100% of the energy stored in the pedestal.

The normalized ELM energy loss  $\Delta W_{ELM}/W_{ped}$  is plotted in figure 5.13(b) as a function of the normalized pedestal poloidal pressure  $\beta_{\theta,ped,X}$ . The color-coding represents the normalized pedestal ion Larmor radius  $\rho_{ped}^*$ . The ejected energy by an ELM event increases strongly with the pedestal pressure and attains its largest value at  $\beta_{\theta,ped,X} \sim 0.2$ , where large ELMs are observed. Further increase in  $\beta_{\theta,ped,X}$  decreases the relative ELM energy loss. Care must be taken in the interpretation of this data since values of  $\beta_{\theta,ped,X} > 0.2$  represent a different magnetic configuration, SF-like SN and SF+, which is additionally heated by X2 in the region of the pedestal upper knee. The X2-heating could destabilize type-I ELMs by reducing the pedestal resistivity thus reinforcing current driven modes and increasing the pedestal pressure gradient faster than for the standard ELM cycle, which would lead to smaller and more frequent ELMs. Additional measure-

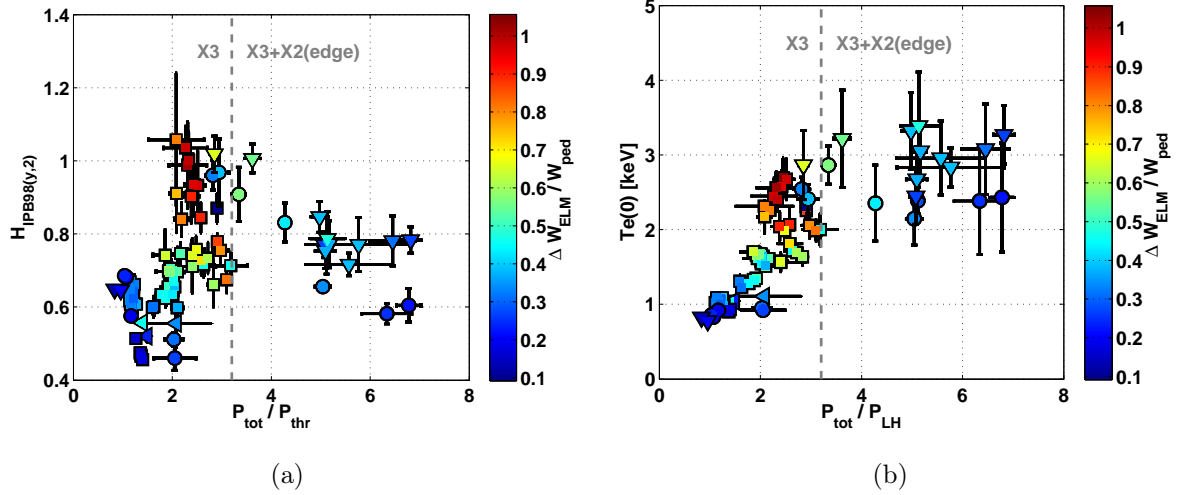


**Figure 5.14.:** (a) The H-mode energy confinement enhancement factor  $H_{IPB98(y,2)}$  plotted as a function of the normalized power  $P_{tot}/P_{thr}$ , where  $P_{tot}$  is the total heating power and  $P_{thr}$  the L- to H-mode transition power. (b) Central electron temperature  $T_e(0)$  plotted as a function of  $P_{tot}/P_{thr}$ . Regions with different heating schemes are indicated by a gray dashed line.

ments of the temporal evolution of the pedestal profiles would be needed to clarify this behavior. A similar effect has been demonstrated on AUG, where EC-current drive in the plasma edge was used to control ELMs [85].

The energy enhancement factor  $H_{IPB98(y,2)}$  for H-mode, equation (2.2.8), is plotted in figure 5.14(a) as a function of the normalized power  $P_{tot}/P_{thr}$ , where  $P_{tot}$  is the total absorbed power and  $P_{thr}$  the threshold power of the L- to H-mode transition, described by equation (2.2.5). Beginning from the onset of the H-mode,  $P_{tot}/P_{thr} \sim 1$ , the H-factor increases gradually with absorbed heating power. The maximum for the SN configurations is achieved where  $P_{tot}/P_{thr} \sim 2.5$ , i.e.  $P_{tot} \sim 1$  MW. After the maximum in  $H_{IPB98(y,2)}$ , the enhancement factor decreases with increasing power. Figure 5.14(b) shows the central electron temperature  $T_e(0)$  plotted versus  $P_{tot}/P_{thr}$ .

We note that for higher heating power solely discharges in SF-like SN and SF configuration exist, which have additional ECRH (X2) injected in the plasma edge. As seen before, the proportionality between  $W_{core}$  and  $W_{ped}$  is no longer valid. Thus, the increase in X2-heating in the edge for these configurations distorts the trend and leads to a strong decrease of  $H_{IPB98(y,2)}$ . However, it is important to mention that the H-factor is not the same for these configurations, in spite of their similar plasma parameters. The increase in  $H_{IPB98(y,2)}$  for the SF+ is, when compared to the SF-like SN, due to an increase

in  $T_e$  and hence  $W_e$  by  $\sim 20\%$ , which has been identified as a particularity of the SF configuration [71].

Due to the limiting X3-heating power, it is still unclear how the ELM energy loss and H-factor would evolve for the SN configuration, without the presence of X2-heating in the plasma edge. Experiments with central EC-heating in O-mode at the second harmonic (O2) are planned for the next TCV campaign to further explore the type-I ELMy regime.

### 5.2.2. Relation between central and pedestal electron temperature and density

To evaluate the edge core relationship in ELMy H-mode plasmas, we investigate the dependence of the central electron temperature and density on the  $T_e$  and  $n_e$  pedestal height. For that purpose, the quantities of the individual time slices in the H-mode database, usually they correspond to the times of the Thomson scattering diagnostic, were averaged over the whole stationary phase of the discharge. This method averages profile fluctuations which can be induced by ELM and sawtooth activity. The error bars correspond to the standard deviation of the averaged profiles. Pedestal quantities are obtained from tanh-fitting, equation (3.6.1), of the edge pedestal data in the inter-ELM phase from the whole stationary phase.

Figures 5.15(a) and 5.15(b) show the relations between central and pedestal electron temperature and density, where the color-coding shows the logarithmic collisionality  $\nu_{60}$  at 60% of normalized poloidal flux radius. We observe that the central electron density  $n_e(0)$  scales linearly as a function of the pedestal electron density  $n_{e,ped}$  for a wide range of collisionality, as was also found for other tokamaks [84].

In purely ohmic heated (OH) discharges,  $T_e(0)$  is only a weak function of  $T_{e,ped}$ . Variations in  $\nu_{ped}^*$  in OH discharges change  $T_{e,ped}$ , but do not, in principle, influence the core electron temperature. This is not surprising, since the only power source is the ohmic drive becoming rapidly less efficient for  $T_e(0) \gtrsim 1\text{keV}$ . Further, we have to keep in mind that  $T_{e,ped}$  and  $n_{e,ped}$  will vary such that  $p_{e,ped} \sim const.$  (see also subsection 5.1.2), permitting some variation in  $T_{e,ped}$ .

Adding central ECH power increases  $T_e(0)$  and  $T_{e,ped}$  accordingly; we find the linear dependence  $T_e(0) \simeq C \times T_{e,ped}$ , where  $C$  is a constant. At very high ECH power, where data is only available for the SF-like SN and SF+ configuration, the linear dependence

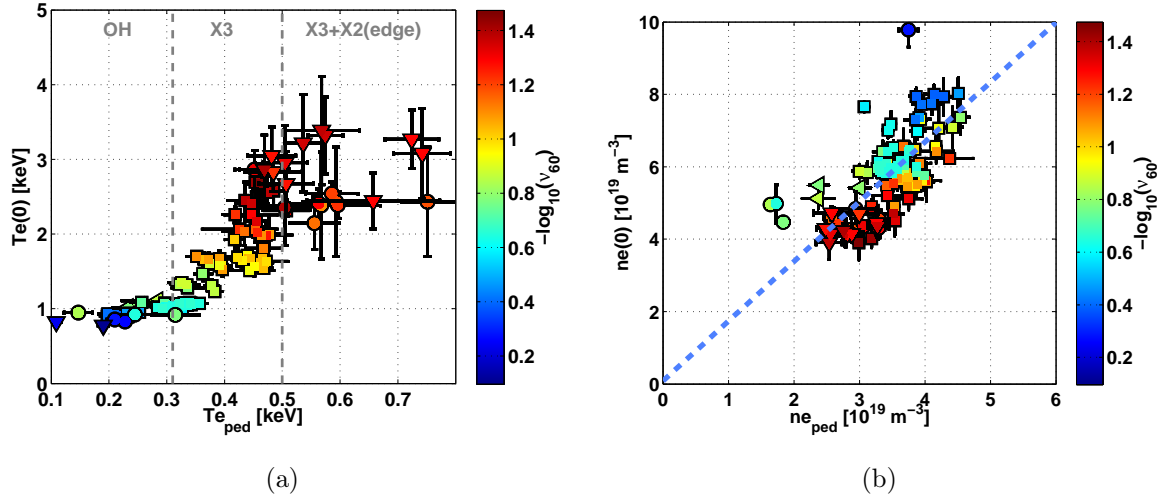


**Figure 5.15.:** Electron temperature and density profile stiffness: (a) The central electron temperature  $T_e(0)$  is plotted as a function of the pedestal electron temperature  $T_{e,ped}$ . Regions with different heating schemes are indicated by a gray dashed line. (b) The central electron density  $n_e(0)$  plotted versus the pedestal electron density  $n_{e,ped}$ . The data is resolved by the logarithmic collisionality at 60% of the normalized poloidal flux radius  $\sqrt{\psi_N}$ .

between central and pedestal electron temperature does not hold anymore, probably due to the X2-heating in the plasma edge.

### 5.2.3. Electron thermal transport in the pedestal

The pedestal density and temperature profiles may also be analyzed to determine the underlying transport controlling the pedestal gradients. The edge pedestal data of 115 discharges is represented by Thomson scattering data fitted in the inter-ELM phase of the whole stationary phase. The collisionality  $\nu_{ped}^*$  is computed from the fitted pedestal values. The fitted data of the individual discharges is plotted as crosses and plus-signs. The data is then binned according to values of  $\nu_{ped}^*$  employing weighted averaging. Horizontal error bars reflect the width of the bins, vertical error bars reflect the data scattering in the bin including the individual uncertainties from the fit. The data in the scatter plot is resolved by the averaged quantity indicated next to the color bar.

Plotting the ratio  $\sigma_e = L_{Te}/L_{ne}$  versus the pedestal collisionality, where  $L_{Te}$  and  $L_{ne}$  are the gradient scale lengths of electron temperature and density in the pedestal, indicates  $\sigma_e \sim 0.5 - 1.25$  or  $\eta_e = \sigma_e^{-1} \sim 0.8 - 2$ . In type-I ELMy H-mode plasmas it

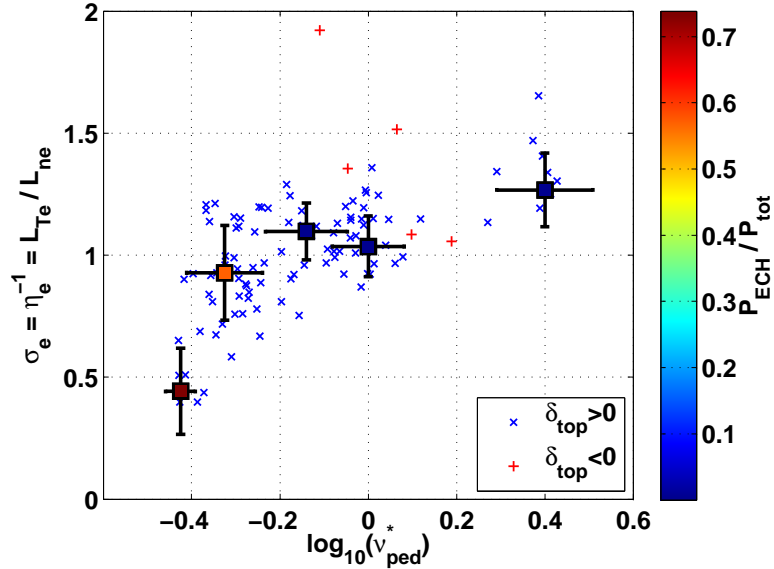


**Figure 5.16.:** Electron thermal transport in the pedestal region: Pedestal  $L_{Te}/L_{ne}$  plotted versus the logarithmic collisionality  $\log_{10}(\nu_{ped}^*)$  at the pedestal top with color-coding showing the EC-heating power.

was found that the electron density scale length is twice the temperature scale length, i.e.  $\eta_e = 2$ , which is indicative of drift wave turbulence dominating electron thermal transport [31]. A similar scale length ratio in type-I ELMy H-mode plasmas has also been observed in DIII-D [72] and AUG [86], indicating some universality of this transport mechanism in the pedestal. The scale lengths of the ion temperature and density could not be measured, however, data from AUG [87] indicates that ion temperature gradient driven drift modes were not thought likely to set the ion temperature profile. Modeling of the AUG data with the fluid code SOLPS indicated that neoclassical ion transport was sufficient to match the measured ion temperature profile.

A value of  $\eta_e \sim 2$  has also been found to describe well the electron transport in strongly EC-heated eITB discharges in TCV [45, 48]. The simulations showed that in these low collisionality eITB regimes, the role of ITG driven turbulence decreases and TEM turbulence is dominant but stabilized by the magnetic shear in the barrier region, so that ITG driven turbulence is still probable.

#### 5.2.4. Density peaking

On the basis of H-mode experiments on JET, AUG and TCV, empirical relations, supported by gyrokinetic transport calculations, were found that describe the density peaking

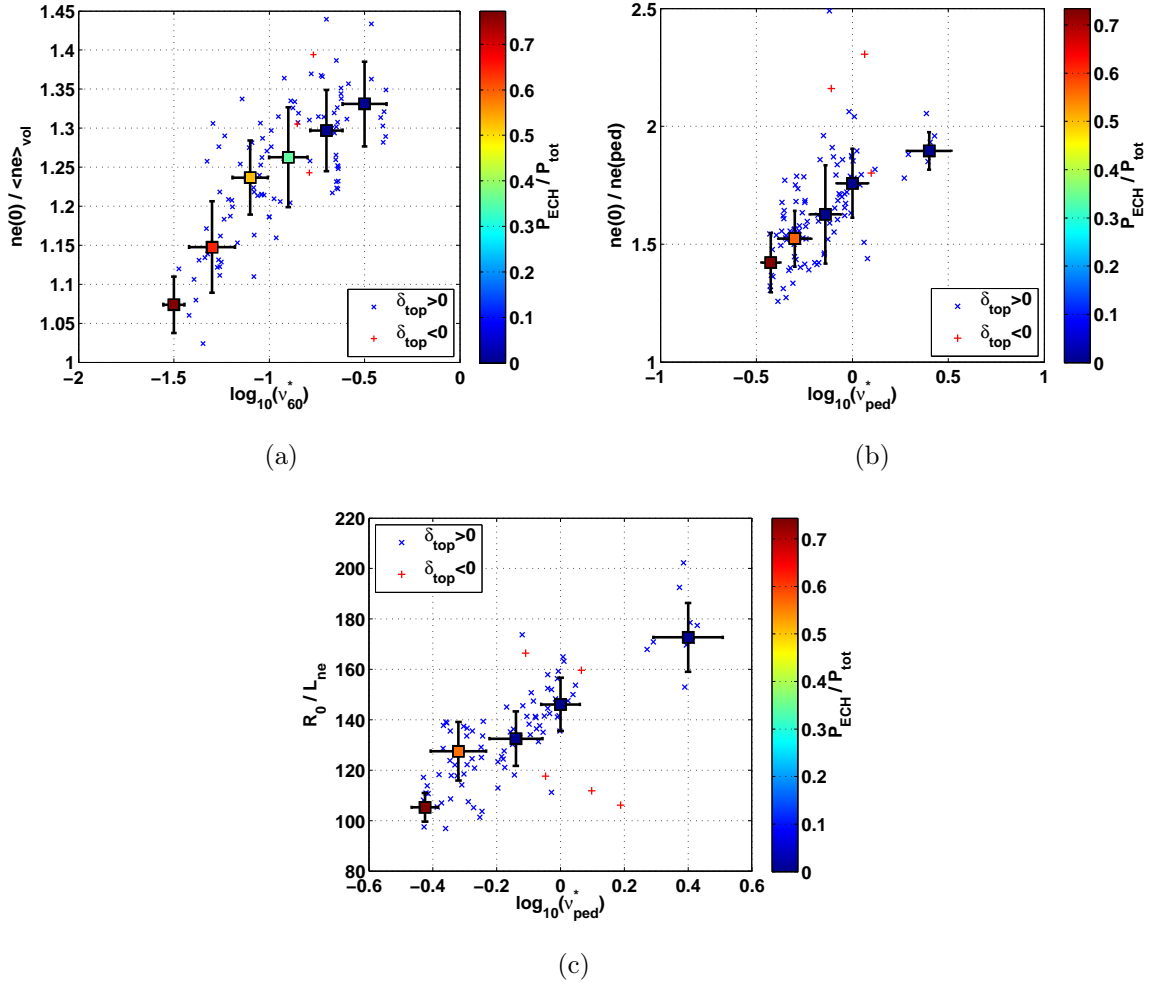


**Figure 5.17.:** (a) Density peaking  $n_e(0)/\langle n_e \rangle$  as a function of the collisionality at  $\rho = 0.6$ , (b) the ratio between central and pedestal density  $n_e(0)/n_e(ped)$  and (c) the normalized density gradient  $R_0/L_{ne}$  in the edge pedestal. The color-coding represents the fraction of ECH power.

as a function of collisionality [75, 81, 88–90]. The general conclusion is that  $\nu^*$  plays the most important role in the density gradient formation in the core. Extrapolation of these experimental observations to ITER parameters predicts moderately peaked density profiles for the baseline H-mode scenario,  $n_0/\langle n \rangle \sim 1.45$ , which is expected to improve fusion performance, as reported in [91]. For temperature profiles as predicted for the inductive scenario [92], a peaking factor  $n_0/\langle n \rangle = 1.5$  results in an approximate 30% increase in fusion power for a given average density and normalized toroidal pressure  $\beta_N$  [91].

One of the main difficulties of an extrapolation towards reactor conditions is that the majority of H-mode plasmas were obtained with dominant NBI heating, few of them



with pure ion or electron cyclotron resonance heating (ICRH & ECH). Theory predicts a strong trapped electron mode (TEM) destabilization [93] in case of dominant ECH which may result in density profile flattening by the appearance of an outward convective particle flux. Former studies of TCV H-mode discharges [90] indicated that significantly peaked profiles can persist in EC-heated H-mode plasmas at reactor relevant values of  $\beta_N \sim 2$ .

During this work, the TCV H-mode database was expanded to a range in normalized toroidal pressure of  $\beta_N = 0.2\text{--}1.9$ . Here, we consider only discharges with SN divertor and line-integrated electron density  $n_e \geq 3.5 \times 10^{19} \text{ m}^{-2}$ , but all plasma shapes as indicated in section 5.1. We observe that the density profile, measured by Thomson scattering, flattens considerably in the presence of strong EC-heating, contrary to what had formerly been reported.

Figure 5.17(a) shows the electron density peaking, i.e. the central electron density  $n_e(0)$  normalized by the volume averaged electron density  $\langle n_e \rangle$ , as a function of the collisionality at  $\rho = 0.6$ . Figures 5.17(b) and 5.17(c) show the ratio between central and pedestal density and the normalized density gradient as function of the collisionality at the pedestal top. The data from the individual discharges was binned in intervals of  $\log(\nu_{ped}^*)$ . As mentioned above, error bars represent the bin width and the weighted error bar from the scattering of the data.

We indeed observe that density peaking decreases by  $\sim 15\%$  when increasing the ECRH power as reported in [93]. It is believed that this effect is due to a destabilization of electron driven modes (TEM and/or ETG), but this must be confirmed by further studies. To this purpose, gyrokinetic transport simulations with the GS2 code [94] are ongoing [95] and will be presented elsewhere.

### 5.3. Impact of plasma shaping on pedestal parameters

While it has long been observed that plasma shaping significantly affects edge MHD stability and pedestal height [70, 73, 96–98], the contribution of the pedestal stability to pedestal characteristics has not generally been determined. The variations observed so far in the normalized pressure gradient in dependence of plasma shaping makes models based on infinite- $n$  ballooning limits doubtful. To date, it remains unclear if a simple power law shape dependence is appropriate when the data spans different stability regimes [85]. Considering the plasma shaping capability of TCV, it is uniquely placed to investigate

the H-mode pedestal performance dependence upon plasma shape to compare firstly the results with those of other machines and secondly to extend the parameter space considerably, even examining extreme shapes such as negative upper triangularity.

It is generally understood that stabilization of coupled kink-ballooning modes permits higher edge pressure gradients. This implies a relatively sensitive dependence of the pressure limit on discharge conditions such as shape and poloidal beta [70]. Encouraged by studies of the MHD stability limit of the edge pedestal in variously shaped plasmas, subsections 4.3.3 and 4.3.4, and also to verify the accuracy of these simulations by experiments, H-mode discharges with various shapes were conducted.

Discharges were designed such that an initial stationary ELMy H-mode phase, elongation  $\kappa \sim 1.7$ , total and upper triangularity  $\delta \sim 0.45$  and  $\delta_{top} \sim 0.2$  and low squareness  $\lambda \sim 0$ , were maintained for  $\sim 500$  ms (the reference shape). This configuration is often able to access the second ballooning stable region. After the first phase, an abrupt change in shape at  $t \sim 0.95$  s, usually within 50 – 100 ms, initiated the second half of the H-mode phase with one of the above mentioned shape parameters being changed. The plasma current was adjusted such that  $q_{95}$  was kept constant during both phases, however, constant density can only be obtained in the presence of ELMs with approximately constant frequency. Electron cyclotron heating at the third harmonic (X3) with a nominal power  $P_{ECH}$  ranging between 0.5 – 1 MW, dependent on the discharge, was applied throughout the discharge to keep pedestal parameters as close as possible at the ideal MHD stability limit. The poloidal angle of the X3-launcher was pre-programmed such that it followed the resonance position to optimize the absorbed power. Due to variation in energy confinement related to the plasma shape, the X3 power absorption, strongly dependent on the electron (central) temperature, varied to some extent. The local plasma shaping parameter were obtained by fitting the upper plasma boundary with the formulas (4.3.2).

The method of performing single discharges featuring two different shapes has general advantages: (1) Switching the shape in an established discharge to more extreme parameters avoids instabilities which could occur during direct plasma formation of a somewhat less stable configuration. (2) Passing through two different plasma shapes during one discharge generally facilitates the comparability of plasma and pedestal parameters between different shapes. However, the acquired data for one shape is also halved making the statistical analysis of pedestal profile evolution during an ELM cycle more difficult.

The plasma parameters are presented in figures 5.18(c), 5.18(a), 5.19(a) and 5.19(c),

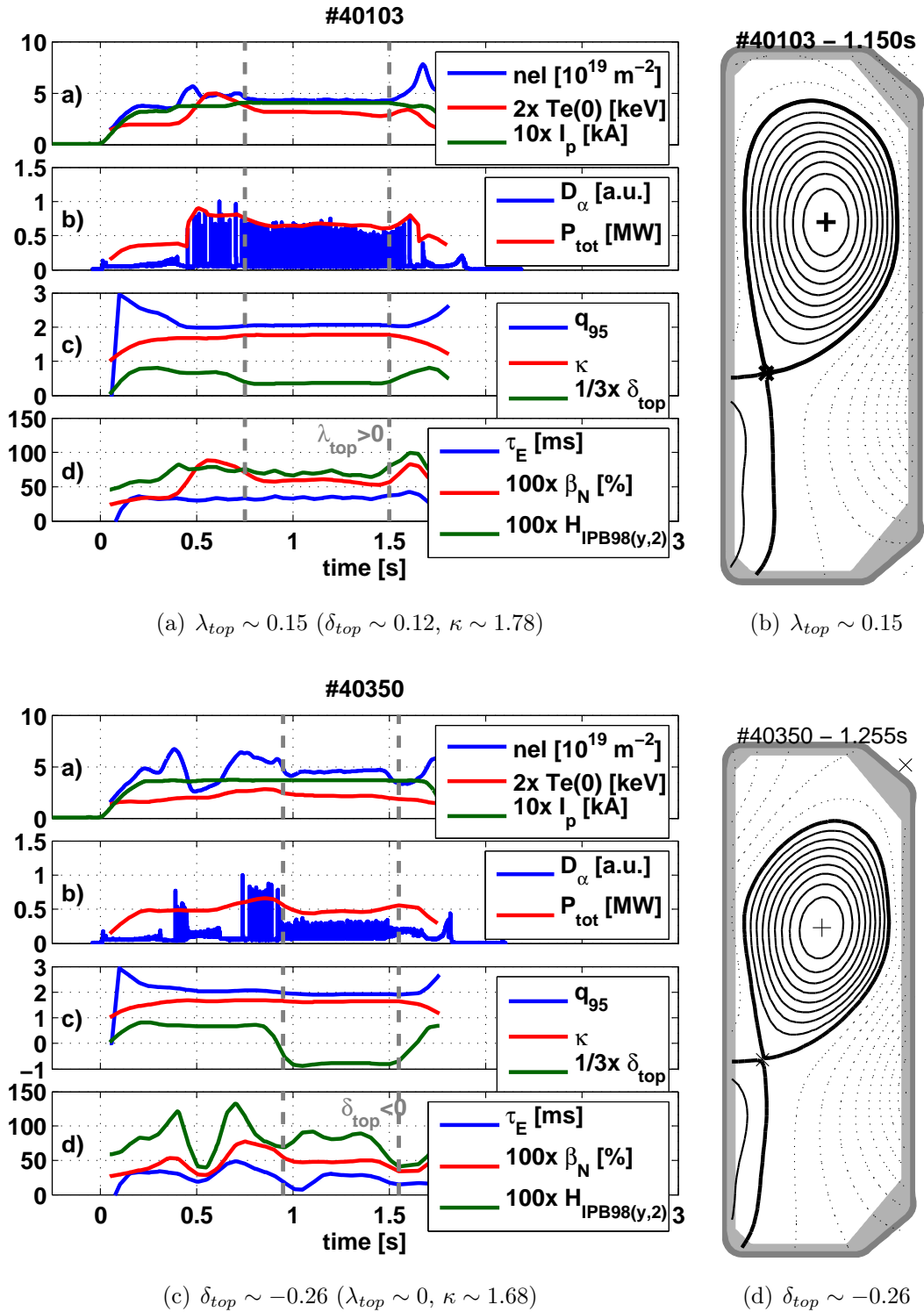


**Figure 5.18.:** Plasma shapes and parameters for different upper triangularity  $\delta_{top}$  and squareness  $\lambda_{top}$ . Dashed vertical lines represent the discharge phase with different plasma shaping.

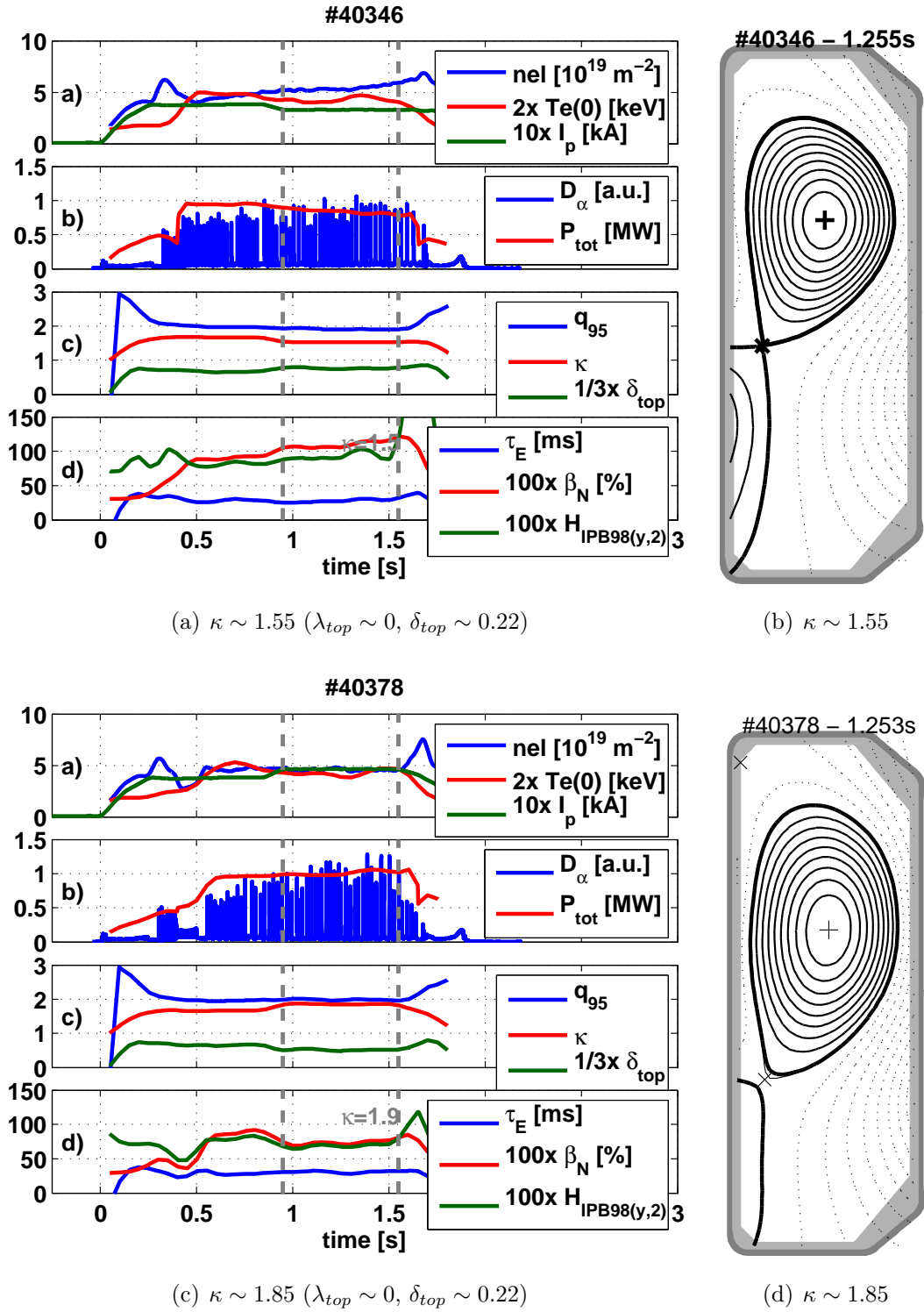


**Figure 5.19.:** Plasma shapes and parameters for different plasma elongations  $\kappa$ . Dashed vertical lines represent the discharge phase with different plasma shaping.

with subplot a) line-integrated density  $n_{el}$ , central electron temperature  $T_e(0)$ , plasma current  $I_p$ , subplot b) divertor recycling signal  $D_\alpha$ , total absorbed power  $P_{tot}$ , subplot c) safety factor  $q_{95}$ , elongation  $\kappa$ , upper triangularity  $\delta_{top}$ , and subplot d) energy confinement time  $\tau_E$ , normalized toroidal beta  $\beta_N$  and H-factor  $H_{IPB98(y,2)}$ . The corresponding shapes are shown in figures 5.18(d), 5.18(b), 5.19(b) and 5.19(d).

We observe that a decrease in  $\lambda_{top}$  or an increase in  $\delta_{top}$  yields higher toroidal beta and confinement, figures 5.18(a) and 5.18(c). Shaping that decreases the length of the field lines in the bad curvature region (on the LFS), is generally associated with improvements in the edge MHD stability limit generally leading to a higher pedestal pressure. The global energy confinement then responds to the higher pedestal pressure and improves, when the temperature profile is stiff. Decreasing  $\kappa$  increases  $\beta_N$  whilst energy confinement remains approximately, figure 5.19(a) and 5.19(c). The energy confinement factor increases with decreasing  $\kappa$  and vice versa, because of the dependence  $\tau_{IPB98(y,2)} \propto \kappa^{0.78}$ . This observation suggests that the pedestal pressure height decreases with increasing  $\kappa$ , which is investigated in more detail in subsection 5.3.2.

### 5.3.1. ELM behavior

The divertor  $D_\alpha$  recycling signal gives a good indication of the pedestal performance. Improvements in shape and thus pedestal height are usually accompanied by more regular ELMs at lower frequency and higher ELM energy loss [25, 70]. Figure 5.20 shows the ELM frequency  $f_{ELM}$ , the ELM energy loss normalized to the total plasma energy  $\Delta W_{ELM}/W_{tot}$ , computed from the diamagnetic loop, and the ELM fractional power loss  $P_{ELM}/P_{tot} = f_{ELM} \times \Delta W_{ELM}/P_{tot}$  normalized by the total heating power  $P_{tot}$ . The upper triangularity was varied between  $\delta_{top} = -0.25$  and 0.2. The scans in elongation ranged between  $\kappa = 1.55 - 1.85$ . The quantities of  $\sim 5$  discharges for each shape configuration  $\kappa$  and  $\delta_{top}$  were binned according to values of the abscissa and weighted averaged. Horizontal error bars indicate the scatter of the data in the bins; vertical error bars represent the weighted standard deviation of the data. Data points from one single discharge with  $\lambda_{top} = 0.15$  (instead of  $\lambda_{top} = 0$ ) is marked by a gray dashed ellipse.

It can be seen in figure 5.20(a) that upper triangularity strongly affects the ELM behavior. Increasing  $\delta_{top}$  from  $-0.25 \rightarrow 0.22$  decreases  $f_{ELM}$  by  $\sim 80\%$  and increases  $\Delta W_{ELM}/W$  by a factor of  $\sim 3\times$ . Thus, the fractional power loss due to ELMs decreases by  $\sim 10\%$ . This result is in good agreement with experimental results from other ma-

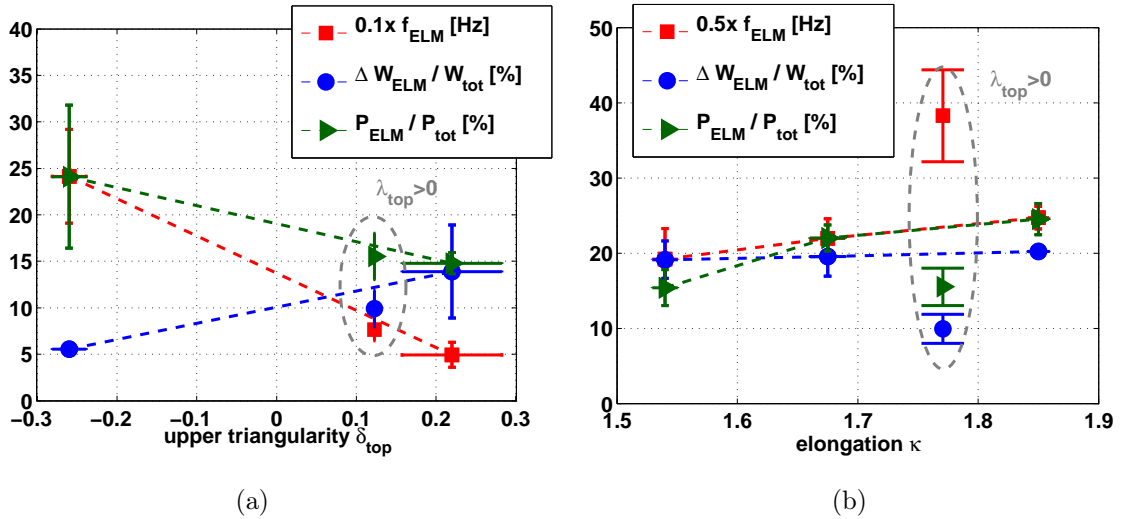


**Figure 5.20.:** Dependence of ELM characteristics upon plasma shaping: ELM frequency  $f_{ELM}$ , ELM energy loss  $\Delta W_{ELM}$  normalized by the total plasma energy  $W_{tot}$  and normalized fractional ELM power loss  $P_{ELM}/P_{tot}$  as a function of (a) upper triangularity  $\delta_{top}$  ( $\kappa = 1.67, \lambda_{top} = 0$ ) and (b) elongation  $\kappa$  ( $\delta_{top} = 0.23, \lambda_{top} = 0$ ).

chines [25, 73, 96–98] and modeling of the pedestal stability [18, 19, 28, 70, 99–101]. Changes in the ELM behavior as a function of  $\kappa$ , figure 5.20(b), are less pronounced than in the case of  $\delta_{top}$ . Increasing  $\kappa$  from 1.55  $\rightarrow$  1.85 increases  $f_{ELM}$  by  $\sim 20\%$  whilst keeping  $\Delta W/W_{tot}$  approximately constant, hence increasing  $P_{ELM}/P_{tot}$  by  $\sim 30\%$ . The increase in  $f_{ELM}$  with increasing elongation suggest that the operational point is closer to stability limits throughout the whole ELM cycle, thus causing ELMs more frequently. Since the normalized ELM power loss increases with increasing  $\kappa$ , we expect that the pressure pedestal height decreases. In subsection 5.3.2, the electron pedestal properties for these discharges are investigated in more detail.

Note that the ELM characteristics for modified upper squareness follow well the tendency in  $\delta_{top}$ . This is most probably due to the fact that  $\delta_{top}$  and  $\lambda_{top}$  are in some sense coupled and represent a very local change in magnetic geometry thus selectively modifying the MHD stability of the pedestal.

### 5.3.2. Pedestal properties

The electron pedestal temperature and density profile are analyzed by fitting the data from Thomson scattering measurements time-averaged over the ELM cycle by equa-

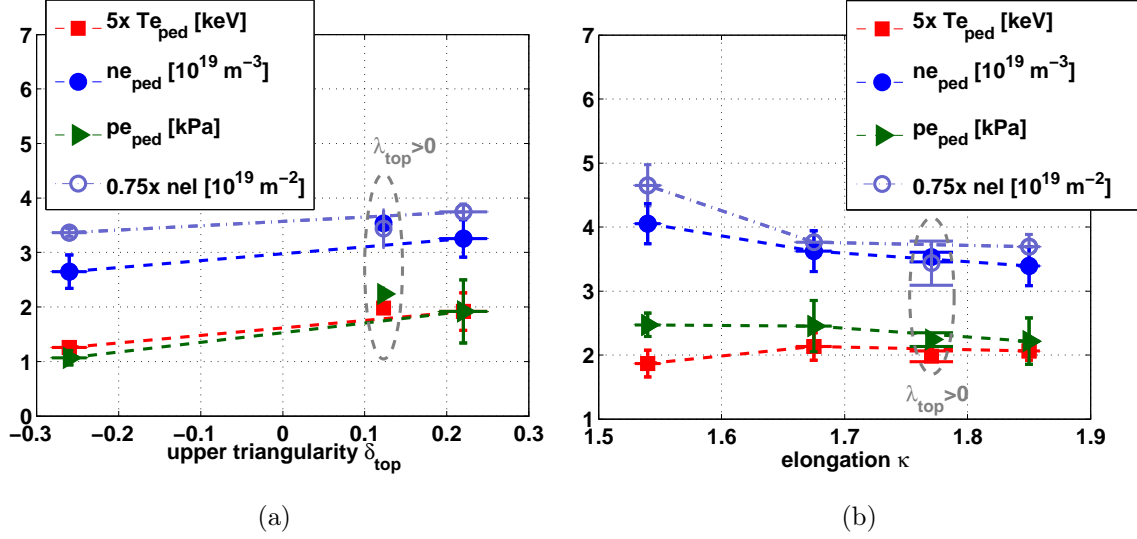


**Figure 5.21.:** Electron pedestal temperature, density and pressure as a function of plasma shape: Electron pedestal temperature  $T_{e,ped}$ , density  $n_{e,ped}$  and pressure  $p_{e,ped}$  and line-integrated density  $n_{el}$  as a function of (a) upper triangularity  $\delta_{top}$  ( $\kappa = 1.67$ ,  $\lambda_{top} = 0$ ) and (b) elongation  $\kappa$  ( $\delta_{top} = 0.23$ ,  $\lambda_{top} = 0$ ).

tion (3.6.1). The height of the  $T_e$ ,  $n_e$  and  $p_e$  pedestal extracted from the hyperbolic tangent fitting and the line-integrated density  $n_{el}$  from interferometry are plotted in figure 5.21(a) and 5.21(b) as a function of  $\delta_{top}$  and  $\kappa$ , respectively.

### Pedestal height

The pedestal pressure increases by  $\sim 100\%$  when increasing  $\delta_{top}$  from  $-0.25 \rightarrow 0.22$ . It is known that a higher triangularity permits a higher pedestal pressure through a higher MHD stability limit. The pedestal pressure decreases by  $\sim 15\%$  when increasing  $\kappa$  from  $1.68 \rightarrow 1.85$ , which is mainly due to the strong decrease in  $n_{e,ped}$  by  $\sim 20\%$ . From the sparse set of data it is not clear if this decrease in  $n_{e,ped}$  is due to a general decrease in  $n_{el}$ , or if other factors may play a role. However, the data suggest that  $p_{e,ped}$  decreases with  $\kappa$ .

The model of Sugihara [102] based on turbulence suppression by the combined effect of magnetic and  $\mathbf{E} \times \mathbf{B}$  shear proposes that the pedestal electron pressure scales as  $p_{e,ped} \propto T_{e,ped}^{0.5} \kappa^{-2}$ , equation (2.2.11). One has to mention that this model assumes that the pressure gradient in the plasma edge is limited by ballooning modes, equation (2.2.14), which does not have to be the general case when access to the second ballooning stable

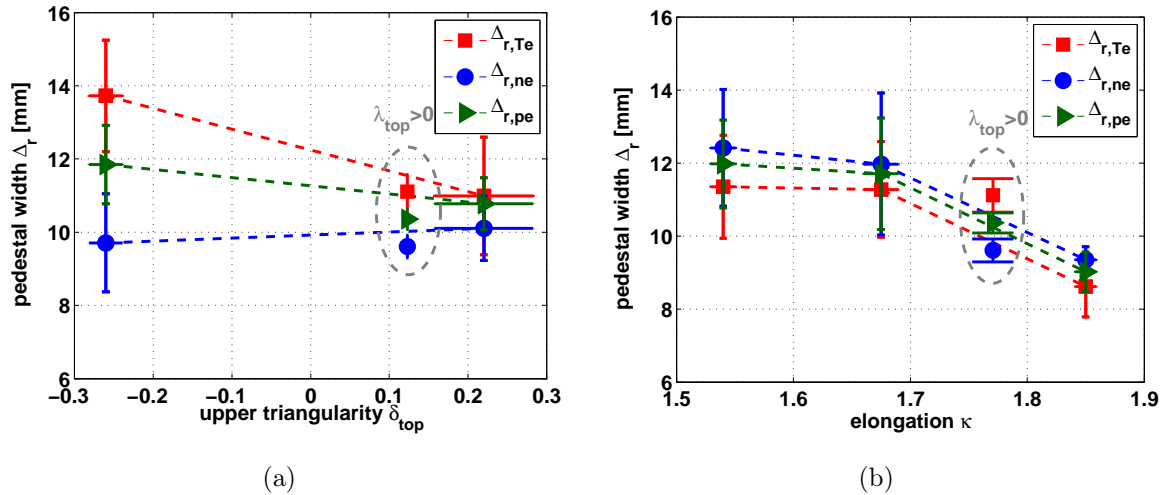


**Figure 5.22.:** Electron pedestal temperature, density and pressure width as a function of plasma shape: Electron pedestal temperature  $T_{e,ped}$ , density  $n_{e,ped}$  and pressure  $p_{e,ped}$  width as a function of (a) upper triangularity  $\delta_{top}$  and (b) elongation  $\kappa$ .

region is possible. In contrary, a model based on log-linear fit of pedestal data of type-I ELM discharges from five different machines [103], equation (2.2.12), found  $p_{e,ped} \propto \kappa^{1/3}$ .

The contradicting scalings highly recommend further studies to clarify this issue. Further on, it cannot be ruled out that the X3-heating power density was sufficient to keep the pedestal close at the current driven MHD limit for high  $\kappa$ 's. For this reason, the stability limit of the pedestals was analyzed to clarify, if the limiting instability is of ballooning or external kink character (see subsection 5.3.3).

### Pedestal width

The pedestal width of the electron temperature  $\Delta_{r,Te}$ , density  $\Delta_{r,ne}$  and pressure  $\Delta_{r,pe}$  profile in radial coordinates is plotted as a function of  $\delta_{top}$  and  $\kappa$  in figure 5.22(a) and 5.22(b), respectively. Increasing  $\delta_{top}$  from  $-0.25 \rightarrow 0.22$  decreases  $\Delta_{r,pe}$  by  $\sim 10\%$ , although this is within the error bar. While  $\Delta_{r,ne}$  remains approximately constant, despite the large error bars, the decrease of  $\Delta_{r,Te}$  by  $\sim 20\%$  exists. Increasing  $\kappa$  from  $1.68 \rightarrow 1.85$  decreases  $\Delta_{r,Te}$  and  $\Delta_{r,ne}$  simultaneously by  $\sim 20\%$ , thus  $\Delta_{r,pe}$  decreases by the same amount.

The pedestal quantities in the discharge with  $\lambda_{top} \sim 0.15$  (instead of  $\lambda_{top} = 0$ ) are in good agreement with the trend observed when varying  $\delta_{top}$  or  $\kappa$ . In the trend of pedestal width as a function of  $\kappa$ , we observe a swap of sizes of  $\Delta_{r,Te}$  and  $\Delta_{r,ne}$  for  $\lambda_{top} > 0$ . It is



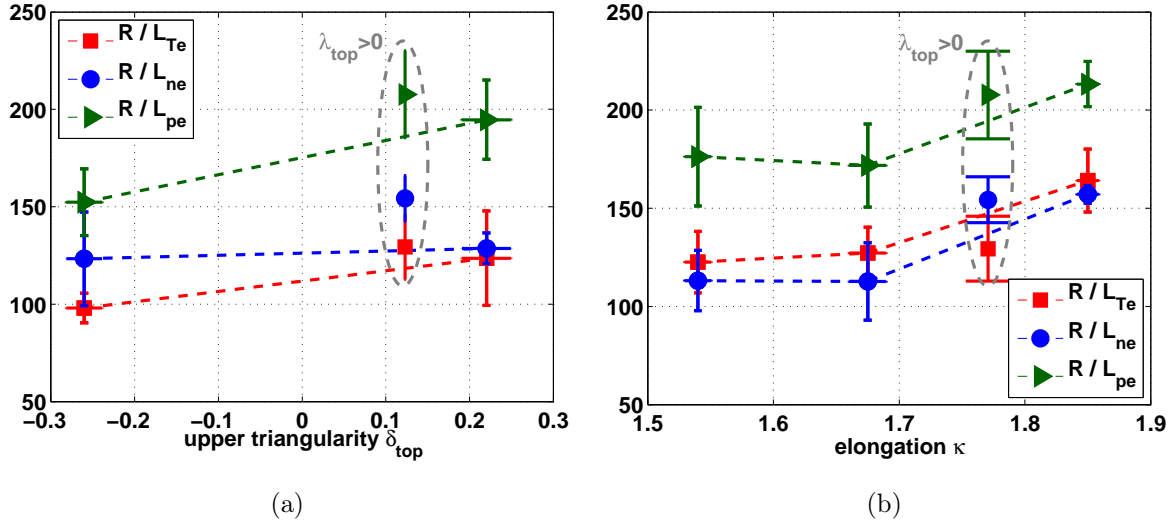


**Figure 5.23.:** Normalized electron pedestal temperature, density and pressure gradient as a function of plasma shape: Normalized electron pedestal temperature  $T_{e,ped}$ , density  $n_{e,ped}$  and pressure  $p_{e,ped}$  gradient as a function of (a) upper triangularity  $\delta_{top}$  and (b) elongation  $\kappa$ .

unclear if this effect is related to the different ELM frequency and energy loss as described in subsection 5.3.2 or just a coincidence.

### Normalized gradient

The normalized gradient  $R/L_x$  is linked to changes in pedestal height and width.  $R/L_{pe}$  increases by nearly 30% mainly due to the strong increase in  $R/L_{Te}$  by  $\sim 25\%$  when increasing  $\delta_{top} = -0.25 \rightarrow 0.22$ , whereas  $R/L_{ne}$  increase only little or remains constant. A similar tendency is observable when increasing  $\kappa = 1.68 \rightarrow 1.85$ ;  $R/L_{pe}$  increases by  $\sim 25\%$  due to a simultaneous increase in  $R/L_{Te}$  and  $R/L_{ne}$  by  $\sim 25\%$ . Whereas the most important contribution of increase in  $R/L_{pe}$  is the pedestal height in case of varying  $\delta_{top}$ , the more relevant factor in case of varying  $\kappa$  is  $\Delta_{r,pe}$ . This could be explained by reduced pedestal pressure and hence beta. Since  $\Delta_p \propto \beta^\gamma$ , where  $\gamma > 0$  is some positive exponent (see subsection 5.1.4), we would expect a decrease in pedestal width when decreasing the pedestal height and thus beta.

Qualitatively we observe that shaping, such that the length of magnetic field lines in the unfavorable region (LFS) is minimized, increases the maximum pedestal gradient as predicted by ideal MHD simulations (see also subsections 4.3.3 and 4.3.4). In the case of higher upper squareness, we observe that the ELM frequency and energy loss are not

directly linked to the height and width of the pedestal. However, more data would be needed to make quantitative statements and allow for testing of scaling laws.

### 5.3.3. Variation of MHD stability with shaping

The MHD stability of the discharges in the shape scan was analyzed to provide insight into the limits governing the variation of the pedestal pressure observed in the experiment. We refer to subsection 2.3.4, where the method of calculating the stability diagram is described in detail. The experimental point is computed assuming  $T_{i,ped} = T_{e,ped}$ , where  $T_{e,ped}$  is obtained from measurements by Thomson scattering, and (1)  $n_{i,ped}$  from equation (3.6.2) with  $C^{6+}$  as single impurity and  $Z_{eff} = 3$  (magenta square) or (2) assuming  $p_{i,ped} = p_{e,ped}$  (black square). The current density contains the ohmic profile from the equilibrium reconstruction LIUQE and the edge current density from the bootstrap current, equation (2.1.10), that is calculated from the experimental profiles. A self-consistent equilibrium including these profiles was then computed by the CHEASE code.

Uncertainties in the experimental points, depicted as horizontal and vertical error bars, represent the uncertainty in the fitting of the electron edge gradient and height and the subsequent uncertainty in the determination of the bootstrap current density. Since the ion profile pressure is not based on independent measurements, but assumed proportional to the electron pressure profile, no plausible uncertainties can be given for the gradient and pedestal height of the ion contribution. Keeping these uncertainties in mind, the two experimental points (magenta and black square) mark the region, where the true operational point is expected.

The stability diagram shows the ballooning (red line and red dashed line for some flux surfaces) and external kink stability limits (bluish lines), collisionless bootstrap and shear reversal as a function of normalized pedestal parallel current density  $J_{||}/\langle J \rangle$  and normalized pedestal gradient  $\alpha$ .  $J_{||}$  is taken at the position where the pressure gradient is maximal,  $\langle J \rangle$  is the total plasma current divided by the plasma cross sectional area. We use  $\alpha \equiv -\mu_0 (dp/d\psi) (dV/d\psi) \sqrt{V/(2\pi^2 R)}/2\pi^2$  [35] at the point of maximum pressure gradient in the pedestal, where  $p$  is the total pressure,  $V$  is the plasma volume,  $R$  the major radius and  $\psi$  the poloidal flux. The pedestal width  $\Delta_\rho$  is given in  $\sqrt{\psi_N}$ . The ratio between edge and maximum pressure gradient  $p'_{edge}/p'_0$  and the ratio between edge and maximum current density  $j_{edge}/j_0$ , which influences the stability of ballooning and external kink modes, are given for each stability map.

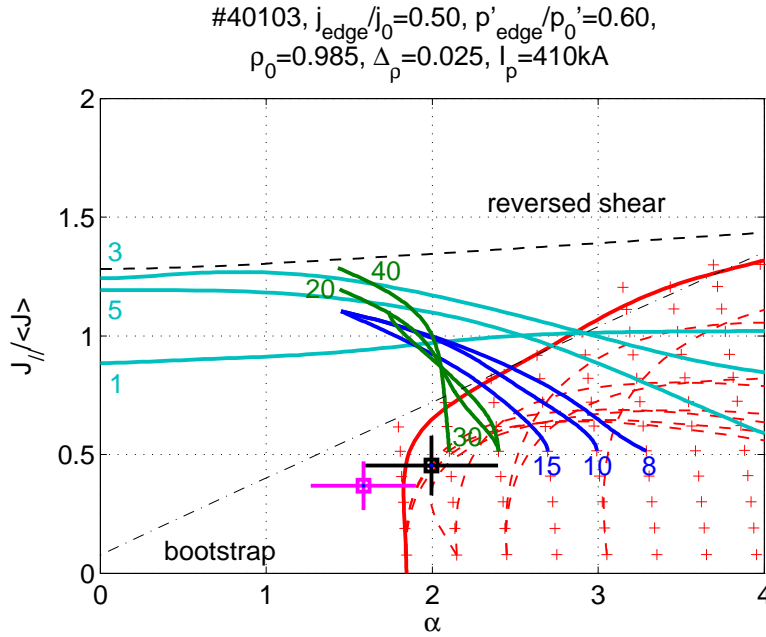


**Figure 5.24.:** MHD stability diagram for  $\lambda_{top} = 0.15$ : Ballooning and external kink stability represented as a function of the normalized pressure gradient.  $J_{||}/\langle J \rangle$  is the normalized pedestal parallel current density at maximum pressure gradient.

We expect that high- $n$  external kink modes are stabilized due to diamagnetic effects in the transport barrier [27, 39]. The largest unstable  $n_{max}$  is computed from equation (2.3.17) with  $R/L_{pi} = 100$ ,  $n_e = 3 \times 10^{19}$  and  $T_i = T_e$  for all configurations presented in the following.

### Squareness

Figure 5.24 shows the stability diagram of discharge #40103 ( $\lambda_{top} = 0.15$ ) as a function of normalized pressure gradient  $\alpha$ . The access to the second ballooning stable region is closed off. The increase in upper squareness increases the fraction of the trajectory of magnetic field lines in the unfavorable curvature region located on the outside of the torus, hence destabilizing pressure-driven modes. An increase of the current density above the collisionless bootstrap current density would be required to reduce the magnetic shear to a value low enough in order to give access to the ballooning second stable regime.

External kink modes with high  $n$  are stabilized by diamagnetic effects. Modes with  $n > n_{max} \sim 20$ , i.e. all dark green  $n$ 's, are expected to be stabilized. Medium  $n$ 's are closed off by the ballooning limit. Low  $n$ 's destabilize in the vicinity of the shear reversal,

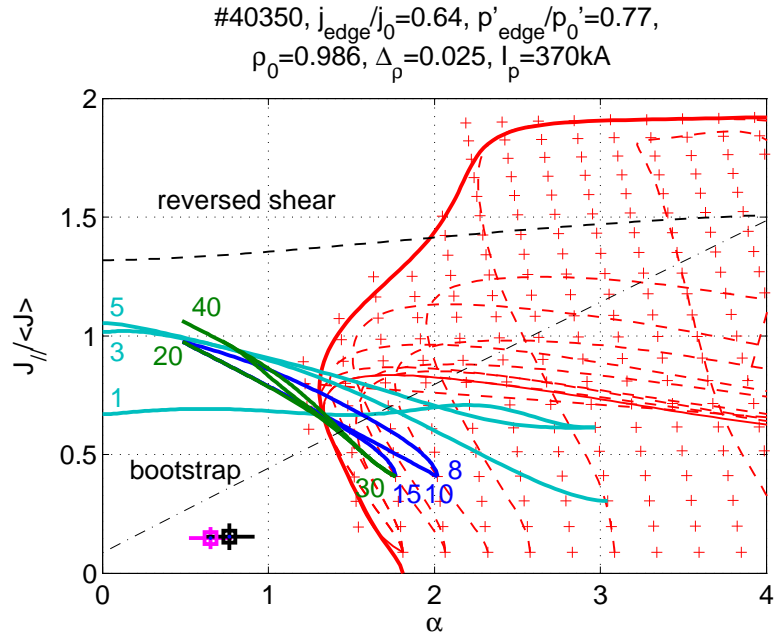


**Figure 5.25.:** MHD stability diagram for  $\delta_{top} = -0.25$ : Ballooning and external kink stability represented as a function of the normalized pressure gradient.  $J_{||}/\langle J \rangle$  is the normalized pedestal parallel current density at maximum pressure gradient.

where the mode structure exhibits modes with  $m/n = 13/5$ ,  $8/3$  and  $3/1$  close to the plasma edge (not shown here).

### Triangularity

Figure 5.25 shows the stability map of discharge #40350 ( $\delta_{top} = -0.25$ ,  $\lambda_{top} = 0$ ) as a function of  $\alpha$ . As for the case of  $\lambda_{top} = 0.15$  ( $\delta_{top} = 0.12$ ), the access to the second ballooning stable region is closed off. The decrease in upper triangularity reduces the fraction of the trajectory of magnetic field lines in the favorable curvature region located on the inside of the torus, hence destabilizing pressure-driven modes. Increased edge current density cannot improve the edge stability; external kinks destabilize for values of current density which are comparable to the collisionless bootstrap current density.

External kink modes with mode numbers higher than  $n_{max} \sim 30$  are stabilized by diamagnetic effects, medium and low  $n$ 's destabilize well below currents where shear reversal occurs. This is due to the relatively high ratio of  $j_{edge}/j_0 = 0.64$ , i.e. high current density on the separatrix which is in general destabilizing for external kinks. The mode amplitudes for  $n = 3 - 5$  are largest for the modes  $m/n = 14/5$  and  $8/3$ . It is

remarkable that  $n = 1$  is destabilized close to the rational surface  $q = 2$ , i.e. at high values of normalized current density.

The two experimental points are far away from any ideal MHD limit indicating that resistive effects may trigger the ELM. Despite the “relatively” low pedestal collisionality  $\nu_{ped}^* \sim 1-2$ , this result suggests that we observe resistive type-III ELMs as were previously suggested for TCV [104]. This hypothesis is supported by the degradation of energy confinement, figure 5.14(a), leading to low central and pedestal electron temperature, figure 5.15(a), regardless of the coupled ECH power. Further, the high ELM frequency and the low ELM energy loss, figure 5.18(c), compare well with those of high  $\nu_{ped}^*$  ELMy discharges.

### High elongation

In figure 5.26, the edge stability of discharge #40378 ( $\kappa = 1.85$ ) is presented. The access to the second ballooning stable region exists due to more favorable shaping. In accordance with the Mercier criteria [10], a combination of elongation and sufficient outward pointing triangularity is stabilizing ballooning modes. The improved stability associated with elongated “D” shaped plasmas is related to the fact that for such cross section a magnetic line has a relatively large fraction of its trajectory located in the favorable curvature region on the inside of the torus.

The low ratio of edge current density,  $j_{edge}/j_0 = 0.35$ , is favorable for the stability of external kink modes and, also due to the low value  $p'_{edge}/p'_0 = 0.39$ , high normalized pressure gradients can be reached before destabilizing ballooning modes. As before, high- $n$  modes with  $n > n_{max} \sim 20$  are stabilized by diamagnetic effects. Medium- $n$  modes represent the stability boundary for current-driven modes at relatively high edge pressure gradient. The low- $n$  modes become unstable close to shear reversal; we observe in the mode spectrum  $m/n = 13/5, 8/3$  and  $3/1$ . The  $n = 1$  mode destabilizes near the separatrix, i.e.  $q \sim 3$ , but has also a finite component  $2/1$  (not shown here).

### Small elongation

We expect that decreasing the elongation has the inverse effect on the pedestal stability than when increasing, as the same arguments mentioned before hold for small plasma elongation.

Figure 5.27 shows the pedestal stability as a function of  $\alpha$ . Not surprisingly, we

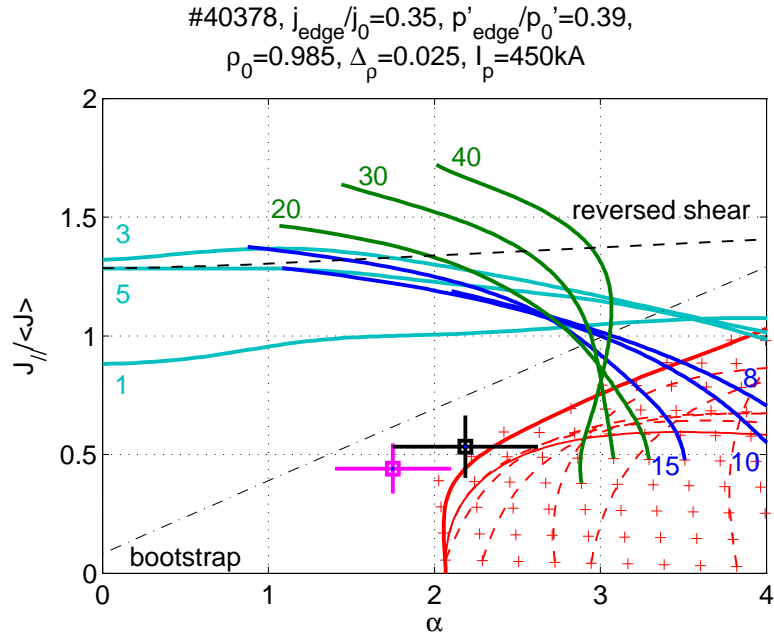


**Figure 5.26.:** MHD stability diagram for  $\kappa = 1.85$ : Ballooning and external kink stability represented as a function of the normalized pressure gradient.  $J_{\parallel}/\langle J \rangle$  is the normalized pedestal parallel current density at maximum pressure gradient.

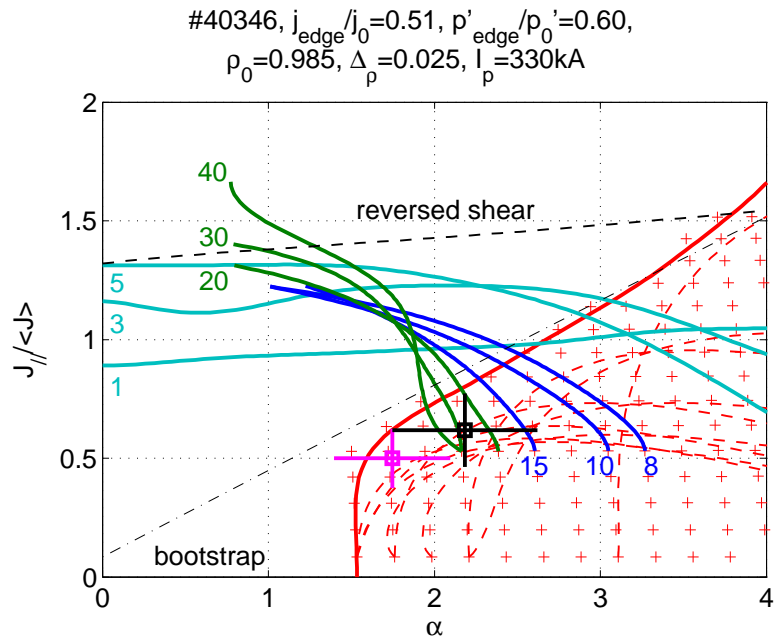


**Figure 5.27.:** MHD stability diagram for  $\kappa = 1.55$ : Ballooning and external kink stability represented as a function of the normalized pressure gradient.  $J_{\parallel}/\langle J \rangle$  is the normalized pedestal parallel current density at maximum pressure gradient.

find indeed opposite behavior of edge stability when decreasing  $\kappa$ . The access to second ballooning stability closes off, because of an increase in the ratio  $p'_{edge}/p'_0$  (see figure title) compared to the case with  $\kappa = 1.85$ . Likewise, external kink modes destabilize at lower values of normalized pressure gradient. High- $n$  toroidal modes are stable for  $n > n_{max} \sim 20$ , medium- $n$  restrict the second ballooning stable region. Low- $n$  modes become unstable at the plasma edge, with  $m/n = 13/5$  and  $8/3$  modes appearing in the mode structure. Modes with  $n < 5$  destabilize at current densities below that needed for shear reversal;  $m/n = 2/1$  is marginal stable (not shown here).

In general we conclude that the ideal MHD analysis of the pedestal stability describes well the pressure gradient limits met in the experiment for a wide range of different shapes. Only negative upper triangularity is an exception, where no high enough edge pressure gradient was attained to be relevant for ideal MHD. This observations suggests that, in this case, resistive effects play a role in triggering the ELMs.

## 5.4. Conclusion

In this chapter we investigated the ELMy H-mode regime in terms of ELM characteristics, pedestal quantities, plasma shape and divertor configuration. There is evidence that the type-I ELM regime is attainable on TCV at  $\sim 1$  MW of total heating power. The operational boundary of the edge pedestal is well explained by the Alfvén drift wave, ballooning and external kink stability limits. The energy loss per ELM was shown to vary with the pedestal collisionality; the fractional power loss is approximately constant over wide ranges of pedestal collisionality, but exhibits a bifurcation between standard single-null and snowflake configuration. A more thorough exploration of the type-I ELM regime, however, would require heating powers above 1 MW, which was only available towards the end of these studies.

We confirmed the scaling of pedestal width for electron pressure as a function of poloidal beta [79]. Other proposed scalings, based on ion Larmor radius, electron density of collisionality, did not fit our data very well. The exponent in the  $\beta$  dependence found by fitting the experimental data is somewhat smaller than what is indicated in the literature, which may be related to the different heating of H-mode plasmas at TCV compared to other machines. In order to reduce uncertainties in this model, further studies are

necessary to extend the parameter space towards higher poloidal pressure and a larger range in pedestal density.

The pedestal height, width and gradient of the electron temperature and density edge profile were separately investigated. It was found that their scaling with heating power follows in general the scalings found on other machines. Exceptions are observed for discharges with low collisionality, where in some sense inverse trends are observed suggesting a change in the transport regime from ITG to TEM dominated transport. This interpretation is backed up by the observation of decreasing density peaking at lower plasma collisionality, which is contrary to observations on other tokamaks where ion heating is dominant.

Finally, the dependence of pedestal properties upon plasma shape was investigated taking advantage of TCV's unique capability plasma shaping. Important changes in the ELM frequency and energy exhaust as well as in the pressure pedestal height were found when varying upper triangularity and squareness. By increasing the plasma elongation, the maximum stable pedestal pressure gradient could be increased. The limiting pedestal pressure gradient were computed by ideal MHD and agreed well with the experimental observations. The H-mode database featuring various plasma shapes, however, is still sparse and needs further experiments to prove scaling of pedestal quantities with plasma shape parameters.



## 6. Temporal evolution of the H-mode pedestal during an ELM cycle

The behavior of the electron pressure pedestal during an ELM cycle is subject of study on several machines. It has been found that the gradient of the edge pressure profile tends to saturate shortly before a type-I ELM, whilst the pressure pedestal height may still increase [69, 105]. These experimental results are partly in contradiction with common models of coupled external kink-ballooning modes causing the destabilization of the pedestal and, eventually, an ELM. Also, distinct phases have been found in the build-up of the plasma edge profiles after their relaxation caused by an ELM crash indicating that the recovery of electron temperature and density are correlated [106].

In this chapter, the temporal evolution of the electron pressure pedestal during an ELM cycle is investigated for type-I, large and type-III ELMs. By means of coherent data averaging including data from several discharges, draw-backs of the low time resolution of the Thomson scattering system can be partly overcome. Composite profiles are constructed in the millisecond range before and after the ELM crash revealing the critical pressure gradient before and the pedestal relaxation after the ELM onset time. Ideal MHD calculations of the pedestal stability have been carried out to interpret the experimental data and verify the theory of coupled external kink-ballooning modes.

## 6.1. Diagnostic methods and discharge operation parameters

In this section, the method of coherent data averaging is presented, its limitations and error sources discussed. In the second part, typical plasma parameters for the discharges used in this study are presented.

### 6.1.1. Coherent data averaging and binning technique

Coherent averaging of repetitive and reproducible single events is an established technique to reduce the effects of fluctuations and noise [107]. It is particularly appropriate to ELMs in the sense that the  $D_\alpha$  peak, attributed to enhanced divertor recycling, can be reliably identified. Assigning the peak in  $D_\alpha$  to zero in a new timebase permits for sorting and averaging of data with respect to this relative timebase, yielding a coherently averaged set of data. Since the ELM frequency is sufficiently constant, a well defined interval on either side of the reference time can be fixed. Coherent averaging is also of particular interest to increase the effective time resolution of a data set if it is acquired at marginal sampling frequency. In this case, the data from many measurements, from a single shot or several reproducible shots, are binned in short time intervals according to the new timebase [76, 104]. Binning of the data decreases the sampling rate of the coherent data but improves statistics considerably.

For the analysis of the temporal evolution of the H-mode pedestal during an ELM cycle, the randomly sampled Thomson scattering data from several identical discharges has been resampled in time with respect to the time of the next ELM event. This procedure allows to obtain profile measurements with high temporal resolution for a typical ELM cycle and is applicable, if the ELM frequency does not vary strongly. In a second step, the profile measurements were binned according to narrow time intervals in the ELM cycle. The data averaging allows for a better coverage of the pedestal and, therefore, improves considerably the results of the pedestal fitting.

Figure 6.1 shows the number of individual profiles that are combined as function of the coherent ELM timebase for the three data sets which will be discussed in this chapter. The width of the histogram bar represents the width of the bin in time. The binned data was mapped onto a horizontal plane crossing the magnetic axis and fitted by a modified tanh-function, equation (3.6.1), yielding pedestal height, width, gradient and normalized

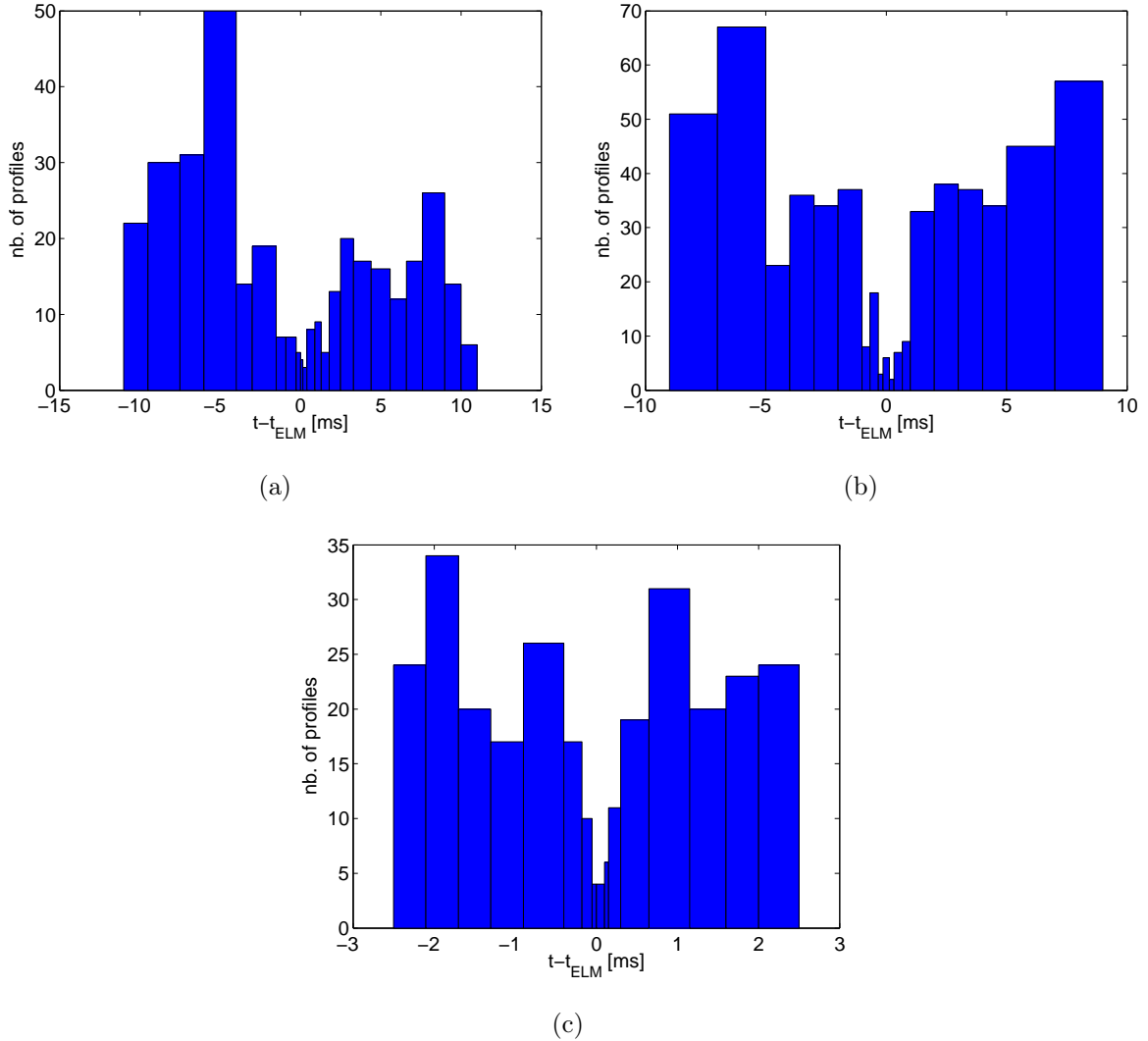


**Figure 6.1.:** Histograms of number of profiles used for fitting of temporal evolution of H-mode pedestal during an ELM cycle: Data set for pedestal fitting in H-mode with (a) type-I, (b) large ELMs and (c) type-III ELMs.

radial position during a “coherent” ELM cycle. For comparison and verification of the results, soft X-ray emission traces from DMPX, line-integrated density and the gas flux were also coherently averaged.

The uncertainties in the pedestal quantities are estimated using standard error propagation techniques. Due to the large number of data points in the fitting procedure, the statistical uncertainties are usually smaller than one would obtain from a single fitted profile. The errors of more concern are systematic errors, which might be caused by (1) variations in individual profiles due to underlying turbulence, (2) limitations of the

spatial resolution of the Thomson scattering system, (3) limitations in the energetic resolution of the polychromators and other sources. It is possible that there is an additional systematic error related to the position of the Thomson data in poloidal flux coordinates relative to the separatrix. Such errors are thought to be small and if they exist, would cause all estimated pedestal widths to be erroneous in some way but would have little effect on the temporal trends, which are of primary interest in this chapter.

### 6.1.2. Discharge characteristics

The temporal evolution of the pedestal height, width and gradient of electron temperature, density and pressure are examined, in the following, for three different power cases. Multiple repeat discharges were obtained for each power level and were used to produce composite data sets for studying the temporal pedestal evolution. Table 6.1 gives the typical plasma parameters for these discharges. All values are given in absolute values (except of the normalized ELM energy loss); no renormalization of quantities to ELM amplitude or others was applied during the pedestal fitting procedure. The first two series of discharges, exhibiting relatively low values of plasma collisionality, had the ion  $\mathbf{B} \times \nabla \mathbf{B}$  drift directing towards the X-point. In the third series of discharges with high pedestal collisionality, the ion  $\mathbf{B} \times \nabla \mathbf{B}$  drift was directed away from the X-point. All discharges had a single-null magnetic divertor.

For a better coverage of the edge pedestal by the spatial channels of the Thomson scattering system, a slow vertical plasma sweep was programmed with a displacement of the whole plasma by  $\Delta z \sim \pm 1.5$  cm during  $\sim 0.5$  s of the stationary ELMing phase.

## 6.2. Temporal evolution of pedestal properties

In this section, the temporal evolution of pedestal parameters based on composite pedestal profiles is presented for type-I, large and type-III ELMs. The behavior of electron temperature, density and pressure pedestal during an ELM cycle is analyzed. Finally, results are presented that show a radial displacement of the location of maximum gradient during the ELM cycle.

Here, we will only show the results from the fitting procedure of the electron pedestal profiles. The individual profiles, including experimental data and the fit, can be found in chapter D.

ELM type	I	large	III
nb.	14	14	10
$P_{tot}$	1.0	0.6	0.5
$P_{thr}$	0.3	0.3	0.4
$f_{ELM}$	$40 \pm 10$	$65 \pm 15$	$215 \pm 30$
$\frac{\Delta W_{ELM}}{W_{tot}}$	$0.20 \pm 0.03$	$0.14 \pm 0.03$	$0.02 \pm 0.01$
$I_p$	370	370	420
$q_{95}$	2.3	2.3	2.6
$n_{el}$	$3.2 \pm 0.2$	$3.4 \pm 0.2$	$4.2 \pm 0.15$
$\delta$	0.45	0.45	0.60
$\kappa$	1.68	1.68	1.70
$\nu_{ped}^*$	$0.40 \pm 0.05$	$0.65 \pm 0.08$	$2.5 \pm 0.25$
$\beta_N$	$1.05 \pm 0.05$	$0.80 \pm 0.05$	$0.45 \pm 0.02$
$H_{IPB98(y,2)}$	$0.95 \pm 0.05$	$0.75 \pm 0.05$	$0.45 \pm 0.02$

**Table 6.1.:** Operational parameters for discharges used in this study: Given is the ELM type, the number of discharges used for coherent averaging, the total heating power  $P_{tot}$  [MW], the threshold power  $P_{thr}$  [MW] for L-H transition, ELM frequency  $f_{ELM}$  [Hz], normalized ELM energy loss  $\Delta W_{ELM}/W_{tot}$  measured by the diamagnetic loop, plasma current  $I_p$  [kA], safety factor  $q_{95}$  at  $\rho = 0.95$ , line-integrated electron density  $n_{el}$  [ $10^{19}\text{m}^{-2}$ ], plasma elongation  $\kappa$  and triangularity  $\delta$ , pedestal resistivity  $\nu_{ped}^*$ , normalized global toroidal beta  $\beta_N$  and confinement enhancement factor relative to the  $H_{IPB98(y,2)}$  scaling prediction.

### 6.2.1. Type-I ELMs

The analysis of the time evolution of pedestal parameters is complicated due to variable time delays between adjacent ELMs. In addition, after an ELM crash, it is difficult to determine when the pedestal starts to rebuild. These problems are addressed by forming coherent time histories from many ELMs and several reproducible discharges. Composite pedestal profiles were assembled for a series of 14 identical discharges with high heating power, whose discharge characteristics are summarized in table 6.1. The ELMs were identified as type-I at low frequency ( $\sim 40$  Hz) with energy losses of  $\Delta W_{ELM}/W_{tot} \sim 20\%$  and a pedestal collisionality of  $\nu_{ped}^* \sim 0.5$ . The total plasma energy  $W_{tot}$  and the ELM

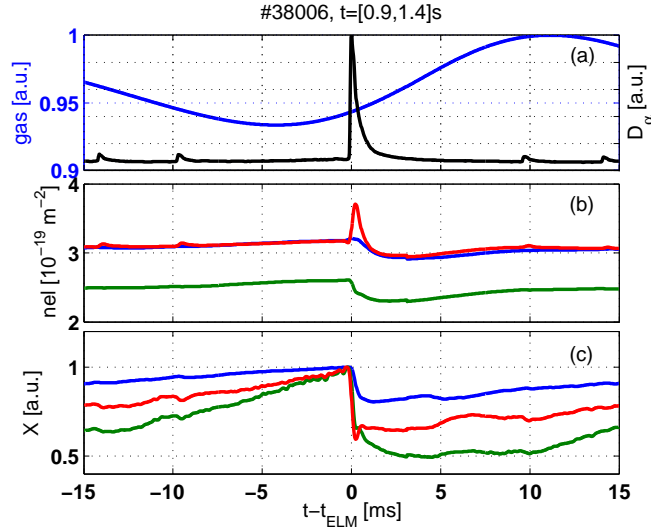


**Figure 6.2.:** Coherently averaged signals from (a) the gas valve with  $D_\alpha$  in black, (b) central (blue), HFS-edge (red) and LFS-edge (green) line-integrated density and (c) central (blue), HFS-edge (red) and LFS-edge (green) soft X-ray emission for a type-I ELM cycle. The profiles were coherently averaged over  $\sim 10$  ELMs.

energy loss  $\Delta W_{ELM}$  were measured by the diamagnetic loop. The profiles were measured during the stationary ELMing phase.

The electron temperature pedestal quantities are generally noisier than those of the electron density pedestal for two reasons: (1) The  $n_e$  pedestal is generally more pronounced and broader than the  $T_e$  pedestal leading to smaller uncertainties in the fits applying the modified tanh-function. (2) The sensitivity of the TCV edge Thomson scattering system to  $T_e$  variations is limited due to a configuration with only 3 spectral filters in the polychromators (see subsection 3.3.2). Simultaneous triggering of several lasers can improve the signal-to-noise ratio, but at the loss of time resolution (see subsection 3.7.2). The following analysis contains data from discharges with and without simultaneous laser triggering as well as from discharges, where the laser triggers were synchronized in real-time with the ELM events to improve the probability of a measurement close to an ELM crash (see subsection 3.7.3).

Figure 6.2 shows coherently averaged traces from a) the gas valve (normalized), b) the central and edge (HFS & LFS) line-integrated density from FIR and c) the central and edge (HFS & LFS) soft X-ray emission measured by DMPX (normalized). The edge channels observe a radial position that is approximately located at the pedestal top. The trace of the gas valve is given as an indicator for time intervals during the ELM cycle, in

which we may expect perturbations of the pedestal by re-ionization processes due to gas injection by the TCV control system. We note a general decrease in the gas flux during the coherent ELM cycle that is due to a linearly decreasing offset in the time interval used for the coherent average. The traces of line-integrated density show a clear drop of density on the LFS and even in the plasma center caused by the ELM event. The density overshoot on the HFS is due to increased particle flux in the divertor region shortly after the ELM event. The soft-X ray emission exhibits a clear drop in signal at the ELM crash, even in the center, and shows sawtooth (ST) activity synchronized with the ELMs, since every random behavior is averaged out.

The temporal evolution of the pedestal gradient, width and height are shown in figures 6.3-6.5 for the electron temperature, density and pressure. Steady-state values, i.e. the average value of the quantity during the ELM cycle, are shown as horizontal dashed lines.

### Temperature profile

The pedestal profiles show characteristic variations during the ELM cycle, figure 6.3. Gradient and height of the  $T_e$  pedestal increase throughout the pre-ELM phase, whilst the pedestal width remains approximately constant. It is unclear, if they start to approach saturation shortly before the ELM ( $\sim 1$  ms), as was found in ASDEX Upgrade (AUG) [105, 106, 108], and DIII-D [76]. Approximately  $100 \mu\text{s}$  before the characteristic ELM peak on  $D_\alpha$ , the  $T_e$  pedestal collapses possibly as a result of the onset of turbulence that is also observed on the magnetic pick-up coils (not shown here). Note that the  $D_\alpha$  emission is delayed by  $\sim 50 - 100 \mu\text{s}$  with respect to the collapse of the pedestal [107]. The gradient drops from  $\nabla T_e \approx 100 \rightarrow 50$  keV/m during the ELM crash, the pedestal height from  $T_e \approx 0.6 \rightarrow 0.4$  keV. The pedestal width strongly increases at the onset of the ELM indicating the disintegration of the barrier (figure 6.2(b)). We have to keep in mind that, in a narrow time window  $[-100, 100] \mu\text{s}$  around the ELM event, the profiles may be perturbed by filaments and others structures. The tanh-fit is not applicable in these cases and absolute values are erroneous.

In the first phase, until  $\sim 300 \mu\text{s}$  after the ELM crash, pedestal gradient and height quickly recover almost to the steady value. The observed time for the rebuild of the pedestal is  $\sim 10$  times shorter (here  $P_{tot} = 1$  MW,  $f_{ELM} \sim 40$  Hz,  $\Delta W_{ELM}/W_{tot} \sim 20\%$ ,  $H_{IPB98(y,2)} = 0.95$ ) than was found in AUG [105] ( $P_{tot} = 5$  MW,  $f_{ELM} \sim 100$  Hz,

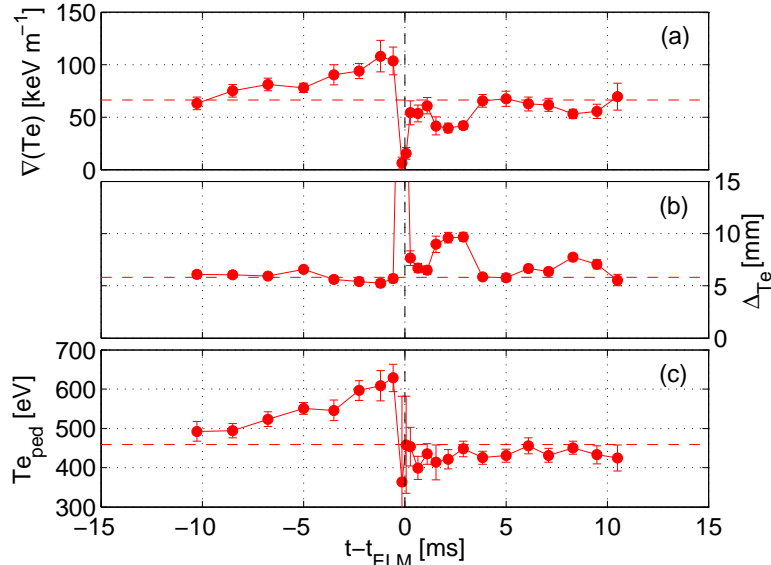


**Figure 6.3.:** Temporal evolution of the electron temperature pedestal in type-I ELMy H-mode: Shown are (a) pedestal radial gradient  $\nabla T_e$ , (b) pedestal width  $\Delta T_e$  and (c) pedestal height  $T_{e,ped}$ .

$\Delta W_{ELM}/W_{tot} \sim 5 - 10\%$ ,  $H_{IPB98(y,2)} \sim 0.9 - 1.0$ ) for typical type-I ELMs. The difference might be attributed to the fact that ELM energy losses in TCV are usually much larger than in other machines. For this series of discharges, the energy loss per ELM normalized to the plasma energy was  $\sim 20\%$ , a factor ten higher than for AUG. However, on TCV there appears to be a connection of the edge to the core region that permits fast energy exchange. We also observe a fast and significant collapse of  $T_e(0)$  at the time of the ELM.

A second fluctuation phase is observed after  $1 - 1.5$  ms, where the gradient suddenly drops and pedestal width increases, whilst pedestal height remains approximately constant. There is evidence of sawtooth (ST) activity during this phase, as can be seen on the soft X-ray traces in figure 6.2(c). The ST follows the ELM by  $\sim 4.5$  ms and is visible on both central and edge chord of the DMPX. We use a coherent ELM cycle, random behavior and noise should be averaged out, so we conclude that the ST is synchronized to the ELM. Comparison with the raw signal from a central channel of the DMPX shows that, in  $\sim 80\%$  of all cases, a ST follows the ELM with the time delay given above (not shown here).

A third phase follows  $\sim 4$  ms after the ELM indicating some steady-state condition for the height, while gradient and width slightly fluctuate.



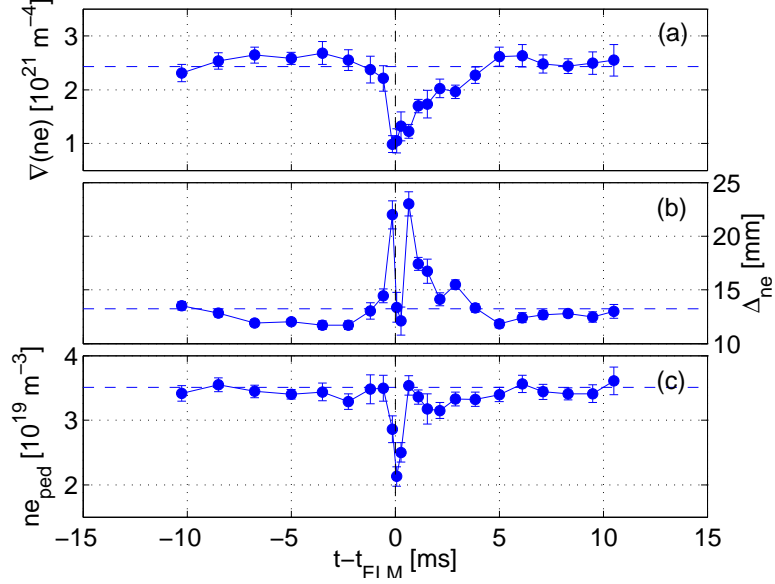


**Figure 6.4.:** Temporal evolution of the electron density pedestal in type-I ELMy H-mode: Shown are (a) pedestal radial gradient  $\nabla n_e$ , (b) pedestal width  $\Delta_{n_e}$  and (c) pedestal height  $n_{e,ped}$ .

### Density profile

During the pre-ELM phase, the density pedestal width decreases slightly by  $\sim 15\%$  of the steady value, figure 6.4(b). As consequence, the density gradient increases initially, whilst pedestal height is constant, yet error bars are within the steady value. At around 2 ms before the ELM, the pedestal width starts to grow. Thus, while the pedestal height remains approximately constant, the gradient decreases. Analysis of measurements from the magnetic probes revealed that damped low- $n$  modes can exist during this period. However, these modes do not seem to be a precursor, since cases with no mode activity occur as frequently as with activity.

The pedestal width strongly increases at  $\sim 500 \mu\text{s}$  or less before the ELM initiating the pedestal collapse. This increase happens before the peak on the magnetic probes. At the ELM, the pedestal density drops from  $n_e \approx 3.5 \rightarrow 2.5 \times 10^{19} \text{ m}^{-3}$ ; the gradient decreases from  $\nabla n_e \approx 2.2 \rightarrow 1.3 \times 10^{21} \text{ m}^{-4}$ . Pedestal values close to the ELM event should be used with caution due to the disadvantages of the fitting technique. It is also noticeable that the ELM crash provokes a peaking and subsequent drop in density even in the very center of the plasma (compare with figure 6.2(b)).

In the first phase, around 1 ms after the ELM, the density pedestal height has already reached the steady value, whilst the gradient increases only slowly due to the pedestal

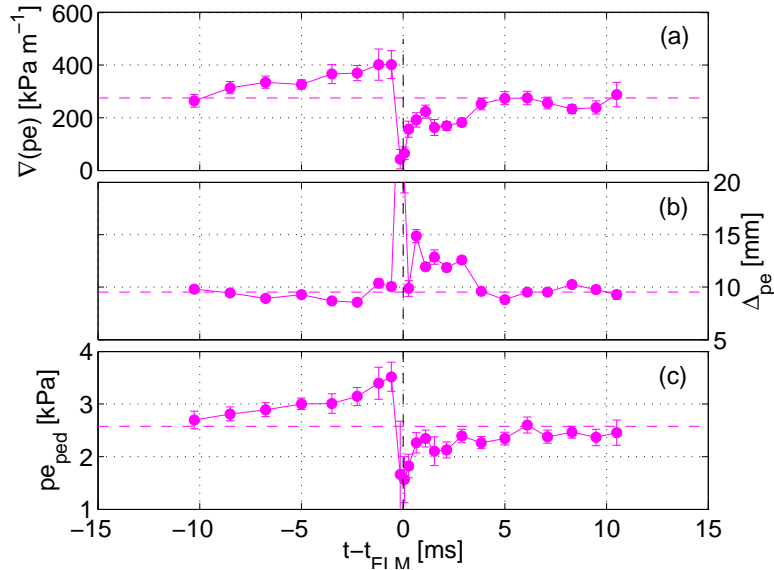


**Figure 6.5.:** Temporal evolution of the electron pressure pedestal in type-I ELMy H-mode: Shown are (a) pedestal radial gradient  $\nabla p_e$ , (b) pedestal width  $\Delta_{pe}$  and (c) pedestal height  $p_{e,ped}$ .

width that remains large. In the second phase, 1 – 3 ms after the crash, the pedestal properties exhibit some perturbations, although the general trend is a strong decrease in width, small decrease in height and increase in gradient. In the third phase starting at  $\sim 3$  ms, pedestal quantities relax slowly to their steady-state values. The general trends and the time delays are comparable with those of the density pedestal evolution measured in AUG [105].

### Pressure profile

Figure 6.5 shows the temporal evolution of (a) the pressure pedestal gradient, (b) width and (c) height. During the pre-ELM phase, pedestal gradient and height gradually increase, while the pedestal width remains constant or somewhat decreases. During 0.5 – 1.2 ms before the onset of the ELM, the pressure gradient appears to have reached its maximum, whilst pedestal height is still increasing. During this period it is observed that the temperature gradient increases and the density gradient decreases. The pedestal pressure height is mainly dominated by the increase in  $T_e$ , since  $n_e$  remains approximately constant. However, the size of the error bars and the “relatively” low time resolution does not allow to draw further conclusions. Shortly before the ELM crash, we observe anew the strong increase of the pedestal width. The pedestal gradient drops from

$\nabla p_e \approx 400 \rightarrow 150$  kPa/m, as observed in AUG [106], and the pedestal height exhibits a decline from  $p_e \approx 3.5 \rightarrow 1.8$  kPa.

In the first phase, the pressure pedestal starts to rebuild till  $\sim 1$  ms after the ELM, which is mainly due to the recovering of the pedestal height (or more explicitly the pedestal temperature). The pedestal width initially decreases strongly and then fluctuates at some value above steady-state, while the gradient is gradually evolving. In the second phase, 1–3 ms after the ELM, the recovery of the profile stagnates or even regresses, which is correlated with the appearance of ST activity. The pressure gradient decreases mainly due to a decrease in pedestal height. In the third phase, beginning around 4 ms after the ELM, pedestal quantities start to relax and approach steady-state values with some fluctuations mainly due to variations in the temperature pedestal width and gradient.

The small change of pressure gradient and the continuing increase in pedestal pressure, shortly before an ELM, makes the interpretation of these ELMs as infinite- $n$  ballooning instability improbable. As MHD simulations will show in subsection 6.3.1, the operational point of these discharges is close to stability limits set by coupled kink-ballooning modes.

### 6.2.2. Large ELMs

A series of 14 identical discharges with low additional EC-heating power, whose discharge characteristics is summarized in table 6.1, was chosen to obtain coherently averaged profiles. The ELMs were at low frequency ( $\sim 60$  Hz) and decelerated with increasing heating power, i.e. type-III ELM behavior. However, they exhibited relatively large ELM energy losses of  $\Delta W_{ELM}/W_{tot} \sim 15\%$  at relatively low collisionality  $\nu_{ped}^* \sim 0.7$ , typical for type-I ELMs, and are, therefore, called large ELMs.

The coherently averaged traces from (a) the gas valve (normalized), (b) the central and edge (HFS & LFS) line-integrated density from FIR and (c) the central and edge (HFS & LFS) soft X-ray emission measured by DMPX (normalized) are shown in figure 6.6. The locations of the edge signals correspond approximately to the position of the pedestal top. In this series of discharges we also observe ST synchronized with the ELMs. The traces of line-integrated density show a clear drop of density on the LFS and even in the plasma center caused by the ELM event. The density overshoot on the HFS is due to an increase in density in the divertor region shortly after the ELM crash. The soft-X ray emission exhibits a clear drop in signal at the ELM crash, even in the center, and exhibits a clear

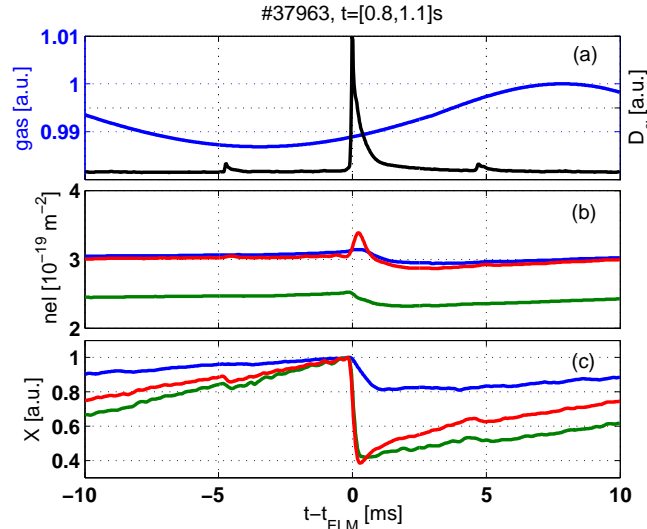


**Figure 6.6.:** Coherently averaged signals from (a) the gas valve with  $D_\alpha$  in black, (b) central (blue), HFS-edge (red) and LFS-edge (green) line-integrated density and (c) central (blue), HFS-edge (red) and LFS-edge (green) soft X-ray emission for a large ELM cycle. The profiles were coherently averaged over  $\sim 15$  ELMs.

sign of ST activity  $\sim 3.7$  ms before and after an ELM, whilst heating power was constant throughout the whole stationary ELMing phase.

The temporal evolution of pedestal gradient, width and height during the ELM cycle is shown in figures 6.7-6.9 for electron temperature, density and pressure.

### Temperature profile

The evolution of the temperature pedestal quantities is presented in figure 6.7. The temperature pedestal exhibits rebuilding during the pre-ELM phase that is mainly due to the pedestal height. The gradient remains approximately constant, while pedestal height and width increase. However, the pedestal build-up undergoes significant perturbations and trends appear to be broken, when a large ST crash occurs at  $\sim 4.7$  ms before the ELM. It is not totally clear what causes the strong break-in of the temperature gradient at  $\sim 1.5$  ms before the ELM crash, which is also visible on the density pedestal. It is no artifact from fitting, but seems to correlate with small ST crashes around this time, which are not visible on the averaged traces of the soft X-ray emission. Until  $\sim 0.5$  ms before the ELM crash, all pedestal quantities appear to be approximately stationary. At around  $200 \mu\text{s}$  before the ELM, the pedestal height starts to drop from  $T_e \approx 500 \rightarrow 360$  keV at

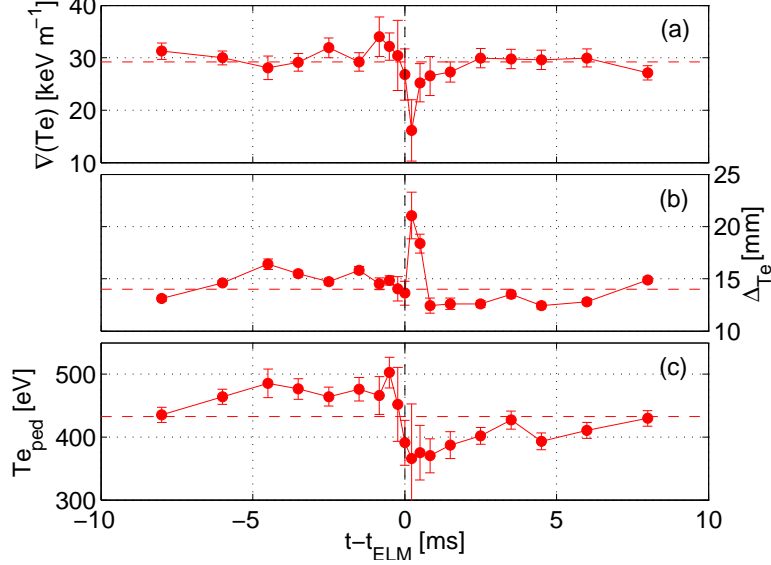


**Figure 6.7.:** Temporal evolution of the electron temperature pedestal in ELMy H-mode discharges with large ELMs: Shown are (a) pedestal radial gradient  $\nabla T_e$ , (b) pedestal width  $\Delta T_e$  and (c) pedestal height  $T_{e,ped}$ .

$\sim 200 \mu\text{s}$  after the ELM crash. During the same time interval, the gradient decreases from  $\nabla T_e \approx 30 \rightarrow 15 \text{ keV/m}$ , whilst the pedestal width strongly increases.

In the first recovery phase,  $200 - 500 \mu\text{s}$  after the ELM, the pedestal gradient rebuilds to around 80% of its value shortly before the ELM, while the pedestal height remains approximately constant below the steady value and the pedestal width strongly decreases. During the second phase till  $\sim 3.5 \text{ ms}$ , the pedestal height gradually increases, which restores the gradient to its steady-state value at approximately constant or slightly increasing pedestal width. In a third phase, between  $3.5 - 6 \text{ ms}$ , the pedestal parameters are perturbed by a post-ELM ST. Perturbations are most visible on pedestal height and width, whereas the gradient appears to be constant. Eventually the pedestal is fully rebuild  $\sim 7 - 8 \text{ ms}$  after the ELM.

### Density profile

Figure 6.8 shows the temporal evolution of the density pedestal parameters during the ELM cycle. In the pre-ELM phase, only little build-up of the density pedestal is observable. The pedestal gradient undergoes some perturbations until  $1.5 \text{ ms}$  before the ELM crash. Pedestal width and height show similar signs, but seem to be increasing. Again, the perturbations tend to coincidence with ST activity. The pedestal parameters

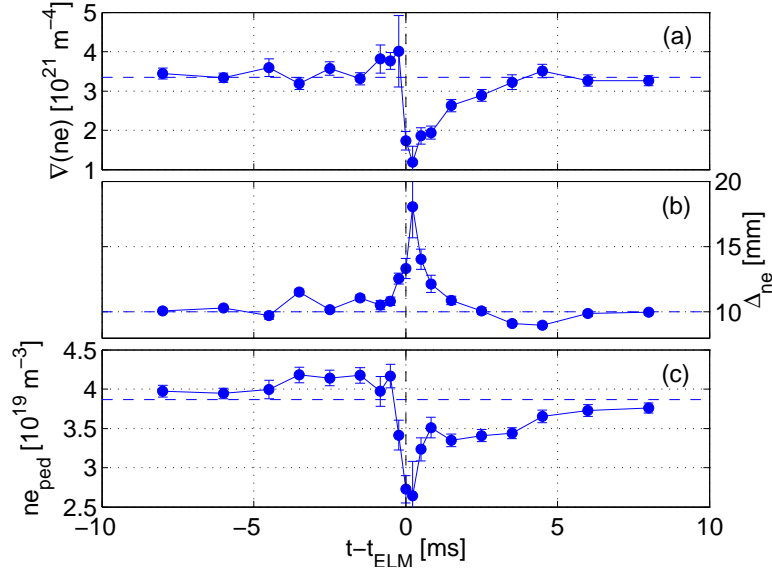


**Figure 6.8.:** Temporal evolution of the electron density pedestal in ELMy H-mode discharges with large ELMs: Shown are (a) pedestal radial gradient  $\nabla n_e$ , (b) pedestal width  $\Delta_{n_e}$  and (c) height  $n_{e,ped}$ .

appear to change only little in the interval  $\sim 0.5 - 0.8$  ms before the ELM. At  $\sim 250 \mu\text{s}$ , we observe the onset of strong barrier perturbations. The pedestal width increases, the pedestal height drops and the barrier starts to collapse. At the onset of the ELM, the density pedestal disintegrates and the gradient drops from  $\nabla n_e \approx 3.8 \rightarrow 1.2 \times 10^{21} \text{ m}^{-4}$ , the height from  $n_e \approx 4.2 \rightarrow 2.1 \times 10^{19} \text{ m}^{-3}$ . Central and edge line-integrated density indicates a change in plasma volume and/or shape and radial position at the time of the ELM (see figure 6.6(b)).

In the first recovery phase, till  $\sim 0.85$  ms after the crash, the pedestal height rebuilds gradually, whilst the gradient recovers only slowly due to a decreasing but still large pedestal width. In a second phase, around 1.5 ms after the ELM, the gradient recovers to its steady value, the pedestal height increases but stays below the steady value and the pedestal width decreases strongly and falls below its steady value. In a third phase, till  $\sim 6$  ms after the ELM, the pedestal rebuilds completely to its steady-state properties. Surprising is the fact that the post-ELM ST activity provokes fluctuations in the pedestal, as observed in the pre-ELM phase, which restore the steady-state conditions of the pedestal.

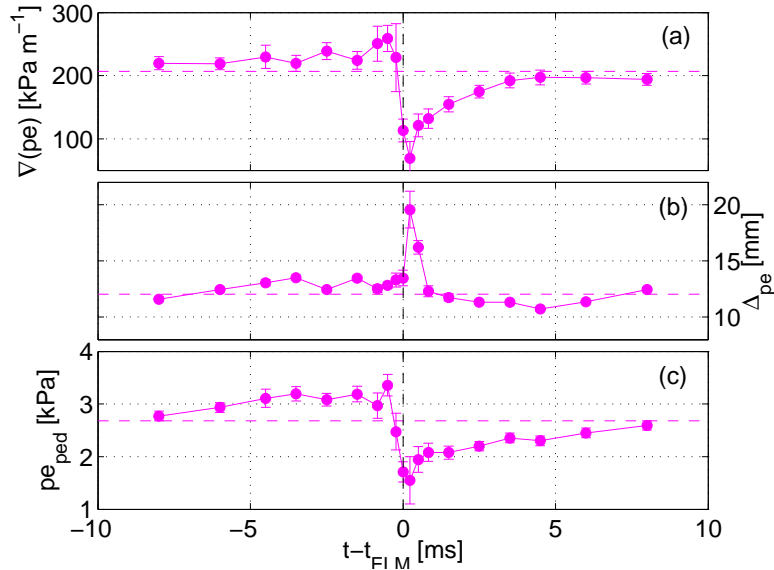


**Figure 6.9.:** Temporal evolution of the electron pressure pedestal in ELMy H-mode discharges with large ELMs: Shown are (a) pedestal radial gradient  $\nabla p_e$ , (b) pedestal width  $\Delta p_e$  and (c) height  $p_{e,ped}$ .

### Pressure profile

The temporal evolution of the pressure pedestal is shown in figure 6.9. In the pre-ELM phase, the pedestal quantities exhibit a build-up of the barrier. Pedestal gradient, width and height increase gradually, but are perturbed by ST activity. It is not clear, if pedestal parameters saturate before the ELM. There are indications that the pedestal height approaches saturation around 4 ms and the gradient around 0.5 – 1 ms before the crash, but large uncertainties do not allow further conclusions. At 200  $\mu$ s before the peak on  $D_\alpha$ , the pedestal start to collapse; the gradient drops from  $\nabla p_e \approx 260 \rightarrow 120$  kPa/m, the height from  $p_e \approx 3.2 \rightarrow 2.0$  kPa, whilst the width increases. At the ELM event, soft X-ray emission drops in the plasma core and edge, figure 6.6(c).

In the first post-ELM phase, the barrier quickly rebuilds till  $\sim 1$  ms after the ELM. From there on, during the second phase, the pedestal parameters evolve gradually. The gradient increases to its steady value mainly due to a decrease in pedestal width, whilst the pedestal height recovers slowly. Pedestal width and height are perturbed by the post-ELM ST activity, while the gradient remains constant. A final recovery of the pedestal is observed in the third phase beginning at around 6 ms after the ELM.

Strong fluctuations in the pressure gradient supposedly caused by ST activity make

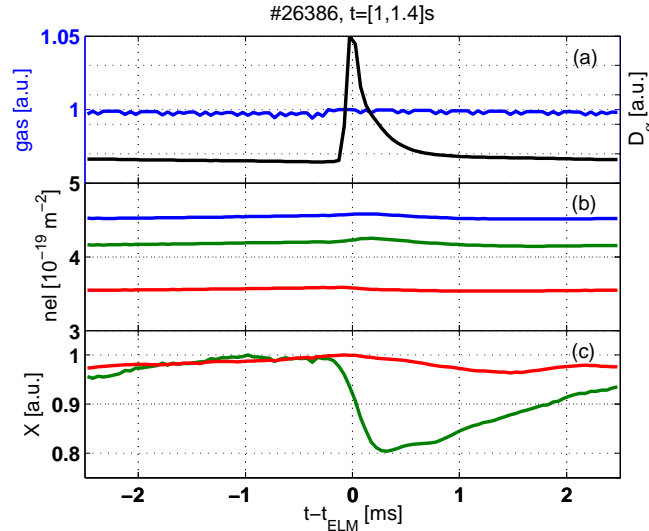


**Figure 6.10.:** Coherently averaged signals from the (a) gas valve, (b) central (blue) and edge (green) line-integrated density and (c) central (red) and LFS (green) soft X-ray emission for a type-III ELM cycle. The profiles were coherently averaged over  $\sim 85$  ELMs.

it difficult to quantify the change of the pressure gradient before the ELM. However, the data indicates that the pedestal gradient increases only by  $\sim 10\%$  in the last 2.5 ms before the ELM, which can be mainly attributed to an increase in pedestal height by about the same percentage. An investigation of the vicinity of the operational point to MHD stability limits is necessary to clarify this issue and is presented in subsection 6.3.2.

### 6.2.3. Type-III ELMs

The composite time history of the pedestal evolution during the ELM cycle is obtained from the Thomson data of 10 identical discharges, whose characteristics are given in table 6.1. The ELMs were identified as type-III at high frequency ( $\sim 215$  Hz,  $\Delta W_{ELM}/W_{tot} \sim 2 - 3\%$ ,  $\nu_{ped}^* \sim 2.5$ ). The total absorbed power of these discharges is of the order of the threshold power needed to obtain L-H transition. The data was taken from the stationary ELMing phase, the time marker for the ELM onset was chosen to be the peak in the  $D_\alpha$  signal.

Figure 6.10 shows coherently averaged traces from (a) the gas valve (normalized), (b) the central and edge line-integrated density from FIR and (c) the central and LFS soft X-ray emission measured by DMPX (normalized). The edge line-integrated density is measured at a radial position which is approximately at the pedestal top and shows



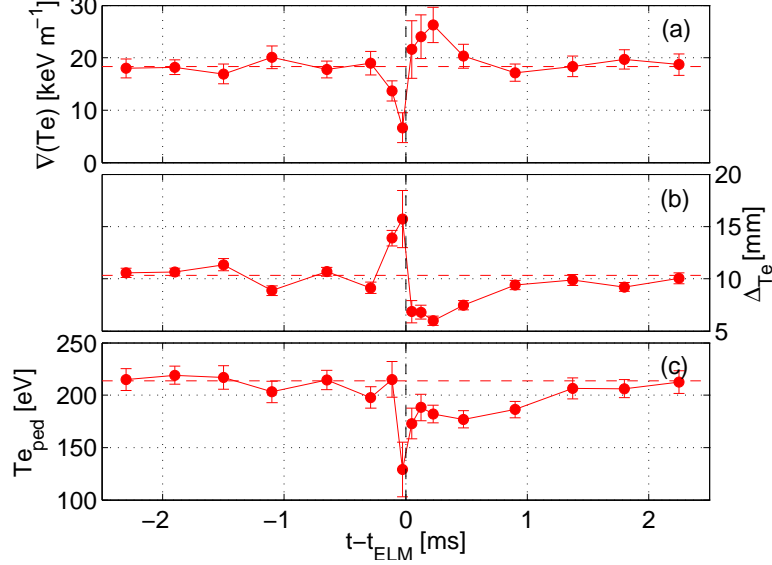


**Figure 6.11.:** Temporal evolution of the electron temperature pedestal in type-III ELMy H-mode: Shown are (a) pedestal radial gradient  $\nabla T_e$ , (b) pedestal width  $\Delta T_e$  and (c) pedestal height  $T_{e,ped}$ .

no significant change when the ELM occurs. The X-ray emission from the LFS chord exhibits a slow drop in intensity, while the central emission is only weakly affected by the ELM. Temporal evolution of the pedestal gradient, width and height are shown in figures 6.11-6.13 for the electron temperature, density and pressure.

### Temperature profile

In the pre-ELM phase, pedestal quantities are not subject to a pedestal build-up. Pedestal gradient, width and height slightly vary around their steady values till around  $250 \mu\text{s}$  before the  $D_\alpha$ -peak, when the gradient starts to drop as the pedestal width increases. The pedestal height remains approximately constant. During the ELM, the pedestal gradients drops from  $\nabla T_e \approx 19 \rightarrow 7 \text{ keV/m}$  and the height drops from  $T_e \approx 215 \rightarrow 150 \text{ eV}$ .

In the first post-ELM phase, until  $\sim 150 \mu\text{s}$  after the ELM onset, the pedestal height has recovered around 90% of its steady value, the gradient overshoots due to a very small pedestal width and reaches  $\sim 125\%$  of its steady or pre-ELM value. In the second phase, a gradual rebuild of pedestal width and height to steady-state values with a simultaneous decrease in pedestal gradient takes place until  $0.9 - 1.4 \text{ ms}$  after the ELM crash. It appears that the pedestal height recovers slightly slower than gradient and width.

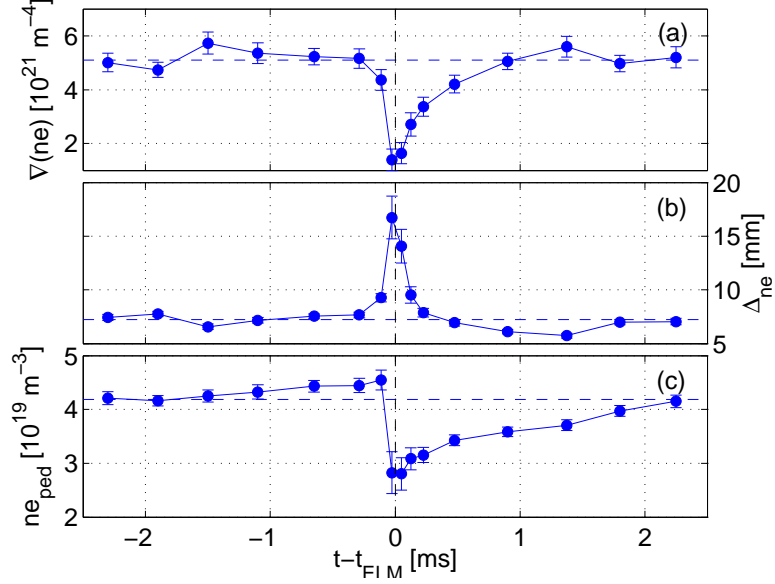


**Figure 6.12.:** Temporal evolution of the electron density pedestal in type-III ELMy H-mode: Shown are (a) pedestal radial gradient  $\nabla n_e$ , (b) pedestal width  $\Delta_{n_e}$  and (c) pedestal height  $n_{e,ped}$ .

### Density profile

During the pre-ELM phase, we observe an increase of the pedestal height by about 10%, while pedestal gradient and width remain approximately constant. At around  $100 \mu\text{s}$  before the ELM, the density gradient decreases as the pedestal width increases. During the ELM, the gradient drops from  $\nabla n_e \approx 5.2 \rightarrow 2.7 \times 10^{21} \text{ m}^{-4}$  and the height drops from  $n_e \approx 4.5 \rightarrow 3.1 \times 10^{19} \text{ m}^{-3}$ . In contrary, central and edge line-integrated density are subject to a small perturbation, but do not exhibit a significant drop in density.

In the post-ELM phase, the gradient rebuilds to steady value rather quickly in the time  $\sim 0.1 - 0.9 \text{ ms}$  after the ELM onset, while the pedestal width reaches its steady value at around  $1.8 \text{ ms}$  after the crash. The pedestal height needs the full post-ELM cycle to recover and reaches steady-state around  $2.25 \text{ ms}$  after the ELM.

### Pressure profile

Apart of some variations, pedestal gradient, height and width remain approximately at their steady-state values during the pre-ELM phase. Around  $100 \text{ ms}$  before the  $D_{\alpha}$ -peak, the gradient starts to decrease while the pedestal width increases. During the ELM crash, pedestal gradient drops from  $\nabla p_e \approx 150 \rightarrow 70 \text{ kPa/m}$  and pedestal height drops from

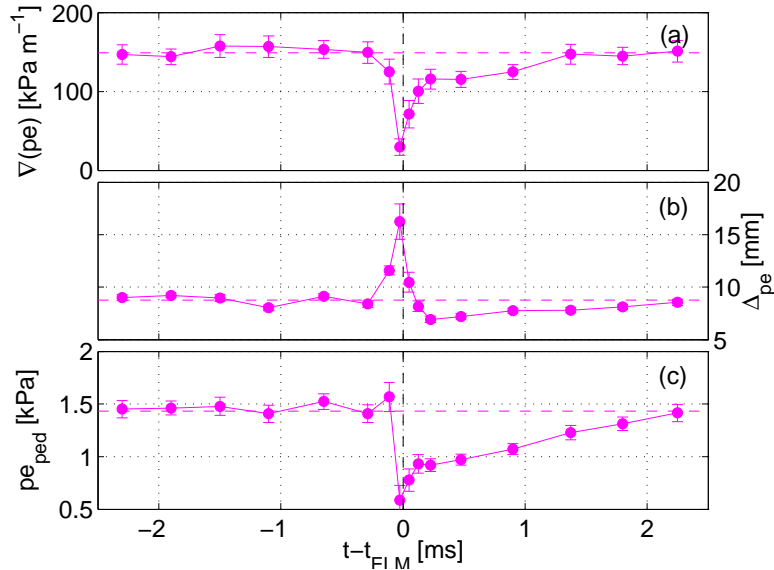


**Figure 6.13.:** Temporal evolution of the electron pressure pedestal in type-III ELMy H-mode: Shown are (a) pedestal radial gradient  $\nabla p_e$ , (b) pedestal width  $\Delta_{pe}$  and (c) pedestal height  $p_{e,ped}$ .

$p_e \approx 1.6 \rightarrow 0.8$  kPa. The central soft X-ray emission decreases slowly starting before the ELM; its drop is less sharp than in EC-heated H-modes.

In the first phase, until  $\sim 200 \mu\text{s}$  after the ELM onset, the pedestal gradient recovers quickly to around 75% of its steady value, while the pedestal height has regained only  $\sim 60\%$  of its steady value. In the second phase till  $\sim 1.4$  ms after the ELM, the gradient recovers to steady-state conditions, while the pedestal width seems to continue to increase. Slowest is the recovery of the pedestal height that approaches its steady value around 2.2 ms after the ELM onset.

The temporal evolution of the pressure profile does not provide evidence of pedestal build-up in the pre-ELM phase. Solely a relatively slow rebuild of the pedestal height in the post-ELM phase is visible. These observations suggest that ideal MHD stability arguments cannot explain this category of ELMs; more information is given in subsection 6.3.3. Taking into account plasma collisionality, this result is not surprising. A more realistic interpretation of the experimental results would require a resistive MHD analysis which is outside the scope of this work.

### 6.2.4. Displacement of the edge pedestal during the ELM cycle

A radial displacement of the H-mode pedestal has been predicted by models based on turbulence suppression by  $\mathbf{E} \times \mathbf{B}$  shear flow [109, 110] and recently measured in type-I ELMy H-mode in AUG [106]. Figures 6.14(a)-6.14(c) show the radial positions ( $R_0$ ) of the electron temperature (red), density (blue) and pressure (magenta) pedestal center with respect to the position of the separatrix ( $R_{LCFS}$ ) for type-I, large and type-III ELMy H-mode cases. Horizontal colored dashed lines represent the pedestal position in steady-state condition. The radial position of the barrier is computed from the results of the modified tanh-fit of the edge pedestal. A distance of 1 mm corresponds approximately to a difference of  $\Delta\rho = 5 \times 10^{-3}$  in  $\sqrt{\psi_N}$ .

The measurements show a clear sign of pedestal displacement from the separatrix towards the inside throughout the whole pre-ELM cycle for large and type-I ELMs, although the ST activity perturbs significantly the pedestal evolution. The displacement of the pedestal is mostly seen on the temperature profile and in type-I ELMy H-mode. It has been observed that the magnitude of this movement increases with increasing heating power. In type-I ELMy H-mode, the steady value of the radial position of the pressure pedestal is  $\rho_{stat.} \approx 0.995$  (not included are corrections in case of a high bootstrap current fraction). During the pre-ELM build-up of the pedestal, its radial position moves gradually inwards. Shortly before the ELM is observed on the  $D_\alpha$  signals, its position is  $\rho_{final} \approx 0.985$ . A similar but somewhat smaller movement is observed in type-III ELMy H-mode. The steady radial value of the pressure pedestal center is  $\rho_{stat.} \approx 0.985$ , the final position shortly before the ELM  $\rho_{final} \approx 0.980$ . The data sets suggest that in all cases the density pedestal is located closer to the LCFS than the temperature pedestal and that the radial position of the pressure profile is dominated by the temperature profile.

Errors in the absolute and relative values of the pedestal position  $R_0 - R_{LCFS}$  may occur for several reasons: (1) The exact determination of the LCFS is a non-trivial problem and is only accurate to within a few millimeters. For the set of discharges presented in this study, the equilibrium reconstructions were verified and, if necessary, corrected by matching the Thomson profiles from the upper and lower part of the plasma. The maximum correction applied on the vertical plasma position was  $< 2$  mm. (2) The effect of the bootstrap current density is not taken into account in the LIUQE [11] equilibrium reconstruction. In the case of a high and steep pedestal, the bootstrap current fraction is important. For the cases with high bootstrap current fraction, edge current

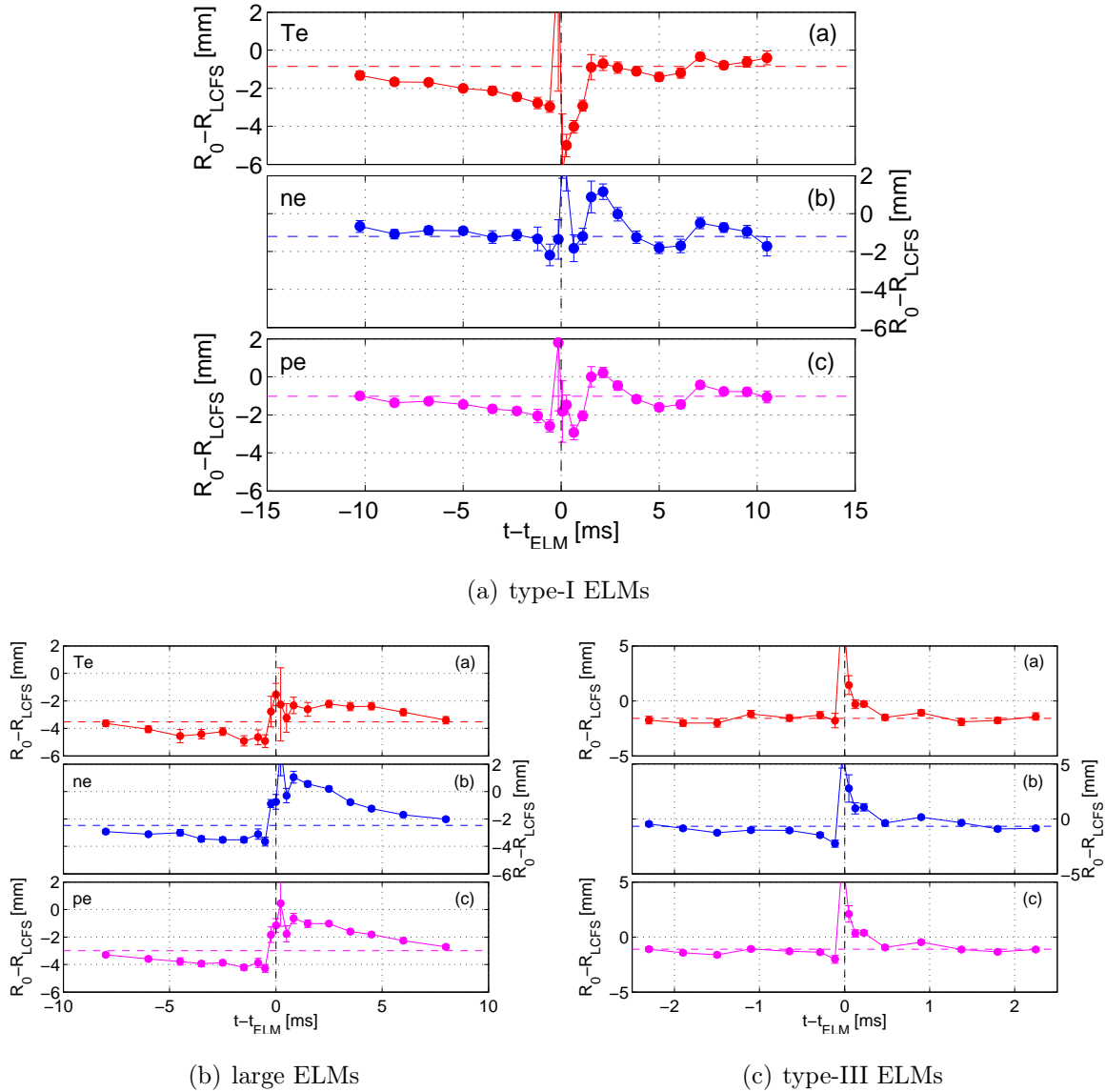


**Figure 6.14.:** Edge pedestal displacement during the ELM cycle: Shown are the positions of the pedestal center of electron temperature (red), density (blue) and pressure (magenta) pedestal during a (a) type-I, (b) large and (c) type-III ELM cycle.

increases the differential change in poloidal flux, i.e. the magnitude of radial pedestal movement would be presumably larger as indicated before. (3) The analysis of coherent profiles could amplify hidden systematic errors, however, would also average out statistical errors. Recent measurements of the pedestal electron temperature by ECE at 31 kHz and pedestal electron density by Li-beam at 20 kHz in AUG [106] reveal very similar trends of the temporal pedestal evolution.

Figure 6.15 shows examples of the pedestal profile during a type-I ELM cycle taken

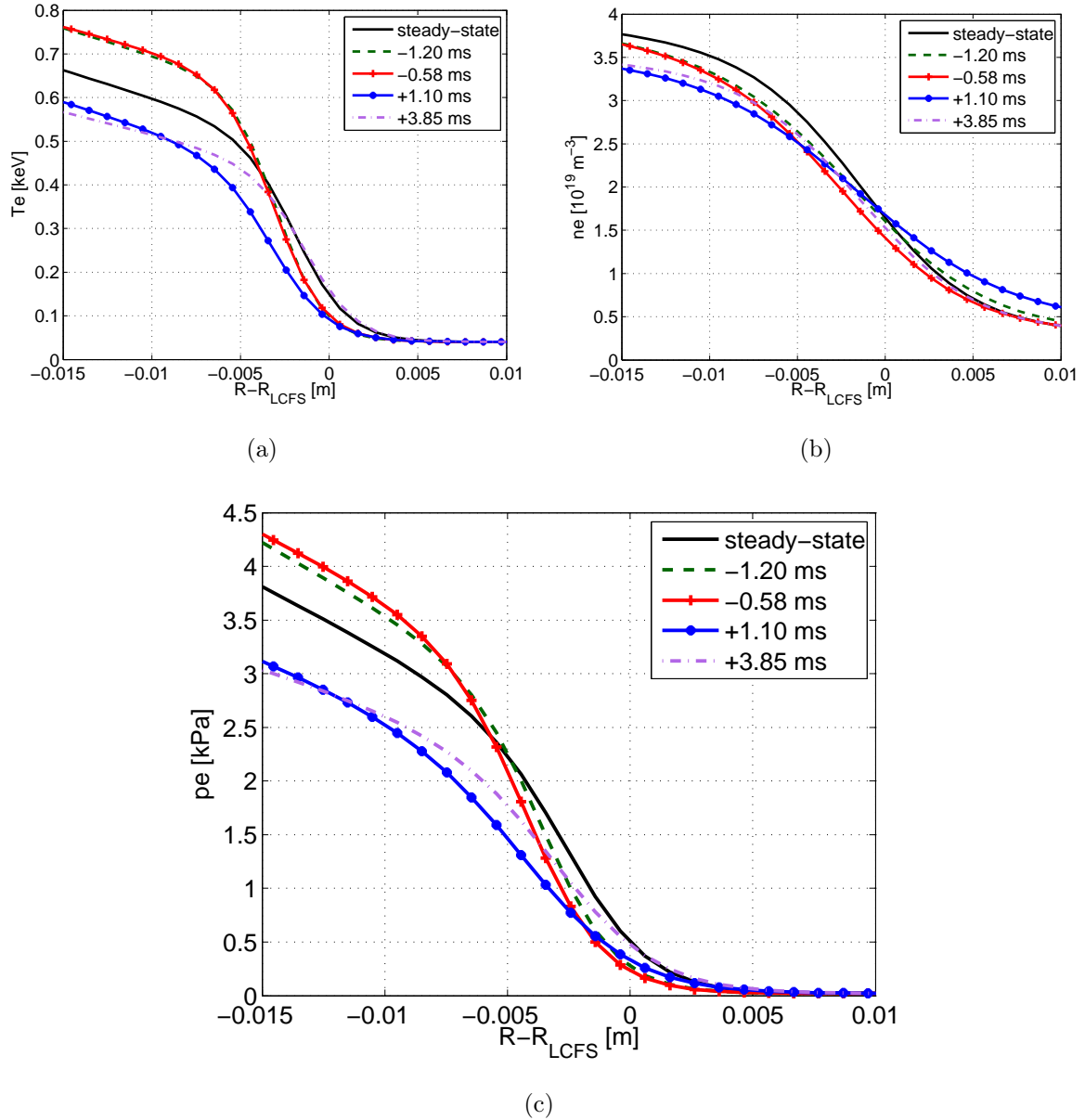


**Figure 6.15.:** Temporal evolution of electron pedestal during the type-I ELM cycle: Shown are (a) temperature, (b) density and (c) pressure profile evolution during the ELM cycle as function of a normalized radial coordinate, where  $R_{LCFS}$  denotes the position of the LCFS. Negative times correspond to the pre-ELM, positive times to the post-ELM phase. The different times are marked by different colors and line styles.

from the data set which also produced the results shown in figure 6.14(a). Starting from the “stationary” profile, i.e. a profile averaged over the whole ELM cycle, the central position of the  $T_e$ ,  $n_e$  and  $p_e$  pedestal propagates towards the plasma center during the

build-up in the pre-ELM phase. Noticeable is the significant increase in the temperature pedestal height and gradient. Approximately 1 ms before the ELM onset, the  $T_e$  pedestal is fully developed and stationary, while the density profile still evolves. The pressure pedestal also moves inwards as consequence of  $T_e$  and  $n_e$ . In the post-ELM phase, after collapse of the pedestal, the  $T_e$  profile recovers quickly and evolves towards the stationary profile located closer to the LCFS. The center of the  $n_e$  pedestal moves only little during the recovery phase. Consequently, the  $p_e$  pedestal exhibits an outward movement towards the stationary profile, mainly due to  $T_e$ . These observations are similar to data from AUG showing that the radial movement of the  $T_e$  pedestal is much stronger than that of the  $n_e$  pedestal.

At least two different theoretical models exist that describe time-dependent pedestal expansion [109–111]. Both models predict that the pedestal should expand inwards and are based on the hypothesis that pedestal transport coefficients are reduced by  $\mathbf{E} \times \mathbf{B}$  shear, which has been successfully modeled with ASTRA for a DIII-D discharge [112].

One model [109] is based on the numerical solution of coupled model equations for ion density and pressure. Calculated time histories predict a temporal increase in width and height of the ion density pedestal during an ELM cycle. This quantity could not be measured on TCV, but similar trends were observed on DIII-D [76]. The temporal evolution of width and height of the electron density pedestal in the additionally heated TCV discharges shows increasing height, but rather constant width.

The calculations also predict an increase in width and height for the ion temperature pedestal, which is consistent with DIII-D measurements, but could not be verified so far on TCV due to the lack of measurements of the ion pedestal. If one compares the temporal evolution of the electron temperature pedestal in TCV and AUG [105, 106], an increase in pedestal height is clearly visible in both machines. The TCV data also suggest that the electron temperature pedestal width increases during the ELM cycle. In summary, this numerical model makes several predictions that are qualitatively similar to the experimental observations on TCV and other machines.

Another time-dependent model describes the temporal evolution of fluctuating density, poloidal flow shear and pressure [110, 111]. Poloidal flow, radial electric field and pressure are linked through the force balance equation. The model predicts pedestal propagation as an advance of the region of reduced confinement that is able to push its way further into the plasma core.

Summarizing, both models describe barrier propagation as a natural phenomenon to be expected when a barrier is formed when turbulence is suppressed by  $\mathbf{E} \times \mathbf{B}$  shear. There is evidence that some of the trends observed in experiments on TCV and other machines can be described to some extent by these models.

### 6.3. Identification of the pedestal pressure gradient limit by ideal MHD

The ideal MHD stability limits of the pedestal were computed for equilibria of representative TCV discharges in ELMy H-mode (TCV-#: 38008, 37966, 26386). In these shots different types of ELMs were observed, if we follow the classification described in subsection 2.3.4. The stability map is computed with the stationary profile presented before, thus, for the sake of simplicity, does not include effects of pedestal propagation during the pre-ELM phase. We refer to subsection 4.3.2, where the general effect of the pedestal location onto pedestal stability is investigated.

The stability maps, figures 6.16-6.18, are plotted as function of the normalized pedestal parallel current density  $J_{//}/\langle J \rangle$  and normalized pedestal gradient  $\alpha$ .  $J_{//}$  is taken at the position where the pressure gradient is maximal,  $\langle J \rangle$  is the total plasma current normalized to the plasma cross sectional area. For the normalized pressure gradient, we use the definition  $\alpha \equiv \mu_0 (dp/d\psi) (dV/d\psi) \sqrt{V/(2\pi^2 R)}/2\pi^2$  [35] taken at the point of maximum pressure gradient in the pedestal, where  $p$  is the total pressure,  $V$  is the plasma volume,  $R$  the major radius and  $\psi$  the poloidal flux. The diagrams show the ballooning stability boundary as a solid red line and a dashed red line for the destabilization limit of the flux surface, where the pedestal gradient is maximal. The external kink stability limits are presented as cyan lines. Collisionless bootstrap and shear reversal are depicted as dash-dotted and dashed line, respectively. The pedestal width  $\Delta_\rho$  is given in  $\sqrt{\psi_N}$ , the pedestal center location  $\rho_0$  in the same coordinate. The ratio between edge and maximum pressure gradient  $p'_{edge}/p'_0$  and the ratio between edge and maximum current density  $j_{edge}/j_0$ , which influences the stability of ballooning and external kink modes, are given for each stability map.

The growth rate of the external kink modes was computed on a  $N_\psi \times N_\chi = 224 \times 224$  and  $256 \times 256$  grid and then extrapolated for a infinite grid size, where  $N_\psi$  and  $N_\chi$  are the number of radial and poloidal grid points. We expect that high- $n$  external kink modes



are stabilized due to diamagnetic effects in the transport barrier [27, 39]. The maximum unstable  $n$  is computed from equation (2.3.17) with  $R_0/L_{pi} = 100$ ,  $n_e = 3 \times 10^{19}$  and  $T_i = T_e$  for all configurations presented in the following. In general we find that high- $n$  ( $n \gtrsim 20 - 25$ ) external kinks are stable.

The experimental point corresponding to the stationary profiles is labeled as **A** and is computed from the electron pedestal profiles assuming  $T_i = T_e$  and  $Z_{eff} = 3$  (see also subsection 2.1.2). The current density is computed from the ohmic profile of the LIUQE reconstruction and the bootstrap current calculated on the basis of the kinetic profiles (see also subsection 2.1.2). The equilibrium is self-consistent including all corrections stated above. The horizontal error bar accounts for the propagation of the uncertainty in the electron pressure gradient into the total pressure gradient. The vertical error bar takes into account the uncertainty in the bootstrap current. The points **B** and **C** represent the conditions for certain times shortly before an ELM in the pre-ELM pedestal evolution. The point **D** is computed from profiles in the post-ELM phase around 0.5 – 1.5 ms after the ELM crash. For this equilibrium, the current density profile is taken from the last pre-ELM profile under assumption of negligible current diffusion during a total time delay of less than  $\sim 3$  ms during the ELM crash.

### 6.3.1. Type-I ELMs

In the frame of ideal MHD, high pedestal pressure gradients can lead to the destabilization of coupled external kink-ballooning modes which are generally associated with ELMs. The triggering of ELMs does not appear to be a simple threshold effect. Operation near a stability limit is a necessary but not a sufficient condition for triggering.

Figure 6.16 shows the stability map of a discharge taken from the set of type-I ELMy H-modes presented in subsection 6.1.2. The point corresponding to the inter-ELM profiles is marginal stable to high- and infinite- $n$  ballooning modes. Including the data from the profile build-up during the pre-ELM phase yields the points **B** ( $t - t_{ELM} = -5$  ms) and **C** ( $t - t_{ELM} = -1.5$  ms). We observe that pedestal conditions gradually evolve in such a way that they approach the medium- $n$  external kink mode stability limit. Eventually the ELM occurs and the pedestal relaxes. Point **D** ( $t - t_{ELM} = 1.5$  ms) represents the pedestal shortly after the ELM crash assuming negligible current diffusion during the ELM.

In general, experimental observations and predictions based on ideal MHD stability

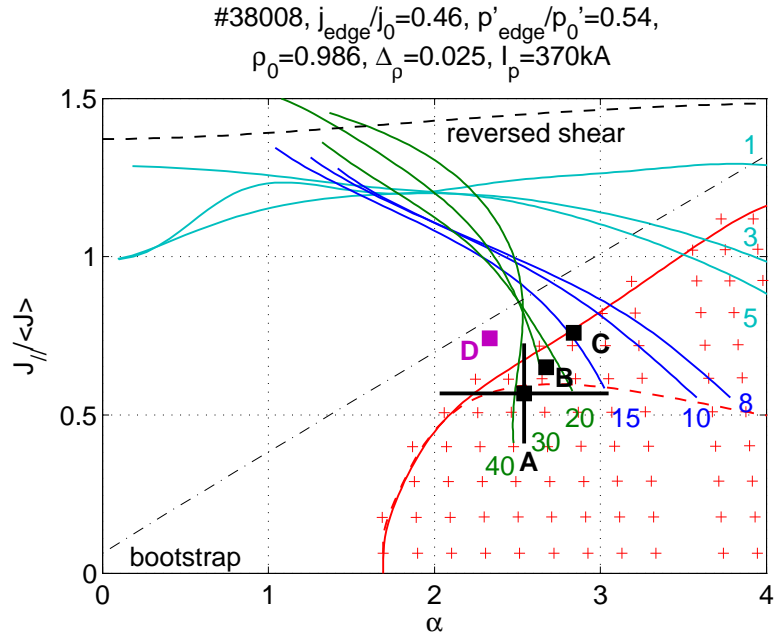


**Figure 6.16.:** Ideal MHD stability map for H-mode plasma with type-I ELMs: Shown is the experimental point **A**, which corresponds to the profile of the inter-ELM phase, and points **B**, **C** & **D** referring to the times  $t - t_{ELM} = \{-5.0, -1.0, +1.5\}$  ms in the ELM cycle with respect to the  $D_\alpha$ -peak, where negative times mean pre- and positive times post-ELM phase.

are in good agreement indicating that a high pressure gradient is a necessary but not sufficient criterion to trigger an ELM of type-I. At low pedestal resistivity, this pressure gradient can drive enough bootstrap current to destabilize medium- $n$  external kink modes, which is suggested as the main protagonist for the ELM destabilization. However, the pedestal shift towards the plasma center during the pedestal build-up in the pre-ELM phase may change the class of modes responsible for the stability limit (see also subsection 4.3.2).

### 6.3.2. Large ELMs

The discharges from the set of H-modes with large ELMs are characterized by a relatively low value of pedestal resistivity, which makes them well suited for analysis by means of ideal MHD. Figure 6.17 shows the stability map of one of these discharges and includes the temporal evolution of the operational point during the ELM cycle.

Under conditions described by the inter-ELM profile **A**, high- $n$  pressure-driven ballooning modes are unstable. Points **B** ( $t - t_{ELM} = -2.5$  ms) and **C** ( $t - t_{ELM} = -0.8$  ms)

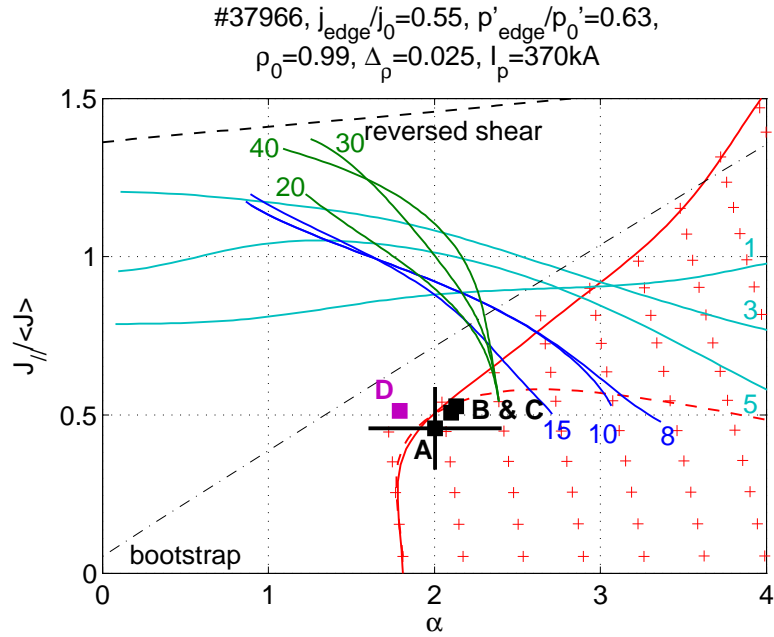


**Figure 6.17.:** Ideal MHD stability map for H-mode plasma with large ELMs: Shown is the experimental point **A**, which corresponds to the profile of the inter-ELM phase, and points **B,C & D** referring to the times  $t - t_{ELM} = \{-2.5, -0.8, +1.0\}$  ms in the ELM cycle with respect to the  $D_\alpha$ -peak, where negative times mean pre- and positive times post-ELM phase.

remain in the vicinity of the ballooning limit and show only little profile evolution with respect to **A**. The separation of point **D** ( $t - t_{ELM} = 0.5$  ms) from points **A-C** is insignificant. In general it is observed that the plasma state is in the vicinity of the ballooning stability limit during the whole pre-ELM cycle. The consideration of the pedestal displacement would move the experimental points **B** and **C** further in the ballooning unstable region.

For this type of discharges we conclude that an interpretation of the stability limits by ideal MHD gives a good agreement with the experimental data. The pressure gradient in the pedestal is mainly limited by large- $n$  modes, i.e. a narrow mode structure, which is coherent with common models.

### 6.3.3. Type-III ELMs

Type-III ELMs, exhibiting small ELM energy loss and high frequency, are found in discharges with high density and thus relatively high pedestal resistivity. These ELMs are likely driven by resistive modes beyond the scope of ideal MHD analysis. Data shown in figure 6.18 supports this hypothesis.

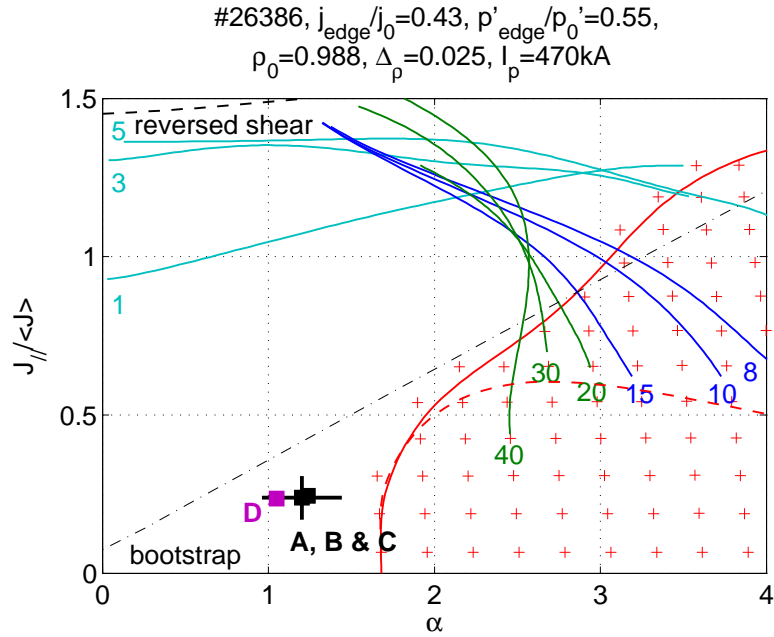


**Figure 6.18.:** Ideal MHD stability map for H-mode plasma with type-III ELMs: Shown is the experimental point A, which corresponds to the profile of the inter-ELM phase, and points B,C & D referring to the times  $t - t_{ELM} = \{-0.7, -0.2, +0.5\}$  ms in the ELM cycle with respect to the  $D_\alpha$ -peak, where negative times mean pre- and positive times post-ELM phase.

We observe that all experimental points are far off any ideal MHD stability limit, which agrees with former investigations [104]. The inclusion of the temporal evolution of the pedestal during the pre-ELM phase does not significantly alter the location of the experimental points. An interpretation by resistive MHD would be necessary to identify the corresponding unstable modes, but is beyond this work.

## 6.4. Conclusion

In this chapter, we investigated the temporal evolution of the pedestal properties during a type-I, large and type-III ELM cycle using results from Thomson scattering. We found coherent data averaging to be an appropriate method to study the profile evolution on a millisecond-scale, which cannot be naturally attained by the Thomson scattering diagnostic on TCV. The results show very similar trends to those from DIII-D and AUG. In particular, they indicate that the pedestal pressure gradient may saturate shortly before

the ELM onset. From the observations it is concluded that a high pedestal pressure gradient is a necessary but not sufficient explanation of the ELM event.

An analysis of the radial pedestal position during the ELM cycle was performed. The data shows clearly that the pedestal moves slightly outwards during the post-ELM and inwards during the pre-ELM phase, an effect that will clearly have an impact on the stability limits obtained from ideal MHD. The experimental observations compare well with results of similar experiments on AUG.

The interpretation of stability limits by ideal MHD agrees well with the experimental observations. The medium- $n$  current-driven and large- $n$  pressure driven modes play an important role in setting the maximal achievable pedestal pressure gradient in type-I and type-III ELMy H-mode, when plasma resistivity is sufficiently low. The limits of the ideal MHD theory become apparent in the case of small type-III ELMs, observed under conditions of high plasma resistivity.

## 7. Summary and conclusion

This thesis primarily presents experimental studies and MHD stability calculations in the investigation of the H-mode pedestal in different plasma configurations in the TCV tokamak. The pedestal was characterized with experimental results from Thomson scattering and interpreted by modeling of the ideal MHD stability limits in the plasma edge region. The study comprises type-I and type-III ELM regimes as well as various shapes in single-null (SN) and snowflake (SF) divertor configurations. It takes advantage of the unique capabilities of TCV in terms of plasma shaping and heating by electron cyclotron waves.

### **Thomson scattering**

The TCV Thomson scattering system was upgraded for measurements of transport barriers in the core (eITBs) and near the edge (ETB). This task implied an adaptation of the optical system for high spatial resolution measurements, optimization of the polychromators for high temperature regimes, improvements of the analysis of the recorded signals, development of a cross-calibration against the FIR interferometer and the development of a method to synchronize the Thomson scattering measurements with plasma events. These upgrades have contributed to the performance and reliability of the diagnostic for all scenarios exploited at the present time and for future experiments on TCV.

### **Snowflake divertor**

The H-mode pedestal properties and stability limits of the novel snowflake divertor were addressed by modeling and experiment.

It was found that H-mode in SF configurations in TCV can be obtained without penalties from increased vertical instability. Modeling showed that a SF configuration

in H-mode has higher MHD stability limits in the pedestal region than an equivalent SN that is mainly due to an increase in edge magnetic shear. This is a consequence of the magnetic field topology of this configuration and this advantage is retained in the presence of bootstrap current in the pedestal. Comparison with the SN configuration however revealed that pedestal stability in the SF is more sensitive to the radial position of the pressure gradient and edge bootstrap current, which affects the magnetic shear profile.

Experiments with a SF-plus configurations (a variety of the SF, closer to SN) displayed improved energy confinement accompanied by a lower average ELM power loss, whilst the pedestal properties do not change significantly. According to MHD stability calculations, the achievable pressure gradient ought to be higher, but was not observed experimentally.

These investigations lead to the conclusion that a SF configuration has significant advantages for H-mode operation with regard to confinement, MHD stability and ELM characteristics, but further studies are needed. The SF configuration may be varied considerably and a comparison between experiment and modeling over a wider configuration range may lead to further performance increases.

### **H-mode scenarios**

Experiments in H-mode plasmas, for many plasma shapes, divertor configurations (SN and SF), and heating power levels were performed, compared and interpreted using ideal MHD stability calculations. Measurements of pedestal temperature and density allowed an identification of the operational boundaries for type-III, type-I and large ELM regimes.

Applying additional heating by electron cyclotron waves (ECRH), it was found that energy confinement increases as a consequence of changes in pedestal properties. The scaling of the pedestal pressure width was tested against different models and it was found that, for TCV, the scaling with the normalized poloidal pressure at the pedestal top is weaker than the square root dependence found elsewhere.

With increasing heating power a transition from type-III to type-I ELM is observed. The stability limits of the different ELM regimes were identified by means of ideal MHD. It was found that high- $n$  ballooning modes define the limit in case of type-III and large ELMs, whereas type-I ELMs are limited by intermediate- $n$  external kink modes.

As already known from experiments on other tokamaks, plasma shaping has strong impact on the pedestal properties and ELM characteristics. Strong changes in the ELM

frequency and energy exhaust as well as in the pressure pedestal height were found on TCV when upper triangularity and squareness were varied. By increasing the plasma elongation, the maximum stable pedestal pressure gradient was increased. These results are in good agreement with expectations based on ideal MHD stability.

### **Temporal evolution of the H-mode pedestal during an ELM cycle**

The temporal evolution of the pedestal properties was investigated for different ELM regimes using Thomson scattering to measure electron temperature and density profile near the edge with high spatial resolution.

In these experiments, random sampling, combined with coherent averaging, was used to map out the time evolution of the pedestal on the millisecond scale, with an effective sampling rate that was not attainable by the intrinsic diagnostic sampling rate.

Results from this analysis agree well with results reported from other machines. The electron pressure gradient tends to saturate shortly before an ELM, whilst the pedestal height of the pressure profile still increases. This leads to the conclusion that a critical pressure gradient only, as derived from MHD stability calculations, is not sufficient to explain ELM triggering, but rather the combination of pedestal height and gradient.

Most of the H-mode scenarios and plasma configurations presented in this thesis have implications for the performance of a tokamak in general. The observations contribute to the validation of theoretical models which will be applied to predict stability and performance of future devices. The TCV results have confirmed the strong influence of plasma shaping on the stability of the H-mode pedestal and the ELM characteristics. These findings will contribute to the development of advanced scenarios of tokamak operation in future devices.



# A. Code settings

## A.1. CHEASE settings

Input parameter file for CHEASE:

```
&EQDATA
CURRT=0.37264048600348, ROEXP=8.79999995E-01, BOEXP=1.4347283,
SIGNIPXP=1.00000000E+00, SIGNBOXP=1.00000000E+00,
NSURF=6, ELONG=1.7, TRIANG=0.4, BEANS=0, CETA=0.24, SGMA=0, ASPCT=3.92531276E+00,
NFUNRHO=0,
RELAX=0.5, NDIAGOP=1, NBSEXPQ=0000,
NPROPT=2,
NIDEAL=6, NPLOT=1, NTCASE=0, NSMOOTH=1,
NS=72, NT=72, NPSI=256, NCHI=512, NISO=256, NTNNOVA=72,
NPPFUN=4, NPP=1, NFUNC=4,
NSTTP=3, NPROPT=3,
CPRESS=1, QSPEC=0.95, CSSPEC=0.0,
NRSCAL=0, NCSCAL=4, NTMFO=0,
CFNRESS=1.00, NBAL=1, NBLOPT=0,
CFBAL=10.00, NOPT=-2, ROEXP=8.79999995E-01,
ETA EI=1.0, RPEOP=0.60, RZION=3.0,
NDIFPS=1, NDIFT=1,
NMESHA=2, NPOIDQ=10, SOLPDA=.30,
QPLACE=0.95, 0.95, 1.00, 1.00, 2.00, 2.00, 3.00, 3.00, 4.00, 4.00,
QWIDTH=0.10, 0.06, 0.02, 0.08, 0.05, 0.02, 0.05, 0.02, 0.04, 0.01,
NMESHA=2, NPOIDQ=10, SOLPDA=.30,
```

```

QPLACE=0.95, 1.00, 2.00, 3.00, 4.00, 5.00, 6.00, 7.00, 8.00, 9.00,
QWIDTH=0.06, 0.06, 0.05, 0.05, 0.05, 0.05, 0.05, 0.05, 0.05, 0.05,
NMESHA=1, NPOIDA=10, SOLPDA=.40,
APLACE=0.95, 0.96, 0.96, 0.97, 0.97, 0.98, 0.98, 0.99, 0.99, 1.00,
AWIDTH=0.10, 0.06, 0.02, 0.06, 0.02, 0.06, 0.02, 0.06, 0.02, 0.01,
NMESHB=1, NPOIDB=10, SOLPDB=.40,
BPLACE=0.95, 0.96, 0.96, 0.97, 0.97, 0.98, 0.98, 0.99, 0.99, 1.00,
BWIDTH=0.10, 0.06, 0.02, 0.06, 0.02, 0.06, 0.02, 0.06, 0.02, 0.01,
NMESHC=1, NPOIDC=10, SOLPDC=.30,
CPLACE=0.95, 0.96, 0.96, 0.97, 0.97, 0.98, 0.98, 0.99, 0.99, 1.00,
CWIDTH=0.10, 0.10, 0.02, 0.10, 0.02, 0.10, 0.02, 0.10, 0.02, 0.01,
NMESHD=1, NPOIDD=4, SOLPDD=.50,
DPLACE=-1.80, -1.80, 1.80, 1.80,
DWIDTH=.18, .08, .18, .08,
NMESHE=1, NPOIDE=2, SOLPDE=.50,
EPLACE=-1.80, -1.80, 1.80, 1.80,
EWIDTH=.18, .08, .18, .08,
EPSLON=1.0E-10, GAMMA=1.6666666667,
NTURN=20, NBLCO=32, NPPR=24,
MSMAX=1, NINMAP=60, NINSCA=60,
NSYM=0, NEGP=-1, NER=1, NV=60, NVEXP=1, REXT=10.0, ROW=1., RZOW=0.,
NEQDSK=0, NEQDXTPO=1,
PSISCL= 1.0, NRBOX=257, NZBOX=257, NBPSOUT=320,

```

## A.2. CAXE settings

Input parameter file for CAXE:

```

e14463.eq
dummy
1 IREQ !0 no read-standard init. guess, 1 read eq.
320 NA11 !number of magnetic surfaces
320 NT1 !number of poloidal points

```

## A. CODE SETTINGS

---

```
0 NA2 !dummy
0.00,0.0, 0.000, 1.0,.0,-.00 !RM(default if 0),ZM, dummy, EK1,DK1,SK1
0.000,0.0, 0.33333, 1.0,.0,-.00 !RK(read if 0),ZK, AK, EK2,DK2,SK2
0 IPA1 !flux mesh: 0 - s, 1 - psi
5 NPA1 !number of mesh packing points
0.0,0.0 SPA1 DPA1 !cluster point in s, localization delta
0.97, 0.05 SPA1 DPA1 !cluster point in s, localization delta
0.98, 0.05 SPA1 DPA1 !cluster point in s, localization delta
0.99, 0.05 SPA1 DPA1 !cluster point in s, localization delta
1.0, 0.001 SPA1 DPA1 !cluster point in s, localization delta
3 NPT1 !number of cluster points
0.25, 0.00 SPT1 DPT1 !cluster point in arclength, localization delta
0.75, 0.00 SPT1 DPT1 !cluster point in arclength, localization delta
1.00, 0.00 SPT1 DPT1 !cluster point in arclength, localization delta
0 IPA2 !dummy
0 NPA2 !dummy
0 NPT2 !dummy
2.000 ROM !CG solver : preconditioner choice =2.0(ILU), =other(D)
100 ITMAX!CG solver : max number of iterations, ITMAX=ITMAX*5 if IREQ=0
1.E-6 EPS !CG solver : accuracy in norm(residual)/norm(r.h.s.)
-3,-3 IFC,ICU !IFC=0,1,2 - given ff',i*,jb IFC=0&ICU=1,2 - computed i*,jb
0.,2.0,1. CF1, PFE11, PFE12 !params for ff' or i* or jb
0.,2.,1. CP1, PPE11, PPE12 !params for p'! read profiles if CF1+CF2+CP1+CP2=0
0.,0.,1. CF2, PFE21, PFE22 !PFE21=1. for eq. profiles, 0. - from 'dcxlib.pro'
0.,1.,0. CP2, PPE21, PPE22 !if PFE21=1. then PPE21 scales p'
3 IQAE !0 - for qaxis, 1 - for qbound
0.970725274350149 QAE !q value
2 KPA !diff. scheme parameters
2 KPB
1 KPG
400 IGLOB !max number of iterations
10 IGLOUT !output frequency
1.E-5 EPSLEV !accuracy in level lines
1.E-5 EPSRO !accuracy in geometry change
```

2 ISKIP ! make calculations of ffp from current at every ISKIP iter.  
0.5,0.5 ruw,raxwm!weights for Picard iterations

### A.3. KINX settings

Input parameter file for KINX:

```
./e14463.eq
dummy
320 NA11 !NUMBER OF FLUX INTERVALS
320 NT11 !NUMBER OF POLOIDAL INTERVALS
-0.9 SNSCR !NUMBER OF SCRAPED SURFACES FROM EQ. (neg.-> EDGE, pos.-> CORE)
2 IPA1 !FLUX MESH SWITCH: -2 READ, 0 S=SQRT(PHI), 1 PHI, 2 MATCHED
5 NPA1 !number of mesh packing points
0.0,0.0 SPA1 DPA1 !cluster point in s, localization delta (ignored)
0.97, 0.05 SPA1 DPA1 !cluster point in s, localization delta
0.98, 0.05 SPA1 DPA1 !cluster point in s, localization delta
0.99, 0.05 SPA1 DPA1 !cluster point in s, localization delta
1.0, 0.001 SPA1 DPA1 !cluster point in s, localization delta
2 IPT1 !ARCLENGTH MESH SWITCH:-1 READ, 0 ARCLENGTH, 2 MATCHED
3 NPT1 !number of cluster points
0.25, 0.00 SPT1 DPT1 !cluster point in arclength, localization delta
0.75, 0.00 SPT1 DPT1 !cluster point in arclength, localization delta
1.00, 0.00 SPT1 DPT1 !cluster point in arclength, localization delta
0 IRES !RESONANCES FIX SWITCH: 1 FIX, 0 NO FIX
3 IQAE !q 0 axis 1 boundary switch
0.970725488907885 QAE !Q AXIS OR BOUNDARY
0 IBAL !compute ballooning
20 WN !toroidal wave number
1.67 GA !adiabata
0. EQSC !=1.(eq. normalization)
2 IOR !=2
0 IZD !=0
```

## A. CODE SETTINGS

---

```
-1 IDW !DELTA DW SWITCH 0 FULL NORM, 1 DW NORM, -1 DW WITH RO=PSI
12.5 CRW !STABILIZING CORRECTION WEIGHT, DEFAULT=1, PUT CRW>1 FOR EDGE PEDESTAL
0 ISN !SPECTRAL SHIFT SWITCH: 1 ON, 0 OFF (OFF WHEN CRW>0)
-2 NAV !NUMBER OF VACUUM INTERVALS
1.2 WAC !WALL DISTANCE, WAC<=1. NO VACUUM
0,1.0,0.,.928,3.00,.45,-0.0 IWAC,RWP,ZWP,AWP,EWP,DWP,SWP !wall type,wall par,
TCV wall IWAC=3, conformal wall IWAC=0
-5e-1 ALO !EIGENVALUE INITIAL GUESS
200 NITMAX!MAX ITERATIONS IN PAMERA
1.E-3 EPSPAM!EPS IN PAMERA
2 IG !GRAPHICS SWITCH
-3,-1,-4,0 ! jobf switch, x-point at bottom, left, top
```

## B. KINX convergence studies

### B.1. Vertical stability

In the ideal MHD-code KINX, the convergence of  $\omega(N)^2/\omega_A^2$  is expected to be quadratic with  $1/N^2$ , where  $N$  is the number of radial and poloidal grid points. For the analysis, the perfectly conducting wall  $(R_{wall}, Z_{wall})$  was selected to be conformal to the plasma boundary. To avoid intersection with the toroidal axis, a minimum radial offset was chosen to be  $0.01R_{geom}$ . The wall was parameterized by:

$$R_{wall,j} = \max[R_{geom} + r_w (R_{bound,j} - R_{geom}), 0.1R_{geom}], \quad (\text{B.1.1})$$

$$Z_{wall,j} = Z_{geom} + r_w(Z_{bound,j} - Z_{geom}), \quad (\text{B.1.2})$$

where  $(R_{geom}, Z_{geom})$  is the geometric axis,  $r_w$  the ratio of the conformal wall radius to the minor radius  $a$ , and  $(R_{bound}, Z_{bound})$  the plasma boundary [113]. The results, figure B.1, show that  $\omega^2/\omega_A^2$  exhibits  $1/N^2$  convergence for grid sizes with  $N \geq 160$ .

### B.2. Higher toroidal mode numbers

The KINX convergence study was carried out for two different normalized radii  $r_w = \{1.2, 10\}$  of the conformal wall and for the TCV wall and is presented in figure B.2. The results shows that it is necessary to use a grid size of  $N \geq 192$ . For equilibria with higher shape complexity, uncertainties in the computation of the mode spectrum decrease when increasing the resolution of the computational grid. Thus, a grid size of  $N \geq 256$  with mesh packing close to the separatrix is recommended.

KINX provides an option for a stabilizing correction factor (CRW) [114] when applying the reduced energy norm ( $\delta W$ -norm). This reduces the so-called numerical destabilization, produced by convergence from below to the continuous spectrum boundary  $\omega^2 = 0$ , in

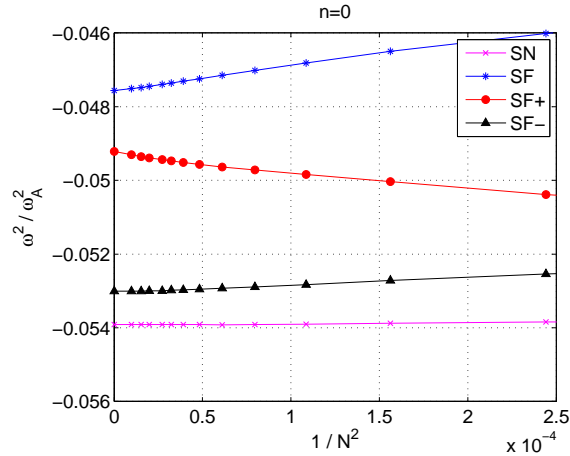


**Figure B.1.:** Convergence of the normalized growth rate  $\omega^2/\omega_A^2$  of the vertical stability as function of the inverse quadratic grid size  $1/N^2$ . KINX settings: conformal wall radius  $r_w = 10$ , full  $W$ -norm, stabilization correction factor  $CRW = 1$ .

the case of stable equilibria when there is a resonant surface in the plasma. Numerical destabilization means distortion of the positive lower boundary of the spectrum  $\omega^2$ . The violation of the necessary stability condition  $D_M \leq 1/4$  (Mercier/Newcomb) results in the solutions of the Lagrangian  $W(\xi, xi) - w^2 K(\xi, \xi)$  oscillating in arbitrarily close vicinity to the position of the resonant surface. In general, increasing the value of  $CRW$  results in a smoother convergence, figure B.3.

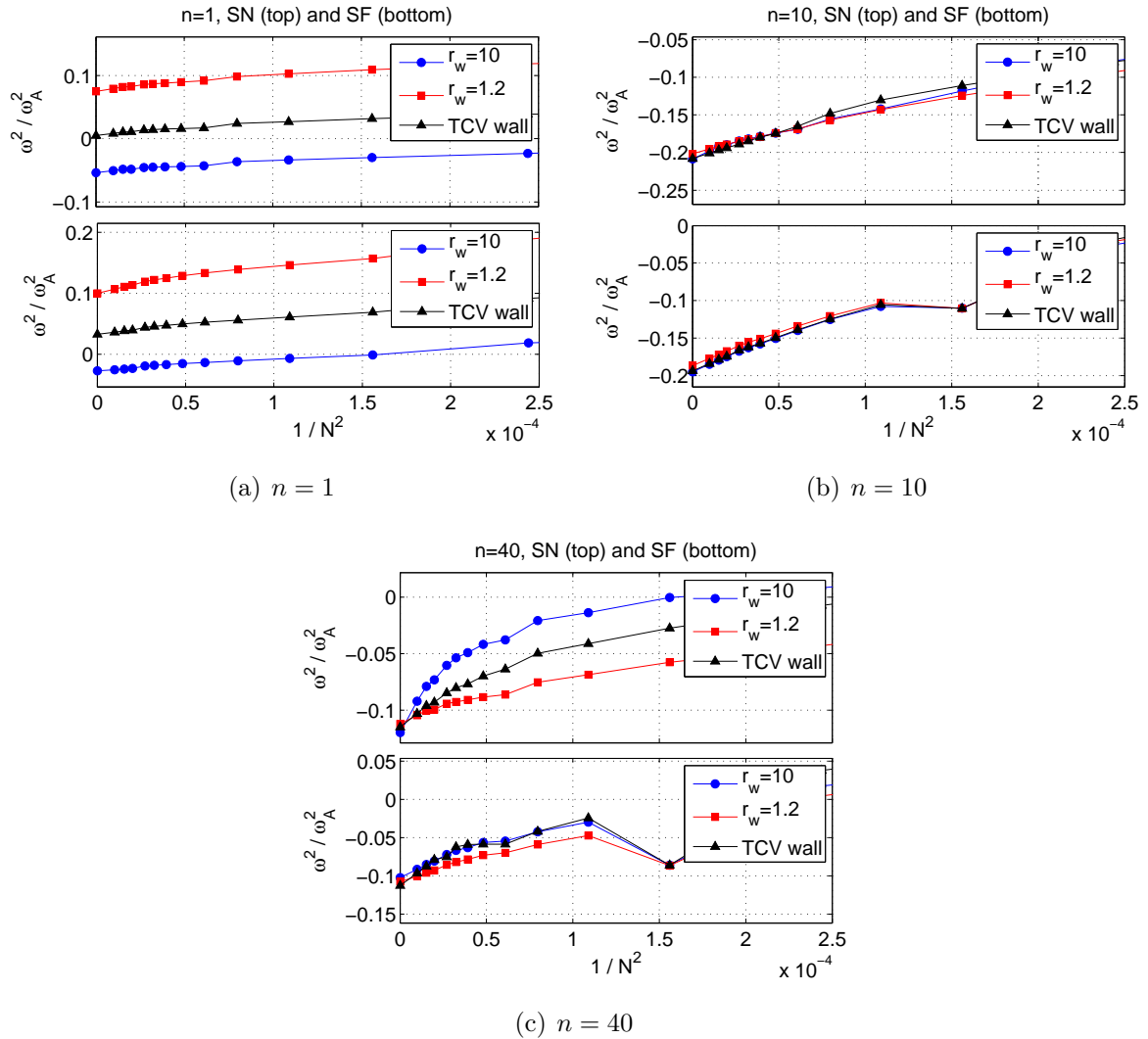


**Figure B.2.:** Convergence of the normalized growth rate  $\omega^2/\omega_A^2$  for different toroidal mode numbers  $n$  as function of the inverse quadratic grid size  $1/N^2$ . KINX settings:  $\delta W$ -norm, stabilization correction factor  $CRW = 10$ , various flux surface scraping  $SNSCR$

- (a)  $n = 1$ , SN (top) and SF (bottom),  $SNSCR = 0.0$ ,
- (b)  $n = 10$ , SN (top) and SF (bottom),  $SNSCR = 0.0$ ,
- (c)  $n = 40$ , SN (top) and SF (bottom),  $SNSCR = -0.9$



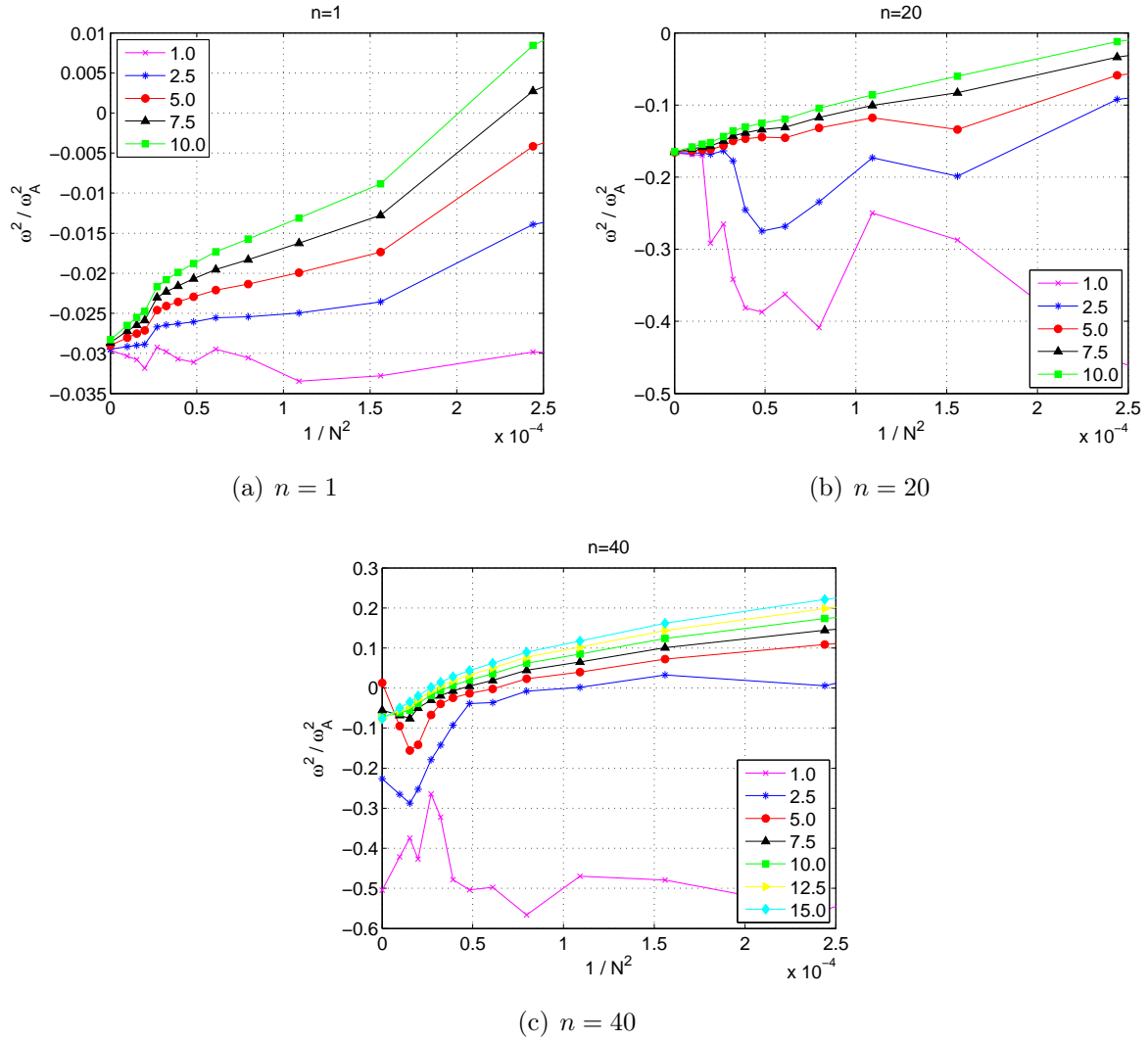


**Figure B.3.:** Convergence of the normalized growth rate  $\omega^2/\omega_A^2$  for different toroidal mode numbers  $n$  as function of the inverse quadratic grid size  $1/N^2$ . KINX settings:  $\delta W$ -norm, stabilization correction factor  $CRW = 10$ :  
 (a)  $n = 1$ , SN (top) and SF (bottom),  $SNSCR = 0.0$ ,  
 (b)  $n = 10$ , SN (top) and SF (bottom),  $SNSCR = 0.0$ ,  
 (c)  $n = 40$ , SN (top) and SF (bottom),  $SNSCR = -0.9$

## C. Ideal MHD stability diagrams for snowflake diverted H-mode

The MHD-stability of the synthetic H-mode equilibria snowflake (SF), snowflake plus (SF+), snowflake minus (SF-) and snowflake-like single-null configuration and of the SF with different shaping parameters are presented in the following. For the analysis, a conformal and perfectly conducting wall with  $r_w = 1.2$  was chosen to ensure good comparability. The mode stability was computed on a grid with size  $N_\chi \times N_\psi = 320 \times 320$ ; the growth rate  $\gamma$  was extrapolated for infinite grid size assuming inverse quadratic convergence in  $\gamma$  as function of the grid size [36].

The ballooning unstable region is depicted by red crosses, its boundary by a thick solid red line. The external kink modes are represented by solid bluish lines with toroidal mode number  $n$ , respectively. The bullet represents the operation point of the reference type-III ELMing H-mode. The error bar is determined by the uncertainty of the total pressure (gradient). It covers a range of  $p_e/p_{tot} = 0.9 - 0.5$ , where  $p_e$  is the electron and  $p_{tot}$  the total pressure. The diagonal dotted-dashed line shows the collisionless bootstrap current, whereas the horizontal dashed line represents the local reversal of the magnetic shear  $s$ .

## C.1. Snowflake and snowflake-like configurations

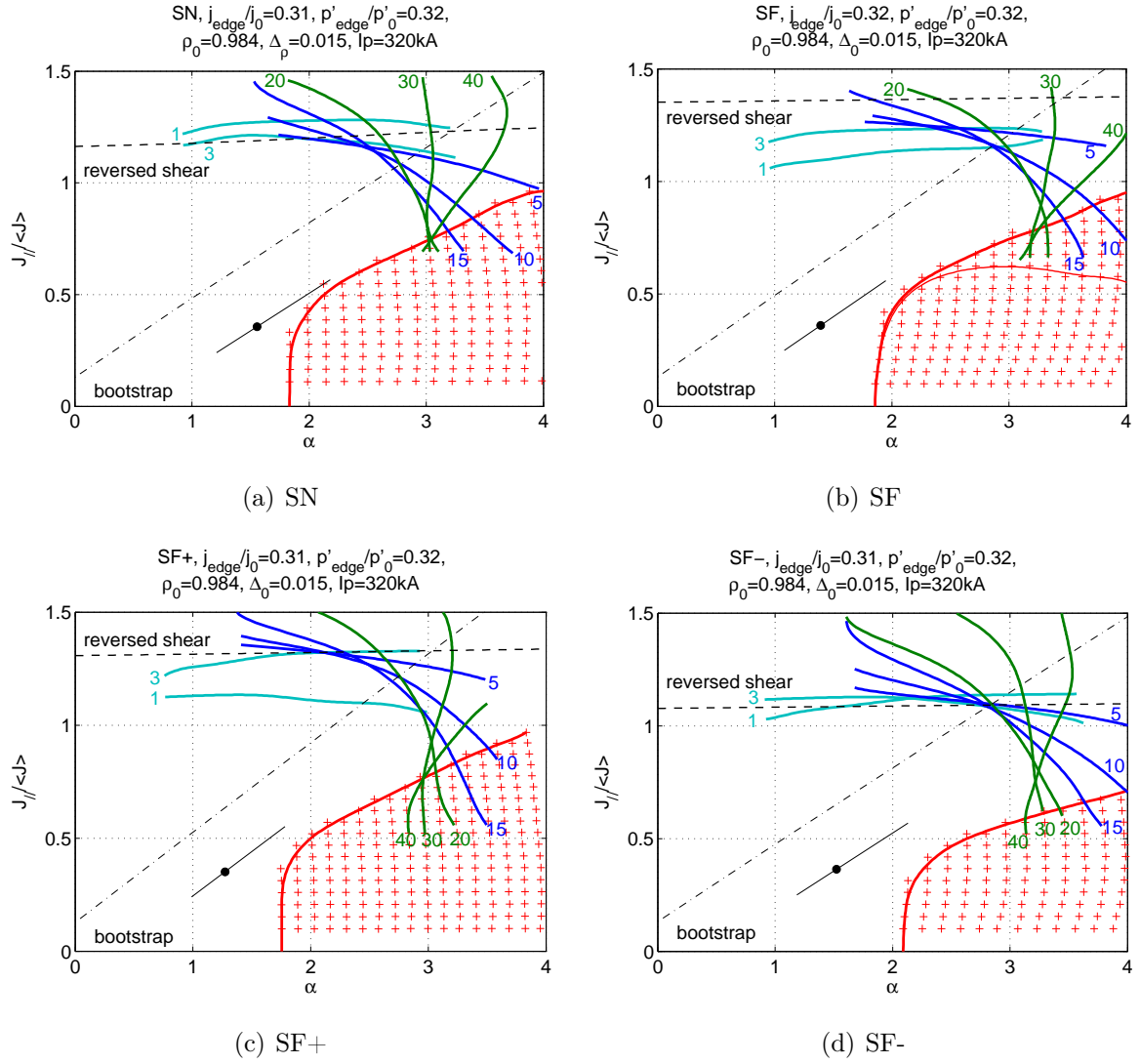


**Figure C.1.:** Ideal MHD-stability of the edge pedestal for synthetic snowflake-diverted H-mode equilibria: Stability maps for (a) snowflake-like single null (SN), (b) snowflake (SF), (c) snowflake plus (SF+) and (d) snowflake minus (SF-).

## C.2. Snowflake and snowflake-like configurations for different radial positions

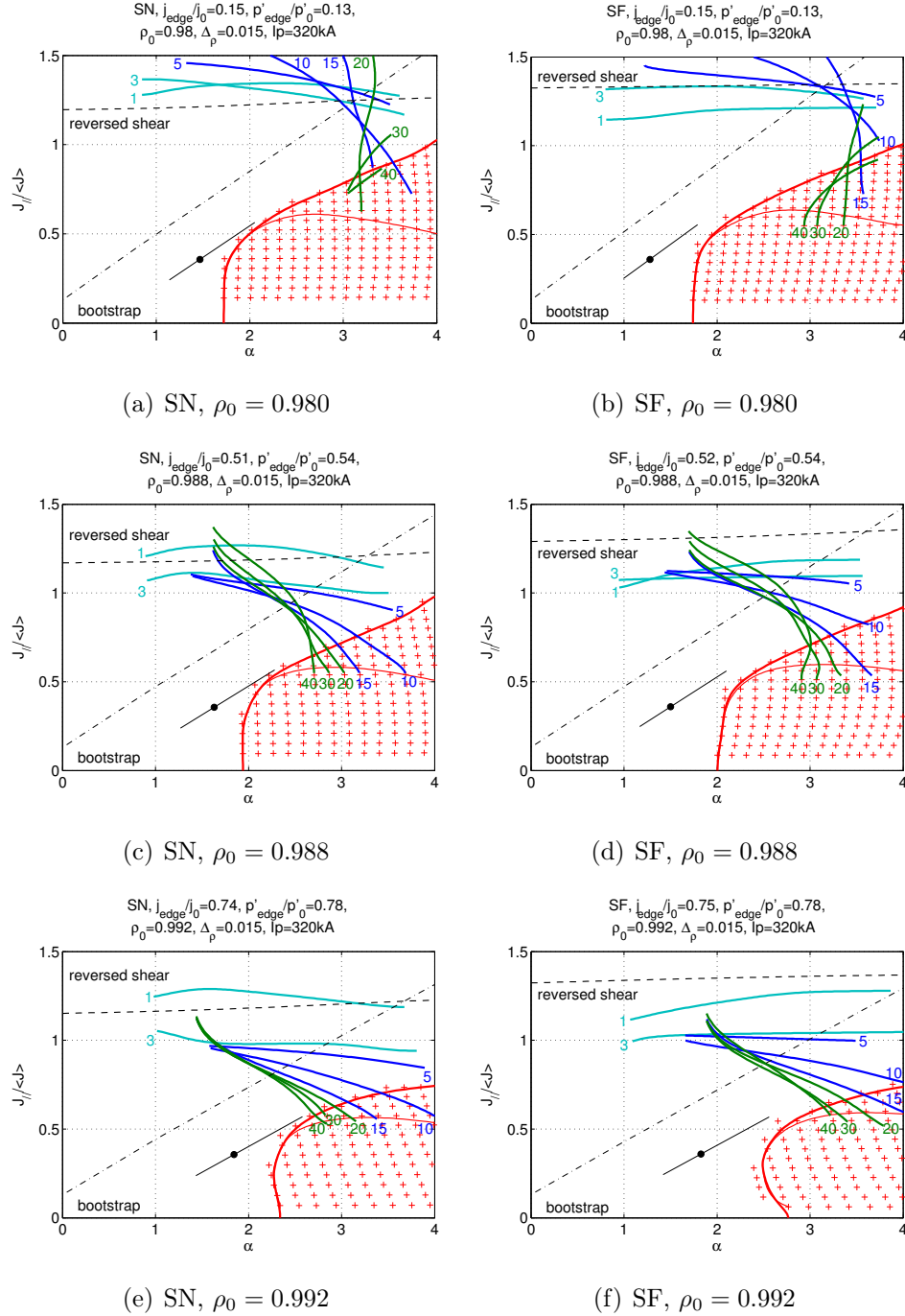


**Figure C.2.:** Ideal MHD-stability of the edge pedestal for different radial positions  $\rho_0$  of the edge pedestal

### C.3. Snowflake configuration with different upper triangularity

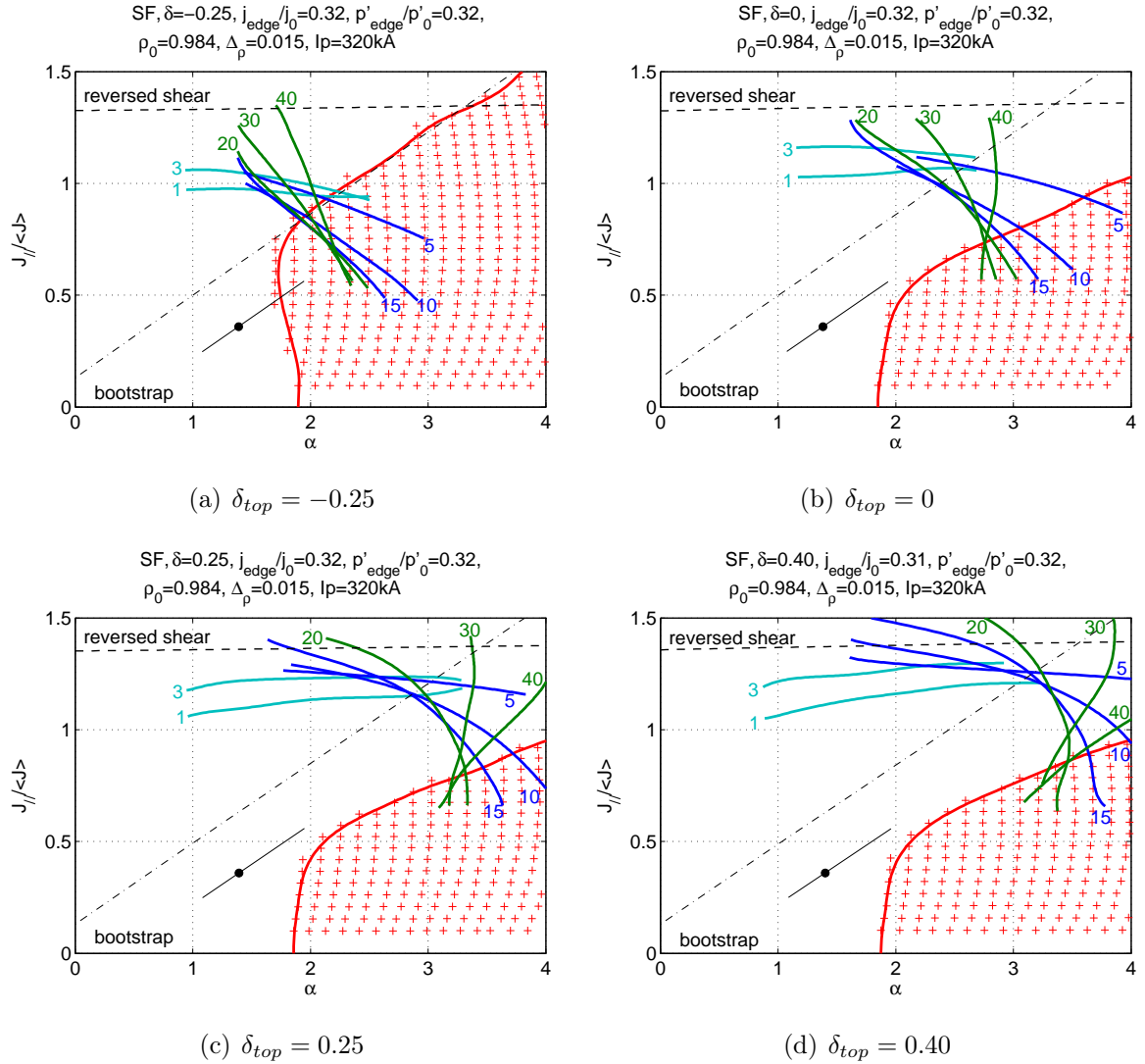


**Figure C.3.:** Ideal MHD-stability diagrams of the SF configuration for different triangularities

$\delta_{top}$

## C.4. Snowflake configuration with different upper squareness

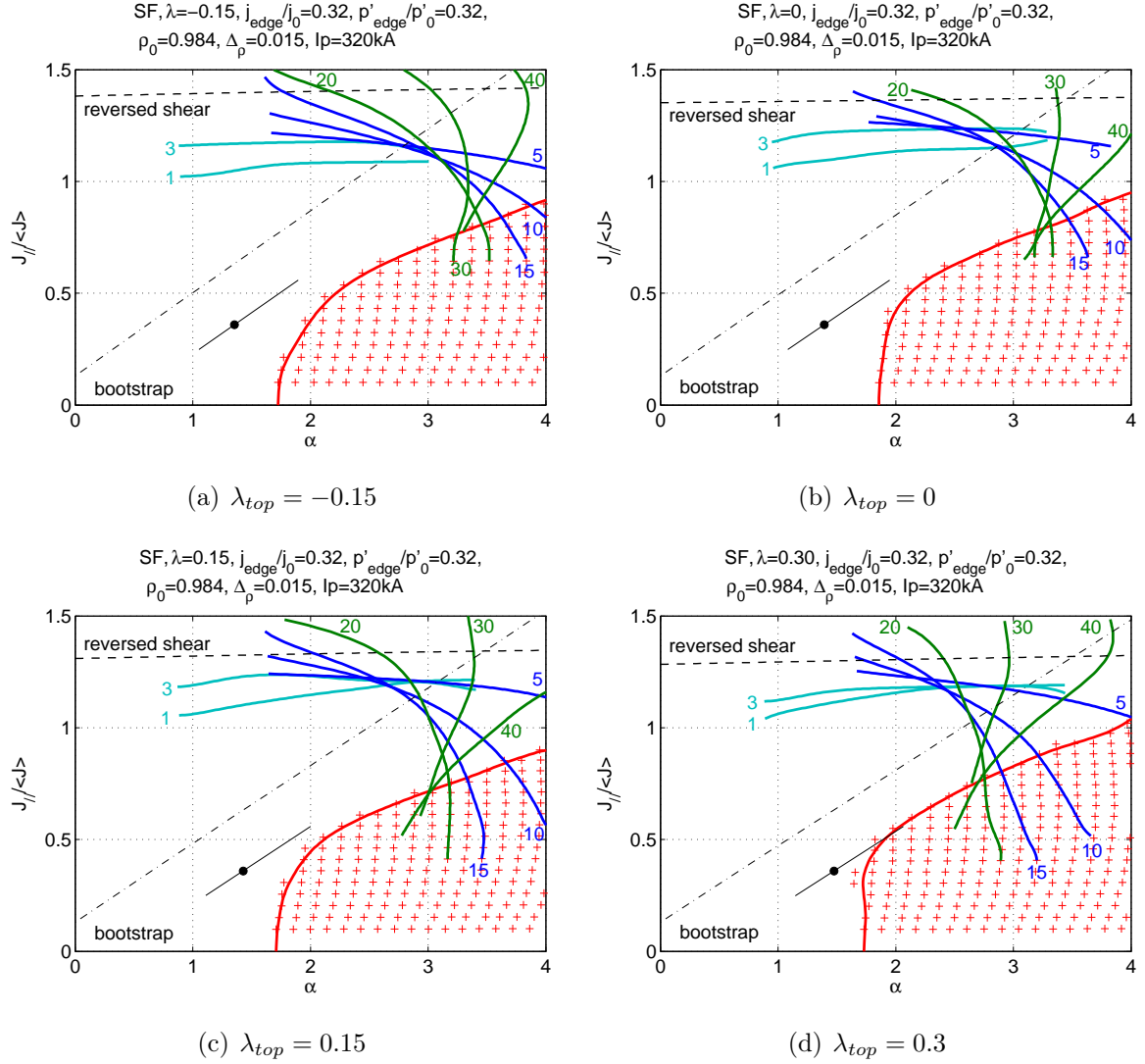
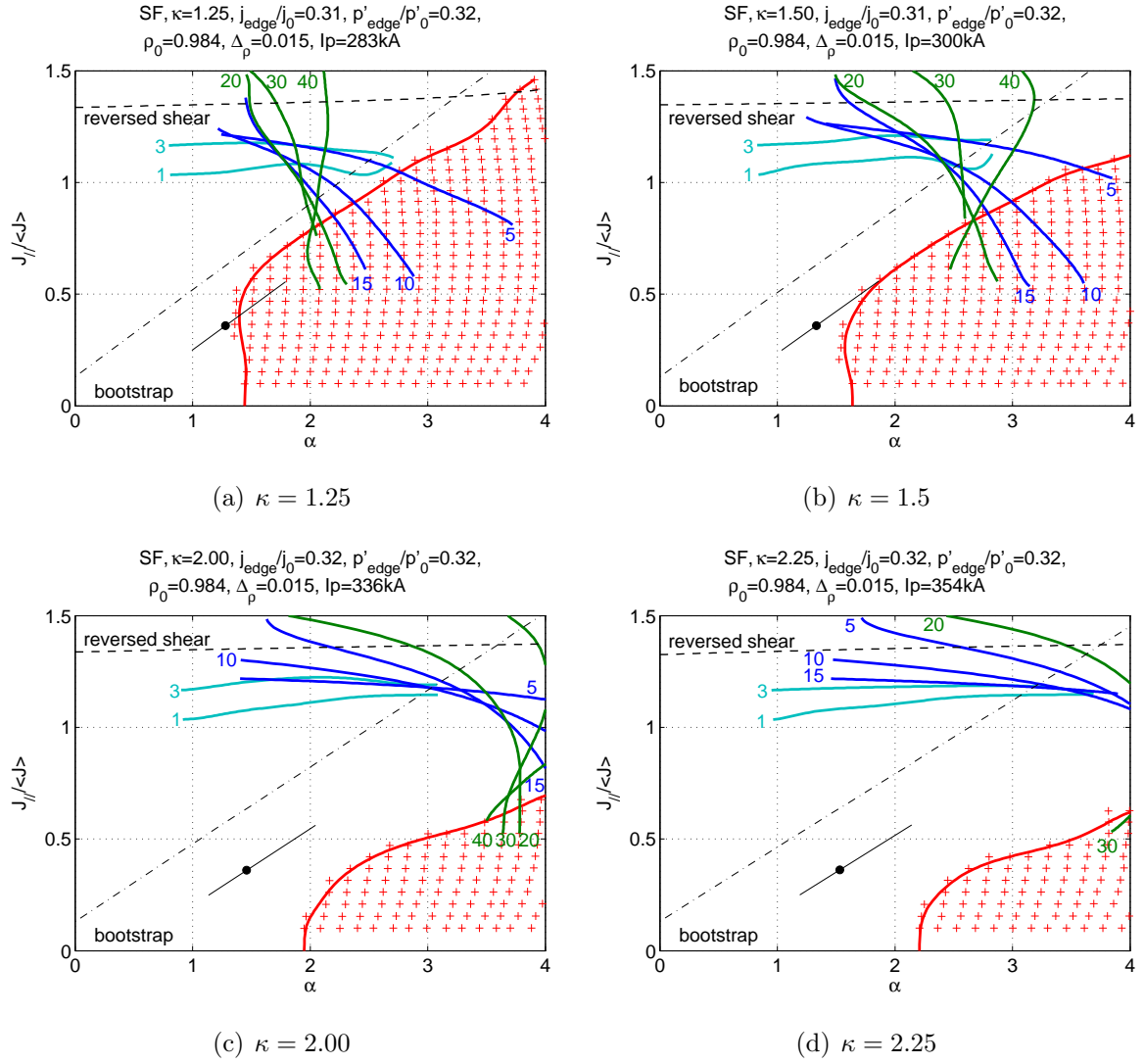


Figure C.4.: Ideal MHD-stability diagrams of the SF configuration for different squareness

$\lambda_{top}$

## C.5. Snowflake configuration with different elongation



**Figure C.5.:** Ideal MHD-stability diagrams of the SF configuration for different elongation  $\kappa$

## D. H-mode electron pedestal profiles during an ELM cycle

In this chapter, the electron temperature, density and pressure profiles during an ELM cycle, measured by Thomson scattering, are shown. The following color coding is kept throughout the whole chapter: electron temperature  $T_e$  [keV] in red, electron density  $n_e$  [ $10^{19}\text{m}^{-3}$ ] in blue and electron pressure  $p_e$  [kPa] in magenta. The profiles were mapped on radial coordinates on the plasma midplane. They are plotted as function of the relative radius  $R - R_{LCFS}$  [m], where  $R_{LCFS}$  is the radius of the separatrix. The time  $\Delta t$  indicates the time of the profile with respect to the ELM time  $t_{ELM}$ , i.e.  $\Delta t = t - t_{ELM}$ . The profiles were fitted by a modified-tanh function, equation (3.6.1), in least-square sense. The profile fit is shown as black solid line; its normalized  $\chi^2$  is given for each fit.



## D.1. Type-I ELMs

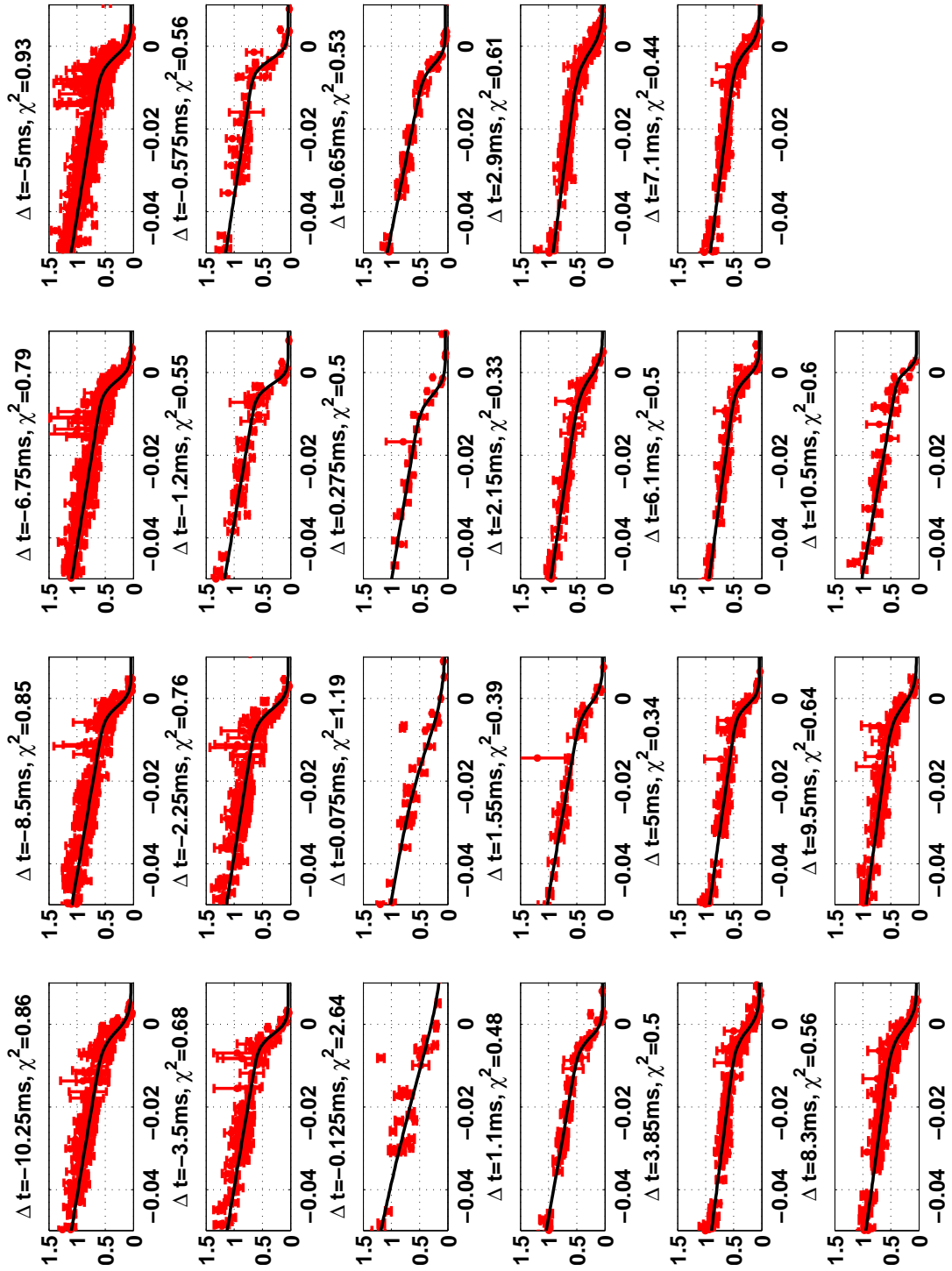


Figure D.1.: Electron temperature edge profiles from H-mode plasmas with type-I ELMs

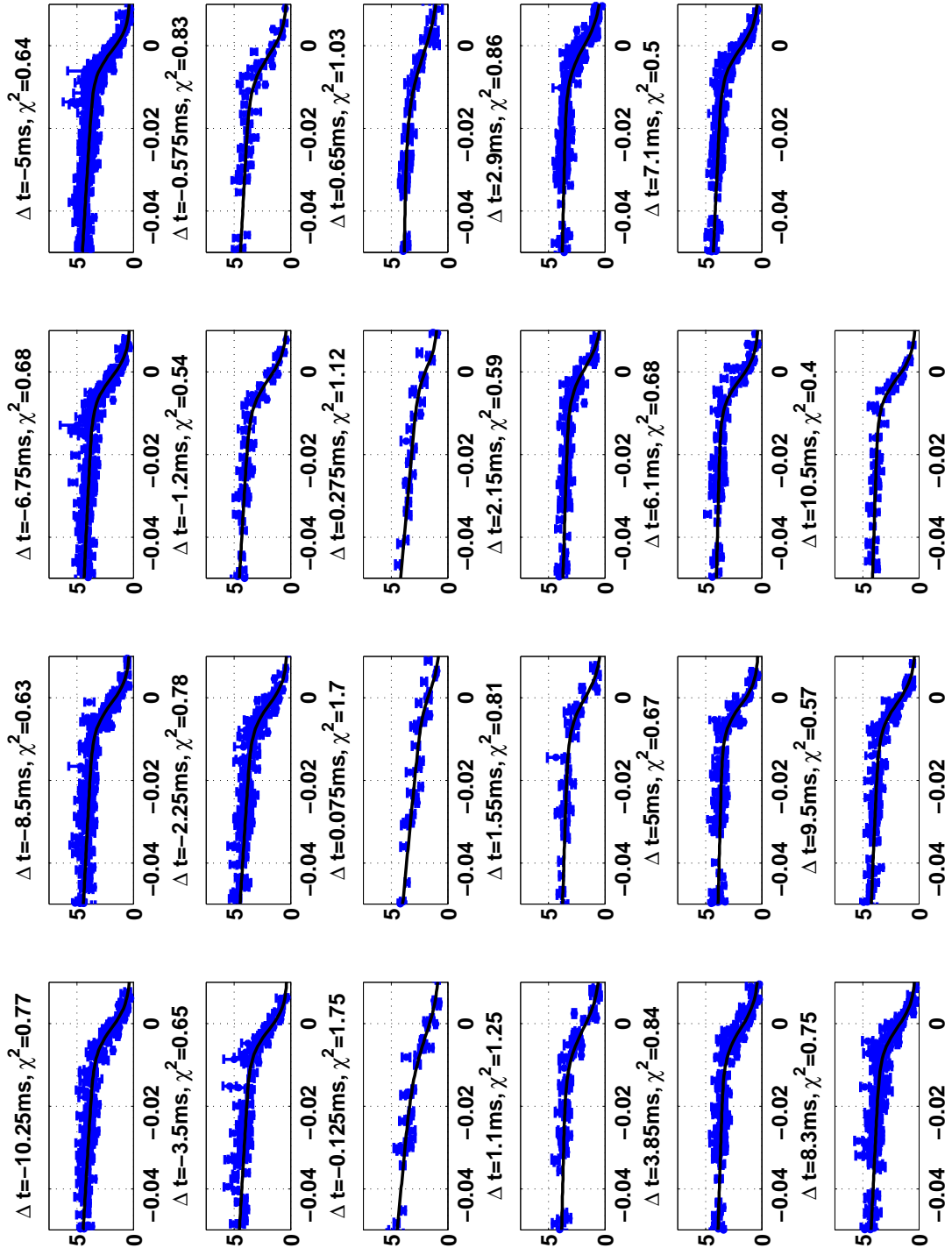


Figure D.2.: Electron density edge profiles from H-mode plasmas with type-I ELMs

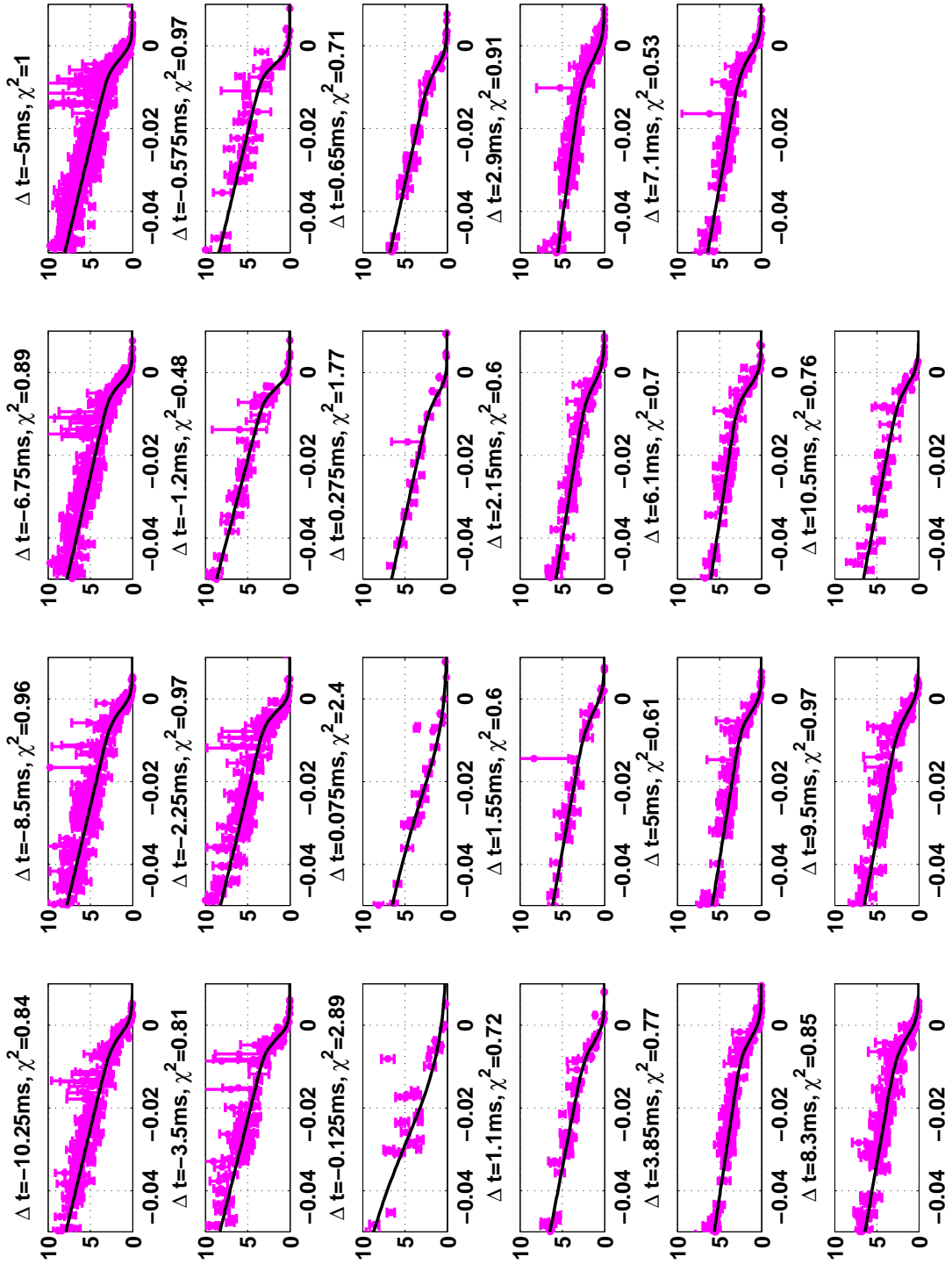


Figure D.3.: Electron pressure edge profiles from H-mode plasmas with type-I ELMs

## D.2. Large ELMs

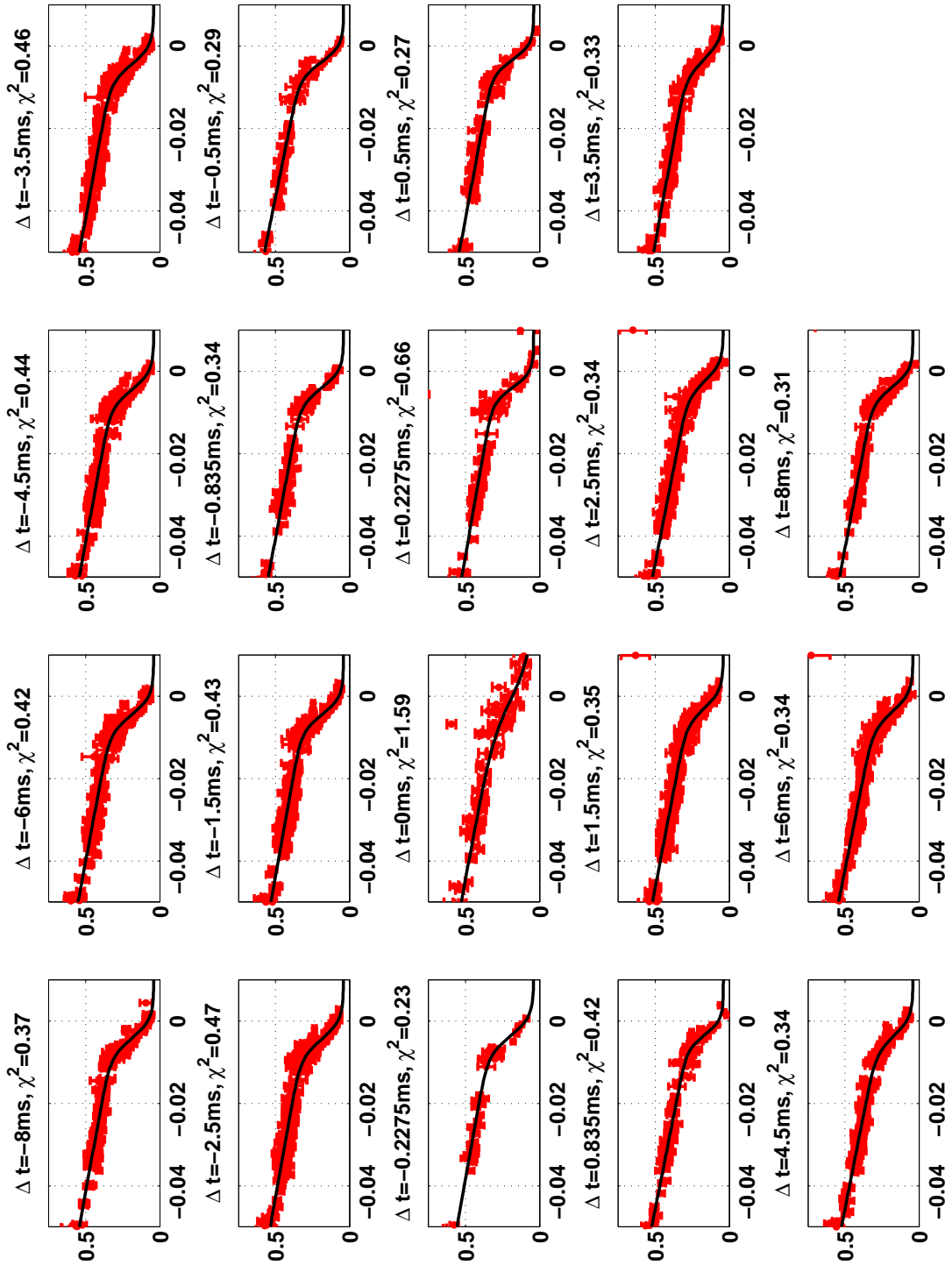


Figure D.4.: Electron temperature edge profiles from H-mode plasmas with large ELMs

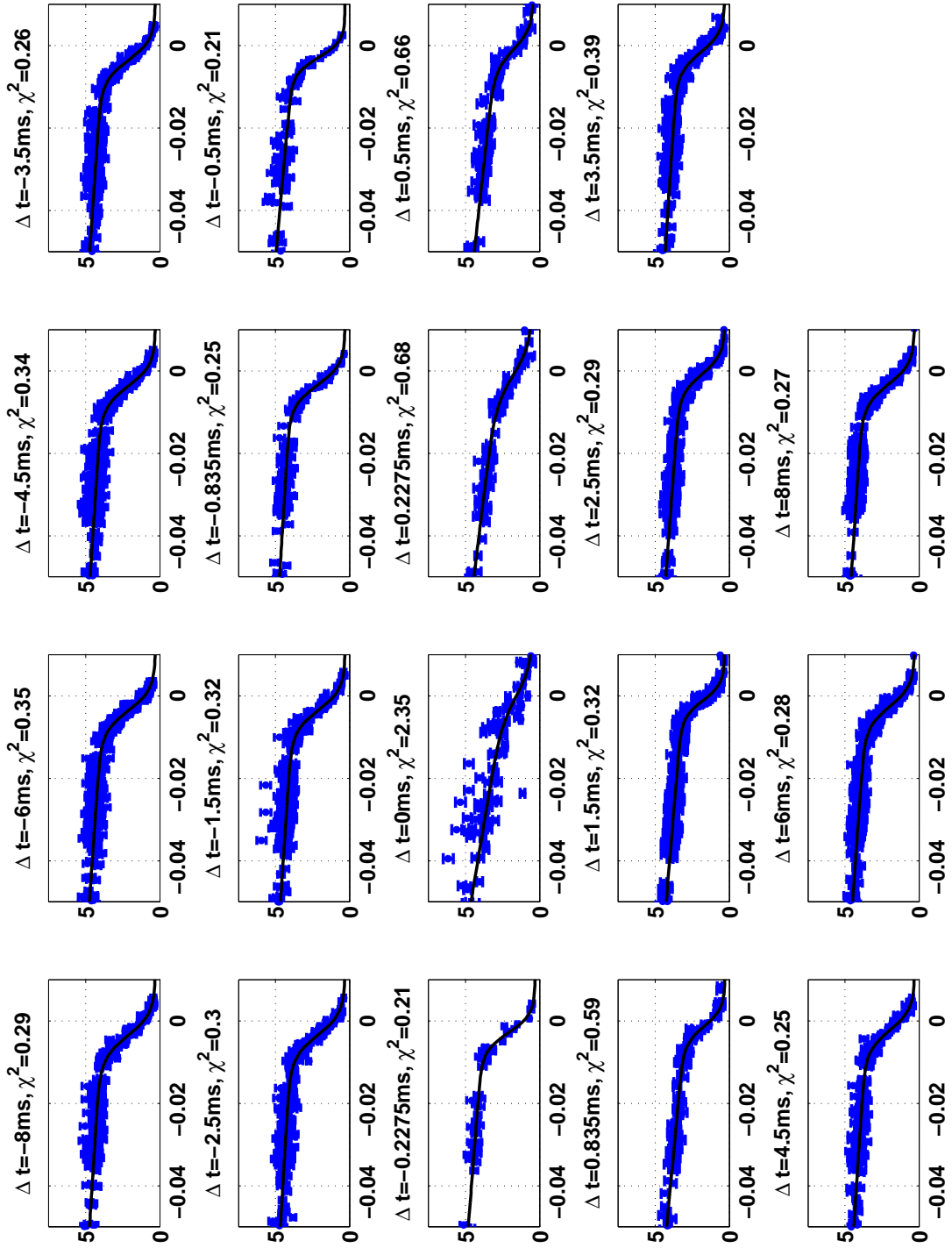


Figure D.5.: Electron density edge profiles from H-mode plasmas with large ELMs

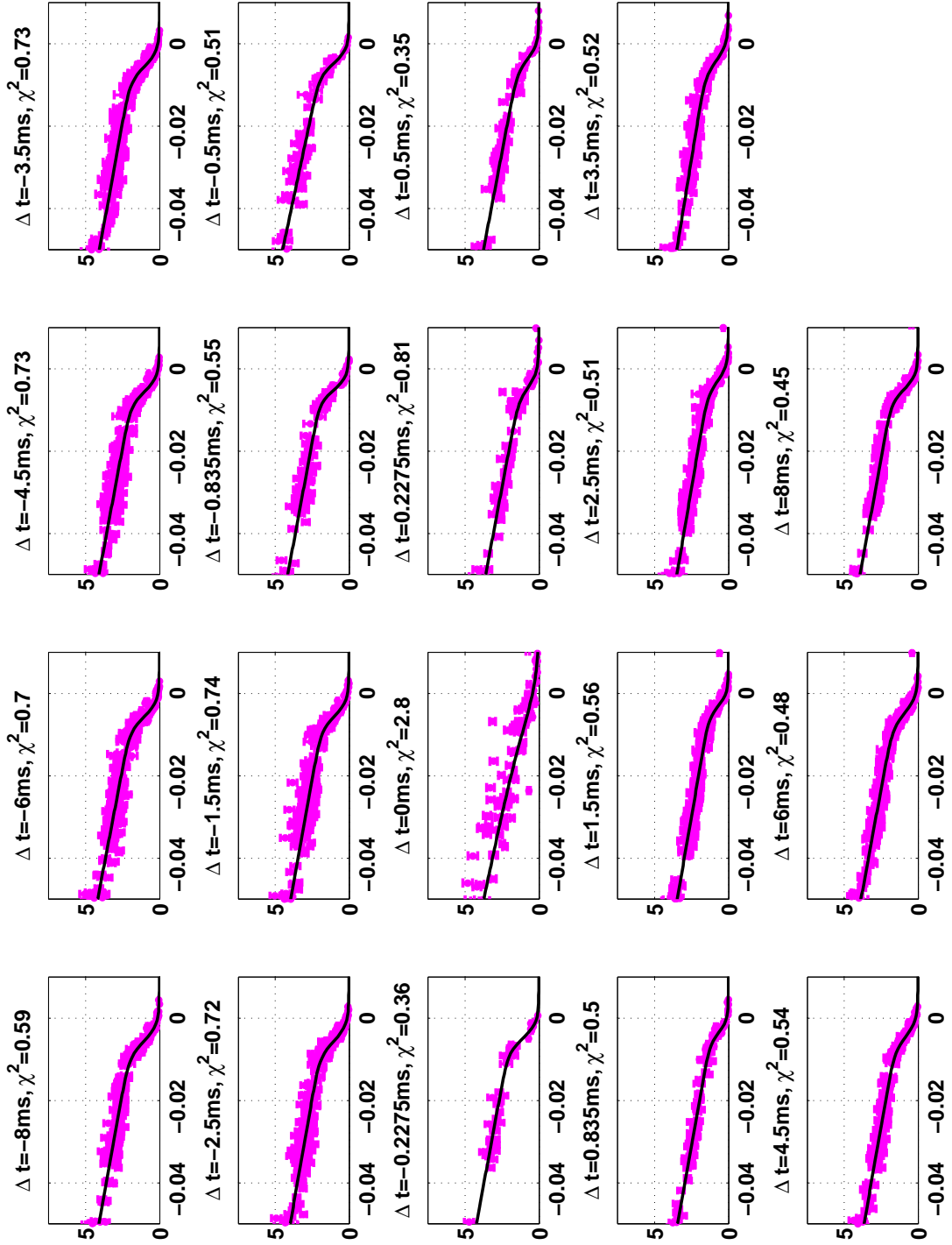


Figure D.6.: Electron pressure edge profiles from H-mode plasmas with large ELMs

## D.2.1. Type-III ELMs

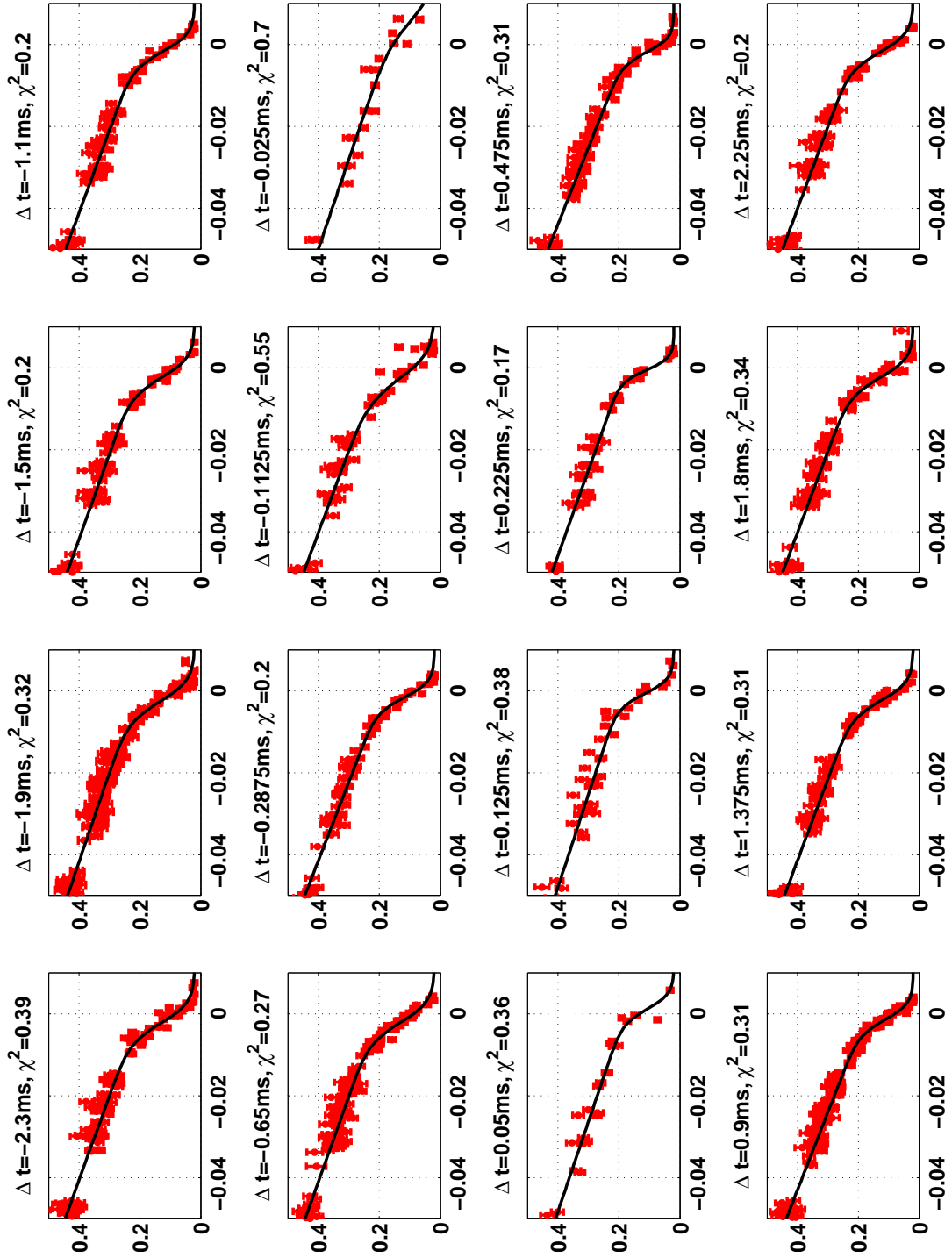


Figure D.7.: Electron temperature edge profiles from H-mode plasmas with type-III ELMs

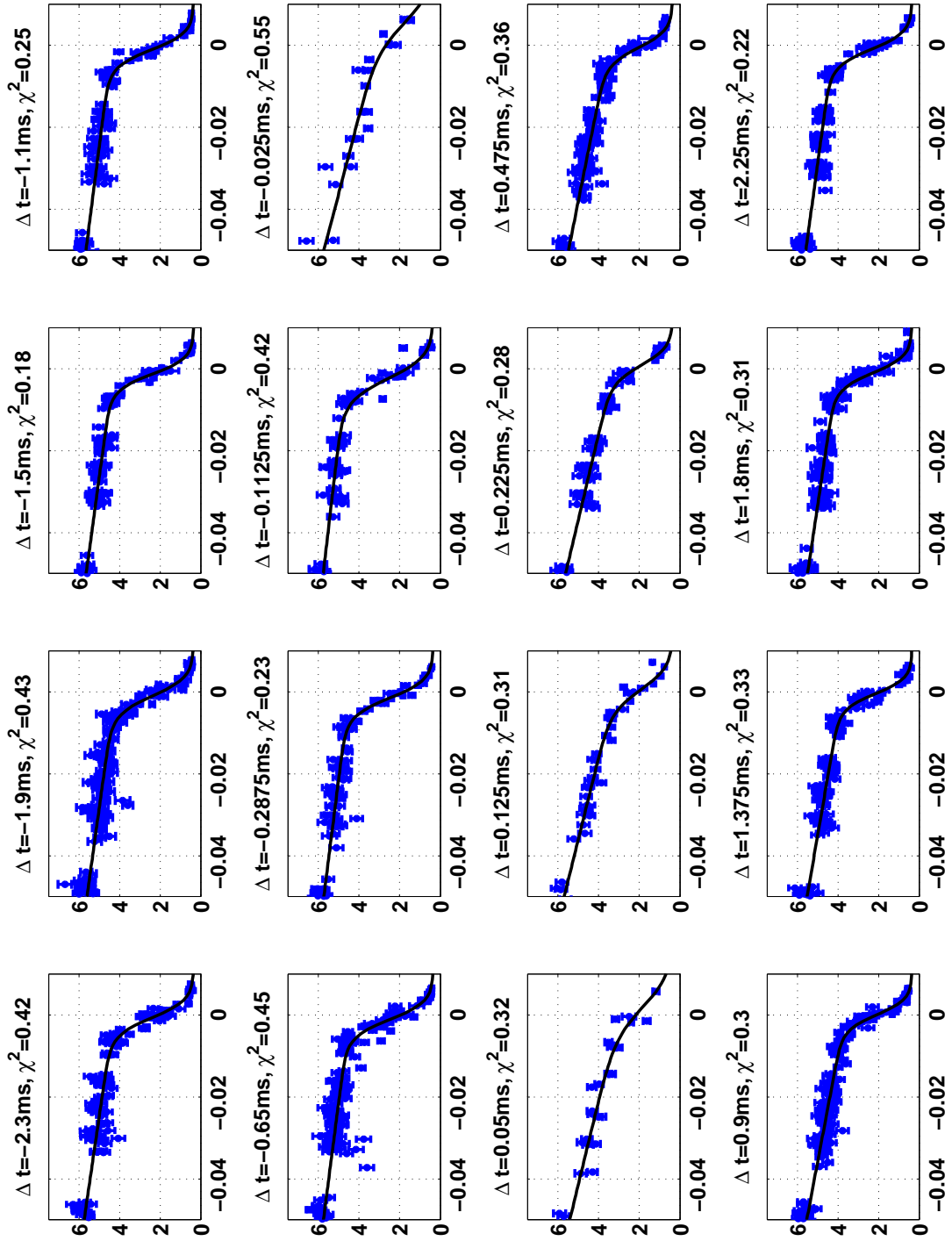


Figure D.8.: Electron density edge profiles from H-mode plasmas with type-III ELMs



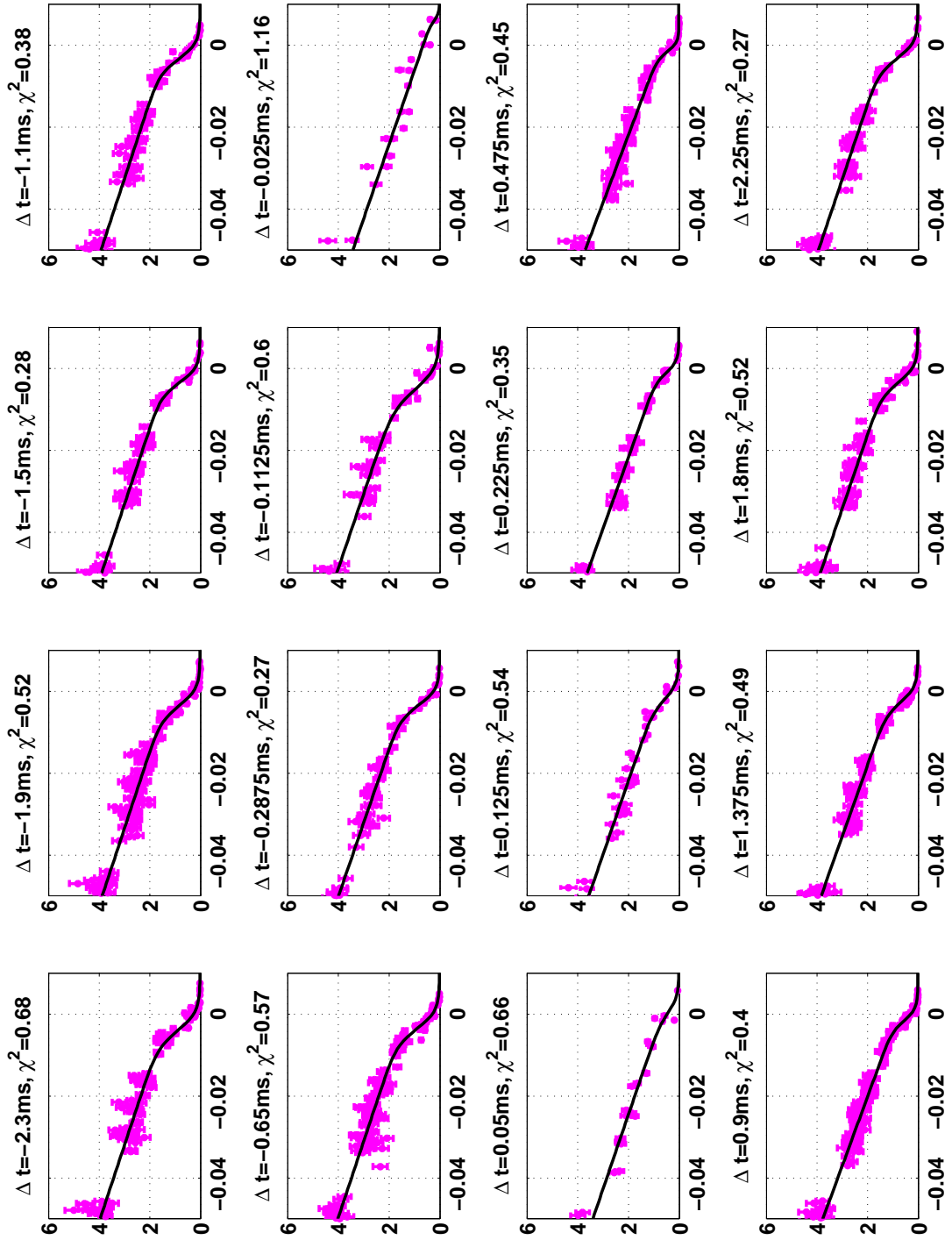


Figure D.9.: Electron pressure edge profiles from H-mode plasmas with type-III ELMs

# Bibliography

- [1] J. Wesson, *Tokamaks*. Clarendon Press Oxford, 2004.
- [2] ITER Physics Expert Group on Confinement and Transport and ITER Physics Expert Group on Confinement Modelling and Database and ITER Physics Basis Editors, *Chapter 2: Plasma confinement and transport*. Nucl. Fusion, 1999, vol. 39, no. 12.
- [3] T. Goodman, S. Alberti, M. Henderson *et al.*, *Design and installation of the electron cyclotron wave system for the TCV tokamak*, in *Proc. 19th Symposium on Fusion Technology*, 1997, proc. 19th Symposium on Fusion Technology, Lisbon, Portugal, September 1996, 565 - 568 (1996).
- [4] A. Manini, J.-M. Moret, S. Alberti *et al.*, *Modulated ECH power absorption measurements using a diamagnetic loop in the TCV tokamak*, *Plasma Phys. Control. Fusion*, vol. 44, no. 2, p. 139, 2002.
- [5] K. Matsuda, *Ray Tracing Study of the Electron Cyclotron Current Drive in DIII-D Using 60 GHz*, *IEEE Trans. Plasma. Sci.*, vol. 17, no. 1, pp. 6–11, 1989.
- [6] H. Reimerdes, *MHD stability limits in the TCV tokamak*, Ph.D. thesis, École Polytechnique Fédérale de Lausanne, published as Lausanne Report LRP 595/98, 2001.
- [7] I. H. Hutchinson, *Principles of plasma diagnostic*. Cambridge University Press, 1992.
- [8] S. Franke, *Application of Thomson scattering at 1.06  $\mu\text{m}$  as a diagnostic for spatial profile measurements of electron temperature and density on the TCV tokamak*, Ph.D. thesis, École Polytechnique Fédérale de Lausanne, published as Lausanne Report LRP 576/97, 1997. URL: <http://library.epfl.ch/en/theses/?nr=1654>
- [9] S. Barry, *The extension of the FIR interferometer of TCV to a polarimeter and measurements of the Faraday rotation caused by the poloidal magnetic*

- field*, Ph.D. thesis, École Polytechnique Fédérale de Lausanne, published as Lausanne Report LRP 638/99, 1999.
- [10] J. Freidberg, *Ideal Magnetohydrodynamics*. Plenum Press - New York and London, 1987.
- [11] F. Hofmann and S. C. Jardin, *Plasma shape and position control in highly elongated tokamak*, *Nucl. Fusion*, vol. 30, p. 2013, 1990.
- [12] C. Angioni, *Modelling of electron transport and of sawtooth activity in tokamaks*. Ph.D. thesis, École Polytechnique Fédérale de Lausanne, published as Lausanne Report LRP 2469/01, Lausanne, 2001.
- [13] O. Sauter, C. Angioni, and Y. R. Lin-Liu, *Neoclassical conductivity and bootstrap current formulas for general axisymmetric equilibria and arbitrary collisionality regime*, *Phys. of Plasmas*, vol. 6, pp. 2834–2839, 1999.
- [14] H. Luetjens, A. Bondeson, and O. Sauter, *The CHEASE code for toroidal MHD equilibria*, *Computer Physics Communications*, vol. 97, pp. 216–260, 1996.
- [15] H. Zohm, *Edge localized modes (ELMs)*, *Plasma Phys. Control. Fusion*, vol. 38, pp. 105–128, 1996.
- [16] J. W. Connor, *Edge-localized modes - physics and theory*, *Plasma Phys. Control. Fusion*, vol. 40, pp. 531–542, 1998.
- [17] W. Suttrop, *The physics of large and small edge localized modes*, *Plasma Phys. Control. Fusion*, vol. 42, pp. A1–A14, 2000.
- [18] P. B. Snyder, H. R. Wilson, J. R. Ferron *et al.*, *Edge localized modes and the pedestal: A model based on coupled peeling-ballooning modes*, *Phys. of Plasmas*, vol. 9, pp. 2037–2043, 2002.
- [19] S. Y. Medvedev, A. A. Martynov, Y. R. Martin *et al.*, *Edge kink/ballooning mode stability in tokamaks with separatrix*, *Plasma Phys. Control. Fusion*, vol. 48, pp. 927–938, 2006.
- [20] S. Y. Medvedev, A. Ivanov, A. Martynov *et al.*, *Beta Limits and Edge Stability for Negative Triangularity Plasmas in the TCV Tokamak*, in *35th EPS Conference on Plasma Phys.*, ECA, Ed., vol. 32D, 2008, pp. P–1.072.

- [21] S. Y. Medvedev, A. A. Ivanov, A. A. Martynov *et al.*, *Edge Stability and Pedestal Profile Sensitivity of Snowflake Diverted Equilibria in the TCV Tokamak*, *Contrib. to Plasma Phys.*, vol. 50, pp. 324–330, 2010.
- [22] W. Kerner, Y. Igitkhanov, G. Janeschitz *et al.*, *The Scaling of the Edge Temperature in Tokamaks Based on the Alfvén Drift - Wave Turbulence*. *Contrib. Plasma Phys.*, vol. 38, no. 1/2, pp. 118–123, 1998.
- [23] Y. Martin and T. team, *H-mode threshold power in TCV Ohmic plasmas*, *Plasma Phys. and Control. Fusion*, vol. 44, no. 5A, p. A143, 2002.
- [24] C. Angioni, A. Peeters, F. Jenko *et al.*, *Collisionality dependence of density peaking in quasilinear gyrokinetic calculations*, *Phys. of Plasmas*, vol. 12, p. 112310, 2005.
- [25] L. Horton, T. Hatae, A. Hubbard *et al.*, *Dependence of H-mode pedestal parameters on plasma magnetic geometry*, *Plasma Phys. and Control. Fusion*, vol. 44, no. 5A, p. A273, 2002.
- [26] T. Onjun, G. Bateman, and A. H. Kritz, *Models for the pedestal temperature at the edge of H-mode tokamak plasmas*, *Phys. of Plasmas*, vol. 9, no. 12, pp. 5018–5030, 2002.
- [27] G. Huysmans, S. Sharapov, A. Mikhailovskii *et al.*, *Modeling of diamagnetic stabilization of ideal magnetohydrodynamic instabilities associated with the transport barrier*, *Phys. of Plasmas*, vol. 8, no. 10, p. 4292, 2001.
- [28] P. Snyder, H. Wilson, T. Osborne *et al.*, *Characterization of peeling-ballooning stability limits on the pedestal*, *Plasma Phys. and Control. Fusion*, vol. 46, no. 5A, p. A131, 2004.
- [29] M. Sugihara, V. Mukhovatov, A. Polevoi *et al.*, *Scaling of H-mode edge pedestal pressure for a Type-I ELM regime in tokamaks*, *Plasma Phys. and Control. Fusion*, vol. 45, no. 9, p. L55, 2003.
- [30] A. Hubbard, *Physics and scaling of the H-mode pedestal*, *Plasma Phys. Control. Fusion*, vol. 42, pp. A15–A35, 2000.
- [31] A. Leonard, *Progress in characterization of the H-mode pedestal*, *Journal of Physics: Conference Series*, vol. 123, no. 1, p. 012001, 2008.

- [32] K. Shaing, *Poloidal magnetic field dependence of the edge electric field layer width in the H mode in tokamaks*, *Phys. Fluids*, vol. B4, p. 290, 1992.
- [33] T. H. Osborne, K. H. Burrell, R. J. Groebner *et al.*, *H-mode pedestal characteristics in ITER shape discharges on DIII-D*, *Journal of Nucl. Materials*, vol. 266-269, pp. 131 – 137, 1999.
- [34] F. Hinton and G. Staebler, *Particle and energy confinement bifurcation in tokamaks*, *Phys. Fluid*, vol. B5, p. 1281, 1993.
- [35] R. J. Groebner and T. H. Osborne, *Scaling studies of the high mode pedestal*, *Phys. of Plasmas*, vol. 5, pp. 1800–1806, 1998.
- [36] L. M. Degtyarev, A. A. Martynov, S. Y. Medvedev *et al.*, *The KINX ideal MHD stability code for axisymmetric plasmas with separatrix*, *Computer Physics Communications*, vol. 103, pp. 10–27, 1997.
- [37] J.-S. Lönnroth, G. Bateman, M. Bécoulet *et al.*, *Integrated ELM Modelling*, *Contrib. Plasma Phys.*, vol. 46, no. 7-9, pp. 726–738, 2006.
- [38] J. W. Connor, R. J. Hastie, and J. B. Taylor, *Shear, Periodicity, and Plasma Ballooning Modes*, *Phys. Rev. Letter*, vol. 40, pp. 396–399, 1978.
- [39] R. Hastie, P. Catto, and J. Ramos, *Effect of strong radial variation of the ion diamagnetic frequency on internal ballooning modes*, *Phys. of Plasmas*, vol. 7, p. 4561, 2000.
- [40] S. Y. Medvedev, L. Villard, L. M. Degtyarev *et al.*, *MHD equilibrium and stability of doublet configurations*, in *20th EPS Conf. on Controlled Fusion and Plasma Phys.*, Lisbon, *Proc. Contrib. Papers*, vol. 17C-IV, 1993, p. 1279ff.
- [41] J. Sheffield, *Plasma Scattering of Electromagnetic Radiation*. Academic Press London, 1975.
- [42] A. Selden, *Simple analytic form of the relativistic Thomson scattering system*, *Phys. Letters*, vol. 79A, nb. 5,6, pp. 405–406, 1980.
- [43] P. Webb, R. McIntyre, and J. Conradi, *Properties of Avalanche Photodiodes*, EG&G, RCA review 35, June 1974.

- [44] Y. Camenen, *Étude du transport d'énergie thermique dans les plasmas du tokamak à configuration variable au moyen de chauffage électronique cyclotronique*, Ph.D. thesis, École Polytechnique Fédérale de Lausanne, published as Lausanne Report LRP 3618/06, Lausanne, 2006. URL: <http://library.epfl.ch/theses/?nr=3618>
- [45] E. Fable, O. Sauter, S. Coda *et al.*, *Inward thermodiffusive particle pinch in electron internal transport barriers in TCV*, *Plasma Phys. Control. Fusion*, vol. 48, pp. 1271–1283, 2006.
- [46] F. Jenko, W. Dorland, M. Kotschenreuther *et al.*, *Electron temperature gradient driven turbulence*, *Phys. of Plasmas*, vol. 7, pp. 1904–1910, 2000.
- [47] Y. Idomura, S. Tokuda, and Y. Kishimoto, *Stable ion temperature gradient driven mode in reversed shear tokamaks*, *New Journal of Phys.*, vol. 4, pp. 101.1–101.13, 2002.
- [48] E. Fable, *Experimental and theoretical study of particle transport in the TCV tokamak*, Ph.D. thesis, École Polytechnique Fédérale de Lausanne, published as Lausanne Report LRP 4334/09, Lausanne, 2009. URL: <http://library.epfl.ch/theses/?nr=4334>
- [49] R. Fischer, C. Wendland, A. Dinklage *et al.*, *Thomson scattering analysis with the Bayesian probability theory*, *Plasma Phys. Control. Fusion*, vol. 44, pp. 1501–1519, 2002.
- [50] W. Press, S. Teukolsky, W. Vetterling *et al.*, *Numerical Recipes in FORTRAN: The Art of Scientific Computing*. Cambridge University Press, 1992.
- [51] R. Hogg, *Statistical Robustness: One View of Its Use in Applications Today*, *The American Statistician*, vol. 33, 3, pp. 108–115, 1979.
- [52] P. Huber, *Robust Estimation of a Location Parameter*, *Annals of Mathematical Statistics*, vol. 35, pp. 73–101, 1964.
- [53] C. Carey, I. Furno, H. Weisen *et al.*, *Application of the singular value decomposition method for inversion of interferometer measurements in fusion plasmas*, *Review of scientific instruments*, vol. 75, no. 10, pp. 3411–3412, 2004.

- [54] W. Mandl, K. Burrell, R. Groebner *et al.*, ***Investigation into ion edge temperature behaviour using CER spectroscopy at DIII-D***, *Nucl. Fusion*, vol. 35, no. 3, p. 347, 1995.
- [55] R. Maingi, R. Bell, B. LeBlanc *et al.*, ***The enhanced pedestal H-mode in the National Spherical Torus experiment***, *Journal of Nucl. Materials*, vol. 390-391, pp. 440 – 443, 2009, proceedings of the 18th International Conference on Plasma-Surface Interactions in Controlled Fusion Device.
- [56] M. Reich, E. Wolfrum, L. Horton *et al.*, ***Edge ion temperature measurements at ASDEX Upgrade***, in *31st EPS Conference on Plasma Phys. London*, ser. 28G, no. P-4.118, 2004.
- [57] J. Paley, J. Berrino, S. Coda *et al.*, ***Real time control of plasmas and ECRH systems on TCV***, *Nucl. Fusion*, vol. 49, no. 085017, pp. 1–6, 2009.
- [58] A. Degeling, Y. Martin, J. Lister *et al.*, ***Magnetic triggering of ELMs in TCV***, *Plasma Phys. Control. Fusion*, vol. 45, no. 9, pp. 1637–1655, 2003.
- [59] P. Lang, A. Degeling, J. Lister *et al.*, ***Frequency control of type-I ELMs by magnetic triggering in ASDEX Upgrade***, *Plasma Phys. and Control. Fusion*, vol. 46, no. 11, p. L31, 2004.
- [60] S. H. Kim, M. M. Cavinato, V. Dokuka *et al.*, ***Comparing magnetic triggering of ELMs in TCV and ASDEX Upgrade***, *Plasma Phys. and Control. Fusion*, vol. 51, no. 5, p. 055021, 2009.
- [61] L. L. Lao, J. R. Ferron, T. S. Taylor *et al.*, ***High internal inductance improved confinement H-mode discharges obtained with an elongation ramp technique in the DIII-D tokamak***, *Phys. Rev. Lett.*, vol. 70, no. 22, pp. 3435–3438, 1993.
- [62] D. D. Ryutov, ***Geometrical properties of a snowflake divertor***, *Phys. of Plasmas*, vol. 14, p. 064502, 2007.
- [63] D. D. Ryutov, R. H. Cohen, T. D. Rognlien *et al.*, ***The magnetic field structure of a snowflake divertor***, *Phys. of Plasmas*, vol. 15, p. 092501, 2008.
- [64] F. Piras, S. Coda, I. Furno *et al.*, ***Snowflake divertor plasmas on TCV***, *Plasma Phys. Control. Fusion*, vol. 51, p. 055009 (8pp), 2009.

- [65] F. Hofmann, M. Dutch, D. Ward *et al.*, ***Vertical instability in TCV: comparison of experimental and theoretical growth rates***, *Nuclear Fusion*, vol. 37, no. 5, p. 681, 1997.
- [66] A. A. Ivanov, R. R. Khayrutdinov, S. Y. Medvedev *et al.*, ***New Adaptive Grid Plasma Equilibrium Reconstruction Solver as Module of the SPIDER Code***, in *33th EPS Conference on Plasma Phys.*, ECA, Ed., vol. 30 I P-4.155, June 2006.
- [67] A. A. Ivanov, S. Y. Medvedev, Y. Y. Poshekhonov *et al.*, ***Reconstruction of Tokamak Equilibria with Pedestal Profiles Using the SPIDER Code***, in *34th EPS Conference on Plasma Phys.*, ECA, Ed., vol. 31F P-4.068, July 2007.
- [68] J. W. Connor, R. J. Hastie, H. R. Wilson *et al.*, ***Magnetohydrodynamic stability of tokamak edge plasmas***, *Phys. of Plasmas*, vol. 5, pp. 2687–2699, 1998.
- [69] R. Groebner, T. Osborne, A. Leonard *et al.*, ***Temporal evolution of H-mode pedestal in DIII-D***, *Nucl. Fusion*, vol. 49, no. 4, p. 045013, 2009.
- [70] A. Leonard, T. Casper, R. Groebner *et al.*, ***Pedestal performance dependence upon plasma shape in DIII-D***, *Nucl. Fusion*, vol. 47, no. 7, p. 552, 2007.
- [71] F. Piras, S. Coda, B. Duval *et al.*, ***Snowflake H-mode in a tokamak plasma***, *Phys. Rev. Lett.*, vol. 105, no. 15, p. 155003, 2010.
- [72] R. Groebner, A. Leonard, T. Luce *et al.*, ***Comparison of H-mode pedestals in different confinement regimes in DIII-D***, *Plasma Phys. and Control. Fusion*, vol. 48, no. 5A, pp. A109–A119, 2006.
- [73] T. Osborne, J. Ferron, R. Groebner *et al.*, ***The effect of plasma shape on H-mode pedestal characteristics on DIII-D***, *Plasma Phys. and Control. Fusion*, vol. 42, no. 5A, p. A175, 2000.
- [74] A. Leonard, R. Groebner, T. Osborne *et al.*, ***Influence of global beta, shape, and rotation on the H-mode pedestal structure in DIII-D***, *Phys. of Plasmas*, vol. 15, p. 056114, 2008.
- [75] M. Maslov, C. Angioni, and H. Weisen, ***Density profile peaking in JET H-mode plasmas: experiments versus linear gyrokinetic predictions***, *Nucl. Fusion*, vol. 49, no. 7, p. 075037, 2009.



- [76] R. Groebner, A. Leonard, P. Snyder *et al.*, ***Progress towards a predictive model for pedestal height in DIII-D***, *Nucl. Fusion*, vol. 49, no. 8, p. 085037, 2009.
- [77] F. Jenko and W. Dorland, ***Nonlinear electromagnetic gyrokinetic simulations of tokamak plasmas***, *Plasma Phys. and Control. Fusion*, vol. 43, no. 12A, p. A141, 2001.
- [78] B. Scott, ***Computation of electromagnetic turbulence and anomalous transport mechanisms in tokamak plasmas***, *Plasma Phys. and Control. Fusion*, vol. 45, no. 12A, p. A385, 2003.
- [79] P. B. Snyder, R. J. Groebner, A. W. Leonard *et al.*, ***Development and validation of a predictive model for the pedestal height***, *Phys. of Plasmas*, vol. 16, p. 056118, 2009.
- [80] P. Schneider, E. Wolfrum, B. Guenter *et al.*, ***Alternative method for characterization of inter ELM edge profiles of type-I ELMy H-modes in ASDEX Upgrade***, in *37th EPS Conf. on Plasma Phys.*, ser. P2.157, 2010.
- [81] C. Angioni, H. Weisen, O. Kardaun *et al.*, ***Scaling of density peaking in H-mode plasmas based on a combined database of AUG and JET observations***, *Nucl. Fusion*, vol. 47, no. 9, p. 1326, 2007.
- [82] T. Takizuka, ***An offset nonlinear scaling for ELMy H-mode confinement***, *Plasma Phys. and Control. Fusion*, vol. 40, no. 5, p. 851, 1998.
- [83] H. Urano, W. Suttrop, L. Horton *et al.*, ***Energy and particle losses during type-I ELMy H-mode in ASDEX Upgrade***, *Plasma Physics and Controlled Fusion*, vol. 45, no. 9, p. 1571, 2003.
- [84] H. Urano, Y. Kamada, T. Takizuka *et al.*, ***Pedestal Characteristics of H-Mode Plasmas in JT-60U and ASDEX Upgrade***, *J. Plasma Fusion Res.*, vol. 81, no. 4, pp. 280–287, 2005.
- [85] L. Horton, G. Conway, A. Degeling *et al.*, ***ITER-relevant H-mode physics at ASDEX Upgrade***, *Plasma Phys. and Control. Fusion*, vol. 46, no. 12B, p. B511, 2004.
- [86] J. Neuhauser, D. Coster, H. Fahrbach *et al.*, ***Transport into and across the scrape-off layer in the ASDEX Upgrade divertor tokamak***, *Plasma Phys. and Control. Fusion*, vol. 44, no. 6, p. 855, 2002.

- [87] E. Wolfrum, D. Coster, C. Konz *et al.*, ***Edge ion temperature gradients in H-mode discharges***, in *Proc. 34th EPS Conference on Plasma Phys. (Warsaw)*, ser. P-2.039, vol. 31F, 2007.
- [88] C. Angioni, A. G. Peeters, G. V. Pereverzev *et al.*, ***Density Peaking, Anomalous Pinch, and Collisionality in Tokamak Plasmas***, *Phys. Rev. Lett.*, vol. 90, no. 20, p. 205003, 2003.
- [89] H. Weisen, A. Zabolotsky, C. Angioni *et al.*, ***Collisionality and shear dependences of density peaking in JET and extrapolation to ITER***, *Nucl. Fusion*, vol. 45, no. 2, p. L1, 2005.
- [90] M. Maslov, H. Weisen, A. Zabolotsky *et al.*, ***Density peaking in TCV and JET H-modes***, in *33rd EPS Conf. on Plasma Phys.*, ser. O-3.005, vol. 30I, 2006.
- [91] H. Weisen, C. Angioni, M. Maslov *et al.*, ***Peaked Density Profiles in Low Collisionality H-modes in JET, ASDEX Upgrade and TCV***, in *21st IAEA Fusion Energy Conf.*, ser. EX8-4, 2006. URL: [http://www-pub.iaea.org/MTCD/Meetings/FEC2006Presentations/Presentations/20-oct-06/talk\\_EX8-4.ppt](http://www-pub.iaea.org/MTCD/Meetings/FEC2006Presentations/Presentations/20-oct-06/talk_EX8-4.ppt)
- [92] V. Mukhovatov, Y. Shimomura, A. Polevoi *et al.*, ***Comparison of ITER performance predicted by semi-empirical and theory-based transport models***, *Nucl. Fusion*, vol. 43, no. 9, p. 942, 2003.
- [93] X. Garbet, P. Mantica, C. Angioni *et al.*, ***Physics of transport in tokamaks***, *Plasma Phys. and Control. Fusion*, vol. 46, no. 12B, p. B557, 2004.
- [94] M. Kotschenreuther, G. Rewoldt, and W. Tang, ***Comparison of Initial Value and Eigenvalue Codes for Kinetic Toroidal Plasma Instabilities***, *Comp. Phys. Comm.*, vol. 88, no. 2-3, p. 128, 1995.
- [95] D. Wagner, E. Fable, A. Pitzschke *et al.*, ***Particle transport in TCV H-modes***, in *37th EPS Conf. on Plasma Phys.*, ser. P1.1101, 2010. URL: <http://ocs.ciemat.es/EPS2010PAP/pdf/P1.1101.pdf>
- [96] T. Hatae, Y. Kamada, S. Ishida *et al.*, ***Characteristics of edge pedestal width in JT-60U ELM-free H-mode plasmas***, *Plasma Phys. and Control. Fusion*, vol. 40, no. 6, p. 1073, 1998.

- [97] J. Stober, O. Gruber, A. Kallenbach *et al.*, ***Effects of triangularity on confinement, density limit and profile stiffness of H-modes on ASDEX upgrade***, *Plasma Phys. and Control. Fusion*, vol. 42, no. 5A, p. A211, 2000.
- [98] G. Saibene, R. Sartori, A. Loarte *et al.*, ***Improved performance of ELMy H-modes at high density by plasma shaping in JET***, *Plasma Phys. and Control. Fusion*, vol. 44, no. 9, p. 1769, 2002.
- [99] J. Ferron, M. Chu, G. L. Jackson *et al.*, ***Modification of high mode pedestal instabilities in the DIII-D tokamak***, *Phys. of Plasmas*, vol. 7, no. 5, pp. 1976–1983, 2000.
- [100] L. Lao, Y. Kamada, T. Oikawa *et al.*, ***Dependence of edge stability on plasma shape and local pressure gradients in the DIII-D and JT-60U tokamaks***, *Nucl. Fusion*, vol. 41, no. 3, p. 295, 2001.
- [101] S. Saarelma, S. Guenter, T. Kurki-Suonio *et al.*, ***ELM phenomenon as an interaction between bootstrap-current driven peeling modes and pressure-driven ballooning modes***, *Plasma Phys. Control. Fusion*, vol. 42, pp. A139–A145, 2000.
- [102] M. Sugihara, Y. Igitkhanov, G. Janeschitz *et al.*, ***A model for H mode pedestal width scaling using the International Pedestal Database***, *Nucl. Fusion*, vol. 40, no. 10, p. 1743, 2000.
- [103] **O. Kardaun *et al.***, in *IAEA Proceedings*, ser. *CN-77-ITERP/04*, Sorrento, 2000.
- [104] R. Behn, A. Alfier, S. Y. Medvedev *et al.*, ***Edge profiles of electron temperature and density during elmy H-mode in ohmically heated TCV plasmas***, *Plasma Phys. Control. Fusion*, vol. 49, 8, pp. 1289–1308, 2007.
- [105] E. Wolfrum, A. Burckhart, R. Fischer *et al.*, ***Investigation of inter-ELM pedestal profiles in ASDEX Upgrade***, *Plasma Phys. and Control. Fusion*, vol. 51, no. 12, p. 124057, 2009.
- [106] A. Burckhart, E. Wolfrum, R. Fischer *et al.*, ***Inter-ELM behaviour of the electron density and temperature pedestal in ASDEX Upgrade***, *Plasma Phys. and Control. Fusion*, vol. 52, no. 10, p. 105010, 2010.
- [107] R. Pitts, S. Alberti, P. Blanchard *et al.*, ***ELM driven divertor target currents on TCV***, *Nucl. Fusion*, vol. 43, no. 10, p. 1145, 2003.

- [108] C. Maggi, *Progress in understanding the physics of the H-mode pedestal and ELM dynamics*, *Nucl. Fusion*, vol. 50, no. 6, p. 066001, 2010.
- [109] G. Staebler, F. Hinton, J. Wiley *et al.*, *High and very high modes from energy, particle, and momentum transport models*, *Phys. of Plasmas*, vol. 1, p. 909, 1994.
- [110] P. Diamond, V. Lebedev, D. Newman *et al.*, *Dynamics of spatiotemporally propagating transport barriers*, *Phys. of Plasmas*, vol. 2, p. 3685, 1995.
- [111] P. H. Diamond, V. B. Lebedev, D. E. Newman *et al.*, *Dynamics of Transition to Enhanced Confinement in Reversed Magnetic Shear Discharges*, *Phys. Rev. Lett.*, vol. 78, no. 8, pp. 1472–1475, Feb 1997.
- [112] A. Pankin, I. Voitsekhovitch, G. Bateman *et al.*, *Combined model for the H-mode pedestal and ELMs*, *Plasma Phys. and Control. Fusion*, vol. 47, no. 3, p. 483, 2005.
- [113] M. J. Hole, R. J. Akers, L. C. Appel *et al.*, *Ideal MHD stability of the mega-ampere spherical tokamak*, *Plasma Phys. Control. Fusion*, vol. 47, pp. 581–613, 2005.
- [114] L. Degtyarev and S. Y. Medvedev, *Methods for numerical simulation of ideal MHD stability of axisymmetric plasmas*, *Computer Physics Communications*, vol. 43, pp. 29–56, 1986.

# Acknowledgements

Although being glad that it is finally over, and despite the feeling that after all the endeavor only half of the things are completed, I enjoyed my time at CRPP and in Lausanne. During my 5 years of thesis work I learned many interesting and useful things, met many kind people and enjoyed skiing in the Alps.

My thesis work on TCV would not have been possible without the work and support of my colleagues. For that I want to thank Dr. K. Appert for having me given the opportunity of starting a Ph.D. at the CRPP. I still remember his rough greeting the first time we met. Maybe it was due to the fact that I was late, inexcusable for a Citizen of the watch country. I rejoiced a lot the discussions about wooden houses, gardening and the subtle differences between Swiss, French and German mustard etc.

I would like to thank a lot the Thomson scattering crew. I appreciated the support of Dr. R. Behn, my supervisor, during the years of my thesis work. He never hesitated to give me advice and directional hints when I was in troubles. I also want to thank him for his patience in explaining me laser physics, optics and everything else a good diagnostician would need to know. The co-pilot of the Thomson team, Y. Andrebe, who accompanied me all these years with his helping hand, I want to thank especially. I always marveled about his sheer endless willingness, patience and accuracy in improving the diagnostic. I will never forget the hours/days we spent together seeking for broken mirrors, crawling through the basement of the TCV building. I also like to thank him for his patience in teaching me the (lack of) logic in French language.

On the theory side of the world, I would like to warmly thank Dr. O. Sauter. He has been always willing to discuss about the interpretation of the data, giving another point of view from which everything suddenly became much clearer and, finally, discussing about the beauty of code-writing.

Special thanks go to the people that were contributing to this work: Dr. B. Duval, the psychologist for Ph.D. students, Dr. L. Porte, Dr. T. Goodman and M. Silva for heating up the atmosphere, Dr. S. Coda for keeping TCV working, X. Llobet for his help with TDI and MDS, S. Yu. Medvedev for helping with CAXE and KINX, Dr. J. Paley for closing me out from the

LAC-cluster when I was exaggerating, Prof. L. Villard correcting parts of my thesis draft, J. Rossel for his marvelous figure export routine, E. Grüter for helping me with the administrative tasks and a thank you to whoever I may have accidentally forgotten.

I would also like to thank the bunch of Ph.D. students, friends and geeks for the good atmosphere, the aperos, SAT evenings, skiing, cycling, dancing and so on and so forth. Special thanks go to my office mates, Dr. Scarface who dances with avalanches, Loïci, Silvano le chat, Gennady, Sun Hee, Arnold Schwarzenegger and Gustavo.

A big thank you goes to Claudia on whom I could always count and who accompanied me all these years. Thank you to Céline for the evenings full of dancing. A sorry to Anna, who had to endure me and my bad mood during the months of writing.

The acknowledgements would not be complete without mentioning my parents, whose contribution cannot be cast into words.

# Andreas Pitzschke

Graduate physicist

École Polytechnique Fédérale de Lausanne  
Centre de Recherches en Physique des Plasmas  
Building PPH, office 277, station 13,  
CH-1015 Lausanne, SWITZERLAND

☎ ++41 21 69 31 917

✉ andreas.pitzschke@epfl.ch

---

## Personal

14.11.1979 Born in Bautzen, Germany  
German Citizen

---

## Education

- 2005 – 2011 **Ph.D. in Physics**, *Centre de Recherches en Physique des Plasmas, École Polytechnique Fédérale de Lausanne, Switzerland*, “Pedestal Characteristics and MHD Stability of H-mode Plasmas in TCV”.
- 1999 – 2005 **Diploma in Physics**, *Institut für Medizinische Physik und Biophysik, Universität Leipzig, Germany*, “Investigations of the interactions of  $\beta$ -Amyloid-peptides with phospholipid membranes using fluorescence spectroscopy and atomic force microscopy”.
- 2002 **Erasmus student exchange program**, *University of Oulu, Finland*.
- 1998 **Scientific baccalaureate**, *Friedrich Schiller Gymnasium Bautzen, Germany*.

---

## Postgraduate courses

École Polytechnique Fédérale de Lausanne

- “Physics of magnetically confined plasmas”
- “Advanced theory of plasma”
- “Diagnostics of plasmas”
- “Using Mathematica to analyse and model experimental data”

---

## References

- S. Yu. Medvedev, A. Pitzschke, et al. Edge Stability and Pedestal Profile Sensitivity of Snowflake Diverted Equilibria in the TCV Tokamak. In *12th International Workshop on Plasma Edge Theory in Fusion Devices*. Moscow, Russia, 2009.
- S. Yu. Medvedev, A. Pitzschke, et al. Edge Stability and Pedestal Profile Sensitivity of Snowflake Diverted Equilibria in the TCV Tokamak. *Contrib. to Plasma Phys.*, 50(3-5):324–330, 2010.
- F. Piras, A. Pitzschke, et al. Snowflake Divertor Plasmas on TCV. In *36th EPS Conference on Plasma Phys.*, volume ECA Vol.33E, pages P–2.141. Sofia, Bulgaria, 2009.
- F. Piras, A. Pitzschke, et al. Snowflake H-mode in a tokamak plasma. *Phys. Rev. Lett.*, 105(15):155003, 2010.
- P. Piras, A. Pitzschke, et al. Snowflake divertor experiments on TCV. In *37th EPS Conference on Plasma Phys.* Dublin, Ireland, 2010.
- A. Pitzschke et al. Optimization of the TCV Thomson scattering system for high resolution measurements of transport barriers in Tokamak plasmas. Number 509. SPS, Geneva, Switzerland, 2008.
- A. Pitzschke et al. Ideal MHD stability calculations for H-mode plasmas with snowflake divertor configuration. Number 502. SPS-ÖPG-ÖGAA, Innsbruck, Austria, 2009.
- D. Wagner, A. Pitzschke, et al. Particle transport in TCV H-modes. In *37th EPS Conf. on Plasma Phys.*, P1.1101. Dublin, Ireland, 2010.